NON-PHOTOTROPIC HYPOCOTYL 3 (NPH3): A Link Between Blue Light Perception and Endocytic Regulation During Plant Phototropism?

Dissertation

der Mathematisch-Naturwissenschaftlichen Fakultät
der Eberhard Karls Universität Tübingen
zur Erlangung des Grades eines
Doktors der Naturwissenschaften
(Dr. rer. nat.)

vorgelegt von
Atiara Fernández Espinoza
aus Providencia, Chile

Tübingen
2026

Gedruckt mit Genehmigung der Mathematisch-Naturwissenschaftlichen Fakultät der Eberhard-Karls-Universität Tübingen.

Tag der mündlichen Qualifikation:	06.05.2026
Dekan:	Prof. Dr. Thilo Stehle
1. Berichterstatter/-in:	Prof. Dr. Claudia Oecking
2. Berichterstatter/-in:	Prof. Dr. Klaus Harter

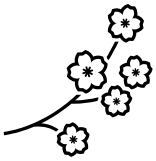

“We have to be able to abandon everything we are,
to become what we might be”

Demian (1919)
H. Hesse

Table of Contents

List of Abbreviations

A. thaliana	*Arabidopsis thaliana*
A. tumefaciens	*Agrobacterium tumefaciens*
AGC	cAMP-dependent protein kinase A, cGMP-dependent protein kinase G and phospholipid-dependent protein kinase C
AP	Affinity Purification
AP-2	Adaptor Protein complex 2
ARF7	AUXIN RESPONSE FACTOR 7
AtEH1	ARABIDOPSIS THALIANA EH-DOMAIN CONTAINING PROTEIN 1
ATP	Adenosine triphosphate
AUX1/LAX	AUXIN RESISTANT 1/LIKE AUX1 (auxin influx carriers)
BFA	Brefeldin A
BirA*	Biotin ligase mutant from *E. coli* (TurboID)
BL	Blue light
BLUS1	BLUE LIGHT SIGNALING 1
BTB	Broad-complex, Tramtrack and Bric-à-brac domain
CC	Coiled Coil domain
CCR4-NOT	CARBON CATABOLITE REPRESSION 4-NEGATIVE ON TATA LESS Complex
CCV	Clathrin-coated vesicle

CHX	Cycloheximide
CIE	Clathrin-independent endocytosis
CLC2/CLC3	Clathrin light chain 2/3
CLSM	Confocal laser scanning microscopy
CME	Clathrin-mediated endocytosis
Col-0	Columbia-0, wild type
CPT1	COLEOPTILE PHOTOTROPISM PROTEIN 1
CRL3	CUL3 RING E3 UBIQUITIN LIGASE
D6PK	D6 PROTEIN KINASE
DR5	Direct Repeat 5, auxin-responsive synthetic promoter
DRPs	Dynamin-related proteins
E. coli	*Escherichia coli*
ENP	ENHANCER OF PINOID (NRL protein family)
FAPS	Fluorescence-Activated Particle Sorting
FDR	False discovery rate
FM4-64	Styryl dye for membrane labelling
FMN	Flavin mononucleotide
FRET-FLIM	Förster resonance energy transfer-fluorescence lifetime imaging microscopy
GFP	Green fluorescent protein
h	hour
HBL	High Intensity Blue light
HSP70	HEAT SHOCK PROTEIN 70 kDa
IAA	Indole-3-acetic acid
iBAQ	intensity-Based Absolute Quantification
IDR	Intrinsically disordered region
IP	Immunoprecipitation
IP-GFP	Immunoprecipitation using GFP-tagged bait
KEGG	Kyoto Encyclopedia of Genes and Genomes
LC-MS/MS	Liquid chromatography tandem mass spectrometry
LFQ	Label-free quantification

LLPS	Liquid-liquid phase separation
LOV	Light-oxygen-voltage domain
mA	milli ampere
MAB4	MACCHI BOU-4 (NRL protein family)
MEL	MAB4/ENP/NPY1-LIKE (NRL protein family)
min	Minute
MS	Mass spectrometry
MS medium	Murashige & Skoog growth media
mTQS2	mTurquoise2
N. benthamiana	*Nicotiana benthamiana*
NCH1	NRL PROTEIN FOR CHLOROPLAST MOVEMENT 1 (NRL protein family)
NOT9B	Component of CCR4-NOT complex
NPH3	NON-PHOTOTROPIC HYPOCOTYL 3 (NRL family)
NPY	NAKED PINS IN YUCCA (NRL family)
P.S.	Ponceau staining
PCT	Proteome Center Tübingen
phot1/phot2	PHOTOTROPIN 1/2
PID	PINOID kinase
PIN	PIN-FORMED auxin efflux carriers
PKS	PHYTOCHROME KINASE SUBSTRATE
PM	Plasma membrane
PP2C	Protein phosphatase 2C
p.S.	phosphoserine residue
p-value	Probability value
q-value	Adjusted p-value
RFP	Red Fluorescent Protein
RNA	Ribonucleic acid
RPT2	ROOT PHOTOTROPISM 2 (NRL protein family)
RT	Room temperature
S_0	variance-stabilizing parameter in Perseus analysis

SA	Streptavidin
SDS-PAGE	Sodium dodecyl sulfate polyacrylamide gel electrophoresis
TPC	TPLATE complex
TSET	Ancient adaptor complex
TurboID	Biotin ligase
UV	Ultra violet
UVR8	UV RESISTANCE LOCUS 8
WAG	WAVY ROOT GROWTH
WT	Wild type
Y2H	Yeast two hybrid
YFP	Yellow fluorescent protein
μmol m^{-2} s^{-1}	Micromoles per square meter per second

Index I: Introduction Figures

Index II: Material and Methods Tables

Index III: Results Tables

Index IV: Results Figures

Index V: Supplementary Information

1. Introduction

1.1 Plant Phototropism and auxin transport

Plants are able to dynamically adjust their growth in response to environmental cues. Phototropism is a light-directed growth response in which shoots reorient towards an incoming light source, thereby enhancing light capture. Shoots typically grow toward the light (positive phototropism), whereas young roots typically grow away from it (negative phototropism). The resulting phototropic bending is primarily driven by an asymmetric distribution of the phytohormone auxin, which translates light perception into differential cell elongation and growth across different plant tissues (Fankhauser and Christie, 2015; Liscum et al., 2020, 2014; Whippo and Hangarter, 2006).

The theoretical framework for phototropism originates from Darwin's pioneering work. Using grass coleoptiles, Darwin and his son demonstrated that light is perceived at the tip of the plant and proposed that a signal transmitted from there induces bending in the lower tissues (Darwin and Darwin 1880). This signal was later identified as the growth-promoting hormone auxin (Went, 1935). These findings led to the *Cholodny-Went* theory, which proposes that unilateral light causes auxin redistribution toward the shaded side of the organ, generating a gradient that drives differential cell elongation and bending (Adamowski and Friml, 2015; Christie and Murphy, 2013; Thimann, 1992; Went and Thimann, 1937).

In monocot coleoptiles, phototropic bending occurs in sequential phases: an early, rapid tip response to low light fluences (first positive phototropism) is followed by slower basal growth under prolonged irradiation in a time-dependent manner (second positive phototropism). In dicots such as *Arabidopsis thaliana*, hypocotyl curvature is likewise fluence- and time-dependent but primarily occurs along the hypocotyl elongation zone rather than through a tip-to-base mechanism (Briggs, 2014; Christie and Murphy, 2013; Everett and Thimann, 1968; Haga and Sakai, 2023; Yamamoto et al., 2014).

In seedlings, auxin is synthesized predominantly in young aerial tissues, including the shoot apex and young leaves, and is transported basipetally through the hypocotyl under conditions such as overhead illumination. In contrast, upon unilateral irradiation one side of the plant receives light (the illuminated side), while the opposite side remains deprived (the shaded side). Under these conditions, auxin is redistributed laterally, with its transport being diverted from the illuminated side towards the shaded side of the hypocotyl, leading to auxin accumulation on the latter (Intro. Fig. 1) (Dela Fuente and Leopold, 1968; Friml, 2003; Liscum et al., 2014).

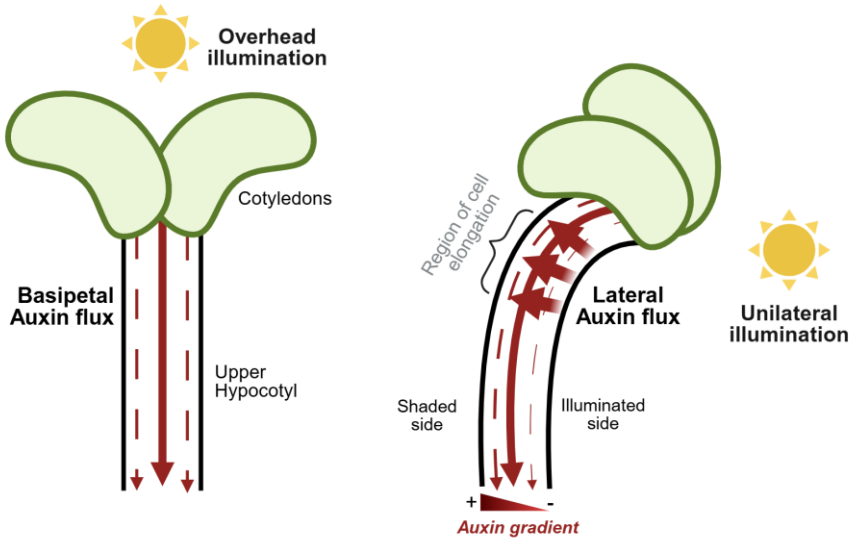

Intro. Figure 1. Auxin transport redistribution during phototropic bending

Schematic representation of a vertically growing seedling under overhead illumination (left), showing basipetal auxin transport from the shoot apex and young leaves through the hypocotyl. Cotyledons are indicated at the shoot apex. Upon unilateral illumination (right), auxin is redistributed laterally, moving away from the illuminated side and accumulating on the shaded side, thereby creating an asymmetric auxin gradient across the hypocotyl. This gradient drive differential cell elongation within the hypocotyl elongation zone (denoted as *region of cell elongation*), resulting in bending toward the incoming light source. Arrows represent the direction and relative magnitude of auxin transport. Adapted from Liscum et al. (2014).

This lateral auxin gradient promotes differential growth rates within the hypocotyl elongation zone, resulting in plant curvature towards the incoming light source (Han et al., 2021; Kramer and Bennett, 2006). Because phototropic bending requires directional redistribution of auxin rather than changes in total auxin levels, the mechanisms governing cellular auxin transport are central to understanding phototropism.

Indole-3-acetic acid (IAA) is the most abundant naturally occurring auxin and regulates a wide range of developmental processes and environmental responses in plants (Takubo et al., 2020). Unlike many plant hormones that are transported primarily via the vascular system, auxin exhibits a prominent polar, cell-to-cell transport mechanism, that enables directional signalling at the tissue and cellular level (Anfang and Shani, 2021). According to the chemiosmotic model, IAA is predominantly protonated (IAAH) in the acidic apoplast (pH ~5), enabling its entry into cells by passive diffusion as well as through auxin influx carriers of the AUX1/LAX family (Blakeslee et al., 2005; Péret et al., 2012). Upon entry into the cytosol, IAA is rapidly deprotonated to its anionic form (IAA^-), which limits its ability to passively diffuse across the plasma membrane (PM). This pH-dependent ionization restricts auxin efflux to transporter-mediated pathways and thereby imposes directionality on intercellular auxin movement.

Cellular auxin efflux is primarily mediated by PIN-FORMED (PIN) and ATP-binding cassette subfamily B (ABCB) carriers, although other transporters have also been described (Hammes and Pedersen, 2024). Yet, the asymmetric, polar localization of PIN proteins within the PM largely determines the direction of auxin flow and contributes to the establishment of auxin gradients at the tissue and organ levels (Hammes and Pedersen, 2024; Kramer and Bennett, 2006; Robert and Friml, 2009). Understanding how auxin gradients are established therefore requires dissecting the mechanisms that control PIN polarity, activity, and trafficking.

1.1.1 Regulation of PIN-FORMED auxin efflux carriers

The regulatory principles governing PIN activity and polarity have been largely studied in *A. thaliana* root tissues. Nonetheless, these mechanisms define a general conceptual basis for understanding how PIN polarity can be dynamically modulated in response to environmental cues, including during hypocotyl phototropism.

PIN proteins are auxin efflux carriers named after the *pin1* mutant, which exhibits underdeveloped, *pin-like* inflorescences (Okada et al., 1991). *A. thaliana* encodes eight PINs, classified as canonical (PIN1-4, PIN7) and non-canonical (PIN5, 6, 8), based on sequence features and subcellular localization (Křeček et al., 2009; Sauer and Kleine-Vehn, 2019). All PINs are predicted to contain ten transmembrane helices; however, canonical PINs are distinguished by a long cytosolic hydrophilic loop (HL) between transmembrane helices 5 and 6, whereas non-canonical PINs possess a shorter HL.

Canonical PINs localize predominantly to the PM, where their polar distribution enables long-range, intercellular auxin transport. Their extended HL functions as a regulatory platform, integrating signals that control both transport activity and subcellular localization (Křeček et al., 2009; Luschnig and Friml, 2024). In contrast, non-canonical PINs localize mainly to the endoplasmic reticulum and contribute primarily to intracellular auxin homeostasis rather than directional auxin fluxes (Mravec et al., 2009; Sauer and Kleine-Vehn, 2019).

Canonical PINs also exhibit distinct cell- and tissue-specific expression patterns that shape auxin distribution: PIN1 predominates in vascular tissues, PIN2 in root epidermis and cortex, PIN3 in columella and lateral root cells, PIN4 in the root meristem, and PIN7 in columella and early vascular/embryonic tissues. This coordinated localization and expression patterns underlies their key roles in organogenesis and gravitropism, among other developmental processes (Luschnig and Friml, 2024).

Overall, PIN-mediated auxin transport is regulated at multiple levels, most prominently through phosphorylation-dependent control of activity and polarity. Phosphorylation of conserved serine residues within the HL of PIN1 and PIN3, have been shown to activate auxin efflux (Huang et al., 2010; Weller et al., 2017; Zourelidou et al., 2014). These sites are targeted by members of the so-called AGCVIII kinase family (related to mammalian protein kinase A, protein kinase G, and protein kinase C), including the PM-associated D6 PROTEIN KINASE (D6PK), PINOID (PID), and the related WAVY ROOT GROWTH kinases (WAG1 and WAG2) (Barbosa et al., 2014; Bassukas et al., 2022; Zourelidou et al., 2014). Genetic analyses demonstrated that D6PK family members are essential for efficient basipetal auxin transport, as higher-order *d6pk* mutants exhibit severe transport defects (Zourelidou et al., 2014). Accordingly, *d6pkl1* double mutants show impaired phototropic bending of hypocotyls, likely due to reduced auxin transport from cotyledons toward the hypocotyl (Bassukas et al., 2022; Willige et al., 2013).

In addition to regulating auxin transport activity, AGCVIII kinases play a central role in controlling PIN polarity. PID, WAG1, and WAG2 phosphorylate PINs at conserved RXS motifs within the HL and thereby influence their polar PM localization (Bassukas et al., 2022; Dhonukshe et al., 2010; Huang et al., 2010; Kleine-Vehn et al., 2009; Zourelidou et al., 2014). Notably, this function is mechanistically separate from transport activation, demonstrating that phosphorylation independently regulates PIN activity and polarity.

Moreover, PIN polarity critically depends on continuous intracellular trafficking. Canonical PINs undergo constitutive cycling between the PM and endosomal compartments via clathrin-mediated endocytosis (CME) (Dhonukshe et al., 2007; Kitakura et al., 2011), allowing rapid modulation of PIN abundance and distribution at the cell surface in response to developmental and environmental cues. Following endocytosis, PIN proteins can be recycled back to their original polar PM domain, redirected to an alternative PM domain (as for example, apical versus basal polarity), or sorted into late endosomes for vacuolar and proteolytic degradation (Luschnig and Friml, 2024). A central regulator of basal PIN recycling is the ARF guanine nucleotide exchange factor (ARF-GEF) *GNOM*, which mediates brefeldin A-sensitive recycling in root cells (Geldner et al., 2003; Steinmann et al., 1999).

This regulatory mechanism has been extensively studied in PIN1. Notably, its phosphorylation by PID/WAG kinases instructs recruitment of PIN1 into the apical recycling pathway, competing with GNOM-dependent basal recycling to promote apical PIN1 localization in root cells (Kleine-Vehn et al., 2009). Conserved serine residues (S1-S3) in the PIN1 HL act as key regulatory sites whose phosphorylation state influences

PIN1 polarity and directional auxin transport (Huang et al., 2010). This process is antagonized by protein phosphatase 2A (PP2A)-mediated dephosphorylation (Michniewicz et al., 2007), establishing a reversible phosphorylation mechanism that dynamically tunes PIN trafficking, polarity, and auxin flux.

The HL of PIN proteins contain additional trafficking determinants that integrate multiple sorting signals. It harbours tyrosine- and phenylalanine-based motifs that function as endocytic signals recognized by adaptor protein complexes, including AP-2, thereby promoting CME-driven internalization (Cheng and Wang, 2022; Dhonukshe et al., 2007; Kitakura et al., 2011; Kleine-Vehn et al., 2011; Marcote et al., 2016; Sancho-Andrés et al., 2016). Although functionally analogous, these motifs differ in sequence composition and recognition mechanisms from the classical YXXΦ motifs described in endocytosis of animal systems (Arora and Van Damme, 2021; Ohno et al., 1995).

PIN polarity is thus maintained by several interlinked mechanisms at the PM, including spatially restricted endocytosis, preferential recycling into defined apical or basal domains, and the formation of non-mobile PIN clusters with limited lateral diffusion, which restricts their movement within the PM (Kleine-Vehn et al., 2011).

The resulting polar localization is therefore critical for directional auxin transport and underpins growth responses such as phototropism. In this context, PIN3 plays a particularly central role by undergoing rapid relocalization in response to unilateral light, thereby mediating lateral auxin redistribution and driving differential growth (Ding et al., 2011; Friml et al., 2002; Han et al., 2021).

1.1.2 PIN3 polarization upon unilateral blue light (BL)

Among PINs, PIN3 acts as a key mediator of lateral auxin fluxes during phototropism. As shown by Ding et al., PIN3 undergoes relocalization in response to directional light, directly linking environmental perception to lateral auxin redistribution and hypocotyl bending (Ding et al. 2011). Specifically, unidirectional blue light (BL) triggers PIN3 polarization at the lateral PM of endodermal cells in the hypocotyl (Ding et al., 2011; Rakusová et al., 2015). Genetic evidence indicates that PIN3 acts redundantly with PIN4 and PIN7 in regulating phototropic growth responses: while *pin3/pin4/pin7* triple mutants display severe defects in phototropic bending, *pin3* single mutants show only minor bending defects under long-term unilateral BL (Friml et al., 2002; Willige et al., 2013).

Nevertheless, analysis of DR5 reporter activity in the *pin3* single *loss-of-function* mutant exhibits reduced auxin asymmetry upon unilateral illumination, indicating impaired lateral

auxin redistribution despite the presence of other PINs (Ding et al., 2011). Thus, while PIN4 and PIN7 contribute redundantly to sustained phototropic growth, PIN3 is likely required for proper auxin asymmetry.

In darkness, young seedlings display apolar localization of PIN3 in hypocotyl endodermis cells (Intro. Fig. 2A; Ding et al., 2011). The endodermis is an important barrier between the vasculature and the cortex of the hypocotyl (Cendreau et al. 1997). In endodermis cells, the outer lateral PM faces the cortex, whereas the inner lateral PM faces the vasculature. Upon unilateral BL exposure, PIN3 polarizes toward the inner lateral PM, but only on the illuminated side of the hypocotyl (Intro. Fig. 2B). This relocalization presumable redirects auxin toward the shaded side of the organ, leading to asymmetric auxin distribution and differential growth.

PIN3 polarity requires the PID kinase and GNOM-mediated recycling. Under dark conditions, high PID activity correlates with apolar PIN3 distribution at both inner and outer lateral PMs of endodermal cells. Under unilateral illumination, light-mediated repression of PID transcription occurs on the illuminated hypocotyl side, resulting in less phosphorylated PIN3, which enters a polar GNOM-dependent trafficking pathway that predominantly targets it to the inner lateral PM. Pharmacological and genetic evidence suggests that PIN3 relocalization may also involve transcytosis, a mechanism defined as the spatially restricted endocytic removal of PIN3 from one PM domain followed by targeted recycling to an opposing domain within the same cell (Ding et al., 2011; Luschnig and Friml, 2024).

While transcytosis has not been directly demonstrated in the hypocotyl, this mechanism provides a plausible explanation for BL-induced PIN3 polarization to the inner lateral PM. In this line, studies in gravity-sensing root columella cells provide direct evidence that PIN3 undergoes GNOM-dependent transcytosis. As shown by Kleine-Vehn et al., gravistimulation triggers rapid PIN3 endocytosis, followed by directional recycling to the new basal side, establishing asymmetric auxin fluxes that drive gravitropic bending without requiring *de novo* protein synthesis (Kleine-Vehn et al., 2010). These findings highlight that PIN3 polarity is dynamically regulated through environmentally responsive trafficking pathways, with transcytosis directly demonstrated in roots but only proposed in hypocotyls.

Although the mechanisms controlling PIN3 polarization are only partly understood, it remains unclear how unilateral light perception selectively activates these polarization pathways.

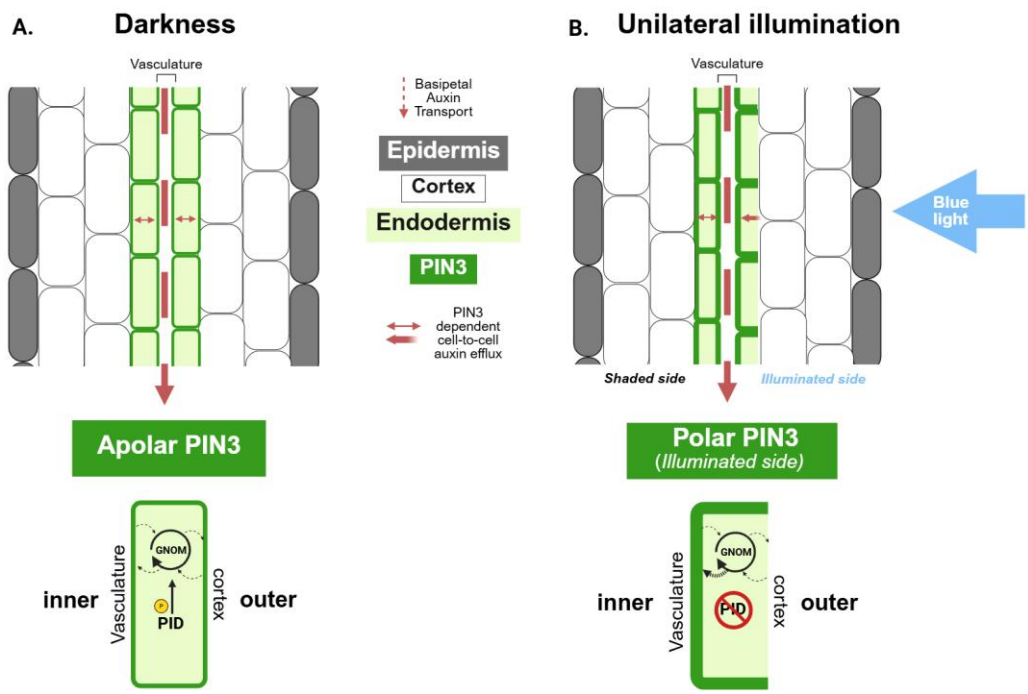

Intro. Figure 2. BL-dependent polarization of PIN3 in hypocotyl endodermis cells

Schematic longitudinal section of an *Arabidopsis* hypocotyl, showing tissue layers from outside to inside: epidermis (grey), cortex (white), endodermis (green), and central vasculature. (A) Dark conditions: PIN3 (dark green) shows an apolar distribution at both inner and outer lateral plasma membranes of endodermal cells, correlating with high PID kinase activity, which phosphorylates the hydrophilic loop (HL) of PIN3. Polar targeting of PIN3 via GNOM-mediated recycling is absent. This apolar distribution allows symmetric lateral auxin transport (red arrows within endodermal cells). (B) Unilateral blue light: PIN3 polarizes toward the inner lateral membrane of endodermal cells on the illuminated side (facing the vasculature), promoting lateral auxin redistribution, presumably toward the shaded side, driving phototropic bending. PIN3 polarization is mediated by light-dependent repression of PID transcription, which results in less phosphorylated PIN3, which can enter a polar GNOM-dependent trafficking pathway, predominantly targeting the inner lateral PM of endodermal cells on the illuminated side of the hypocotyl. Depicted within endodermis cells is GNOM-mediated recycling pathways (black arrows) and the presence/absence of PID. Red arrows indicate the direction of auxin transport. Adapted from Ding et al., 2011; Rakusová et al., 2015.

Because PIN3 relocalization must be initiated by upstream light-sensing mechanisms, understanding how plants perceive directional BL and trigger early signalling events is essential for linking environmental cues such as light, to asymmetric auxin transport. The following section therefore focuses on specialized BL- photoreceptors.

1.2 Plant Photoreceptors: Phototropins and early BL signal perception

In plants, phototropic curvature is specifically triggered by the perception of blue light (BL; ~400-500 nm), with phototropins (phot1 and phot2) acting as the primary photoreceptors mediating this response (Briggs and Christie, 2002; Christie, 2007; Christie et al., 2018; Fankhauser and Christie, 2015; Liscum et al., 2014). Genetic analyses demonstrated that phototropins are essential for canonical BL-induced phototropism, as loss of phototropin function abolishes directional hypocotyl bending

(Doi et al., 2004; Ohgishi et al., 2004). Phototropic light perception occurs predominantly in the upper hypocotyl, where BL rapidly activates phototropin1 and initiates signalling events that precede curvature (Preuten et al., 2013).

In *A. thaliana*, additional photoreceptor families have been identified, including phytochromes (phyA-E), cryptochromes (cry1 and cry2), UVR8, and members of the ZEITLUPE family (De Melo and Alves, 2025; Paik and Huq, 2019). These photoreceptors primarily regulate a broad range of developmental processes, such as seed germination, circadian timing, and photomorphogenesis (Chen and Chory, 2011; Jenkins, 2014; Li and Yang, 2007; Somers et al., 2000; Wang and Lin, 2020). Although cryptochromes and phytochromes can modulate the amplitude and sensitivity of phototropic responses, they are largely dispensable for phot1-mediated BL-induced hypocotyl curvature (Liscum et al., 2020; Stowe-Evans et al., 2001; Sullivan et al., 2019). Accordingly, phototropins constitute the central focus of this chapter.

Phototropins (phot1 and phot2) are PM-associated AGCVIII serine/threonine kinases (Kong et al., 2006; Rademacher and Offringa, 2012; Sakamoto and Briggs, 2002). In contrast to most plant photoreceptors, phototropins initiate rapid, largely non-transcriptional BL-induced responses, enabling direct modulation of growth and cellular processes. These responses include phototropic bending, chloroplast accumulation and avoidance movements, stomatal opening, and leaf positioning (Briggs and Christie, 2002; Christie, 2007; Sakai et al., 2001). Phot1 primarily mediates phototropic responses under low-fluence BL, whereas phot2 contributes more strongly under higher fluence rates and prolonged illumination (Demarsy and Fankhauser, 2009).

Structurally, phototropins contain two N-terminal LOV (Light, Oxygen, Voltage) domains, LOV1 and LOV2, which bind flavin mononucleotide (FMN) and function as BL-sensing modules, followed by a C-terminal kinase domain (Briggs and Christie, 2002; Christie, 2007; Demarsy and Fankhauser, 2009). BL absorption induces conformational changes that relieve autoinhibition of the kinase domain, resulting in phot1 activation through autophosphorylation at conserved serine residues (Ser849/Ser851) leading to subsequent downstream signalling (Inoue et al., 2008; Matsuoka and Tokutomi, 2005). Despite extensive characterization of phototropin activation, the mechanisms by which phot1 signalling is coupled to auxin transporters rearrangement remain largely unknown.

To date, only a limited number of direct substrates of phot1 have been identified. One example is BLUE LIGHT SIGNALING 1 (BLUS1), whose phot1-dependent phosphorylation is required for BL-induced stomatal opening (Takemiya et al., 2013). Additional components acting downstream of phototropins include the protein kinases

CBC1 and CBC2 (CONVERGENCE OF BLUE LIGHT AND CO_2), which function in phototropin-mediated guard cell signalling and stomatal regulation (Hiyama et al., 2017). Moreover, phot1-mediated phosphorylation of the auxin efflux transporter ABCB19 has been shown to inhibit its activity, thereby modulating basipetal auxin transport in the shoot apex (Christie et al., 2011). This regulation affects auxin distribution above the elongation zone during phototropic responses but does not directly generate the asymmetric auxin gradient within the hypocotyl elongation zone.

Phototropins also signal through PHYTOCHROME KINASE SUBSTRATE (PKS1-PKS4) proteins, which act redundantly as positive regulators of phototropism and leaf positioning (De Carbonnel et al., 2010; Kami et al., 2014; Lariguet et al., 2006; Sakai and Haga, 2012). Although PKS4 is directly phosphorylated by phot1, this modification appears to function primarily in feedback regulation rather than being strictly required for phototropic curvature (Demarsy et al., 2012; Schumacher et al., 2018).

Members of the NPH3/RPT2-like protein family, including NPH3 and RPT2, are likewise phosphorylated in a phototropin-dependent manner (Sullivan et al., 2021; Waksman et al., 2023), with NPH3 representing one of the earliest signalling components acting downstream of phototropins during hypocotyl phototropism (Christie et al., 2018; Liscum et al., 2020; Motchoulski and Liscum, 1999; Pedmale et al., 2010). Yet, how these early signalling events are translated into directional auxin transport and growth responses remain unresolved.

1.3 NPH3/RPT2 Like Protein family (NRLs)

The NPH3/RPT2-like (NRL) protein family in *A. thaliana* is named after its two founding members, NON-PHOTOTROPIC HYPOCOTYL 3 (NPH3) and ROOT PHOTOTROPISM 2 (RPT2). The family comprises 33 members that share a conserved NPH3 domain of unknown biochemical function (Christie et al., 2018; Pedmale et al., 2010). Many NRL proteins additionally contain an N-terminal bric-a-brac, tramtrack, and broad complex (BTB) domain and/or a C-terminal coiled-coil (CC) region, suggesting roles in protein-protein interactions. Phylogenetic analyses subdivide the family into six clades, although the biological functions of most members remain poorly characterized. To date, the three best studied subclades are: NAKED PINS IN YUCC (NPY), RPT2/NRL PROTEIN FOR CHLOROPLAST MOVEMENT 1 (RPT2/NCH1) and NPH3 (Christie et al., 2018).

The NPY subclade includes NPY1 (NAKED PINS IN YUCC MUTANT 1, also known as *ENP*- ENHANCER OF PINOID or *MAB4*- MACCHI BOU-4) and its paralogs MEL1-MEL4 (MAB4/ENP/NPY1-LIKE). Members of this subclade regulate PIN-dependent auxin

transport and associated developmental processes. *Loss-of-function* mutants display defects in PIN polarity and auxin-mediated responses, including gravitropism and organogenesis (Cheng et al., 2008; Furutani et al., 2011, 2007). MAB4/MEL proteins function within a regulatory network involving the AGCVIII kinases that phosphorylate PIN proteins, including PID, WAG1/WAG2, and D6PK (I. C. Barbosa and Schwechheimer, 2014; Barbosa et al., 2018; Bassukas et al., 2022). PIN2 phosphorylation by PID promotes the recruitment of MAB4/MEL proteins to the PM, forming a positive feedback loop that maintains PIN polarity by restricting lateral diffusion and reinforcing membrane domain organization (Glanc et al., 2021).

As mentioned earlier, phototropins are also members of the plant AGC kinase family but operate in a distinct signalling context. Their activity promotes phosphorylation of specific downstream phototropic signalling components, including NPH3 and RPT2. Although phototropin-mediated phosphorylation of NPY1 has been demonstrated *in vitro* (Sullivan et al., 2021), *in vivo* evidence is currently lacking. Importantly, phototropins do not directly phosphorylate PIN proteins, indicating that distinct AGCVIII kinase subgroups can independently regulate light signalling and auxin transport pathways that ultimately converge on directional growth responses (Ding et al., 2011; Rakusová et al., 2015).

The RPT2/NCH1 subclade plays a central role in phototropin-mediated responses. NCH1 is required for chloroplast accumulation and can physically associate with phot1, linking it directly to phototropin signalling (Suetsugu et al., 2016). Similarly, PM-associated RPT2 is phosphorylated in a phototropin-dependent manner (Waksman et al., 2023). RPT2 contributes to BL-dependent processes, including hypocotyl phototropism, leaf positioning, and chloroplast movement (Harada et al., 2013). Although *rpt2* mutants show near-normal phototropic bending under low-fluence BL, they exhibit impaired curvature at higher fluence, indicating that RPT2 modulates phototropin photosensory-adaptation (Haga et al., 2015; Inada et al., 2004; Sakai et al., 2000). RPT2 expression is light-dependent, and protein accumulation is stabilized in a phot1-dependent manner (Kimura et al. 2020). Functionally, RPT2 inhibits phot1 BL-dependent autophosphorylation, suggesting that it fine-tunes phot1 photosensitivity and kinase activity by suppressing LOV1 function in a light-dependent manner (Kimura et al., 2020).

The NPH3 subclade comprises NPH3, NRL12, NRL4, and NRL23/DOT3. While NRL12 and NRL4 remain largely uncharacterized, DOT3 (DEFECTIVELY ORGANIZED TRIBUTARIES 3) has been implicated in leaf vein patterning and vascular development, processes tightly linked to auxin-dependent patterning mechanisms (Petricka et al., 2008). NPH3 is the most extensively studied subclade member and a central mediator

of phototropin signalling during phototropic growth (Christie et al., 2018; Liscum et al., 2020; Manishankar et al., 2026; Reuter et al., 2021; Sullivan et al., 2021). In contrast to NPY proteins, which act downstream of AGCVIII kinases to influence PIN polarity, NPH3 functions upstream of auxin redistribution in phototropin-dependent phototropic signalling. Consistent with this role, the NPH3 monocot ortholog COLEOPTILE PHOTOTROPISM PROTEIN 1 (CPT1) in rice is required for establishing lateral auxin gradients that drive phototropic bending (Haga et al., 2005).

Beyond phototropism, NPH3 contributes to leaf positioning and expansion but does not substantially affect chloroplast accumulation, avoidance movements, or stomatal opening (Christie et al., 2018; Inoue et al., 2008; Suetsugu et al., 2016; Sullivan et al., 2019). In the framework of phototropism, RPT2 has been shown to physically interact with NPH3, consistent with its role downstream of phototropin activation (Haga et al., 2015; Inada et al., 2004). In darkness, phot1 and NPH3 appear to form a PM-associated complex, which is disrupted by BL-induced phot1 activation (Haga et al., 2015). Under continuous or high-intensity BL (HBL), RPT2 promotes reconstitution of the phot1-NPH3 PM complex, maintaining efficient PM-level signalling (Christie et al., 2018; Haga et al., 2015). Activation of phot2 under HBL has been suggested to stabilize NPH3 relocation to the PM, facilitating acclimation to these conditions (Zhao et al., 2018). Yet, the precise mechanism by which NPH3 functions downstream of phot1 to establish phototropic responses remains unclear.

1.3.1 NPH3: light-driven and reversible cycling between the PM and cytosolic condensates

NPH3 (also known as ROOT PHOTOTROPISM 3; RPT3) was identified in a genetic screen for *Arabidopsis* mutants defective in phototropic responses, alongside NPH1 (later renamed as phot1) and NPH4 (AUXIN RESPONSE FACTOR 7, ARF7) (Harper et al., 2000; Liscum and Briggs, 1995; Motchoulski and Liscum, 1999). Acting downstream of phot1, NPH3 is essential for proper phototropic bending, as *loss-of-function* mutants exhibit abolished curvature responses under unilateral BL (Motchoulski and Liscum, 1999).

NPH3 displays a striking and highly regulated subcellular localization pattern: it undergoes reversible, light-dependent cycling between the PM and cytosolic, *membrane-less* condensates (Reuter et al., 2021). This dynamic redistribution is a defining feature of NPH3 function in phototropic signalling.

Structurally, NPH3 contains an N-terminal BTB domain, a central NPH3 domain, and a C-terminal CC domain, along with multiple intrinsically disordered regions (IDRs; Intro.

Fig. 3A). Distinct motifs of NPH3 drive its PM association in darkness as well as its light-induced assembly into cytosolic condensates, providing a mechanistic basis for its dynamic subcellular organization (Manishankar et al., 2026; Reuter et al., 2021).

Consistent with its role as a phot1 signalling component, NPH3 C-terminus directly interacts with the LOV domains of phot1 (De Carbonnel et al., 2010; Motchoulski and Liscum, 1999), as well as with PKS1 and PKS2, which are required for low-light phototropic responses (De Carbonnel et al., 2010; Lariguet et al., 2006). NPH3 is also proposed to act as a substrate adaptor in the CULLIN3 (CUL3)-based RING E3 ubiquitin ligase complex ($CRL3^{NPH3}$), mediating light-intensity-dependent ubiquitination of phot1 (Roberts et al., 2011), through a BTB-mediated interaction with CULLIN3. Although this pathway has been linked to phot1 endocytosis and/or proteasomal degradation, constitutive PM anchoring of phot1 does not impair phototropism, suggesting that ubiquitination-mediated internalization or degradation is dispensable for phot1 function in phototropism (Preuten et al., 2015).

For years, NPH3 was considered to follow a simple phosphorylation/dephosphorylation cycle controlling its PM association, with phosphorylation occurring in darkness and dephosphorylation occurring under BL exposure (Pedmale and Liscum, 2007; Tsuchida-Mayama et al., 2008). Kimura et al. identified seven phosphoserine (p.S.) residues: pS7 (or pS5), pS213, pS223, pS237, pS467, pS474 (or pS476), and pS722 (or pS723), to be phosphorylated in darkness, independently of phot1 in etiolated seedlings (Kimura et al., 2022, 2021). The kinase(s) responsible for establishing these dark-state phosphorylation patterns remain unknown, representing a major unresolved aspect of NPH3 regulation.

Recent studies, however, reveal a more complex regulatory system. In dark-grown seedlings, NPH3 predominantly associates with the PM via its C-terminal amphipathic helix (Reuter et al., 2021). Upon BL perception, phot1 phosphorylates NPH3 in a single C-terminal residue (S744), promoting 14-3-3 protein binding (Reuter et al., 2021; Sullivan et al., 2021). This triggers NPH3 dissociation from the PM followed by the formation of cytosolic, *membrane-less* condensates via liquid-liquid phase separation (Manishankar et al., 2026). Simultaneously, several phot1-independent p.S. residues undergo BL-induced dephosphorylation, representing a “general” NPH3 dephosphorylation state. These events are not coupled to PM dissociation in etiolated seedlings, but they do influence the efficiency of NPH3 in the process of re-association with the PM (Kimura et al., 2021; Reuter et al., 2021).

Consistent with this, NPH3 cytosolic condensates can reassociate with the PM upon retransfer to darkness or under prolonged BL conditions (Kimura et al., 2021; Reuter et

al., 2021), demonstrating its dynamic cycling between PM and cytosol. Recent data indicates that the recovery of the PM-associated NPH3 form (dark-state), involves the PM-localized protein phosphatase PP2C19 (Sakai et al., 2025). Independently, Sullivan et al. further demonstrated that the specific dephosphorylation of the phot1-targeted residue S744 requires the combined activity of both, the protein phosphatases PP2C19 and PP2C35 (Bourgade, 2026; Sullivan et al., 2026).

The functional significance of this dynamic cycle is evident: NPH3 variants locked at the PM (NPH3^{S744A}, unable to bind 14-3-3) or constitutively forming cytosolic condensates (NPH3$^{\Delta C51}$, incapable of PM association and 14-3-3 binding) show impaired phototropic bending (Sullivan et al., 2021; Reuter et al., 2021, Intro. Fig. 3B-C). Together, these findings place NPH3 in a reversible pathway in which phot1-dependent phosphorylation, general dephosphorylation, and cytosolic condensate formation are dynamically regulated under different light conditions. This coordination ensures proper phototropic bending and highlights the essential role of the BL-induced reversible phosphorylation in NPH3 function. How this dynamic cycling links phot1 activation to BL-induced PIN3 polarization and lateral auxin redistribution under unilateral illumination, remains an open question.

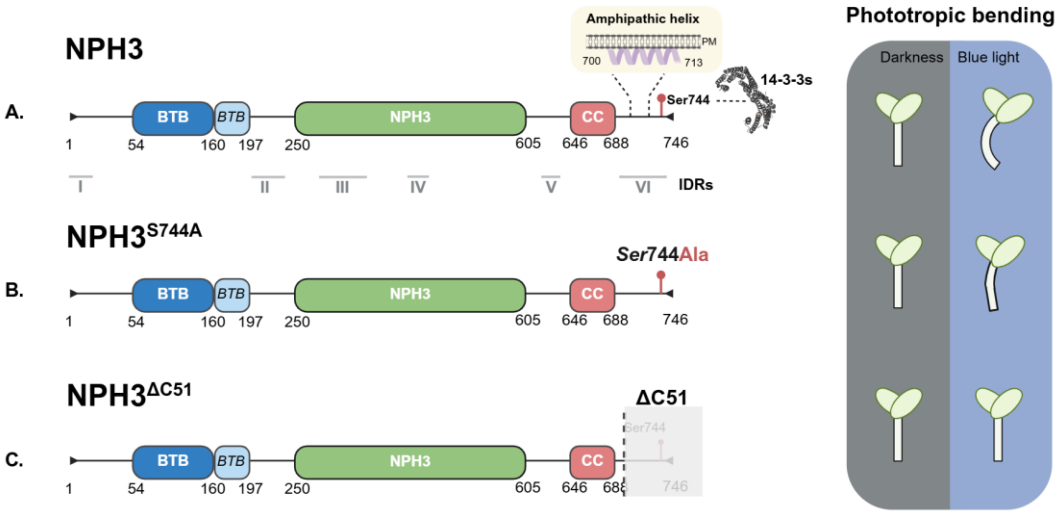

Intro. Figure 3. Structural features of NPH3 and their functional impact on phototropism

(A) Domain architecture of NPH3 (wild type), highlighting the N-terminal BTB domains, the central NPH3 domain, and the C terminal containing a coil coiled (CC) domain. Intrinsically disordered regions (IDRs I-VI) are scattered along the amino acid sequence. The C-terminal domain of NPH3 contains an amphipathic helix (amino acids 700-713) and the blue light regulated phosphorylation site Ser744. Phot1-mediated phosphorylation at Ser744 promotes 14-3-3s binding and correlates with BL induced changes in NPH3 subcellular localization that are required for phototropic bending, observed as approx. a 90° hypocotyl curvature, as shown in the right panel. (B) Structure of the non-phosphorylatable NPH3^{S744A} mutant (Reuter et al. 2021) used in this thesis. Substitution of Ser744 by alanine abolishes phosphorylation and 14-3-3 binding, resulting in a constitutive PM-association. This mutant shows only a partially compromised phototropic bending (±30° curvature). (C) Structure of the C-terminal truncation mutant NPH3$^{\Delta C51}$ (Reuter et

al. 2021), lacking the last 51 amino acids, including the Ser744 and the amphipathic helix that allows for PM-association. This mutant localizes constitutively into cytosolic condensates resulting in completely abolished hypocotyl bending (0°). Domain architectures of NPH3 and NPH3 variants were modified from Manishankar et al. 2026.

1.4 Endocytosis in phototropism and hypocotyl growth

Endocytosis is an essential eukaryotic process that preserves PM homeostasis through vesicle-mediated internalization of PM components (Kraus et al., 2024; McMahon and Boucrot, 2011). Clathrin-mediated endocytosis (CME) therefore regulates the abundance, localization, and turnover of many PM proteins in response to environmental and developmental cues.

During phototropism, BL stimulation is associated with CME of both the photoreceptor phot1 and downstream auxin transport components, albeit with distinct functional roles. Although phot1 undergoes only partial CME-dependent internalization upon BL irradiation (Kaiserli et al., 2009), constitutive PM-anchored phot1 has been shown to be fully functional, indicating that receptor internalization under BL might not be of functional importance (Preuten et al., 2015). In contrast, CME is essential for the BL-induced polar relocalization of the auxin efflux carrier PIN3 in the hypocotyl, a process required for lateral auxin redistribution during phototropic bending (Zhang et al., 2017).

Specifically, unilateral BL triggers clathrin-dependent PIN3 relocalization, as disruption of clathrin light chains CLC2 and CLC3 impairs PIN3 polarization, thereby reducing auxin asymmetry and phototropic curvature (Hu et al., 2021; Zhang et al., 2017).

Notably, NPH3 does not appear to be an endocytic cargo (Haga et al., 2015), but instead undergoes light-regulated dissociation from the PM and reorganization into cytosolic assemblies. Because phot1 signalling, CME-dependent PIN3 polarization, and NPH3 steady-state localization all involve the PM, this compartment likely serves as a coordination platform integrating phototropin signalling, trafficking, and auxin transport during phototropism.

The plant-specific TPLATE complex (TPC) is essential for plant CME, facilitating cargo recognition and recruitment of endocytic machinery. Conditional impairment of the TPC, such as induced-silencing of the TML subunit, reduces endocytosis, evidenced by decreased FM4-64 uptake and reduced accumulation of internalized PIN1 and PIN2 in BFA bodies (Gadeyne et al., 2014). Consequently, CME and TPC-facilitated trafficking are essential for regulating the PM abundance and polarity of key auxin transport components, such as PINs. While the direct molecular links between phot1 activation, NPH3 localization, and PIN3 polarization remain unclear, coordinated endocytic activity

contributes to the establishment of lateral auxin gradients and phototropic growth, providing a cellular framework for the experiments described in this thesis.

1.4.1 The TPLATE Complex and CME in plants

In eukaryotes, the best-characterized endocytic pathway is clathrin-mediated endocytosis (CME), although clathrin-independent mechanisms (CIE) also exist (Sandvig et al., 2011). CME is rapid (~20-70 seconds), temperature-sensitive and proceeds through sequential steps: (i) cargo recognition at the PM, (ii) membrane bending and remodelling, (iii) initiation and maturation of vesicle formation, (iv) vesicle scission and release, (v) actin-mediated transport, and lastly (vi) vesicle uncoating (Intro. Fig. 4). While many CME components are conserved in yeast and mammals, plants have diversified key endocytic proteins (Kraus et al., 2024).

In animal and fungal systems, the heterotetrameric AP-2 complex (Adaptor Protein complex 2. Subunits: α, β, μ, and σ) functions as the canonical clathrin adaptor protein that mediates cargo recognition and vesicle formation at the PM (Boucrot et al., 2010; Collins et al., 2002). Single AP-2 subunit mutants in mice are lethal (Mitsunari et al., 2005). In plants, however, AP-2 mutants are viable and internalize many PM cargos, indicating that AP-2 is not the sole adaptor complex (Bashline et al., 2013; Di Rubbo et al., 2013; Yamaoka et al., 2013).

Comparative analyses revealed an ancestral adaptor-like complex, TSET, present in plants, slime molds, and some protozoa, but not in animals or yeast. TSET comprises four core subunits (TPLATE, TSAUCER, TCUP, and TSPOON), facilitating CME without being essential for survival (Hirst et al., 2014). In plants, this ancestral machinery has been retained and expanded as the TPLATE complex (TPC), which was independently identified in *A. thaliana* through genetic, proteomic, and cell biological approaches (Arora et al., 2020; Gadeyne et al., 2014; Yperman et al., 2021b)

In *Arabidopsis*, TPC is a hetero-octameric complex composed of an inner core: TPLATE, TASH3 (TSAUCER homolog), LOLITA (TSPOON homolog), and TML (TCUP homolog); and an outer core including: Transducin/WD40 repeat-like proteins TWD40-1 and TWD40-2, along with the plant-specific AtEH1 and AtEH2 subunits (illustrated in Intro. Fig. 4A). Functionally, the TPC serves as a central hub for cargo recognition and vesicle initiation during CME, acting cooperatively with the AP-2 at the PM (Intro. Fig. 4B) (Kraus et al., 2024).

While the TPC preserves the core functions of TSET, its subunits have specialized roles. TPLATE acts as the central scaffold required for complex assembly (Gadeyne et al.,

2014; Van Damme et al., 2007). TASH3 contains SH3 domains that recognize ubiquitinated cargo and recruits other TPC subunits (Grones et al., 2022). TML binds cargo via its μ-homology domain (Hirst et al., 2014; Wang et al., 2020), whereas LOLITA stabilizes the inner core. Outer core subunits TWD40-1 and TWD40-2 likely mediate protein-protein interactions, in which TWD40-2 has been proposed to recruit dynamin related proteins (DRPs) involved in vesicle scission (Bashline et al., 2015). The plant-specific subunits AtEH1 and AtEH2 (ARABIDOPSIS THALIANA EH- CONTAINING PROTEINS) mediate membrane-binding and remodelling. They also facilitate cargo recruitment under high turgor pressure and contribute to autophagy, reflecting a plant-specific adaptations (Dragwidge et al., 2024; Johnson et al., 2021; Kraus et al., 2025; Wang et al., 2019; Yperman et al., 2021a).

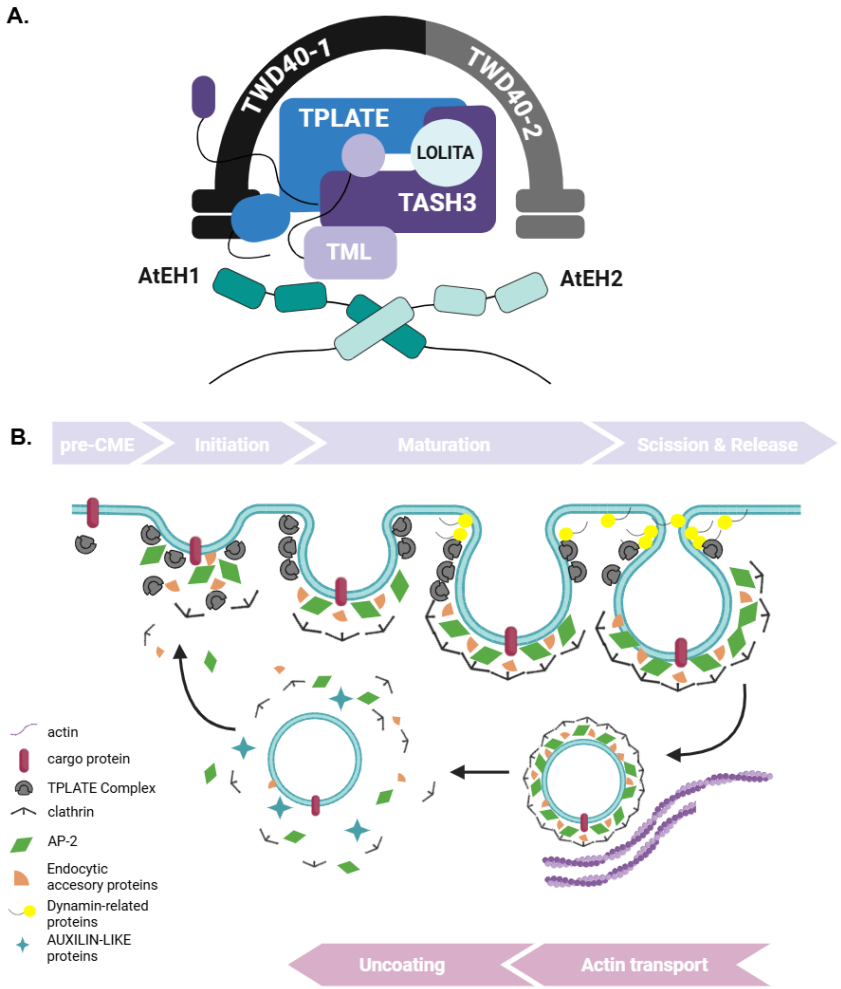

Intro. Figure 4. The TPLATE complex functions at early stages of plant clathrin-mediated endocytosis

(A) Structural organization of the *Arabidopsis thaliana* TPLATE complex (TPC). The inner core consists of TPLATE, TASH3, LOLITA, and TML, which together mediate complex assembly and cargo recognition at the PM. The outer core subunits TWD40-1 and TWD40-2 likely contribute to protein-protein interactions and clathrin coat assembly. The plant-specific AtEH1 and AtEH2 proteins mediate membrane binding and

remodelling and support endocytosis under high turgor pressure. (B) Schematic model of clathrin-mediated endocytosis (CME) in plants. CME proceeds through cargo recognition (pre-CME), initiation, clathrin coat pit maturation, vesicle scission, actin-dependent transport, and vesicle uncoating. Cargo proteins are selectively recognized at the PM by adaptor complexes. The TPC acts at the earliest stages as a scaffold and adaptor that promotes cargo recognition and membrane bending cooperatively with AP-2. AP-2 functions as adaptor complex contributing to cargo selection and clathrin recruitment. Clathrin assembles into a polygonal lattice (clathrin coat). Endocytic accessory proteins support coat assembly and regulatory interactions. Dynamin-related proteins (DRPs) accumulate at the neck of invaginated pits and mediate membrane scission. Actin filaments are required for vesicle transport. AUXILIN-LIKE proteins promote clathrin coat disassembly, enabling vesicle uncoating and vesicle fusion with the recycling machinery or degradation pathways. Once the uncoating process is finished, endocytic machinery components cycle back to the PM. Schemes retrieved and adapted from Kraus et al., 2024.

Unlike AP-2, the TPC is essential for plant growth and viability. *Loss-of-function* mutations in individual TPC subunits either result in male sterility and/or seedling lethality, whereas partial impairment has been shown to affect hypocotyl length (Bashline et al., 2015; Gadeyne et al., 2014; Grones et al., 2022; Wang et al., 2023). TPC partial impairment reduces endocytic event density, leading to flat clathrin assemblies at the PM, indicative of defective membrane curvature, which is essential for vesicle formation (Gadeyne et al., 2014; Wang et al., 2021). At the cellular level, TPC foci arrive at the PM before AP-2 and DRPs, proteins that mediate vesicle formation and scission. TPC subunits biochemically interact with clathrin chains, AP-2 and DRPs (Kraus et al., 2024; Reynolds et al., 2018). This temporal hierarchy places TPC at the very onset of endocytic vesicle formation in plants (Dragwidge et al., 2024; Kraus et al., 2024; Zhang et al., 2015). Overall, TPC represents a distinct evolutionary adaptation of the endocytic machinery in plants, integrating cargo recognition, membrane remodelling, and regulatory functions critical for survival and growth (Gadeyne et al., 2014; Grones et al., 2022; Wang et al., 2021; Yperman et al., 2021b).

1.5 Aims and conceptual model of this thesis

NPH3 is a core component of phototropic signal transduction, acting downstream of the BL receptor phot1 (Motchoulski and Liscum, 1999). While its requirement for phototropic bending is well established, the molecular mechanisms by which NPH3 converts phot1 activation into downstream cellular responses remain poorly understood. Upon BL exposure, phot1 phosphorylates NPH3 at Ser744, promoting 14-3-3 binding, which triggers dissociation from the PM and assembly into cytosolic biomolecular condensates (Manishankar et al., 2026; Reuter et al., 2021; Sullivan et al., 2021). Genetic analyses of NPH3 mutant variants suggest that dynamic cycling between these states is essential for proper phototropic responses (Reuter et al., 2021). However, the molecular environments and interaction partners associated with each state remain largely unknown, limiting mechanistic insight into NPH3 function within the phototropic signalling pathway.

The central aim of this thesis is to define the protein interaction landscape of NPH3 in a subcellular localization-dependent manner. To capture proteins proximal to PM-associated NPH3, TurboID-based proximity labelling is employed. In parallel, immunoprecipitation combined with Fluorescence Activated Particle Sorting (FAPS) is used to enrich and isolate NPH3-containing condensates to identify their molecular constituents. Together, these complementary approaches enable spatially resolved mapping of NPH3 interactomes and direct comparison between functionally distinct states.

To place these interaction networks in a developmental context, this work also investigates how NPH3 contributes to directional growth responses downstream of phototropin activation. In particular, we partially examine NPH3 relationship to the auxin efflux carrier PIN3. By defining light-dependent NPH3 interactomes and evaluating their connection to PIN3 polarization, this thesis aims to provide insights into how phot1 activation is translated into downstream cellular processes that drive phototropic bending. The conceptual framework linking phot1 BL-induced activation, NPH3 dynamics, PIN3 polarization, and phototropic growth is illustrated in Intro. Fig. 5.

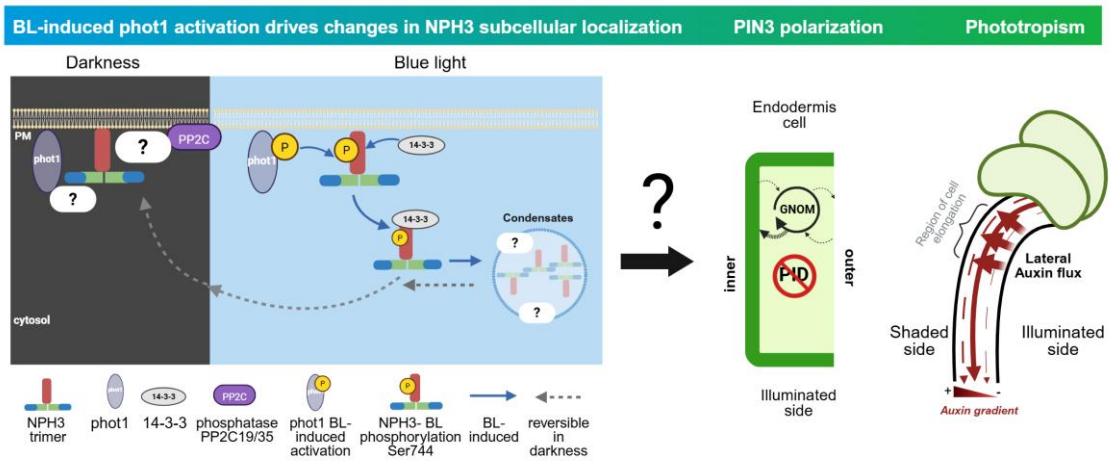

Intro. Figure 5. Conceptual framework for NPH3 function in phototropic signalling

Integrated working model of NPH3 function in phototropism, adapted from Haga et al 2015, Christie et al 2018 and Reuter et al 2021. In darkness, NPH3 (likely in a trimeric conformation, Manishankar et al. 2026) associates with the PM, presumably close to phot1 and other unknown interaction partners (denoted as "?"). BL activation of phot1 induces phosphorylation of NPH3 at Ser744, followed by 14-3-3 binding and PM-dissociation. In the cytosol NPH3 transitions into biomolecular condensates via liquid-liquid phase separation. While these light dependent changes in NPH3 localization are well established, the molecular associations of NPH3 with other proteins at PM/cytosol and their mechanistic connection to PIN3 polarization as well as lateral auxin transport remain unknown. This lack of a defined molecular link represents a central knowledge gap addressed in this thesis.

2. Material and Methods

2.1 Material

Various consumables used for this work (reaction tubes and tips) were purchased from Eppendorf (Hamburg, Germany) or Greiner Bio-One GmbH (Frickenhausen, Germany).

2.1.1 Plasmids

Plasmids containing constructs (under the 35S promoter) were generated by Andrea Bock, Jutta Keicher and Tanja Schmidt using *Gateway Cloning system* (Table 2.1) (Reuter et al. 2021).

Table 2. 1. Gateway Cloning-based constructs used in this study.

Construct	Vector	Resistance	Used for
prom35S::GFP:NPH3^{WT}	pH7WGF2*	Spectinomycin	Transient expression
prom35S::GFP:NPH3^{S744A}	pH7WGF2*	Spectinomycin	Transient expression
prom35S::GFP:NPH3$^{\Delta C51}$	pH7WGF2*	Spectinomycin	Transient expression

(Karimi et al., 2007)*

Plasmids containing constructs (under different promoters) were generated using *Golden Gate Cloning system* (Table 2.2), and produced by Andrea Bock, Jutta Keicher, Tanja Schmidt, Lukas Dittiger and Atiara Fernández.

Table 2. 2. Golden Gate Cloning-based constructs used in this study.

Construct	Vector	Resistance	Used for
prom35SΩEnhancer::mEGFP:NPH3^{WT}	BB10 Plus	Spectinomycin	FRET/FLIM
prom35SΩEnhancer::mEGFP:NPH3^{S744A}	BB10 Plus	Spectinomycin	FRET/FLIM
prom35S::14-3-3Ω:mCherry	BB10 Plus	Spectinomycin	Transient expression
promNPH3::YFP:TurboID:NPH3^{WT}	BB10 Plus	Spectinomycin	Proximity labelling
promNPH3::YFP:TurboID:NPH3^{S744A}	BB10 Plus	Spectinomycin	Proximity labelling
promNPH3::YFP:TurboID:NPH3 $^{\Delta C51}$	BB10 Plus	Spectinomycin	Proximity labelling
prom35SΩEnhancer::mTurquoise2:NPH3^{WT}	BB10 Plus	Spectinomycin	Transient expression
prom35SΩEnhancer::mTurquoise2:NPH3^{S744A}	BB10 Plus	Spectinomycin	Transient expression
promPIN3:PIN:GFP(int)	BB10 Plus	Spectinomycin	Generation of Transgenic lines
prom35SΩEnhancer::HSP70-1:GFP	BB10 Plus	Spectinomycin	Transient expression
prom35SΩEnhancer::HSP70-1:RFP	BB10 Plus	Spectinomycin	Transient expression

Plasmids containing constructs generated by external sources and used in this study are listed in (Table 2.3).

Table 2. 3. Plasmids obtained from external sources.

Construct	Vector	Resistance	Used for	Source
prom35S::mRFP:TPLATE	pH7WGF2*	Spectinomycin	Transient expression	Daniel Van Damme Lab (Ghent University- Belgium)
prom35S::AtEH1:eGFP	pH7WGF2*	Spectinomycin	Transient expression	Daniel Van Damme Lab (Ghent University- Belgium) (Wang et al., 2019)
promUBQ$_{10}$::REM1.2:GFP	pUBN**	Spectinomycin	Transient expression	Julien Gronniers Lab ZMBP- Tübingen)

(Karimi et al., 2007)*, (Grefen et al., 2010)**

Plasmids harbouring TPLATE and AtEH1 variants for yeast two-hybrid (Y2H) experiments were synthesized and purchased from BioCat GmbH (Heidelberg, Germany). The remaining Y2H plasmids were generated by Andrea Bock (Table 2.4) and previously reported. All sequences derived from *Arabidopsis thaliana* (Col-0) unless otherwise indicated.

Table 2. 4. Yeast Two Hybrid plasmids used in this study.

Element	Vector	Resistance	Source/Reference
TPLATE (full length sequence) Eco. Landsberg erecta 3545 bp	pGBKT7	Kanamycin	BioCat GmbH
AtEH1(AT1G20760) N- terminal part (without coiled coiled domain) 1598 bp	pGBKT7	Kanamycin	BioCat GmbH
AtEH1(AT1G20760) N- terminal part (with coiled coiled domain) 1821 bp	pGBKT7	Kanamycin	BioCat GmbH
14-3-3Ω	pGADT7	Ampicillin	(Reuter et al., 2021)
NPH3^{WT}	pGADT7	Ampicillin	(Reuter et al., 2021)
NPH3^{S744A}	pGADT7	Ampicillin	(Reuter et al., 2021)

2.1.2 Plants

In this work *Arabidopsis thaliana*, ecotype Columbia-0 (Col-0) was used. Seeds of the T-DNA induced *loss-of-function* mutant of NPH3, *Arabidopsis thaliana nph3-7* (SALK_110039, Col-0 background) were originally obtained from NASC (Nottingham *Arabidopsis* Stock Centre) and used for the generation of transgenic lines. Stable transformation (*via* the floral dip method) and identification of homozygous lines was

done by Jutta Keicher and Tanja Schmidt. Transgenic *Arabidopsis* lines generated in our lab are listed below (Table 2.5).

Table 2. 5. Arabidopsis transgenic lines.

Construct	Background	Resistance	Independent lines (published)
promPIN3::PIN3(int)	Col-0	Hygromycin	#17-1, #19-1
promPIN3::PIN3(int)	*nph3-7*	Hygromycin	#6-7, #8-6
prom35S::GFP:NPH3^{WT}	*nph3-7*	Hygromycin	#8, #17 (Reuter et al. 2021)
prom35S::GFP:NPH3^{S744A}	*nph3-7*	Hygromycin	#19, #28 (Reuter et al. 2021)
prom35S::GFP:NPH3$^{\Delta C51}$	*nph3-7*	Hygromycin	#23, #19 (Reuter et al. 2021)
promUBQ$_{10}$::GFP	*Col-0*	Hygromycin	(Reuter et al. 2021)
promNPH3::GFP:NPH3^{WT}	*nph3-7*	Hygromycin	#1, #4 (Reuter et al. 2021)
promNPH3::YFP:TurboID:NPH3^{WT}	*nph3-7*	Hygromycin	#7-4, #5-10
promNPH3::YFP:TurboID:NPH3^{S744A}	*nph3-7*	Hygromycin	#3-6, # 7-4
promNPH3::YFP:TurboID:NPH3$^{\Delta C51}$	*nph3-7*	Hygromycin	#13-2, #9-6

In addition, *Arabidopsis* transgenic lines obtained from external sources and used in this study are listed in Table 2.6.

Table 2. 6. Arabidopsis transgenic lines obtained from external sources.

Construct/mutant	Background	Line(s)	Source
nosh	*SALK_011079 x Col-0*	S_9963/**L124** S_9953/**L27**	Daniel Van Damme Lab (Ghent University- Belgium) (Grones et al., 2022)
prom35S::EH1:GFP (AtEH1)	*Col-0*	S_10165/**L1804** S_8001/**L1.2**	Daniel Van Damme Lab (Ghent University- Belgium) (Grones et al., 2022; Wang et al., 2019)
promLAT52::TPLATE:GFP/ prom35S::DRP1A:mRFP	*Col-0 x tplate*	C59	Daniel Van Damme Lab (Ghent University- Belgium)

2.1.3 Bacteria

E. coli strains One Shot™ TOP10 (Thermo Fisher Scientific GmbH, Dreieich) and XL1-Blue were used for plasmid transformation via the heat-shock method to enable plasmid

propagation. The *Agrobacterium tumefaciens* strain GV3101(Koncz and Schell, 1986) was used for transient transformation of *N. benthamiana*. For transient expression assays, the silencing suppressor p19 strain (Win and Kamoun, 2004) was included where indicated in the figure legends.

2.1.4 Chemical, Kits and specific materials

Following chemicals, kits and specific supplies were used during this work (Table 2.7).

Table 2. 7. Utilized chemicals. Kits and specific materials.

Used for	Chemical/kit/material	Manufacturer
Bacterial work	2-(N-morpholino)ethanesulfonic acid (MES)	Carl Roth GmbH + Co. KG, Karlsruhe
	3,5-Dimethoxy-4-hydroxyacetophenone (Acetosyringone)	Sigma-Aldrich Chemie GmbH, Taufkirchen
	Ampicillin	Sigma-Aldrich Chemie GmbH, Taufkirchen
	Ethanol (EtOH)	Sigma-Aldrich Chemie GmbH, Taufkirchen
	GeneJET Plasmid Miniprep Kit	Thermo Fisher Scientific GmbH, Dreieich
	Gentamicin	SERVA Electrophoresis GmbH, Heidelberg
	Kanamycin	Duchefa Biochemie, Haarlem (NL)
	LB-Agar (Luria/Miller)	Carl Roth GmbH + Co. KG, Karlsruhe
	LB-Medium (Luria/Miller)	Carl Roth GmbH + Co. KG, Karlsruhe
	Magnesium chloride ($MgCl_2$) hexahydrate	Carl Roth GmbH + Co. KG, Karlsruhe
	Rifampicin	Duchefa Biochemie, Haarlem (NL)
	Spectinomycin	Duchefa Biochemie, Haarlem (NL)
Plant work	Brefeldin A (BFA)	Thermo Fisher Scientific GmbH, Dreieich
	Hydrochloric acid (HCl)	Sigma-Aldrich Chemie GmbH, Taufkirchen
	Hygromicin	Duchefa Biochemie, Haarlem (NL)
	Murashige and Skoog Medium „Basal Salt Mixture“ (MS medium)	Duchefa Biochemie, Haarlem (NL)

	N-(3-triethylammoniumpropyl)-4-(6-(4-(diethylamino)phenyl)hexatrienyl)pyridinium dibromide (FM 4-64™)	Thermo Fisher Scientific GmbH, Dreieich
	PHYTO AGAR	Duchefa Biochemie, Haarlem (NL)
	Potassium hydroxide (KOH)	Carl Roth GmbH + Co. KG, Karlsruhe
	Sodium hypochlorite (NaClO + H_2O) solution 12%	Carl Roth GmbH + Co. KG, Karlsruhe
	Sucrose	Carl Roth GmbH + Co. KG, Karlsruhe
Protein work	Acetic acid	Carl Roth GmbH + Co. KG, Karlsruhe
	Albumin bovine Fraction V (BSA)	SERVA Electrophoresis GmbH, Heidelberg
	Ammonium bicarbonate (NH_4HCO_3)	Carl Roth GmbH + Co. KG, Karlsruhe
	Ammoniumperoxodisulfate (APS)	Carl Roth GmbH + Co. KG, Karlsruhe
	Biotin	Sigma-Aldrich Chemie GmbH, Taufkirchen
	Bromophenol blue	Carl Roth GmbH + Co. KG, Karlsruhe
	cOmplete™ (Protease Inhibitor Cocktail)	Roche Holding, Basel (CH)
	Dimethylsulfoxide (DMSO)	Carl Roth GmbH + Co. KG, Karlsruhe
	Dithiotreitol (DTT)	Carl Roth GmbH + Co. KG, Karlsruhe
	Dynabeads™ MyOne™ Streptavidin C1	Thermo Fisher Scientific GmbH, Dreieich
	ECL™ Prime Western Blotting Detection Reagent	Cytiva Europe GmbH, Freiburg
	Ethylenediaminetetraacetic acid (EDTA)	Carl Roth GmbH + Co. KG, Karlsruhe
	Ethylene glycol bis(β-aminoethylether) tetraacetic acid (EGTA)	Carl Roth GmbH + Co. KG, Karlsruhe
	Glycerol	Carl Roth GmbH + Co. KG, Karlsruhe
	Milk powder	Carl Roth GmbH + Co. KG, Karlsruhe
	Monosodium phosphate (NaH_2PO4)	Carl Roth GmbH + Co. KG, Karlsruhe
	Nitrocellulose membranes (Amersham™ Protran™)	Sigma-Aldrich Chemie GmbH, Taufkirchen

PD10 desalting columns	GE-Healthcare GmbH Freiburg im Breisgau
Phosphatase Inhibitor Mix I	SERVA Electrophoresis GmbH, Heidelberg
Ponceau S	SERVA Electrophoresis GmbH, Heidelberg
ROTIPHORESE® Gel 30 (37,5:1)	Carl Roth GmbH + Co. KG, Karlsruhe
ROTI®Nanoquant	Carl Roth GmbH + Co. KG, Karlsruhe
Sodium chloride (NaCl)	Carl Roth GmbH + Co. KG, Karlsruhe
Sodium dodecyl sulfate (SDS)	Carl Roth GmbH + Co. KG, Karlsruhe
Tetramethylethylenediamine (TEMED)	Honeywell Fluka®, Seelze
TRIS	Carl Roth GmbH + Co. KG, Karlsruhe
Triton X-100	Sigma-Aldrich Chemie GmbH, Taufkirchen
TWEEN® 20	Carl Roth GmbH + Co. KG, Karlsruhe

2.1.5 Buffers and Solutions

The following buffers and solutions were used for this work. If not stated differently, buffers and solutions were prepared by using double-distilled water (ddH_2O).

Table 2. 8. Utilized buffers and solutions.

Buffer/Solution	Composition
½ MS medium	2.2 g MS „Basal Salt Mixture“/ Liter pH adjusted to 5.7 with KOH 1 % PHYTO AGAR autoclaved
2x SDS sample buffer	125 mM TRIS/HCl (pH 6.8) 4 % SDS 20 % Glycerol 0.01 % Bromophenol blue 1 tablet cOmplete™ per 50 ml 10 % DTT *added fresh*
10x SDS Running buffer	200 mM TRIS 1.5 M Glycine 0.1 % SDS
Ammonium bicarbonate (ABC) buffer (final wash for mass spectrometry analysis)	20 mM pH: ~8.0

AS medium (Infiltration tobacco)	10 mM $MgCl_2$ 150 µM Acetosyringone 10 mM MES/NaOH (pH 5.6)
Biotin solution	2.44 mg biotin/100ml H_2O (100 µM)
Blocking solution	4 % milk powder Dissolved in 1xTBS buffer
Extraction buffer (IP and Co-IP)	50 mM TRIS/HCl (pH 7.5) 150 mM NaCl **1 mM EDTA** **0.75 % Triton X-100** 1 x cOmplete™ Phosphatase Inhibitor Mix I
Extraction buffer (Proximity Labelling)	50 mM TRIS/HCl (pH 7.5) 150 mM NaCl **1 mM EGTA** **1 % Triton X-100** 1 x cOmplete™ Phosphatase Inhibitor Mix I
Extraction buffer (Crude extract)	20 mM TRIS/HCl (pH 7.0) 150 mM NaCl 1 mM EDTA 1 % Triton X-100 0.1 % SDS 10% (v/v) DTT
LB-Agar (Luria/Miller)	40 g LB-Agar / L autoclaved
LB-Medium (Luria/Miller)	25 g LB-Medium / L autoclaved
Ponceau S	0.1 % (w/v) Ponceau S 2 % (v/v) Acetic acid
Stripping buffer	0.2 M Glycine 0.1 % (w/v) SDS 1 % (v/v) TWEEN® 20 pH adjusted to 2.2 with HCl
TBS-T	1 x TBS buffer 0.2 % (v/v)TWEEN® 20
Transfer buffer/Towbin Buffer	25 mM Tris 192 mM Glycine 20 % v/v Ethanol *added fresh*
Washing buffer I	50 mM TRIS/HCl (pH 7.5) 150 mM NaCl 1 mM EDTA

	0.1 % (v/v) Triton X-100
Washing buffer II	50 mM TRIS/HCl (pH 7.5) 150 mM NaCl

2.1.6 Antibodies

Following Antibodies were used in this work.

Table 2. 9. Antibodies

Antibody	Manufacturer	Dilution
α-EH1	Daniel Van Damme (Wang et al., 2019)	1: 500
α-GFP (A1122)	Thermo Fisher Scientific, Sindelfingen	1: 1000
α-GFP (PA1-980A)	Thermo Fisher Scientific, Sindelfingen	1: 1000
α-HA High Affinity	Roche Holding, Basel (CH)	1: 1000
α-Mouse	Promega, Walldorf	1: 10000
α-Myc (9E1)	Chromotek GmbH, Planegg	1: 1000
α-NPH3	Eurogentec, Liege (BEL)	1: 500
α-NPH3 (PS744)	Eurogentec, Liege (BEL)	1: 500
α-Rabbit	Promega, Walldorf	1: 10000
α-Rat	Sigma-Aldrich Chemie GmbH, Taufkirchen	1: 10000
α-RFP (5F8)	Chromotek GmbH, Planegg	1: 1000
α-Streptavidin Pierce™	Thermo Fisher Scientific, Sindelfingen	1: 5000
α-TurboID (BirA*)	Agrisera, Vännäs, (SWE)	1: 5000

The rabbit α-NPH3 and α-NPH3 (PS744) antibodies were generated by using the synthetic peptide NH2-PPRKPRRWRN-S(PO3H2)-IS-COOH followed by affinity purification against the non-phosphorylated and phosphorylated peptide (Eurogentec, Liege, BEL) (Reuter et al., 2021).

2.2 Methods

2.2.1 Cloning procedures

Cloning procedures followed standard techniques of the Gateway Cloning system (Thermo Fisher Scientific GmbH, Dreieich) or the Golden Gate Cloning system (Binder et al., 2014). Cloning was jointly performed by Andrea Bock, Jutta Keicher, Tanja Schmidt, Lukas Dittiger and Atiara Fernández.

2.2.1.1 Transformation of Escherichia coli

For plasmid propagation, One Shot™ TOP10 and XL1-Blue *E. coli* cells were transformed via heat shock. 100 µl of competent cells were thawed on ice, mixed with

plasmid, and incubated on ice for 30 min. Cells were then heat-shocked at 42 °C for 45 s, followed by addition of 900 µl LB to recover the cells and incubation at 37 °C for 1 h. 100 µl of the culture was plated on LB-agar with 100 µg/ml spectinomycin/gentamicin and incubated at 37 °C for 1 day.

2.2.1.2 Plasmid isolation

Plasmids were isolated using the GeneJET Plasmid Miniprep Kit (Table 2.7) per the manufacturer's protocol. DNA concentration and quality were measured with a NanoDrop® Lite plus (Thermo Fisher Scientific).

2.2.2 Yeast two Hybrid (Y2H)

For Y2H analyses, the vectors listed in Table 2.4 were co-transformed into the yeast strain PJ69-4A. ADE2 reporter activity was assessed by growth of co-transformed yeast on synthetic dropout medium lacking adenine. Experiments were repeated three times, and no ADE2 activation was observed. Crude yeast extracts were analysed by Western blot to verify protein expression.

2.2.3 Transient transformation of *Nicotiana benthamiana*

For transient expression *Nicotiana benthamiana* was used. The tobacco plants were cultivated and propagated by the central greenhouse facility of the ZMBP, Eberhard Karls University Tübingen.

2.2.3.1 Transformation of Agrobacterium tumefaciens

Competent *A. tumefaciens* GV3101 cells were transformed by heat shock. 100 µl of competent cells were thawed on ice, and the appropriate binary vector was added. The mixture was incubated on ice for 5 min, snap-frozen in liquid nitrogen for 5 min, and then heat-shocked at 37 °C for 5 min. Cells were recovered in 900 µl LB medium and incubated at room temperature (RT) with gentle rotation for 3 h. 100 µl of the culture were plated on LB agar containing rifampicin, gentamicin, and spectinomycin; for p19 constructs, kanamycin replaced spectinomycin. Plates were incubated at 28 °C for 2 days.

2.2.3.2 Transient transformation of N. benthamiana leaves

Transient transformation was performed as described in (Grefen et al., 2010). From the 5 ml overnight cultures, 1 ml of transformed *A. tumefaciens* (see 2.2.2.1) were diluted into 4 ml fresh LB medium containing the respective antibiotics and grown 3-4 h at 28 °C. Cultures (4 ml) were centrifuged (2000 × g, 5 min), washed with ddH_2O, and

resuspended in 1 ml AS medium (Table 8). OD_{600nm} was adjusted to 0.1-0.3, and suspensions incubated on ice for 30 min. For co-infiltration, agrobacterial cultures were mixed in a 1:1 ratio; if p19 was included a fixed OD of 0.1 was used. Leaves of four-week-old *N. benthamiana* were infiltrated abaxially with a needleless syringe, kept for 24 h in light, and then adapted for ~16 h in darkness. Leaves were either analysed under confocal microscopy or harvested as plant material. Under dark conditions (handled under red safety light) or after BL treatments (10 µmol m^{-2} s^{-1}), and subsequently frozen in liquid nitrogen for transient expression analyses.

2.2.4 Seed sterilization and seedlings cultivation

Seed surface sterilization was performed by chlorine-gas under a fume hood. Seeds were sterilized using chlorine gas generated by combining 12% sodium hypochlorite solution with 37% HCl in a 10:1 v/v ratio (Table 7). Seeds (Tables 5, 6) were placed in 2 ml open microcentrifuge tubes (Eppendorf) in a sealed glass desiccator and exposed overnight. The sterilized seeds were subsequently left opened a laminar flow hood for complete removal of the residual chlorine gas and finally sown on plates containing half strength MS medium (with or without sucrose supplementation, see figure legends for each experiment). For etiolated seedling cultivation, seeds were stratified for at least two nights at 4 °C, exposed to fluorescent white light for 4 h, and then grown in darkness (vertically) at RT. Unless stated otherwise, three- to five-day old *Arabidopsis* etiolated seedlings were used in this study.

2.2.4.1 Generation of A. thaliana transgenic lines

Stable transformation of *Arabidopsis thaliana nph3-7* or Col-0 was carried out using *Agrobacterium tumefaciens*-mediated transformation (see 2.2.2.1) following the floral dip method (Clough and Bent, 1998). Transgenic lines were grown on half strength MS plates and selected through successive generations as follows: T_0 plants were screened for hygromycin resistance; T_1 plants were confirmed by hygromycin selection (and if required genotyping); T_2 lines were evaluated for a 3:1 segregation ratio of hygromycin resistance; and T_3 homozygous lines were verified by detection of the tagged protein via Western blotting. After each selection cycle, positive plants were transferred to soil and grown in a greenhouse under long-day conditions (16 h light/8 h dark) to obtain seeds.

2.2.5 Hypocotyl phototropism analysis

A. thaliana seedlings were grown in darkness on vertically oriented half strength MS plates for 48-36 h. Etiolated seedlings were then transferred to an LED chamber and exposed to unilateral blue light (0.1 µmol m^{-2} s^{-1}) for 24 h. Plates were scanned, and the

inner hypocotyl angle of each seedling was measured using ImageJ (Schneider et al., 2012). Curvature angles were calculated as 180° minus the measured value. For each transgenic line, at least three biological replicates were conducted (≥30 seedlings per replicate), along with the appropriate controls (Col-0 and *nph3-7*).

2.2.6 TurboID-based proximity labelling Approach

To establish a proximity labelling approach, we followed several published protocols (Arora et al., 2020; Mair et al., 2019). TurboID fusion proteins were tested either by transient expression in *N. benthamiana* or using stably transformed transgenic lines of *A. thaliana*.

2.2.6.1 Biotinylation assays in N. benthamiana

Proof of principle experiments were conducted to assess TurboID-mediated biotinylation. Leaf tissues previously transformed with *Agrobacterium* (see Section 2.2.3.2) were re-infiltrated with a biotin solution (50 or 100 µM, see 2.1 Table 8) and incubated at RT for approximately 45 min under overhead blue light (10 µmol m^{-2} s^{-1}). After treatment, leaf tissues were harvested, snap frozen using liquid nitrogen, and further processed for subsequent immunoprecipitation analysis.

2.2.6.2 Biotinylation assays in A. thaliana

Biotin treatments were performed on whole, three to five-day-old, etiolated seedlings grown on solid half strength MS medium with and without sucrose supplementation (specified on each figure legends). Dark-grown seedlings were handled under red safe light, submerged in 100 µM biotin solution, and incubated for defined time intervals at RT (either kept in darkness or under overhead BL 10 µmol m^{-2} s^{-1}). Pools of seedlings (approximately ~100 mg) were collected and washed twice with ice cold water. After rinsing, the plant material was gently dried and snap-frozen in liquid nitrogen. Samples were subsequently processed for Western blot analysis. Similarly, treatments using water (mock, 0 biotin) instead of biotin solution also resulted in detectable protein biotinylation.

2.2.6.3 Streptavidin-Affinity purification (AP) and sample preparation for Mass spectrometry (MS)

TurboID-based proximity labelling was carried without exogenous biotin application in four -to-five days old, etiolated *Arabidopsis* transgenic lines. Protein extraction was performed at 4°C using precooled pestles and mortars. Dark adapted samples were processed under red safe light illumination. Pooled plant material (~ 4 g per sample) was

ground in liquid nitrogen and mixed with extraction buffer (50 mM Tris-HCl, pH 7.0; 150 mM NaCl; 1% Triton X-100; 1 mM EGTA; 1% protease inhibitor cocktail; 1% phosphatase inhibitor mix I) at a 2:1 buffer-to-tissue ratio (2 ml per g tissue), yielding ~8 ml total extract. Thawed extracts were homogenized and incubated for 1 h at 4 °C on a rotating wheel, followed by centrifugation twice at 16,000 rpm for 30 min at 4 °C, transferring the supernatant to fresh tubes after each spin. Each sample was divided into three triplicates (2.5 ml) for biotin depletion. For desalting, 2.5 ml of extract was applied to PD-10 columns (GE healthcare, Sephadex G-25) pre-equilibrated with ~25 ml extraction buffer. Eluates obtained through gravity flow protocol (~3.5 ml) were collected and incubated with pre-equilibrated Streptavidin Dynabeads™ (50 µl beads per ml eluate) in 5 ml Eppendorf tubes for 1.5 h at 4 °C on a rotating wheel. Beads were washed sequentially twice with Washing I (50 mM Tris-HCl, pH 7.0; 150 mM NaCl; 1% Triton X-100; 1 mM EGTA), twice with Washing II (50 mM Tris-HCl, pH 7.0; 150 mM NaCl), and twice with ABC buffer (20 mM ammonium bicarbonate, pH 8.0). For each wash, 1 ml of sample was transferred to low-binding 1.5 ml tubes, beads were separated on a magnetic rack and incubated for 10 min on a rotating wheel at 4 °C, repeating until the full sample volume was processed. Final samples (beads only) were stored at -20°C until delivery at the Proteome centre Tübingen (PCT).

2.2.6.4 MS and Statistical analyses used for TurboID-based proximity labelling

PCT mass spectrometry (MS) analysis was performed with on-bead digestion, using the iST kit (Preomics) with LysC and trypsin. Following purification, samples were adjusted to a final volume of 20 µl, and 1 µl of a 1:10 dilution and injected for LC-MS analysis. LC-MS/MS was conducted on a Proxeon Easy-nLC system coupled to a Q Exactive HF mass spectrometer using a 60 min Top7 HCD method. Raw data were processed with MaxQuant software (version 2.2.0.0) (Tyanova et al., 2016a) incorporating the Andromeda peptide search engine, searching against the *Arabidopsis thaliana* database (Arabidopsis_thaliana_allStrains_2022-12-16.fasta) with iBAQ quantification enabled.

Final peptide identification lists were processed according to (Arora et al., 2020). In which significantly enriched proteins in bait versus control samples were identified using LFQ intensities in Perseus software (Tyanova et al., 2016b). The MaxQuant proteinGroups.txt file (obtained from PCT) was loaded into Perseus, and reverse hits, contaminants, and identifications “only by site” were removed. LFQ intensity values were $\log_2$-transformed, and samples were grouped according to bait and control triplicates using categorical annotation of rows. Proteins were filtered to retain those with at least two valid values in one group, and missing values were imputed from a normal distribution with default

Perseus settings (width = 0.3, downshift = 1.8). A two-sample t-test was then performed between bait and control, and results were visualized in a volcano plot. Significance thresholds were determined using permutation-based FDR, with standard settings of FDR = 0.05 and S_0 = 0.1 were applied to refine the set of proteins significantly enriched with the bait.

2.2.7 Immunoprecipitation (IP) and Co-immunoprecipitation (Co-IP)

Co-IP and IP were performed following protocols modified from Park et al. (2012) and Albert et al. (2015), using either transiently transformed *N. benthamiana* leaves (~500 mg) or etiolated transgenic *A. thaliana* seedlings (~100 mg). Dark-treated samples were handled under red safe light illumination. Plant tissue was ground in liquid nitrogen and extracted with extraction buffer (1 ml for *N. benthamiana*; 200 µL for *A. thaliana*) followed by overhead rotation for 1 h at 4 °C. Extracts were clarified by centrifugation at maximum speed for 40-60 min at 4 °C. In parallel, 15-20 µL of GFP- or RFP Trap® Agarose beads (Chromotek, Planegg) were equilibrated in the respective buffer. The resulting supernatant was incubated with the beads for 1-1.5 h at 4 °C under overhead rotation, followed by sequential washes (three with washing buffer I and one with washing buffer II). Beads were then stored at -20 °C. For SDS-PAGE, 30-40 µl of 2X SDS sample buffer was added, and proteins were denatured at 95 °C for 5 min. “Input” samples were mixed 1:1 with 2X SDS sample buffer and treated identically. Successful CoIP/IP was verified via standard SDS-PAGE, and western blotting followed by immunodetection procedures.

2.2.7.1 Crude Protein Extract Preparation

Plat material was ground using a Tissue Lyser (2 × 30 s). Samples were mixed with 2× SDS loading buffer containing 10% DTT. Mixtures were boiled for 10 min at 95 °C, then used for SDS-PAGE and Western blotting.

2.2.7.2 IP-GFP of NPH3$^{\Delta C51}$ condensates

For IP-GFP-MS experiments, the same protocol was applied (2.2.7), adjusting volumes for ~4 g of four days old *Arabidopsis* etiolated seedlings (grown vertically in solid half strength MS media). Final IPs triplicates from bait and control seedlings (NPH3$^{\Delta C51}$ and GFP, respectively) were washed with ABC buffer (20 mM ammonium bicarbonate, pH 8.0) and processed at the PCT. Proteins were briefly run on SDS-PAGE, subjected to in-gel tryptic digestion, and peptides purified using stage tips. LC-MS/MS analysis was performed on a Proxeon Easy-nLC coupled to a Q Exactive HF (60 min, Top7 PHOSPHO, HCD). Raw spectra were processed with MaxQuant v2.2.0.0 using the Andromeda search engine against the *Arabidopsis thaliana* database

(Arabidopsis_thaliana_allStrains_2024-01-30.fasta), and LFQ intensities were statistically analysed in Perseus, as previously described in *2.2.5.4.*

2.2.7.3 SDS-PAGE, Western blotting (WB) and immunodetection

Proteins were separated by standard SDS-PAGE and analysed by Western blot. Gels (8%) were run at 15 mA at RT using a PageRuler™ prestained ladder. Proteins were transferred to 0.45 µm nitrocellulose membranes (Amersham™ Protran™) using a TE 22 Mini Tank (200 mA, 1.5 h RT or 64 mA overnight 4 °C) and verified with Ponceau staining. Membranes were blocked for 1 h in 4% milk at RT, incubated with the primary antibody for 1.5h at RT or overnight at 4 °C, washed three times with TBS-T, incubated for 1 h (RT) with the secondary antibody, washed three times with TBS-T, and visualized using ECL™ Prime on an Amersham ImageQuant 800.

2.2.8 Fluorescence-Activated Particle Sorting (FAPS)

These experiments were carried at Freiburg University, in the lab of Andreas Hiltbrunner. Four-day-old etiolated transgenic *Arabidopsis* seedlings (~200 mg) overexpressing GFP:NPH3$^{\Delta C51}$ or HA:YFP:NOT9B, grown in solid half strength MS media, were ground on ice in extraction buffer (150 mM NaCl, 50 mM Tris-HCl pH 7.8, 1 mM EDTA, 0.1% Triton X-100, 10 mM $MgCl_2$, protease and RNase inhibitors). The homogenate was cleared by low-speed centrifugation, filtered through Miracloth, and incubated in 1 mM $CaCl_2$, 10 mM $MgSO_4$ buffer for 30 min before high-speed centrifugation. Supernatants were diluted and checked under CLSM for GFP-tagged condensates. Approximately 15 ml of each sample (NPH3$^{\Delta C51}$ or NOT9B) were sorted by fluorescence-activated particle sorting at the CIBSS core facility (Freiburg University). Sorted fractions (5-10 ml) were processed with TRIzol LS to separate proteins from RNA (RNA isolation was not performed), and proteins were precipitated from the phenol-ethanol phase, washed with guanidine-HCl in ethanol, air-dried, and resuspended in denaturation buffer (6 M guanidine-HCl, 50 mM Tris-HCl pH 7.5, 1-5 mM DTT, 0.5% SDS). Proteins were briefly run on SDS-PAGE, subjected to in-gel tryptic digestion, and peptides purified via stage tips. LC-MS/MS was performed on a Proxeon Easy-nLC coupled to a Q Exactive HF (60 min, Top7 PHOSPHO, HCD) and additionally on a Vanquish Neo coupled to an Exploris 480 (60 min, Top20 PHOSPHO). Spectra were processed in MaxQuant v2.2.0.0 with Andromeda against the *Arabidopsis thaliana* database (Arabidopsis_thaliana_allStrains_2024-01-30.fasta) with iBAQ quantification enabled and matching between replicates. LFQ intensities were statistically analysed in Perseus, as previously described in *2.2.6.4.*

2.2.9 Confocal laser scanning microscopy (CLSM)

CLSM was performed using an upright Leica TCS SP8 (Leica Microsystems GmbH, Wetzlar). Imaging was carried out using transiently transformed leaves of *N. benthamiana* or etiolated *Arabidopsis* seedlings stably expressing the protein of interest. The “HC PL APO CS2 63x/1.20 WATER” objective was used for all imaging. Fluorophore detection settings were as follows: mTQS2 excitation at 448 nm, emission collected between 450-479 nm; GFP excitation at 488 nm, emission collected between 505-520 nm; RFP excitation at 552 nm, emission collected between 600-630 nm. To minimize signal crosstalk when detecting two fluorophores simultaneously, line sequential mode was employed (HyD1 and HyD3 detectors). To minimize crosstalk in the detection of three fluorophores simultaneously, sequential scanning mode was employed (HyD1 and HyD detectors). All images within a single experiment were acquired using identical settings and processed with Leica Application Suite X version 3.5.7.23225 (Leica Microsystems GmbH, Wetzlar) or ImageJ.

2.2.9.1 Drug treatments

Three- to five-day-old *Arabidopsis* etiolated seedlings, grown vertically on half-strength MS medium, were used in FM4-64™ (Thermo Fisher Scientific), Cycloheximide (CHX) or Brefeldin A (BFA, Thermo Fisher Scientific) treatments, followed by CLSM analysis of roots or hypocotyls.

For FM4-64 treatment, seedlings were incubated in 2 µM FM4-64 (in half strength MS liquid medium without sucrose) for at least 15 min in the dark at RT, then imaged to assess epidermal root cell trafficking and endocytosis (excitation 552 nm, emission 640-680 nm); for seedlings expressing GFP tagged proteins, fluorescence was briefly recorded only at the end to confirm protein presence without disturbing dark conditions. Image analysis was performed using ImageJ by drawing a segmented line (width = 3) along the PM to measure fluorescence intensity, followed by a polygon selection of the cytosolic region for intensity quantification. The ratio of PM to cytosolic fluorescence intensity (PM/cyt) was calculated and graphs were plotted using GraphPad Prism 8.0. For BFA treatments, 50 µM BFA (in DMSO) was applied directly to the surface of vertically grown seedlings on half strength MS plates without sucrose. Seedlings were either kept in darkness or, for combined BFA and BL treatments, exposed vertically to unilateral BL (0.1 µmol m^{-2} s^{-1}) for 1 h or 12 h following BFA application. For co-incubations with cycloheximide (CHX), seedlings were first incubated with 100 µM CHX for 1 h at RT in darkness, followed by immediate incubation with BFA/CHX solution for an additional hour in darkness. CLSM analysis was performed on the hypocotyl

endodermis after treatment. Control seedlings were treated with an equal volume of 50 µM DMSO under identical conditions. Image processing and data analysis were performed using ImageJ.

2.2.9.2 GFP signal quantification

For GFP signal quantification in PIN3-GFP polarization analysis, CLSM-acquired images were processed in ImageJ using a uniform brightness threshold (min = 15; max = 99) applied to all images. The standardized images were then visualized using the *mpl-inferno* lookup table to enhance contrast. A straight line was drawn across the inner and outer PMs of endodermal cells, and fluorescence intensities (0 - 255 a.u.) were quantified using the Plot Profile tool. The two resulting peaks corresponded to the inner and outer sides of the endodermal cells, representing either the BL irradiated or shaded sides of the hypocotyl. Raw intensity values were converted to relative percentages and plotted using GraphPad Prism 8.0.

2.2.9.3 FRET-FLIM (Förster Resonance Energy Transfer- Fluorescence Lifetime Imaging Microscopy)

For *in planta* FRET-FLIM analyses, *N. benthamiana* leaves were examined two days after transient transformation using a Leica SP8 confocal laser scanning microscope (Leica Microsystems) equipped with Leica Application Suite software and a FastFLIM upgrade from PicoQuant (Sepia multichannel picosecond diode laser, TimeHarp 260 TCSPC module, and Picosecond Event Timer). Measurements were performed following Ladwig *et al.* (2015) and Glöckner *et al.* (2022) with slight modifications. Imaging was conducted using a 63×/1.20 water-immersion objective, focusing on the PM of abaxial epidermal cells. Prior to FRET-FLIM acquisition, the presence of fluorophore fusions was verified using 488 nm and 561 nm excitation for GFP and RFP, respectively. Donor (GFP) lifetimes were recorded in donor-only expressing cells or in cells co-expressing the indicated fluorophore combinations, using a pulsed 470 nm laser operating at 40 MHz. Data acquisition continued until 1000 photons were collected in the brightest pixel, with an image resolution of 256 × 256 pixels and a pixel dwell time of approximately 20 µs. Lifetime data were analysed using PicoQuant SymPhoTime software by fitting fluorescence decay curves to a mono- or bi-exponential decay models. Mean fluorescence lifetimes (τ) were calculated from image ROIs, pooled across replicates, and plotted. FRET efficiency was derived from donor lifetime reduction in the presence of the acceptor.

3. Results

3.1 Proximity labelling-based identification of putative NPH3 interaction partners

The NPH3 interactome was mapped under dark and blue light (BL) conditions to identify spatially distinct interaction partners in *A. thaliana* etiolated seedlings using complementary proteomic approaches. NPH3 PM-associated interaction partners were identified using TurboID-mediated proximity labelling (PL), whereas interaction partners within cytosolic condensates were identified using Fluorescence Activated Particle Sorting (FAPS) and GFP-based immunoprecipitation followed by mass spectrometry analysis.

PL was selected to capture protein interactions *in planta* under near-physiological conditions, enabling detection of weak, transient, low-abundance, and membrane-associated interactions that are often lost using conventional purification-based approaches (Mair and Bergmann, 2022). TurboID is an engineered biotin ligase (BirA*) that, in an ATP-dependent manner, covalently biotinylates lysine residues of proteins in close proximity to a bait in living cells (Arora et al., 2020; Mair et al., 2019). By fusing TurboID to NPH3, interacting and nearby proteins at the PM were biotinylated under our study conditions, allowing their enrichment and identification via streptavidin-based affinity purification and mass spectrometry (Chapter 3.1). In contrast, TurboID did not reliably capture NPH3 interaction partners within cytosolic condensates. Therefore, condensate-associated interactions were identified using FAPS and GFP-based immunoprecipitation, followed by mass spectrometry analysis (Chapter 3.2).

3.1.1 Establishment of the TurboID mediated proximity labelling approach

First, a Golden Gate-based cloning system allowed the generation of YFP:TurboID:NPH3 fusion constructs (L. Dittiger, 2020). Based on earlier studies (Arora et al., 2020; Mair et al., 2019), a flexible linker between NPH3 and TurboID was incorporated to ensure optimal labelling efficiency. Additionally, a YFP fluorophore was included to monitor subcellular localization. Expression was driven by the native NPH3 promoter to reflect endogenous protein levels. NPH3 was N-terminally tagged to avoid interference with its proper localization and function (Reuter et al., 2021; Sullivan et al., 2021). For this study, we made use of NPH3 ($NPH3^{WT}$), and the variants: $NPH3^{S744A}$ and $NPH3^{\Delta C51}$, either associated constitutively to the PM or constitutively localizing in cytosolic condensates, respectively (Intro. Fig. 3A-C; Fig.1A).

TurboID mediated proximity labelling allows for *in vivo* biotinylation of proteins within a distance of ~10-35 nm of the bait (NPH3), capturing both direct partners and nearby proteins (Fig. 1B). Correct subcellular localization of all YFP:TurboID:NPH3 fusion proteins was verified using transient expression in *N. benthamiana* leaves followed by confocal microscopy (Fig. 1C). Both YFP:TurboID tagged $NPH3^{WT}$ (in darkness) and $NPH3^{S744A}$ localized to the PM in leaf epidermal cells, whereas YFP:TurboID:$NPH3^{\Delta C51}$ localized to cytosolic condensates, as described previously for the respective GFP-tagged NPH3 variants (Reuter et al., 2021; Sullivan et al., 2021). Notably, after 1 h of overhead BL (10 µmol m^{-2} s^{-1}), YFP:TurboID:$NPH3^{WT}$ redistributed mostly into condensates, while YFP:TurboID:$NPH3^{S744A}$ remained PM-associated, likewise consistent with prior observations. Accordingly, the N-terminal YFP-TurboID fusion did not modify the light-dependent subcellular localization of the NPH3 variants.

A *proof of principle* experiment was performed in *N. benthamiana* using 14-3-3Ω, a known BL-dependent interactor of $NPH3^{WT}$, but not of $NPH3^{S744A}$ or $NPH3^{\Delta C51}$ (Reuter et al. 2021; Sullivan et al. 2021). Plants transiently co-expressing YFP:TurboID:NPH3 variants and 14-3-3Ω:mCherry were dark-adapted for 16 h, treated with 50 µM biotin, and exposed to BL (10 µmol m^{-2} s^{-1}) for 45 min. Confocal microscopy confirmed expression of the fusion proteins (Supplementary Fig. S1A) and endogenous biotinylated proteins could be detected in the crude extracts, consistent with naturally occurring biotinylation in *N. benthamiana*. Immunoprecipitation of 14-3-3Ω:mCherry followed by streptavidin immunodetection revealed strong biotinylation of both $NPH3^{WT}$ and 14-3-3Ω after BL exposure (Supplementary Fig. S1B). These data demonstrate that the YFP:TurboID:$NPH3^{WT}$ fusion protein retains TurboID enzymatic activity and NPH3-mediated interaction with 14-3-3, whereas the variants $NPH3^{S744A}$ and $NPH3^{\Delta C51}$ fail to biotinylate 14-3-3Ω (Supplementary Fig. S2). Together, these results confirm that YFP:TurboID:NPH3 fusion proteins retain correct localization, enzymatic activity, and interaction specificity *in planta*.

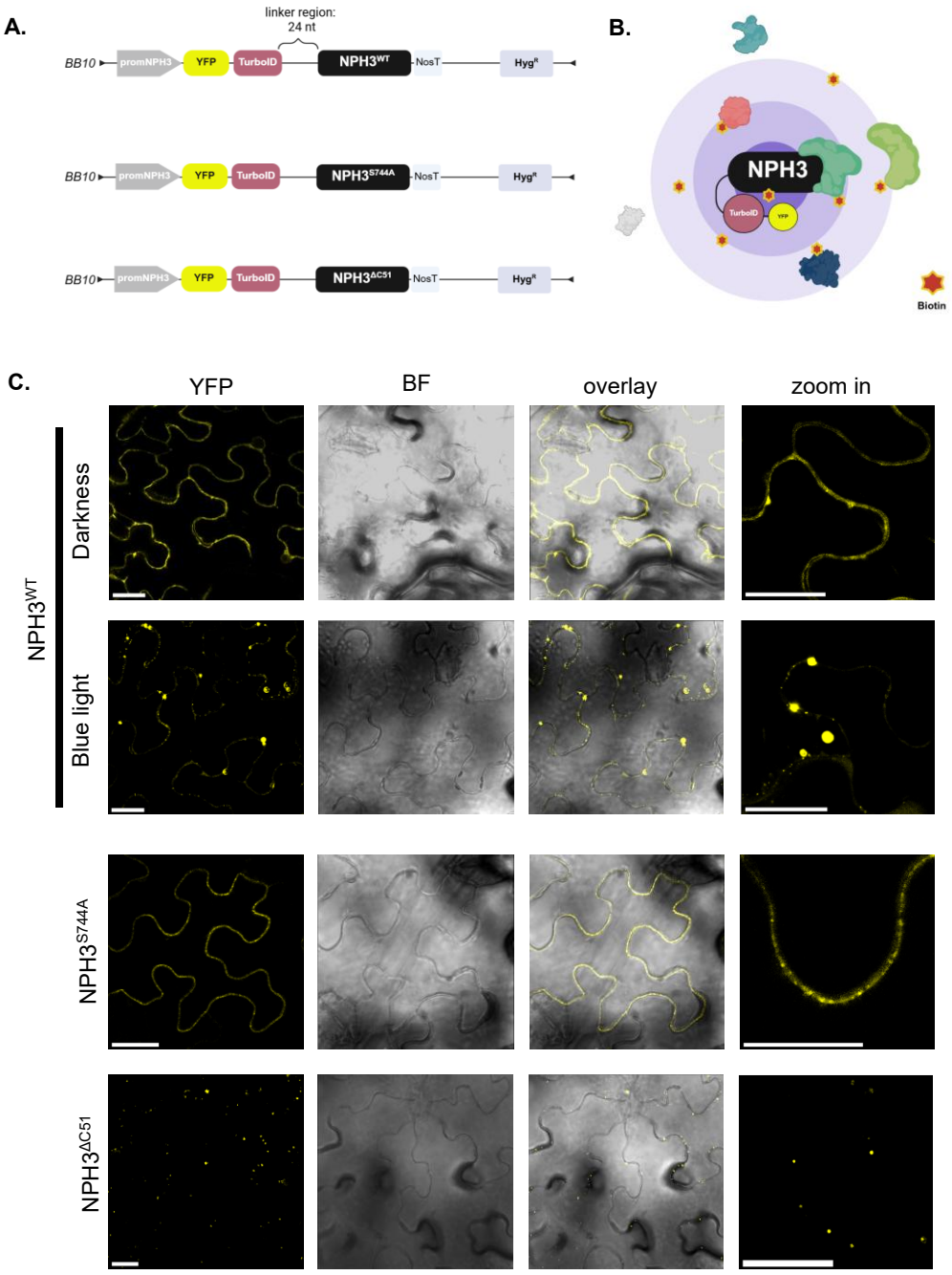

Figure 1. TurboID-based proximity labelling approach and subcellular localization of YFP:TurboID:NPH3 fusion variants in *N. benthamiana*

(A) Golden Gate-based modular plasmid assembly allowing the expression of YFP:TurboID:NPH3 variants under control of the NPH3 promoter. Assembled fusion constructs containing the endogenous NPH3 promoter, YFP fluorophore, TurboID biotin ligase, a linker region of 24 nucleotides (nt) and NPH3 variants. (B) Principle of TurboID-mediated protein labelling within the effective biotinylation radius (each circle represents ~10 nm). (C) Representative confocal microscopy images of leaf epidermal cells from *N. benthamiana* transiently expressing YFP:TurboID:NPH3 variants (under NPH3 promoter). Dark-adapted tobacco plants were either kept in darkness or treated with overhead Blue light (10 µmol m^{-2} s^{-1} for 1 h). Zoom in images show magnifications. Scale bars: 25 µm. BF: bright field. Experiments were repeated at least three times with similar results. All fusion proteins display the correct subcellular localization.

3.1.2 Generation and validation of A. thaliana nph3-7 lines expressing YFP:TurboID:NPH3 variants under control of the endogenous NPH3 promoter

Following verification of fusion proteins subcellular localization and a *proof of principle* in a transient system, stable *A. thaliana* transgenic lines were generated using the floral dip method (Clough and Bent, 1998). The *loss of function* mutant *nph3-7* was used as the genetic background. Homozygous T3 progeny was identified as previously described (Methods *2.2.4.1*).

To evaluate possible phenotypic effects of YFP:TurboID:NPH3 variants expression, rosette morphology and overall development were examined in four-week-old *A. thaliana* plants grown under greenhouse long-day conditions (16 h light/8 h dark, 21 °C) (Supplementary Fig. S3). Leaf number, size and rosette architecture were indistinguishable from controls. No alterations in flower morphology or seed development were observed (data not shown).

The selected *A. thaliana* transgenic lines were further examined by confocal microscopy to confirm correct subcellular localization of the fusion proteins. Confocal imaging of etiolated seedlings revealed that YFP:TurboID:NPH3 variants localize to the PM of epidermal and endodermal cells in both the hypocotyl and root (Supplementary Fig. S4). This localization pattern is consistent with reported NPH3 expression and distribution across *A. thaliana* seedlings (cotyledons, hypocotyl and root), inferred from ePLANT transcriptomic data and partly visualized via NPH3 promoter-driven GUS staining of etiolated seedlings (Waese et al., 2017; Zhao et al., 2018). In darkness, both YFP:TurboID:NPH3^{WT} and YFP:TurboID:NPH3^{S744A} localized properly to the PM in these cell types. After 1 h of BL exposure, YFP:TurboID:NPH3^{WT} relocalized to cytosolic condensates in epidermal and endodermal cells of both organs, whereas YFP:TurboID:NPH3$^{\Delta C51}$ exhibited constitutive cytosolic condensate formation. All fusion proteins displayed proper localization in *Arabidopsis* seedlings.

Plant phototropic responses were assessed by growing seedlings in complete darkness for three days, followed by ~16 h of unilateral BL exposure (0.1 µmol m^{-2} s^{-1}), as shown in Fig. 2A. Wild type Columbia (Col-0) seedlings showed ~90° curvature, while *nph3-7* had no response, as expected. Expression of YFP:TurboID:NPH3^{WT} fully complemented the phototropism defect in *nph3-7*. By contrast, YFP:TurboID:NPH3^{S744A} only partially restores phototropic hypocotyl bending in *nph3-7*, while YFP:TurboID:NPH3$^{\Delta C51}$ failed to do so at all, consistent with previous studies (Reuter et al. 2021). A comparable expression level of the YFP:TurboID:NPH3 fusion proteins could be demonstrated in total protein extracts from etiolated seedlings (Fig. 2B).

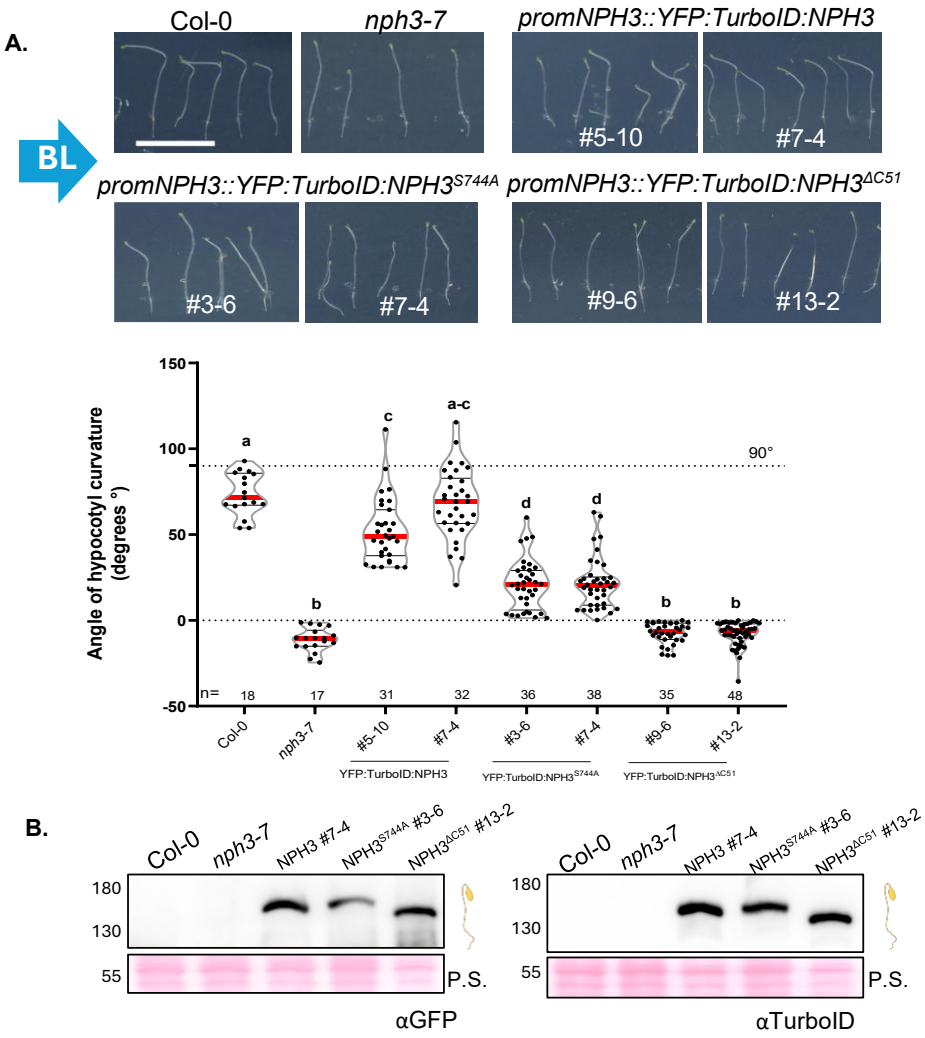

Figure 2. Phenotypic and molecular characterization of etiolated *A. thaliana nph3-7* seedlings expressing YFP:TurboID:NPH3 variants

(A) Representative images of three-day old seedlings grown in darkness on half strength MS medium and exposed to unilateral blue light (0.1 µmol m^{-2} s^{-1}) for 16 h (blue arrow indicates light direction). Scale bar: 1cm. Hypocotyl curvature angles was quantified using Fiji. Data from one representative biological replicate (out of three independent experiments) are shown. In the graph: red line indicates Median angle value; n= number of seedlings analysed. Statistical Analysis: Ordinary One Way Anova (with Tukey's Multiple comparison test $p < 0.05$). (B) Abundance of YFP:TurboID:NPH3 fusion proteins (~150 kDa) in total protein extracts obtained from three days old, etiolated seedlings (approx. 100 mg). P.S., Ponceau staining. Antibodies used: GFP (detection of YFP fluorophore) and TurboID (biotin ligase).

Establishing optimal biotinylation conditions is essential for reliable proximity labelling. As shown by Mair et al. (2019), parameters such as biotin concentration, incubation time, and application method influence labelling efficiency and specificity. After characterizing stable *A. thaliana* YFP:TurboID:NPH3 lines we optimized several parameters, including seedling age and sucrose supplementation (data not shown). In this thesis, we present only the results related to the optimization of exogenous biotin concentration and incubation times, which were used to determine suitable conditions for IP-MS analysis.

These experiments indicate that etiolated seedlings contain sufficient endogenous biotin to support TurboID activity, consistent with the ability of plants such as *A. thaliana* to synthesize biotin *de novo* (Pinon et al., 2005). Biotinylation of the NPH3 bait was detected in crude extracts from etiolated seedlings expressing YFP:TurboID:NPH3^{WT} without added biotin (Supplementary Fig. S5A). Independent reassessment (M. Crnoushev, BSc Thesis, 2025) confirmed these findings (Supplementary Fig. S5B).

Based on these results, the final pipeline for the TurboID-based IP-MS approach employed four- to five-day-old, whole etiolated seedlings grown on half strength MS agar medium without sucrose (to halt any possible microbial contamination) and without exogenous biotin application. Dark-adapted seedlings were handled under red safety light (620-750 nm) to prevent phot1 activation, while BL-treated samples were illuminated from above (overhead BL 10 µmol m^{-2} s^{-1}). Protein extraction was carried at 4 °C under red light. The ground tissue was solubilized, clarified by centrifugation, and desalted using PD-10 columns to remove free biotin. The resulting extracts were incubated with streptavidin beads for affinity purification, followed by extensive washings and on-bead digestion. Peptides were subsequently analysed by LC-MS/MS at the Proteome Centre Tübingen (PCT). Detailed protocols are provided in Methods (Section 2.2.6.3) and summarized in Figure 3.

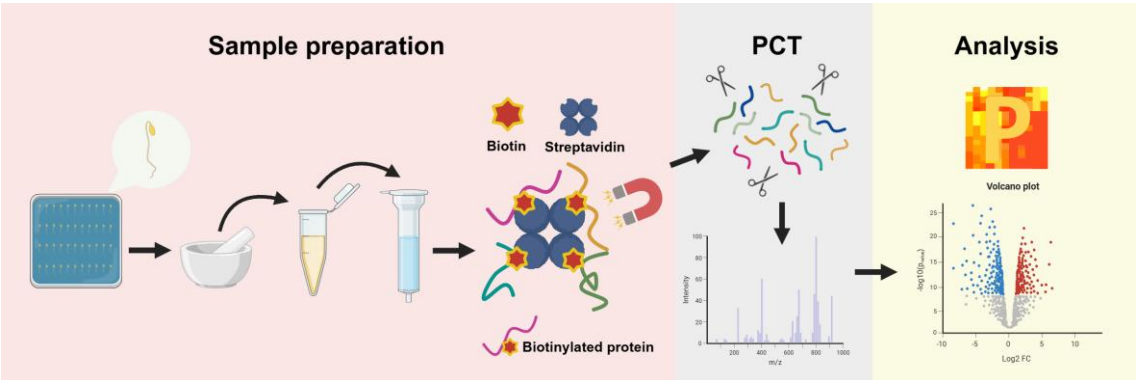

Figure 3. Workflow of TurboID-based proximity labelling and proteomic analysis used in this thesis

Etiolated *Arabidopsis* seedlings expressing YFP:TurboID:NPH3 fusion proteins were harvested without exogenous biotin supplementation. Plant tissue was ground in liquid nitrogen with pestle and mortar, followed by protein solubilization (at 4°C). Total extracts were cleared using PD-10 desalting columns and incubated with magnetic streptavidin beads. After magnetic separation and multiple washes (not shown), bead-bound proteins were analysed by the Proteome Centre Tübingen (PCT) based on tryptic digestion and mass spectrometry analysis. Statistical analyses were done using Perseus v2.0.10.0.

3.1.3 Identification of putative NPH3 interacting proteins at the PM

To elucidate the NPH3 interactome at the PM we employed two NPH3 variants: YFP:TurboID:NPH3^{WT} (line #7-4), and YFP:TurboID:NPH3^{S744A} (line #3-6), which constitutively localizes to the PM, and analysed both under dark conditions. The *A. thaliana nph3-7* mutant was used as a negative control.

In a first large-scale experiment, biotinylated proteins were affinity-purified of etiolated seedlings and compared with those obtained from *nph3-7*. Mass spectrometry identified a total of 2,257 proteins, of which, after filtering for at least two valid *Label Free Quantification* (LFQ) values from three biological replicates, 1,548 proteins were retained for downstream analysis. Based on subcellular localization annotations (UniProt, data not shown), approximately 19% (n = 300) were predicted to be transmembrane proteins and 18% (n = 284) were predicted to be cytosolic. Other compartments included plastids/chloroplasts (11%; n = 167), mitochondria (5%; n = 80), nucleus (6%; n = 87), cell wall or secreted proteins (4%; n = 56), cytoskeleton (1%; n = 20), endoplasmic reticulum (1%; n = 20), Golgi apparatus (1%; n = 17), and peroxisomes (1%; n = 17). Approximately one-third of the proteins (32%; n = 500) lacked complete annotations and could not be assigned automatically a defined subcellular localization. This distribution reflects a broad representation of cellular compartments, consistent with the expected scope of a proximity-labelling approach performed in plants.

Data processing followed established protocols for TurboID-based proximity labelling in *A. thaliana*, using imputation of missing values to retain potential interactors absent in control samples (Arora et al., 2020). To identify proteins specifically enriched with the bait, statistical analyses were performed as described in Methods 2.2.6.4, restricting the dataset to proteins consistently detected across biological replicates. A volcano plot (Fig. 4A) was generated from the identified proteins using a permutation-based False Discovery Rate (FDR) cutoff of 0.05 and an $\mathbf{s_0}$ variance-stabilizing parameter of 0.1, which balances fold-change and variability when defining significance in Perseus.

Proteins were considered enriched if they met both the $\log_2$ fold-change threshold ($\log_2$FC ≥ 1) and statistical significance ($-\log_{10}(p) \geq 1.30$; $p \leq 0.05$). These dual criteria, commonly applied in AP-MS studies, balance the detection of robust interactors with sensitivity to potential transient or low-abundance partners. Adjusted q-values are reported to control the false discovery rate, with $q < 0.05$ providing stronger support for enrichment relative to controls. Because Perseus determines significance using permutation-based FDR and the s_0 parameter, rather than a fixed p-value threshold, some proteins may appear above the significance cutoff in the volcano plot despite raw

p-values slightly exceeding 0.05. Proteins meeting both fold-change and significance criteria were designated as “Enriched” (E), representing high-confidence putative interactors, whereas those consistently detected but not reaching thresholds (often due to limited peptide coverage) were labelled as lower-confidence “Candidates” (C). These classifications reflect the strength of statistical support and help prioritize biologically relevant NPH3 proximity partners for follow-up validation.

Based on this approach, dark-adapted YFP:TurboID:NPH3^{WT} samples displayed strong enrichment of the bait itself (NPH3/RPT3, arrowed in Fig. 4A) and several PM-connected proteins involved in CME. Clathrin heavy and light chains, dynamin-related proteins (DRP1A-C) and dynamin 2B (DRP2B), along with the AP-2 complex subunit μ, satisfied the enrichment criteria (E). Additionally, multiple TPLATE complex components, including: TPLATE, TWD40-1, TWD40-2, TASH3, and TML were enriched (Table 3.1).

KEGG pathway analysis of all enriched proteins (those above the enrichment threshold) revealed a significant overrepresentation of endocytosis-related categories among the top ten pathways in the bait. In contrast, both bait and control samples contained abundant ribosomal and metabolic proteins, likely reflecting nonspecific or naturally occurring biotinylation (Fig. 4B).

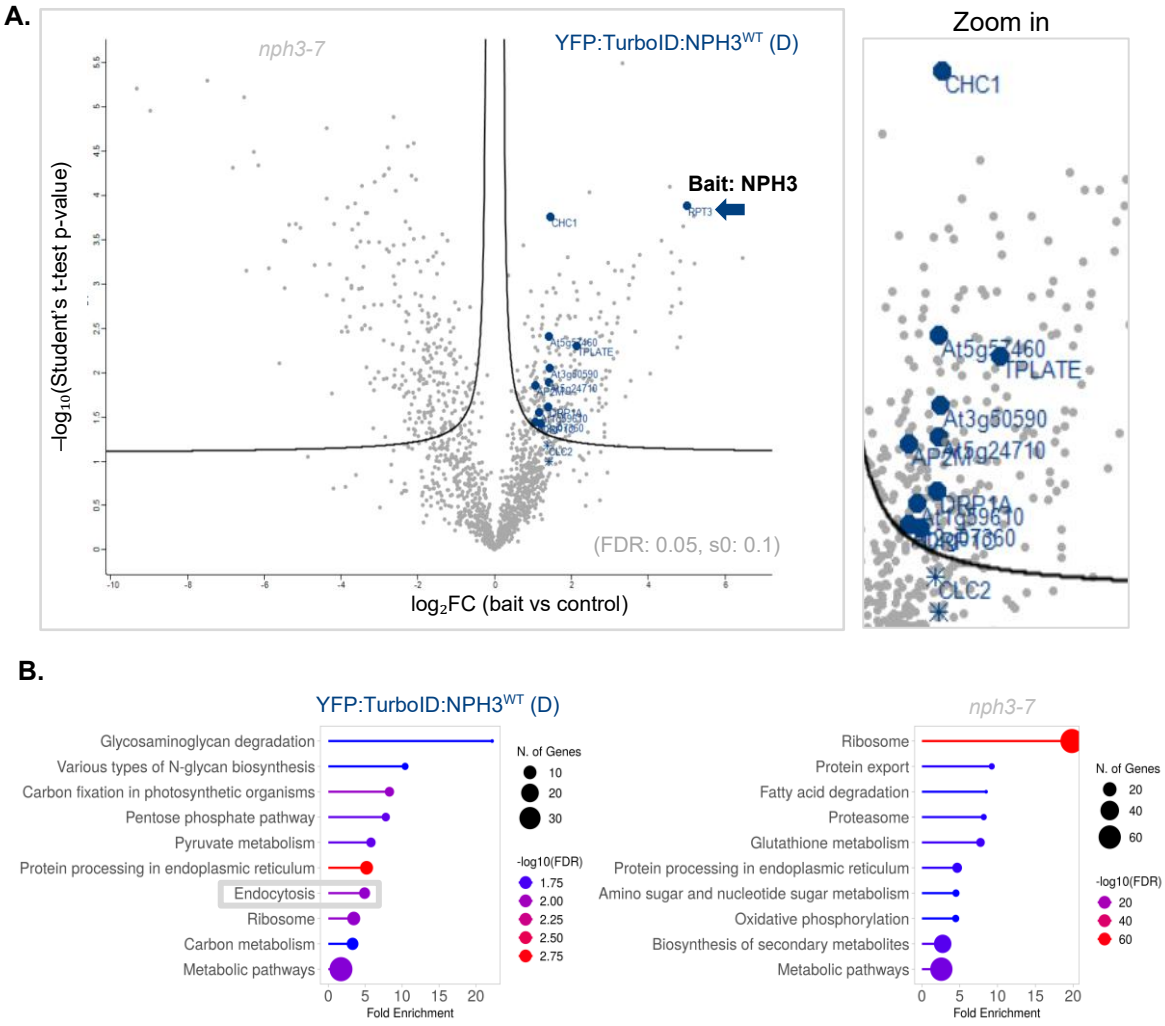

Figure 4. Identification of TPLATE complex components and CME-associated proteins via TurboID mediated proximity labelling of NPH3^{WT} in darkness

(A) Volcano plot of proteins biotinylated in YFP:TurboID:NPH3 seedlings compared with *nph3-7* controls (three biological replicates per condition). Statistically enriched proteins (two-sample t-test with permutation-based FDR < 0.05 and s_0 = 0.1) are shown above the significance threshold (line). The bait and selected clathrin-mediated endocytosis (CME)-associated proteins are highlighted in dark blue. (B) KEGG pathway enrichment analysis comparing NPH3 samples (blue, left) with *nph3-7* controls (grey, right). Endocytosis-related pathways were enriched in the NPH3 samples (grey rectangle). Circle size indicates the number of proteins assigned to each pathway, and colour intensity represents enrichment significance ($-\log_{10}$ FDR).

Table 3. 1. Statistical analysis of selected NPH3^{WT} putative interaction partners in Darkness (two-sample Student's t-test)

Significant enrichment	Protein names (AGI)	Peptides	(raw) Intensity	$-\log_{10}$ (p-value)	Adjusted *q-value* (FDR)	T-test Difference ($\log_2$FC)	T-test Test statistic
Bait	NON PHOTOTROPIC HYPOCOTYL 3 (NPH3/RPT3;At5g64330)	24	5821800000	3.88	0.00	5.02	14.53
(E)	AP-2 complex subunit mu, μ (At5g46630)	11	2273800000	1.86	0.02	1.06	4.19
(E)	Clathrin heavy chain 1 (At3g11130)	36	4990200000	3.76	0.00	1.45	13.52
(C)	Clathrin light chain 1 (At2g20760)	4	393530000	1.00	0.12	1.42	2.13
(C)	Clathrin light chain 2 (At2g40060)	3	31484000	NaN	1.00	0.00	NaN
(E)	Dynamin 2B (At1g59610)	42	12789000000	1.55	0.03	1.16	3.37
(E)	Dynamin-related protein 1A (At5g42080)	32	13383000000	1.61	0.03	1.40	3.52
(E)	Dynamin-related protein 1C (At1g14830)	28	7410600000	1.42	0.04	1.19	3.06
(E)	**Protein TPLATE (At3g01780)**	**18**	**1202200000**	**2.30**	**0.01**	**2.14**	**5.60**
(E)	**TASH3 (At2g07360)**	**15**	**1970200000**	**1.44**	**0.04**	**1.05**	**3.09**
(E)	**TML (At5g57460)**	**2**	**84827000**	**2.41**	**0.01**	**1.40**	**6.01**
(E)	**TWD40-1 (At3g50590)**	**14**	**1493500000**	**2.05**	**0.01**	**1.42**	**4.75**
(E)	**TWD40-2 (At5g24710)**	**21**	**2231800000**	**1.89**	**0.02**	**1.41**	**4.28**

Protein names (+ AGI accessions) are standardized *Arabidopsis* identifiers. Peptides indicate the number of unique peptides detected, providing confidence in protein identification. Raw intensity reflects protein abundance based on MS signal. $-\log_{10}$(p-value) reports two-sample t-test significance on a logarithmic scale; higher values indicate stronger significance, with $-\log_{10}(p) \geq 1.30$ corresponding to $p \leq 0.05$. The adjusted q-value (false discovery rate permutation, FDR) reflects multiple-testing correction. The t-test difference ($\log_2$ fold change, $\log_2$FC) represents the magnitude of abundance change, and the t-test statistic integrates effect size and variability. NaN values indicate that significance metrics could not be calculated due to low peptide detection and/or missing-value imputation. Proteins meeting both statistical thresholds ($\log_2FC \geq 1$ and $-\log_{10}(p) \geq 1.30$) are labelled as enriched (E). Proteins labelled (C) are biologically prioritized candidates that did not meet statistical thresholds but were retained based repeated detection. Proteins in bold represent subunits of the TPLATE complex.

We next analysed the constitutively PM-associated YFP:TurboID:NPH3^{S744A} variant under dark conditions. Biotinylated proteins were affinity-purified from etiolated seedlings following the same procedure and compared with *nph3-7* controls. Mass spectrometry identified a total of ~850 proteins, of which, after filtering for at least two valid LFQ values from three biological replicates, ~600 proteins were retained for downstream analysis. Based on subcellular localization annotations (UniProt, data not shown), approximately

20% (n = 107) were predicted to be transmembrane proteins and 10% (n = 54) were predicted to be cytosolic. Other compartments included plastids/chloroplasts (16%; n = 84), mitochondria (4%; n = 21), nucleus (5%; n = 27), cell wall or secreted proteins (5%; n = 27), cytoskeleton (2%; n = 9), endoplasmic reticulum (1%; n = 6), Golgi apparatus (1%; n = 5), and peroxisomes (1%; n = 6). Approximately one-third of the proteins (35%; n = 186) lacked a defined subcellular annotation. Although the total number of identified proteins was lower than in the $NPH3^{WT}$ dataset, the overall distribution again indicated a broad cellular representation.

Volcano plot analysis (Fig. 5A) revealed significant enrichment of multiple CME components in the $NPH3^{S744A}$ TurboID dataset (Table 3.2). The bait protein itself (NPH3/RPT3, arrowed) was robustly detected with high peptide counts and intensity, confirming efficient proximity labelling, although its fold-change relative to controls was moderate. The photoreceptor phot1 was also enriched (E), consistent with NPH3 and phot1 residing within the effective biotinylation radius of TurboID (~30 nm) at the PM.

Several dynamin and dynamin-related proteins, including DRP2A, DRP2B, DRP1A, DRP1B, and DRP1C, were significantly enriched (E), meeting both of our criteria. Importantly, DRP2A and DRP2B are considered the principal dynamins mediating CME in *A. thaliana*, however, members of the DRP1 family have also been reported to colocalize with clathrin foci at the PM and to participate in endocytic vesicle formation. Thus, DRP2 and DRP1 families act likely redundantly in endocytic processes at the PM (Fujimoto et al., 2010; Konopka et al., 2008). In addition, core CME-associated proteins such as clathrin heavy chains (CHC1/2) and the TPLATE complex subunits TPLATE and TWD40-1 were also identified but considered them as candidates (C), based on our thresholds.

KEGG pathway analysis of the ten most enriched functional categories in our list of enriched proteins did not show significant overrepresentation of endocytosis-related pathways but instead indicated enrichment of ribosomal and general metabolic proteins with the bait (Fig. 5B), suggesting substantial background biotinylation. The relatively modest fold changes observed, despite statistically significant enrichment and low FDR values, likely reflect the broad labelling radius and nonspecific background inherent to TurboID-based proximity labelling. Accordingly, these data were interpreted with caution; nevertheless, relative to $NPH3^{WT}$ in darkness, they reveal a consistent and reproducible proximity of $NPH3^{S744A}$ to CME machinery and TPLATE complex subunits.

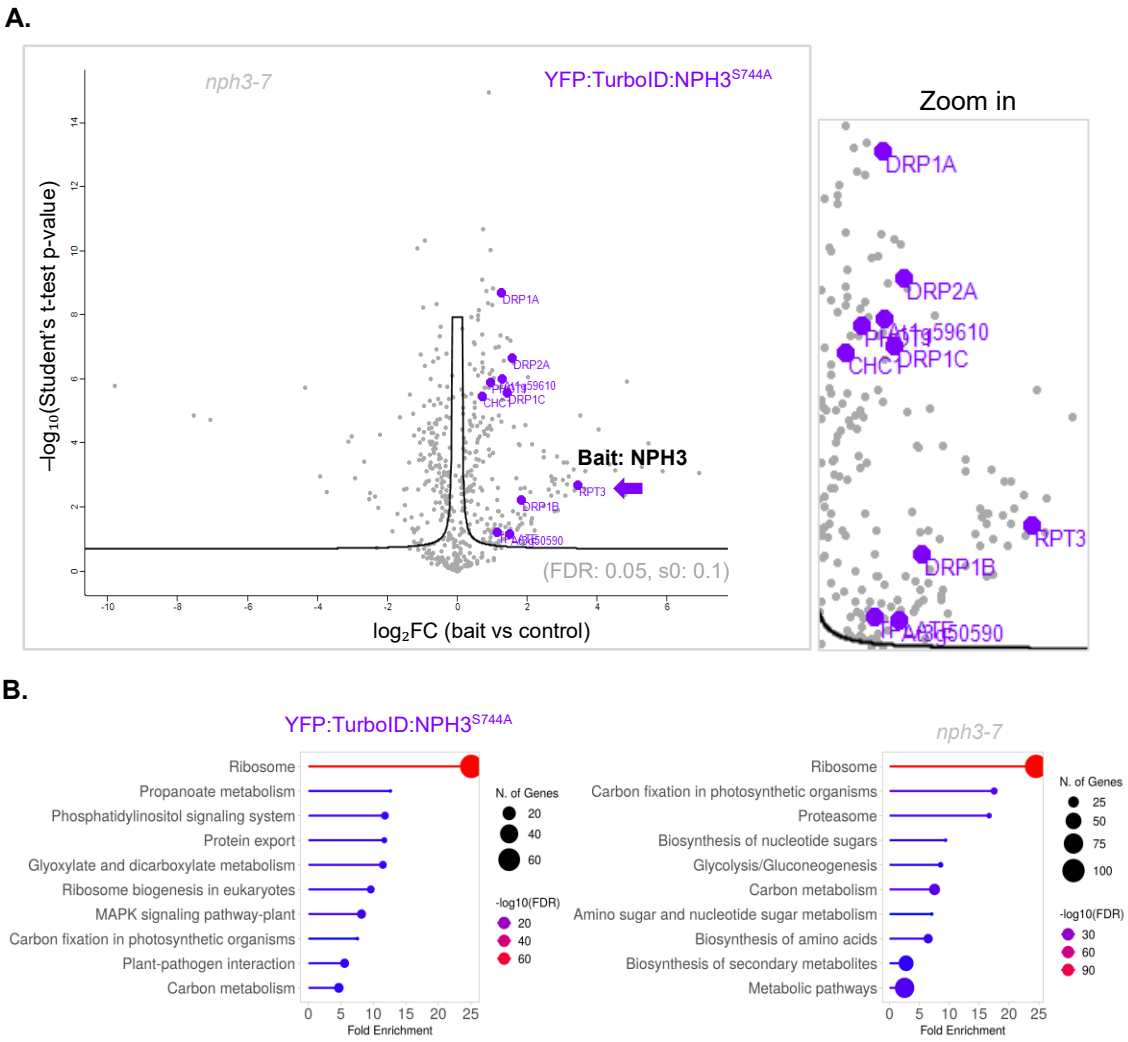

Figure 5. Identification of TPLATE complex components and CME-associated proteins via TurboID proximity labelling of NPH3^{S744A} (control for darkness)

(A) Volcano plot of proteins biotinylated in YFP:TurboID:NPH3^{S744A} seedlings compared with *nph3-7* controls (three biological replicates per condition). Statistically enriched proteins (two-sample t-test with permutation-based FDR < 0.05 and s_0 = 0.1) are shown above the significance threshold (line). The bait, phot1, and selected clathrin-mediated endocytosis (CME)-associated proteins are highlighted in purple. (B) KEGG pathway enrichment analysis of proteins identified in NPH3^{S744A} samples (purple, left) compared with *nph3-7* controls (grey, right). Circle size indicates the number of proteins assigned to each pathway, and colour intensity represents enrichment significance ($-\log_{10}$ FDR).

Consistent with these findings, previously published interaction datasets support the proximity between NPH3 and CME or TPLATE-related proteins at the PM. For instance, in GFP-IP-MS experiments using etiolated seedlings in darkness, GFP:NPH3^{WT} co-enriched with AP-2 adaptor complex (α- and μ- subunits), clathrin chains, dynamin-related proteins, and the TPC subunit TWD40-1 (At3g50590) (T. Schmidt, 2022, not published). Similarly, Sullivan et al. (2021) reported enrichment of TPLATE in GFP immunoprecipitates obtained from GFP:NPH3^{WT} in darkness. Additionally, TurboID-based experiments using the TPC subunit AtEH1 as bait in *A. thaliana* cell suspension

cultures detected strong enrichment of NPH3 (Dragwidge et al., 2024), further supporting the proximity between NPH3 and the TPLATE complex subunits at the PM.

Table 3. 2. Statistical analysis of selected putative NPH3^{S744A} interaction partners in Darkness (two-sample Student's t-test)

Significant enrichment	Protein names (AGI)	Peptides	(raw) Intensity	$-\log_{10}$ (p-value)	Adjusted q-value (FDR)	T-test Difference ($\log_2$FC)	T-test Test statistic
Bait	NON PHOTOTROPIC HYPOCOTYL 3 (NPH3/RPT3;At5g64330)	19	2028300000	2.38	0.000	3.44	7.09
(C)	Clathrin heavy chain 1;Clathrin heavy chain 2 (At3g11130; At3g08530)	19	956280000	5.45	0.000	0.72	6.07
(E)	Dynamin-2A (At1g10290)	36	1151600000	6.65	0.000	1.57	7.02
(E)	Dynamin-2B (At1g59610)	37	7908800000	5.99	0.000	1.29	9.10
(E)	Dynamin-related protein 1A (At5g42080)	31	7272300000	8.68	0.000	1.26	3.48
(E)	Dynamin-related protein 1B (At3g61760)	6	163180000	2.22	0.000	1.83	5.32
(E)	Dynamin-related protein 1C (At1g14830)	22	3370200000	5.56	0.000	1.44	8.31
(E)	Phototropin-1 (At3g45780)	10	780550000	5.88	0.000	1.00	6.18
(C)	**Protein TPLATE (At3g01780)**	**10**	**155190000**	**1.20**	**0.002**	**1.15**	**2.55**
(C)	**TWD40-1 (At3g50590)**	**8**	**90535000**	**1.17**	**0.002**	**1.50**	**2.48**

Protein names (+ AGI accessions) are standardized Arabidopsis identifiers. Peptides indicate the number of unique peptides detected, providing confidence in protein identification. Raw intensity reflects protein abundance based on MS signal. $-\log_{10}$(p-value) reports two-sample t-test significance on a logarithmic scale; higher values indicate stronger significance, with $-\log_{10}(p) \geq 1.30$ corresponding to $p \leq 0.05$. The adjusted q-value (false discovery rate, FDR) reflects multiple-testing correction. The t-test difference ($\log_2$ fold change, $\log_2$FC) represents the magnitude of abundance change, and the t-test statistic integrates effect size and variability. NaN values indicate that significance metrics could not be calculated due to low peptide detection and/or missing-value imputation. Proteins meeting both statistical thresholds ($\log_2FC \geq 1$ and $-\log_{10}(p) \geq 1.30$) are labelled as enriched (E). Proteins labelled (C) are biologically prioritized candidates that did not meet statistical thresholds but were retained based repeated detection. Proteins in bold represent subunits of the TPLATE complex.

Altogether, both TurboID-based experiments using PM-associated NPH3 variants (NPH3^{WT} in darkness and NPH3^{S744A}, constitutively at the PM) reproducibly recovered several subunits of the TPLATE complex and other CME-associated proteins. These results suggest that NPH3 may localize in proximity to the endocytic machinery at the PM under dark conditions.

3.1.4 Identification of putative NPH3 interacting proteins under BL-triggered dynamic cycling: from PM to cytosolic condensates and back to the PM

To investigate the NPH3 interactome under blue light (BL) conditions, we analysed two variants: YFP:TurboID:NPH3^{WT} (line #7-4) and YFP:TurboID:NPH3$^{\Delta C51}$ (line #13-2), the latter of which constitutively forms cytosolic condensates. Initial experiments with YFP:TurboID:NPH3$^{\Delta C51}$ did not yield detectable bait enrichment relative to the *nph3-7* control (Supplemental Fig. S6). No exogenous biotin was added, as endogenous biotin in etiolated seedlings has previously been shown to support sufficient TurboID activity. The lack of enrichment in YFP:TurboID:NPH3$^{\Delta C51}$ may reflect limited accessibility of TurboID within condensates. Consequently, subsequent proximity-labelling (PL) analyses focused exclusively on YFP:TurboID:NPH3^{WT} under BL stimulation, while alternative approaches to identify condensate specific interaction partners using the NPH3$^{\Delta C51}$ bait were explored in Results 3.2.

To determine an appropriate BL treatment duration for PL experiments, we performed time-course analyses in three-day-old, etiolated seedlings expressing YFP:TurboID:NPH3^{WT}. Upon overhead BL exposure (10 µmol m^{-2} s^{-1}), condensate formation increased steadily, peaking at approximately 1 h (Supplemental Fig. S7). After 3 h, most NPH3^{WT} had relocalized to the PM in hypocotyl epidermal cells, although condensates persisted in internal hypocotyl tissues. These observations guided the choice of a 3 h BL exposure for TurboID-based analyses, designed to capture interactors during both: the PM-to-cytosolic condensate transition and subsequent PM re-association.

PL in NPH3^{WT} under 3 h of BL, followed by mass spectrometry, identified a total of 1,084 proteins, of which, after filtering for at least two valid LFQ values from three biological replicates, 742 were retained for downstream analysis. Based on subcellular localization annotations (UniProt, data not shown), approximately 11% (n = 85) were predicted to be transmembrane proteins and 17% (n = 128) were predicted to be cytosolic. Other compartments included plastids/chloroplasts (13%; n = 99), mitochondria (4%; n = 33), nucleus (8%; n = 61), cell wall or secreted proteins (6%; n = 41), cytoskeleton (2%; n = 13), endoplasmic reticulum (<1%; n = 4), Golgi apparatus (<1%; n = 6), and peroxisomes (<1%; n = 4). Approximately one-third (36%; n = 268) of proteins lacked complete annotations and could not be automatically assigned a defined subcellular localization. This distribution reflects a broad cellular representation.

Volcano plot analysis (Fig. 6A) revealed significant enrichment of NPH3 itself (NPH3/RPT3, arrowed) and several TPLATE complex (TPC) subunits, including

TPLATE, TASH3, TWD40-1, and TWD40-2, which all meet our double criteria and are reported as enriched (E). TML was detected but did not reach the enrichment threshold, likely due to limited peptide coverage, and is therefore reported as a candidate (C). Components of the AP-2 adaptor complex (α- and μ-subunits) and phot1, known to phosphorylate NPH3 under BL, were consistently detected but failed to meet the dual enrichment criteria and are classified as candidates (C). Several 14-3-3 isoforms were observed in both bait and control samples but did not reach statistical significance, potentially reflecting weak or transient interactions lost under prolonged BL exposure. KEGG pathway enrichment analysis (Fig. 6B) indicated a significant overrepresentation of endocytosis-related processes among the ten most enriched categories with the bait, whereas the *nph3-7* control was dominated by ribosomal pathways. Table 3.3 summarizes selected putative NPH3 interactors under BL, prioritized based on enrichment and statistical support.

Comparison with the NPH3 interactome obtained in darkness (Results 3.1.3) revealed no additional high-confidence putative interactors. Several NPH3 interaction partners previously reported under BL conditions, including 14-3-3 proteins, CUL3, and PKS proteins, were not identified or enriched under the conditions used in this study. RPT2 and phot2 have also been described to associate with NPH3 specifically under high-intensity BL; because such conditions were not applied here, the absence of these interactions was expected. Further kinases or phosphatases were also not enriched. Interestingly, we observed continued proximity to components of clathrin-mediated endocytosis (CME) and the TPLATE complex (TPC). Whether this proximity occurs prior to BL-induced condensate formation at the PM or during re-association upon PM return cannot be resolved based on our data.

While TurboID can label both PM-associated and cytosolic interactors, including transient ones, its efficiency depends on the physical accessibility of lysine residues and the local molecular environment. Interactions occurring within densely packed or sterically restricted compartments, such as NPH3$^{\Delta C51}$ condensates, which may exhibit gel-like rather than liquid-like properties (Manishankar, personal communication), are therefore likely to be underrepresented. Thus, these results were interpreted with caution. In Chapter 3.2 (Results), we use complementary approaches to identify interaction partners of NPH3$^{\Delta C51}$. In Chapter 3.3, we apply independent analyses to test the putative PM-associated interactions between NPH3 and selected candidates, focusing on the TPLATE complex subunits TPLATE (core) and AtEH1.

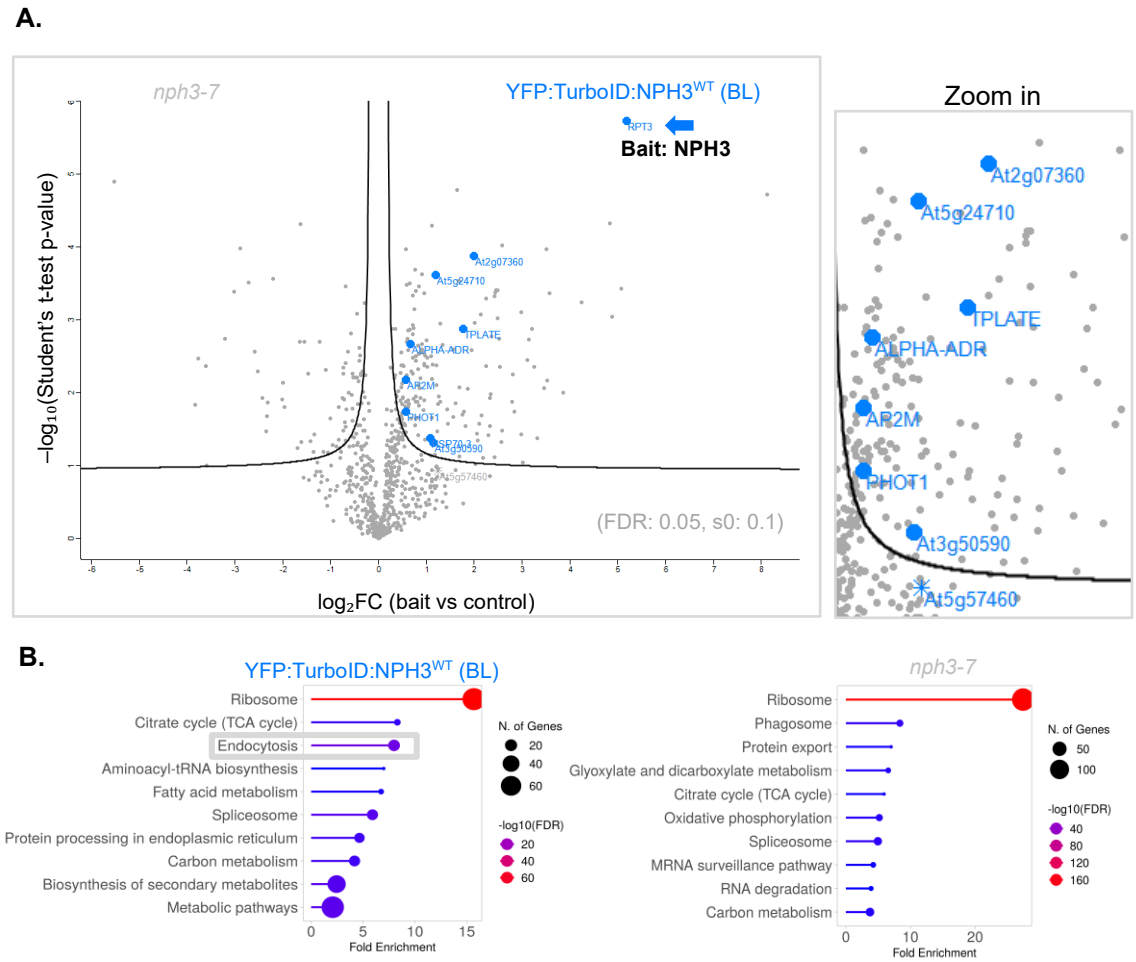

Figure 6. Identification of TPLATE complex components and CME components via TurboID proximity labelling of NPH3^{WT} under dynamic cycling between the PM and condensates

(A) Volcano plot of proteins biotinylated in YFP:TurboID:NPH3^{WT} seedlings following 3 h of overhead blue light (BL; 10 µmol m^{-2} s^{-1}) compared with *nph3-7* controls (three biological replicates per condition). Statistically enriched proteins (two-sample t-test with permutation-based FDR < 0.05 and s_0 = 0.1) are shown above the significance threshold (line). The bait, phot1, and selected clathrin-mediated endocytosis (CME)-associated proteins are highlighted in blue. (B) KEGG pathway enrichment analysis comparing NPH3^{WT} samples (blue, left) with *nph3-7* controls (grey, right). Endocytosis-related pathways were enriched in the NPH3^{WT} samples (grey rectangle). Circle size indicates the number of proteins assigned to each pathway, and colour intensity represents enrichment significance ($-\log_{10}$ FDR).

Table 3. 3. Statistical analysis of selected NPH3^{WT} putative interaction partners under blue light (two-sample Student's t-test)

Significant enrichment	Protein names (AGI)	Peptides	(raw) Intensity	$-\log_{10}$ (p-value)	Adjusted q-value (FDR)	T-test Difference ($\log_2$FC)	T-test Test statistic
Bait	NON PHOTOTROPIC HYPOCOTYL 3 (NPH3/RPT3;At5g64330)	22	2870300000	5.72	0.00	5.19	42.19
(C)	AP-2 complex subunit alpha-1-2 (ALPHA-ADR)	9	528880000	2.66	0.01	0.67	7.0
(C)	AP-2 complex subunit mu (μ, At5g46630)	14	1626600000	2.18	0.01	0.58	5.2
(C)	Phototropin-1 (At3g45780)	18	1946100000	1.74	0.02	0.58	3.9
(E)	**Protein TPLATE**	**18**	**908080000**	**2.87**	**0.01**	**1.77**	**8.0**
(E)	**TASH3 (At2g07360)**	**12**	**549470000**	**3.87**	**0.00**	**2.00**	**14.4**
(C)	**TML (At5g57460)**	**3**	**100090000**	**0.93**	**0.11**	**1.25**	**2.0**
(E)	**TWD40-1 (At3g50590)**	**13**	**518610000**	**1.31**	**0.05**	**1.16**	**2.8**
(E)	**TWD40-2 (At5g24710)**	**27**	**1309000000**	**3.62**	**0.00**	**1.20**	**12.42**

Protein names (+ AGI accessions) are standardized Arabidopsis identifiers. Peptides indicate the number of unique peptides detected, providing confidence in protein identification. Raw intensity reflects protein abundance based on MS signal. $-\log_{10}$(p-value) reports two-sample t-test significance on a logarithmic scale; higher values indicate stronger significance, with $-\log_{10}(p) \geq 1.30$ corresponding to $p \leq 0.05$. The adjusted q-value (false discovery rate, FDR) reflects multiple-testing correction. The t-test difference ($\log_2$ fold change, $\log_2$FC) represents the magnitude of abundance change, and the t-test statistic integrates effect size and variability. NaN values indicate that significance metrics could not be calculated due to low peptide detection and/or missing-value imputation. Proteins meeting both statistical thresholds ($\log_2FC \geq 1$ and $-\log_{10}(p) \geq 1.30$) are labelled as enriched (E). Proteins labelled (C) are biologically prioritized candidates that did not meet statistical thresholds but were retained based repeated detection. Proteins in bold represent enriched subunits of the TPLATE complex.

Summary (Results 3.1): TurboID-based proximity labelling consistently positioned NPH3 near PM-associated components of the endocytic machinery. Although NPH3 itself is not an endocytic cargo, its repeated association with constituents of clathrin-mediated endocytosis (CME) points to a previously unrecognized link to PM-localized endocytic processes. In darkness, NPH3^{WT} localized predominantly to the PM, where proximity labelling captured multiple subunits of the TPLATE complex, clathrin light and heavy chains, dynamin-related proteins, and AP-2 adaptor subunits, suggesting proximity to active CME sites. The constitutively PM-localized NPH3^{S744A} variant largely recapitulated this profile but showed generally reduced enrichment levels. This reduction likely reflects altered interaction dynamics, as constitutive PM association may limit engagement with transient or highly dynamic interactors.

Upon BL exposure, PM-associated NPH3 transiently redistributes into cytosolic condensates before reassociating with the PM. TurboID labelling under these conditions again identified TPLATE complex subunits and AP-2 components as proximal proteins, supporting a persistent spatial relationship between NPH3 and the CME machinery across distinct light-dependent localization states.

3.2. Identification of NPH3 condensates composition

Our previous TurboID proximity labelling attempts to characterize the interactome of NPH3 condensates using the NPH3$^{\Delta C51}$ variant, which constitutively forms cytosolic condensates, were unsuccessful (see Supplemental Fig. S6). NPH3 displays multiple features consistent with biomolecular condensates, including multivalent interaction capacity (Intro Fig. 3A), and hallmarks of liquid-liquid phase separation properties driving assembly into dynamic, *membrane-less* cytosolic particles (Manishankar et al., 2026). In the case of NPH3, both self-association via a C-terminal bipartite motif and interactions mediated by the N-terminal BTB domain appear to contribute to condensate formation (Manishankar et al., 2026; Reuter et al., 2021). However, whether condensate assembly depends on BTB-dependent higher-order homo- or hetero-oligomers in the cytosol is unresolved.

In plants, biomolecular condensates have recently been recognized as key regulators of rapid and efficient responses to environmental cues (Alberti et al., 2019; Field et al., 2023; Peng et al., 2025; Wang and Gu, 2022). Identifying the composition of NPH3 condensates and their interaction partners is therefore critical for understanding their role in phototropism, as well as for determining whether other interaction partners contribute to these assemblies and potentially to signalling. The BL-dependent cycling of NPH3 between PM- association and condensate formation is essential for signalling. Functional studies show that this dynamic cycling is required for proper phototropin-mediated signalling: mutants locked at the PM (NPH3^{S744A}) or in cytosolic condensates (NPH3$^{\Delta C51}$) rescue the phototropic response in *nph3-7* seedlings only partially or not at all, respectively. This indicates that neither NPH3 state alone is sufficient for full activity (Manishankar et al., 2026; Reuter et al., 2021; Sullivan et al., 2021).

To overcome the limitations of the TurboID approach, we applied two complementary techniques to the NPH3$^{\Delta C51}$ variant. Since BL-induced PM dissociation of NPH3^{WT} is gradual and partial, PM-associated interactors cannot be clearly distinguished. In contrast, NPH3$^{\Delta C51}$ forms exclusively cytosolic condensates independently of 14-3-3 binding, enabling selective analysis of condensate-associated interactors while

excluding PM-associated interactions. First, Fluorescence-Activated Particle Sorting (FAPS) was performed, which enables selective isolation and enrichment of GFP-tagged protein fractions, coupled to mass spectrometry analysis. Second, a GFP-based immunoprecipitation (IP-GFP) followed by mass spectrometry analysis was conducted. The experimental design is shown in Fig. 7, with detailed protocols provided in Methods (2.2.7.2 and 2.2.8, respectively).

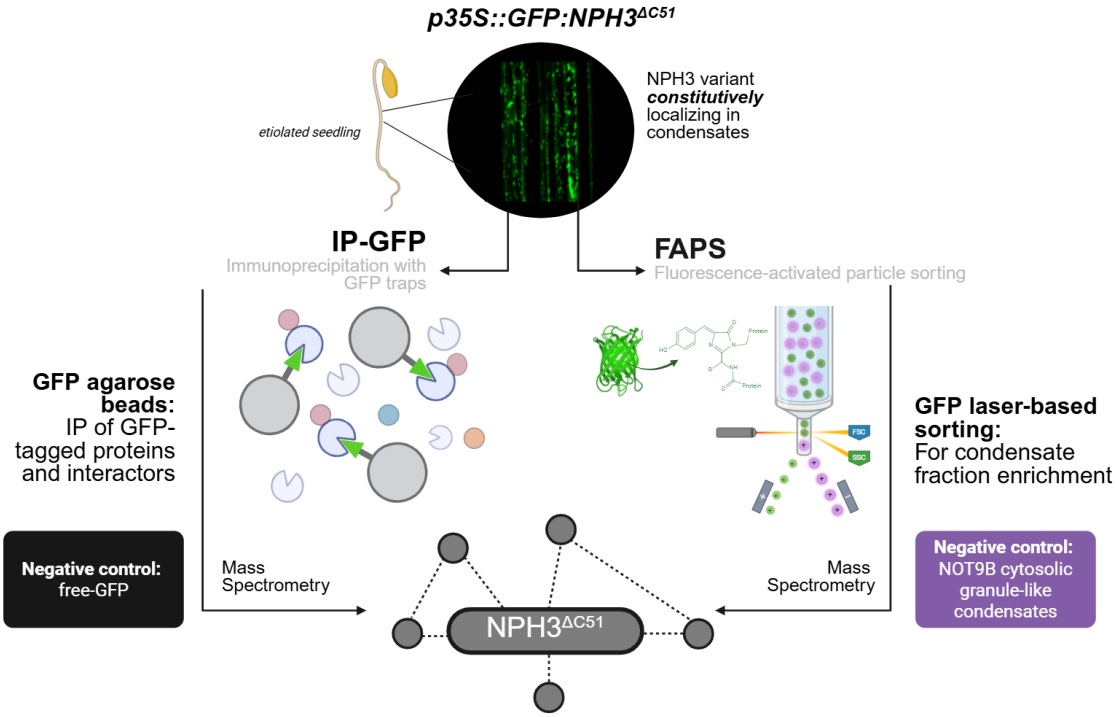

Figure 7. Experimental design for the proteomic analysis of NPH3 $^{\Delta C51}$ condensates in etiolated *Arabidopsis* seedlings

For these experiments, we used the previously reported transgenic line expressing GFP-tagged NPH3$^{\Delta C51}$ under the 35S promoter in the *nph3-7* background (Reuter et al., 2021). GFP immunoprecipitation (IP-GFP) using GFP-Trap agarose beads was performed to isolate GFP-tagged proteins and associated interaction partners for mass spectrometry analysis. Negative control for this approach included a "free-GFP" transgenic line expressing GFP under the ubiquitous UBQ10 promoter in Col-0. Fluorescence-Activated Particle Sorting (FAPS) detects and isolates fluorescently labelled condensates based on light scattering and fluorescence intensity, enabling high-throughput purification of defined condensate populations for mass spectrometry analysis and characterization. Negative control for this approach included the previously reported line expressing HA:YFP:NOT9B under the 35S promoter (Schwenk et al., 2021). The combination of these approaches provides a highly specific and reproducible strategy to characterize the composition of NPH3$^{\Delta C51}$ condensates in *Arabidopsis* seedlings.

3.2.1 Fluorescence-Activated Particle Sorting (FAPS) of NPH3$^{\Delta C51}$ condensates

FAPS is a flow cytometry-based technique that detects and sorts fluorescent particles in solution. While Fluorescence-Activated Cell Sorting (FACS) is designed for intact cells, FAPS applies the same principles to smaller or non-cellular entities such as protein aggregates, organelles, and nanoparticles (Van Gaal et al., 2010; Zölls et al., 2012). Its

ability to combine light scattering and fluorescence detection enables high-throughput isolation of defined particle populations, including biomolecular condensates, as demonstrated by the analysis of phyB photobodies from *Arabidopsis* (Kim et al., 2023).

To investigate potential cytosolic NPH3 interactions, we used FAPS to isolate condensates formed by the constitutively cytosolic NPH3$^{\Delta C51}$ variant. NOT9B condensates served as a control for cytosolic condensates.

NOT9B (NEGATIVE ON TATA 9B) is a subunit of the *A. thaliana* CARBON CATABOLITE REPRESSION 4-NEGATIVE ON TATA-LESS (CCR4-NOT) complex and a homologue of the human protein CNOT9/CAF40 (Schwenk et al., 2021). NOT9B forms cytosolic and nuclear condensate-like granules resembling processing bodies (P-bodies), where it is linked with deadenylase activity, RNA silencing, mRNA processing and light signalling (Schwenk et al., 2021; Schwenk and Hiltbrunner, 2022). Because NOT9B forms cytoplasmic RNA-protein granules, it represents a suitable control for evaluating the performance of FAPS on cytosolic condensates.

In collaboration with the laboratory of Andreas Hiltbrunner (University of Freiburg, Germany), we performed FAPS on extracts from four-day-old, etiolated *Arabidopsis* seedlings overexpressing either GFP:NPH3$^{\Delta C51}$ (Reuter et al. 2021) or HA:YFP:NOT9B (Schwenk et al. 2021). Before sorting, we confirmed the presence of fluorescent condensates in each extract by confocal microscopy, ensuring the suitability and structural integrity of the samples. Each genotype was analysed in three biological replicates.

Sorting efficiency for GFP:NPH3$^{\Delta C51}$ was high (≥20 million particles), whereas HA:YFP:NOT9B exhibited moderate efficiency (≤20 million particles), consistent with the lower brightness of YFP and the generally smaller size of NOT9B foci. Sorted material underwent combined RNA isolation and protein purification (Methods 2.2.8). Fractionation was necessary particularly for NOT9B, which localizes to P-body like, RNA-rich condensates. Only purified protein fractions from both bait and control samples were denatured, transported to Tübingen, and processed for LC-MS/MS at the PCT facility.

Mass spectrometry across all samples identified 1,277 proteins. Principal component analysis (PCA; Fig. 8A) revealed one replicate per condition as an outlier. For NOT9B, the outlier corresponded to the sample with the lowest sorting efficiency, consistent with reduced particle recovery. For NPH3$^{\Delta C51}$, the outlier showed low total peptide intensity, suggesting incomplete protein extraction. These replicates were removed, leaving two biological replicates per condition for subsequent analyses.

The results demonstrated that GFP-based FAPS effectively isolates fluorescent condensates but is not strictly selective for cytosolic proteins, as abundant proteins from other compartments were also recovered, likely due to mechanical disruption of organelles during extraction or co-sedimentation of organelle remnants within the particle size range.

After filtering for proteins with at least two valid LFQ values across samples, approximately 260 proteins were found enriched exclusively in NPH3$^{\Delta C51}$ samples, including the bait itself. A two-sample Student's t-test, visualized as a Volcano plot (Fig. 8B), identified significantly enriched candidates (FDR = 0.05; s_0 = 0.1). Proteins were considered enriched, compared to control, if they had a $\log_2$ fold change ($\log_2$FC) ≥ 1 and a p-value ≤ 0.05 ($-\log_{10}(p) \geq 1.30$), the same threshold used before in this thesis, intended to capture potential interactors from a noisy background. For NOT9B, several proteins involved in cytosolic mRNA metabolism and RNA granule dynamics, including P-body-associated factors PAB8 and PAB2 and additional RNA-binding proteins such as RBG8 and At5g40490, were moderately enriched (Fig. 8B, purple), although one known partner, AGO1 (Schwenk et al., 2021), was not enriched under these conditions (Fig. 8B, turquoise). Downstream analysis for this thesis focused solely on NPH3$^{\Delta C51}$ interaction partners.

Subcellular annotation of the 260 enriched proteins indicated that approximately 21% (n = 51) were predominantly cytosolic, whereas ~40% were annotated as plastid localized. The large plastid fraction likely reflects the release of plastid-derived material during tissue extraction. After manual removal of probable contaminants and non-cytosolic proteins, 31 cytosolic candidates remained (Table 3.4). Proteins were classified as enriched (E) if they passed the predefined enrichment threshold, or as candidates (C) if they did not meet this criterion but were reproducibly identified in both replicates. The resulting candidate set included ribosomal proteins (40S/60S), translation initiation factors (eIF3), elongation factors (EF1γ), 14-3-3 proteins, calmodulins, cytosolic/nuclear chaperones 70 kDa Heat Shock Proteins (HSP70-3 and HSP70-4), clathrin light chain, and calcium-dependent protein kinase 3. Although several proteins appeared enriched in the NPH3$^{\Delta C51}$-FAPS dataset, only the bait (NPH3$^{\Delta C51}$) and the HSP70 isoforms (HSP70-3 and HSP70-4) met both predefined key criteria (cytosolic localization and enrichment threshold) and, in addition, showed high peptide recovery (Table 3.4, grey). The high peptide recovery increases confidence in protein identification by minimizing the likelihood of stochastic detection. To test whether HSP70 enrichment was specific to the bait, we analysed *Intensity-Based Absolute Quantification* (iBAQ) values, which

estimate protein abundance from the sum of peptide intensities normalized to the number of theoretically observable peptides (Rozanova et al., 2021).

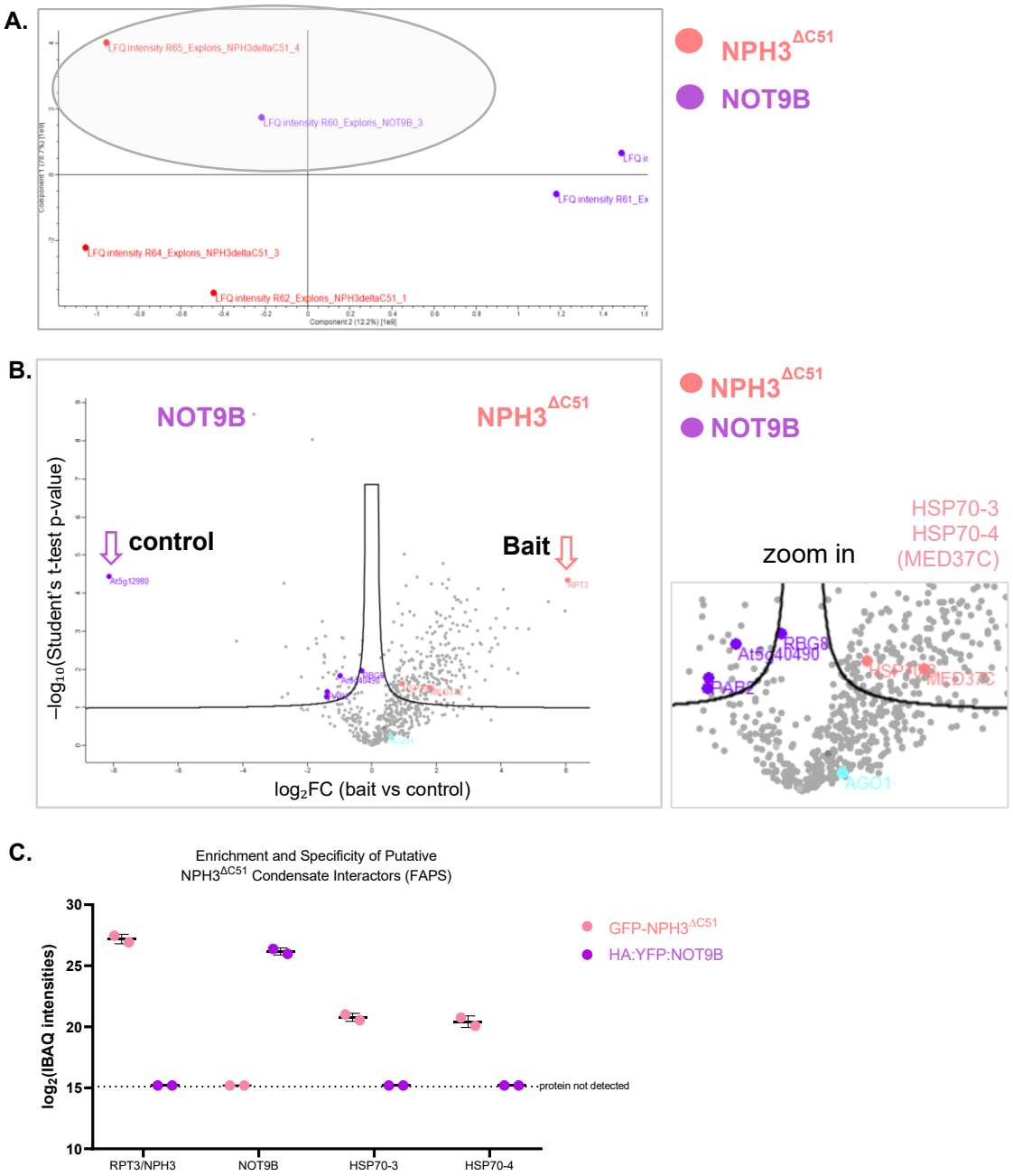

Figure 8. Identification of HSP70s as NPH3$^{\Delta C51}$ condensate-associated proteins using FAPS-based IP-MS

Four-day-old, etiolated seedlings expressing GFP:NPH3$^{\Delta C51}$ in the *nph3-7* background (35S promoter, #23-2) were used to enrich fractions containing NPH3 condensates. HA:YFP:NOT9B (35S promoter, A. Hiltbrunner) served as a negative control. Fluorescence-Activated Particle Sorting (FAPS) was applied to detect, quantify, and isolate fluorescent protein condensates based on laser-induced light scattering and GFP fluorescence. Sorted condensates from three biological replicates of bait and control samples were processed and analysed by mass spectrometry. (A) Principal Component Analysis (PCA) of FAPS-isolated condensates revealed one replicate from GFP:NPH3$^{\Delta C51}$ and one replicate from HA:YFP:NOT9B that deviated strongly from the others (circled). (B) Volcano plot of LFQ-based Statistical analysis (t-test student) was performed only in two biological replicates, which allowed the identification of HSP70-3 and HSP70-4 (MED37C) as enriched in NPH3 condensates compared with the HA:YFP:NOT9B control. (C) To compare

reproducibility and relative abundance across samples, iBAQ values were log_2-transformed, and plotted across two biological replicates. Results indicate that HSP70s were found enriched exclusively with the bait GFP:NPH3$^{\Delta C51}$.

Table 3. 4. Statistical analysis of selected (cytosolic) NPH3$^{\Delta C51}$ putative interaction partners in FAPS experiment (two-sample Student's t-test)

S	Protein names	Pept.	Mol.W. [kDa]	(Raw) Intensity	$-log_{10}$ (p-value)	Adjusted q-value (FDR)	T-test Differ. (log_2FC)	T-test Test statistic
bait	**Non phototropic hypocotyl 3 (NPH3/RPT3)**	**33**	**81.9**	**26451000000**	**4.34**	**0.00**	**6.05**	**18.95**
(E)	60S ribosomal protein L3-1; L3-2	8	44.6	1598100000	3.09	0.01	4.49	9.07
(C)	40S ribosomal protein S18	6	17.5	1362700000	1.20	0.06	2.25	2.55
(C)	40S ribosomal protein S20-1	4	13.9	1293100000	1.05	0.09	3.12	2.24
(E)	40S ribosomal protein S13-2	6	62.7	961900000	1.55	0.02	2.78	3.36
(E)	Ras-related protein RABH1b	7	23.1	911370000	2.29	0.01	2.59	5.57
(E)	60S ribosomal protein L30-3; L30-1	4	12.3	756980000	1.49	0.02	2.43	3.22
(E)	40S ribosomal protein S27; S27-1; S27-2	3	9.4	726480000	1.42	0.03	1.13	3.05
(E)	60S ribosomal protein L27-2	5	15.6	617500000	1.75	0.02	2.17	3.89
(E)	40S ribosomal protein S15-1;S15-4	5	17.1	560430000	2.47	0.02	3.66	6.22
(E)	60S ribosomal protein L23a-2; L23a-1	5	16.7	542570000	4.11	0.01	3.29	16.60
(E)	60S ribosomal protein L13; L13-1; L13-3	6	23.5	485880000	1.60	0.02	2.09	3.49
(E)	60S ribosomal protein L38	4	8.1	471070000	1.90	0.02	2.10	4.31
(E)	60S ribosomal protein L37a-2; L37a-1	3	10.2	459070000	1.98	0.02	2.18	4.53
(E)	Eukaryotic translation initiation factor 3 subunit F	5	31.9	370110000	1.34	0.03	2.11	2.86
(E)	14-3-3-like protein GF14 upsilon	9	30.2	357750000	2.30	0.01	2.41	5.58
(E)	60S ribosomal protein L32-1; L32-2	4	15.5	337040000	1.88	0.02	1.82	4.26
(E)	Probable methyltransferase PMT8	4	70.5	270940000	3.42	0.01	2.12	11.05
(E)	40S ribosomal protein S28-2	2	7.3	266250000	2.24	0.02	2.07	5.39
(E)	Probable elongation factor 1-gamma 2	10	46.4	249590000	1.91	0.02	1.71	4.33
(E)	40S ribosomal protein S6-2	2	22.1	248940000	2.36	0.02	2.35	5.82
(E)	Clathrin light chain 1	3	37.2	233980000	1.76	0.02	1.73	3.92
(E)	Calmodulin-5; 6; 7; 3; 2	3	16.8	214780000	2.52	0.02	2.52	6.42
(E)	**Heat shock 70 kDa protein 3 (HSP70-3)**	**22**	**71.1**	**198010000**	**1.63**	**0.02**	**1.15**	**3.57**
(E)	Eukaryotic translation initiation factor 3 subunit A	9	113.1	196470000	3.51	0.01	1.18	11.65
(E)	**Heat shock 70 kDa protein 4 (HSP70-4; MED37C)**	**23**	**71.1**	**155200000**	**1.52**	**0.02**	**1.79**	**3.30**
(C)	Ribosomal protein L19; L19-2	2	24.2	130680000	1.26	0.04	1.39	2.69
(E)	Calcium-dependent protein kinase 3	3	58.7	120650000	4.20	0.01	1.06	17.43
(C)	Cysteine proteinase inhibitor 6	2	17.5	75787000	1.27	0.04	1.04	2.71

Peptides indicate the number of unique peptides detected, providing confidence in protein identification. (Raw) Intensity reflects protein abundance from MS signal. The T-test p-value reports the significance of abundance differences, and the adjusted q-value (FDR) accounts for multiple testing. The T-test difference (log_2FC) represents the magnitude of enrichment, and the T-test statistic captures the strength of evidence based on effect size and variance. S: significant enrichment: Proteins meeting both statistical thresholds ($log_2FC \geq 1$ and $-log_{10}(p) \geq 1.30$) are labelled as enriched (E). Proteins labelled (C) are biologically prioritized candidates that did not meet statistical thresholds but were retained based repeated detection.

iBAQ values for the two HSP70 isoforms, the bait, and the control were log_2-transformed with a small pseudocount to handle zeros; non-detected proteins were assigned the minimum observed log_2-iBAQ (~15.2). Comparison across samples showed that both

HSP70 isoforms were detected exclusively in NPH3$^{\Delta C51}$ condensates (Fig. 8C), confirming their specific association with NPH3$^{\Delta C51}$.

Together, FAPs results suggest that HSP70 isoforms HSP70-3 and HSP70-4, are potential interaction partners of NPH3$^{\Delta C51}$ cytosolic condensates.

3.2.2 IP-GFP-based Immunoprecipitation of NPH3$^{\Delta C51}$ condensates

To further characterize potential interaction partners of NPH3$^{\Delta C51}$ and complement the FAPS results, which suggested an association with HSP70 isoforms, we performed GFP-based immunoprecipitation (IP-GFP) followed by mass spectrometry. Extracts from five-day-old, etiolated seedlings overexpressing GFP:NPH3$^{\Delta C51}$ (Reuter et al., 2021) were incubated with GFP Trap® agarose beads to isolate GFP-tagged proteins. This allowed the selective capture of the GFP-tagged bait protein and the co-immunoprecipitation of interacting proteins. As a negative control, we used *A. thaliana* seedlings expressing GFP under the Ubiquitin10 promoter (*promUBQ$_{10}$::GFP*, Col-0). IP fractions from three biological replicates of both bait and control were processed at the PCT and analysed by mass spectrometry.

A total of 252 proteins groups were identified in this experiment. Quantitative and statistical analyses were performed in Perseus (v2.0.10.0). Principal Component Analysis (PCA; Fig. 9A) revealed that one bait replicate was more dispersed relative to the other two; however, retaining all replicates did not affect overall statistical outcomes, and no replicate was excluded. Applying a filtering criterion requiring at least two valid LFQ values per condition yielded 61 proteins detected exclusively in bait samples, comprising 5 transmembrane (≈8%), 23 cytosolic (≈38%), 7 plastid (≈12%), and 26 unannotated (≈43%) proteins.

While common proteomics thresholds (e.g., $\log_2$FC ≥ 1, p ≤ 0.05, used previously in this thesis) can detect weaker interaction patterns, we applied a more conservative criteria to prioritize high-confidence interactions with this approach. Proteins were considered significantly enriched if they met $\log_2$FC ≥ 2, -$\log_{10}$(p-value) ≥ 2 (p ≤ 0.01), under FDR: 0.05 and s_0 = 0.1 criteria.

Under these thresholds, the bait (NPH3/RPT3) and the cytosolic/nuclear chaperones HSP70-1 and HSP70-4 were retained as robust interactors (Fig. 9B). The isoform HSP70-3, although showing moderate enrichment ($\log_2$FC = 3.82, −$\log_{10}$p = 1.81), did not meet the FDR cutoff (q = 0.09; Table 3.5) and therefore is not displayed as a significant hit in the volcano plot, likely reflecting higher variability among replicates.

To assess the reproducibility and specificity of HSP70s associations with NPH3$^{\Delta C51}$, we applied the same pipeline used for FAPS, including log_2-transformation of iBAQ values for comparison across replicates (Fig. 9C).

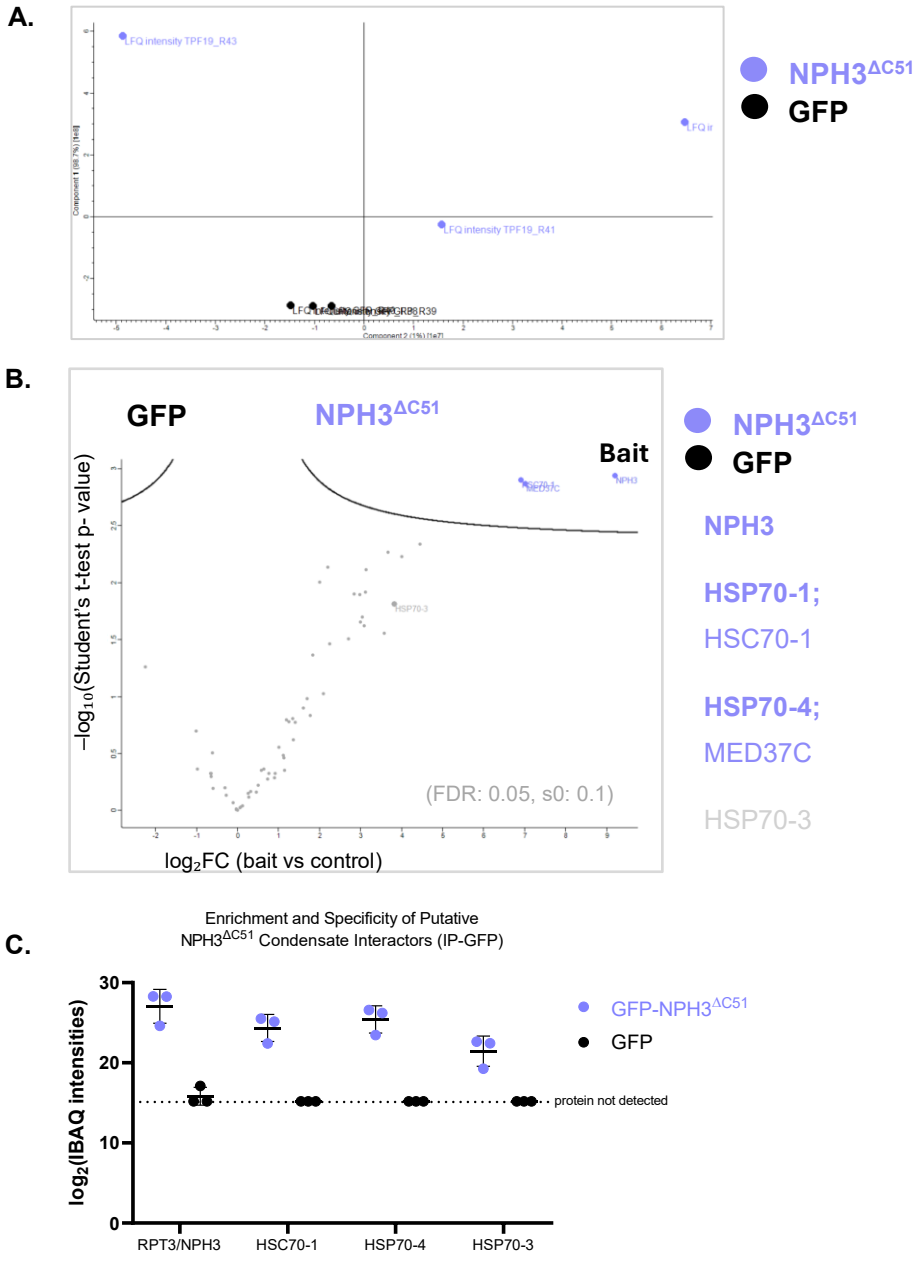

Figure 9. Identification of HSP70s as NPH3$^{\Delta C51}$ condensate-associated proteins using GFP-based IP-MS

Five-day-old etiolated seedlings expressing GFP:NPH3$^{\Delta C51}$ in *nph3-7* (35S promoter, #23-2) (Reuter et al., 2021) were used for GFP-based immunoprecipitation (IP-GFP). As a negative control, we used an *Arabidopsis* line expressing GFP under the control of the ubiquitous Ubiquitin10 promoter (*promUBQ10::GFP*, Col-0). IP fractions from three biological replicates of bait and control samples were processed and analysed by mass spectrometry. (A) Principal Component Analysis (PCA) revealed that one replicate of GFP-NPH3$^{\Delta C51}$ deviated strongly from the others. (B) Volcano plot of LFQ-based statistical analysis (t-test student) identified HSP70-1 (HSC70-1) and HSP70-4 (MED37C) as strongly enriched compared with the free GFP control. HSP70-3 was detected only in bait samples but without significant enrichment. (C) To compare specificity and reproducibility of our findings, iBAQ values were log_2-

transformed, and plotted across the three biological replicates, indicating that HSP70s were found enriched exclusively with the bait GFP:NPH3$^{\Delta C51}$.

Table 3. 5. Statistical analysis of selected NPH3$^{\Delta C51}$ putative interaction partners in IP-GFP experiment (two-sample Student's t-test)

S	Protein names	Pept.	Mol. W. [kDa]	(Raw) Intensity	$-\log_{10}$ (p-value)	Adjusted q-value (FDR)	T-test Differ. ($\log_2$FC)	T-test Test statistic
E	Non Phototropic Hypocotyl 3 (NPH3/RPT3)	32	81.87	2.94E+10	2.94	0.00	9.19	8.30
E	Heat Schock Protein 70 kDa (HSP70-4 / MED37C)	25	71.12	7.73E+09	2.87	0.03	7.02	7.95
E	Heat Schock Protein 70 kDa (HSP70-1/ HSC70-1)	24	71.35	3.5E+09	2.89	0.04	6.91	8.10
	Heat Schock Protein 70 kDa (HSP70-3)	*24*	*71.14*	*4.74E+08*	*1.81*	*0.09*	*3.82*	*4.05*

Peptides indicate the number of unique peptides detected, providing confidence in protein identification. (Raw) Intensity reflects protein abundance from MS signal. The T-test p-value reports the significance of abundance differences, and the adjusted q-value (FDR) accounts for multiple testing. The T-test difference ($\log_2$FC) represents the magnitude of enrichment, and the T-test statistic captures the strength of evidence based on effect size and variance. Proteins were classified as significantly enriched if they met the conservative thresholds of $\log_2$FC ≥ 2, $-\log_{10}$(p-value) ≥ 2 ($p \leq 0.01$), and FDR ≤ 0.05. Proteins fulfilling these criteria are indicated as enriched (E).

Aside from a low-level NPH3 signal in one control replicate, likely reflecting nonspecific binding, the analysis confirmed robust and specific enrichment of HSP70-1 and HSP70-4 with NPH3$^{\Delta C51}$. HSP70-3 remained detectable at lower abundance but was uniquely associated with NPH3$^{\Delta C51}$. Thus, IP-GFP results suggest that HSP70 isoforms HSP70-1 and HSP70-4, are robust potential interaction partners of NPH3$^{\Delta C51}$ cytosolic condensates.

Chaperone proteins, such as members of the HSP70 family, have been associated as components of various plant *membrane-less* assemblies, including nuclear phyB photobodies and cytosolic condensates formed by NPR1 or Rbp47b (Bard and Drummond, 2024; Kim et al., 2023; Kosmacz et al., 2019; Solis-Miranda et al., 2023; Zavaliev et al., 2020). These chaperones are proposed to regulate condensate dynamics, modulating assembly, material properties, and dispersal (Bard and Drummond, 2024), suggesting a general role as molecular remodelers.

Consequently, interaction partners that contribute structurally to NPH3 condensate formation could not be detected using this proteomic approach. These results suggest that NPH3$^{\Delta C51}$ likely forms a single-component condensate regulated by HSP70s.

Summary (Results 3.2.1- 3.2.2): Complementary IP-GFP and FAPS analyses consistently identified HSP70 chaperones, particularly HSP70-1, HSP70-3, and HSP70-4, as components associated with NPH3$^{\Delta C51}$ condensates. These findings are in line with the broader role of HSP70s in plant *membrane-less* assemblies, where they act as molecular remodelers that modulate assembly, material properties, and dispersal. Based on our results, NPH3$^{\Delta C51}$ likely forms a primarily single-component condensate, whose properties are regulated by HSP70 chaperones, including HSP70-1, HSP70-3 and HSP70-4. Together, these observations suggest that NPH3$^{\Delta C51}$ condensates are dynamic, actively regulated assemblies, with HSP70s potentially serving as intrinsic modulators of condensate stability and turnover during phototropic signalling.

3.2.3 HSP70s and their partial association with NPH3 condensates

After identifying HSP70 chaperones as potential regulators of cytosolic NPH3$^{\Delta C51}$ condensates, we first analysed the differences among the isoforms detected via FAPS and IP-GFP: HSP70-1, HSP70-3, and HSP70-4. All three proteins are predominantly cytosolic and cluster together in *A. thaliana* phylogenetic analyses (Lin et al., 2001). Amino acid sequence comparison revealed remarkable conservation among these isoforms, with only ~2% divergence over ~650 residues (i.e., ~12 aa mismatches), mostly from the C-terminus, predicted as a *disordered region* (Supplemental Fig. S8). Given this high similarity, we focused subsequent interaction studies on *HSP70-1* (At5g02500) as a representative isoform.

To assess whether HSP70s can associate with NPH3 condensates, we used transient expression in *N. benthamiana*. Upon single expression, HSP70-1:GFP localized predominantly in the cytosol with occasional PM-proximal signal, whereas RFP:NPH3$^{\Delta C51}$ formed the expected round, dynamic cytosolic condensates (Fig. 10A). Upon co-expression, NPH3$^{\Delta C51}$ condensates showed partial overlap with HSP70-1 (Fig. 10B). When present, HSP70-1 exhibited high mobility within NPH3$^{\Delta C51}$ condensates, consistent with dynamic exchange.

We next compared HSP70-1 behaviour in the presence of different NPH3 variants (Supplemental Fig. S9). As previously observed, HSP70-1:RFP partially co-localized with GFP:NPH3$^{\Delta C51}$ condensates. In contrast, GFP:NPH3^{S744A}, which remains PM-associated, showed primarily PM-proximal overlap with HSP70-1. Blue-light activated GFP:NPH3^{WT} exhibited a similar pattern, with PM-adjacent co-localization and only limited condensate-internal overlap. Immunoprecipitations of GFP-tagged NPH3 variants co-expressed with HSP70-1:RFP recovered HSP70-1 across all variants, indicating that

HSP70-1 can associate with NPH3 independently of its subcellular distribution under transient expression conditions.

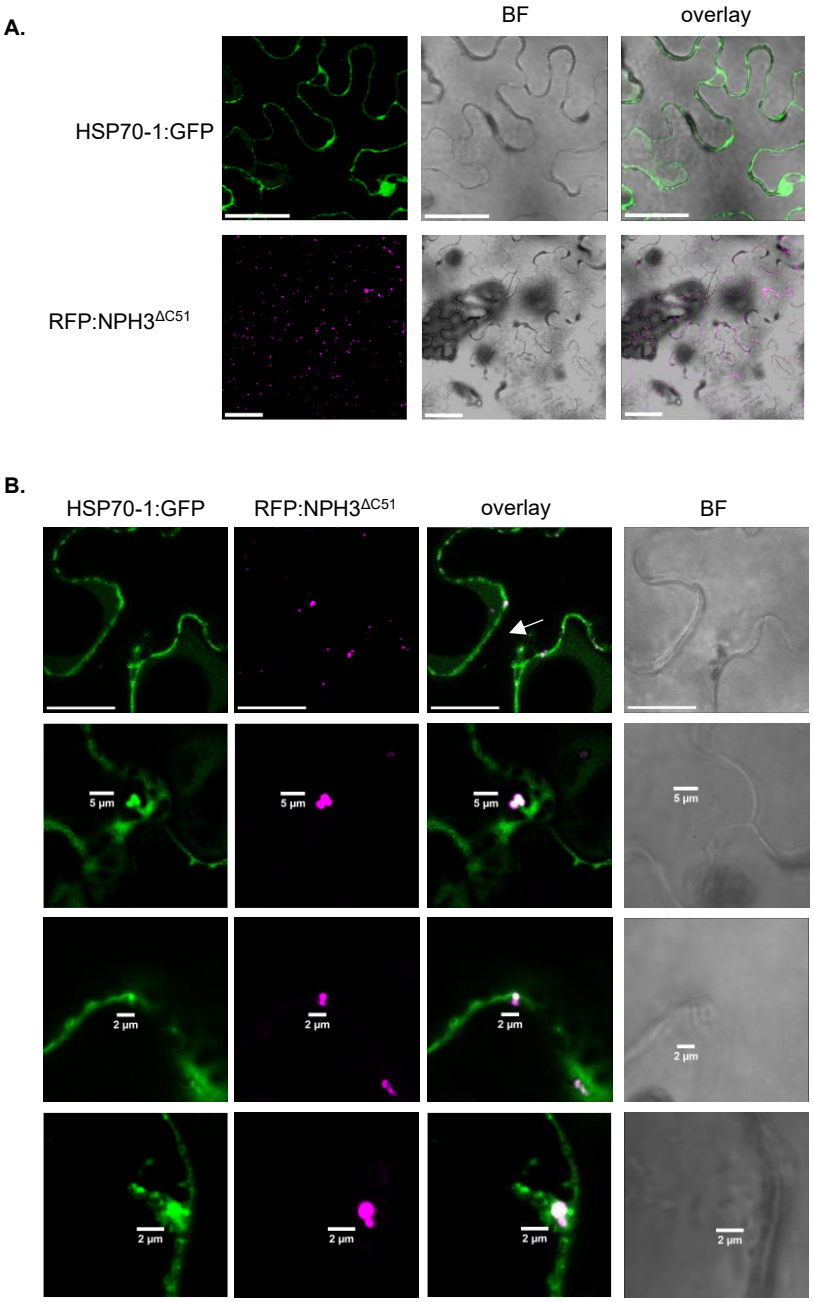

Figure 10. HSP70-1 partially co-localizes with the constitutive condensate-forming NPH3$^{\Delta C51}$ variant *in vivo*

Representative confocal microscopy images of leaf epidermal cells from *N. benthamiana* transiently expressing the indicated constructs under the 35S promoter. Dark-adapted plants were maintained in darkness prior to imaging. (A) Cells expressing HSP70-1:GFP (green) or RFP:NPH3$^{\Delta C51}$ (magenta) individually. HSP70-1:GFP shows diffuse cytosolic localization near the plasma membrane periphery, whereas NPH3$^{\Delta C51}$ forms round cytosolic condensates. Scale bar: 50 µm. (B) Cells co-expressing HSP70-1:GFP and RFP:NPH3$^{\Delta C51}$. RFP:NPH3$^{\Delta C51}$ condensates are observed at the inner leaflet of the PM and show partial overlap with HSP70-1:GFP (white arrow). Higher-magnification views of RFP:NPH3$^{\Delta C51}$ condensates reveal dynamic and partial co-localization with HSP70-1:GFP (white overlay). Scale bar (overview): 50 µm; inset scale bars provided adjacent to condensates: 2 or 5 µm. Images are representative of two independent experiments. BF: bright field

NPH3 contains multiple intrinsically disordered regions (IDRs) including a prion-like domain (Manishankar et al., 2026; Reuter et al., 2021), features previously linked to chaperone interactions (Kolhe et al., 2023). Such interactions have been shown, for example, to inhibit protein aggregation (Chilukoti et al., 2021).

These observations place NPH3 within a growing group of plant proteins whose condensate behaviours intersect with cytosolic chaperone networks. This is consistent with a model in which the formation and dissolution of NPH3 condensate is triggered by light conditions, with cytosolic chaperones modulating the material properties of condensates (Bard and Drummond, 2024),

Summary (Results 3.2): IP-GFP and FAPS analyses identified cytosolic HSP70s as putative interaction partners of NPH3$^{\Delta C51}$ condensates, and transient assays confirmed that NPH3 can recruit HSP70-1 *in vivo.* Current models position HSP70 chaperones as key regulators of biomolecular condensates, supporting the hypothesis that NPH3 forms a single-component condensate (formed primarily by NPH3 itself) whose properties are modulated by chaperones.

3.3 Characterization of the interaction between NPH3 and putative interaction partners from the TPLATE Complex

As mentioned before, NPH3 undergoes a dynamic cycling between PM-associated and cytosolic condensates. This process is reversible, as condensates can re-associate with the PM under favourable conditions. Our observations indicate that NPH3 predominantly forms single-component cytosolic condensates (as no other structural protein was identified), with HSP70 chaperones likely modulating their material properties. These associations may reflect a potential sequestration mechanism within the cytosol.

Together, these findings suggest that NPH3 carries out a functional role at the PM, which appears to require a transient inactivation step, mediated by PM dissociation followed by condensate formation in the cytosol, to initiate and/or sustain phototropic responses.

The TurboID-based proximity labelling approach identified a set of proteins proximal to NPH3 at the PM in darkness and during the complete BL-triggered cycling process, namely initial PM localization, followed by condensate formation in the cytosol and finally PM re-association (Results 3.1). These datasets suggest that NPH3 is in spatial proximity to components of the TPLATE complex (TPC) and the clathrin-mediated endocytosis (CME) machinery. Yet, proximity labelling alone cannot distinguish between direct and indirect associations and does not provide temporal resolution. We therefore applied targeted interaction assays, focussing on the potential interaction between NPH3

and the TPC, as it could provide new insights into the molecular mechanism of NPH3 function. We focused on the TPC core subunit TPLATE and the EH-domain-containing subunit AtEH1, which is essential for both TPC association with the PM and membrane bending during clathrin-coated pit formation (Dragwidge et al., 2024; Johnson et al., 2021; Yperman et al., 2021a)

3.3.1 Subcellular localization of NPH3 and TPLATE in transient expression systems

We first analysed the subcellular localization of the proteins TPLATE, AtEH1 and NPH3 to establish whether they occupy overlapping cellular compartments, a prerequisite, but not proof of interaction. Constructs enabling constitutive expression of mRFP:TPLATE and AtEH1:eGFP (35S promoter; provided by Prof. Dr. Daniel Van Damme) were agroinfiltrated into *N. benthamiana* leaves. When expressed individually (Fig. 11A), the TPLATE subunit localized to both the cytosol and the cell periphery in a uniform manner. In contrast, AtEH1 formed prominent puncta close to the PM, recently described as PM associated biomolecular condensates (Dragwidge et al., 2024).

Upon co-expression of TPLATE with AtEH1, we observed partial recruitment of TPLATE into AtEH1 PM condensates (Fig. 11B). In *Arabidopsis,* AtEH1 has been shown to drive biomolecular condensation at the PM, promoting the local enrichment of TPLATE complex components and other endocytic proteins (Dragwidge et al., 2024). Consistent with this, AtEH1 physically associates with the TPLATE complex and facilitates the formation of endocytic hubs at the PM (Gadeyne et al., 2014; Wang et al., 2020, 2019; Yperman et al., 2021b). This selective enrichment suggests that client proteins can *partition* into AtEH1-driven condensates, a mechanism proposed to spatially organize and concentrate endocytic machinery at the PM (Dragwidge et al., 2024; Dragwidge and Van Damme, 2024).

To assess the spatial relationship between NPH3 and TPLATE, GFP-tagged NPH3 variants were transiently co-expressed with mRFP:TPLATE. In darkness, $NPH3^{WT}$ localized primarily to the PM, whereas TPLATE was present in the cytosol and cell periphery, displaying partial co-localization with $NPH3^{WT}$ at the PM. GFP laser exposure activates phot1 and triggers NPH3 dissociation from the PM followed by condensate formation (Reuter et al., 2021). Accordingly, NPH3 progressively formed condensates at the cell periphery. After prolonged laser exposure (~10-20 minutes), partial overlap between TPLATE and $NPH3^{WT}$ condensates was observed (Fig. 12). Albeit interesting, the co-localization of TPLATE in $NPH3^{WT}$ condensates could also reflect overexpression

artifacts, as TPLATE can exhibit promiscuous localization and/or binding in transient systems (D. Van Damme, personal communication).

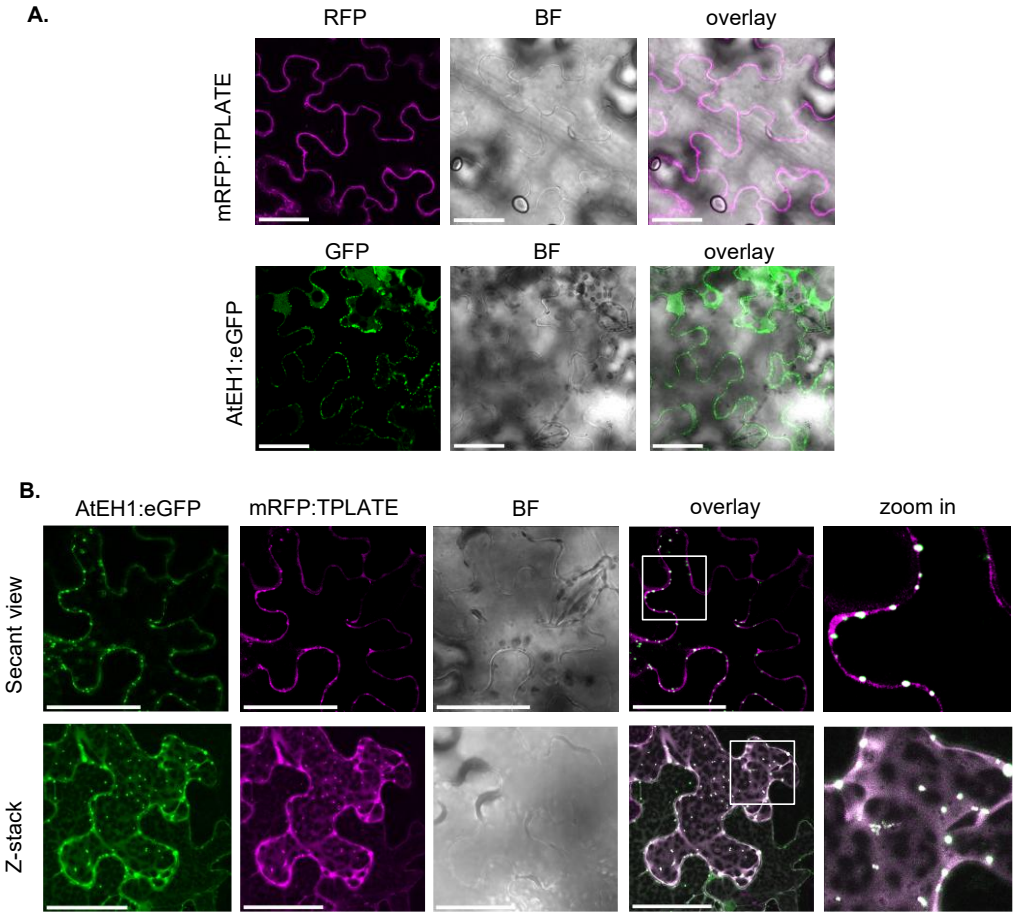

Figure 11. TPLATE and AtEH1 subcellular localization in *N. benthamiana*: Partitioning of TPLATE into AtEH1 PM-condensates

Representative confocal microscopy images of dark-adapted leaf epidermal cells from *N. benthamiana* transiently expressing the indicated constructs under the 35S promoter. Dark-adapted plants were maintained in darkness prior to imaging. (A) Cells expressing mRFP:TPLATE or AtEH1:eGFP individually. TPLATE displays cytosolic and peripheral cell localization, whereas AtEH1 localizes to distinct plasma membrane puncta. (B) Cells co-expressing mRFP:TPLATE and AtEH1:eGFP. Partitioning of TPLATE into AtEH1 plasma membrane condensates is observed. Representative images from three independent experiments. Scale bars: 50 µm. BF: bright field. Z-stack (maximum projection of ≥10 frames).

We next examined two additional NPH3 variants to further constrain the spatial context of a potential association. We used NPH3^{S744A}, which is constitutively PM-associated due to loss of phot1-dependent phosphorylation and NPH3$^{\Delta C51}$, which constitutively forms condensates due to the absence of the amphipathic helix required for PM association (Reuter et al., 2021). Co-expression of GFP:NPH3^{S744A} with mRFP:TPLATE showed partial PM co-localization with TPLATE (Supplemental Fig. S10), similar to what was observed for NPH3^{WT} in darkness. In contrast, GFP:NPH3$^{\Delta C51}$ co-expressed with mRFP:TPLATE did not display detectable spatial overlap (Fig. 13). Although NPH3$^{\Delta C51}$

forms highly dynamic cytosolic condensates and TPLATE partially localizes to the cytosol, both proteins remained spatially separated, as clearly shown in the maximum projections (15 frames Z-stacked obtained over 3 minutes).Together, these observations indicate that detectable spatial overlap between NPH3 and TPLATE is restricted to regions near the PM.

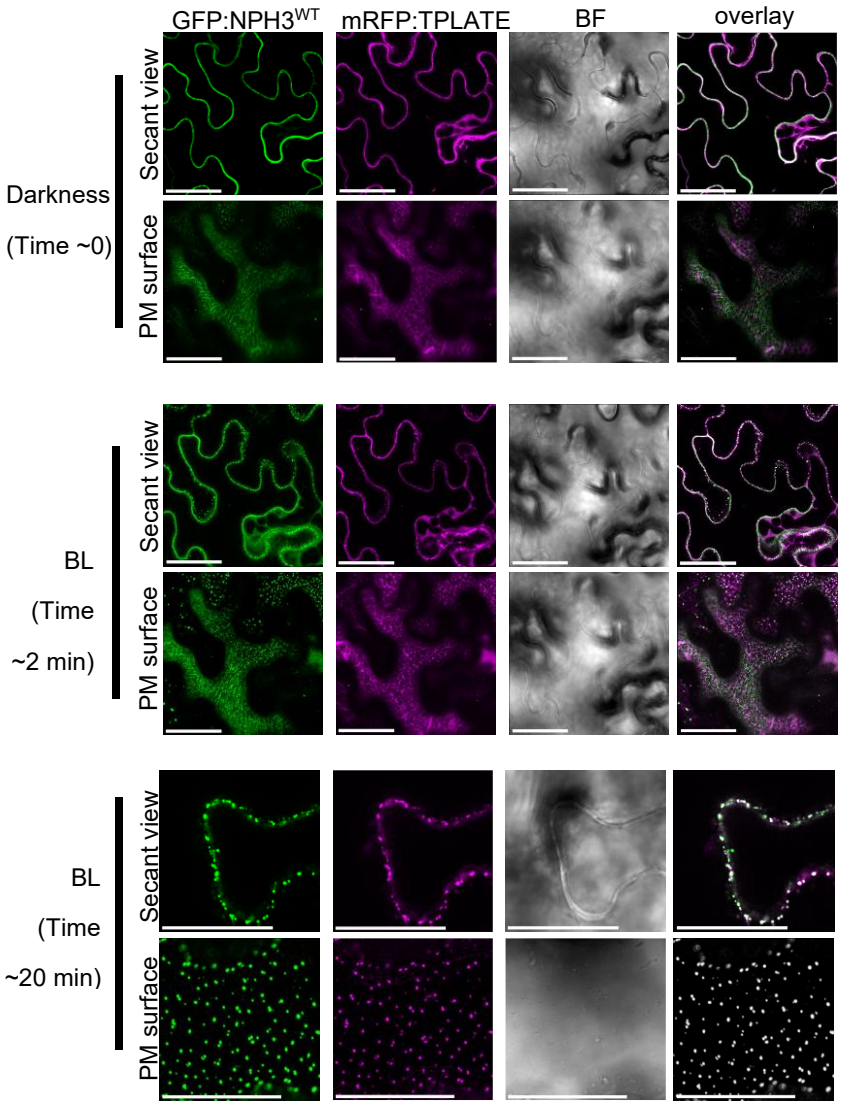

Figure 12. Partial co-localization of TPLATE and NPH3^{WT} in NPH3 condensates during transient co-expression

Representative confocal microscopy images of dark-adapted leaf epidermal cells from *N. benthamiana* transiently co-expressing mRFP:TPLATE and GFP:NPH3. Expression was driven by the 35S promoter. Dark-adapted plants were maintained in darkness prior to BL exposure via GFP laser onset. Partial co-localization of TPLATE and NPH3 close to the plasma membrane (PM) is observed. Secant and PM surface views are provided. Scale bars: 50 µm. Representative of ~15 independent experiments. BF: bright field.

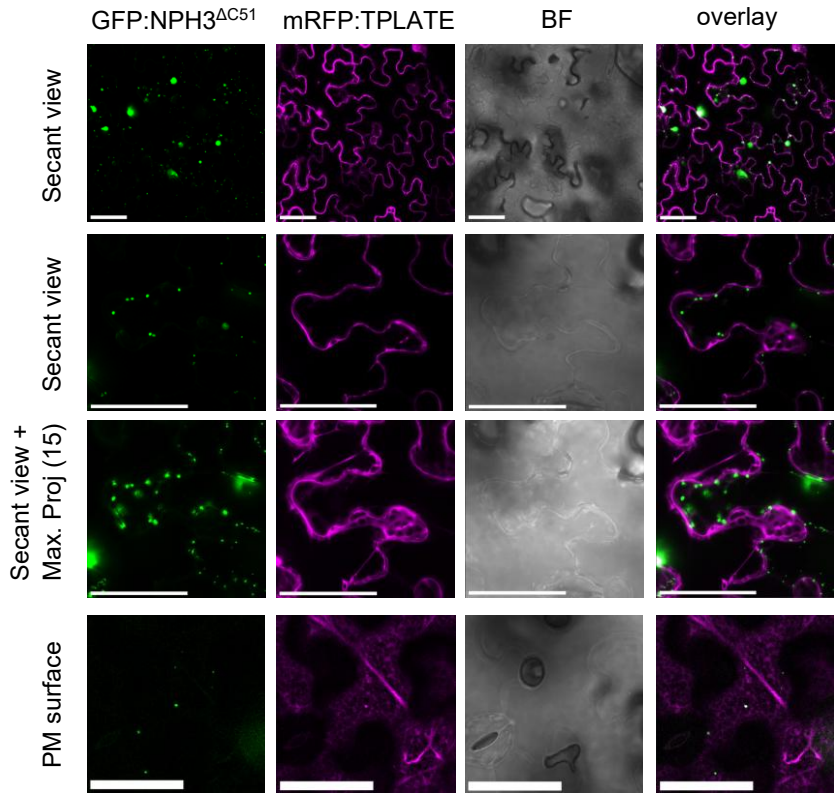

Figure 13. TPLATE and NPH3$^{\Delta C51}$ do not co-localize during transient co-expression

Representative confocal microscopy images of dark-adapted leaf epidermal cells from *N. benthamiana* transiently co-expressing GFP:NPH3$^{\Delta C51}$ and mRFP:TPLATE. Expression was driven by the 35S promoter. Dark-adapted plants were maintained in darkness prior to imaging. NPH3$^{\Delta C51}$ does not co-localize with TPLATE. Scale bars: 50 µm. Representative of ~ 5 independent experiments. BF: bright field.

3.3.2 In vivo interaction analysis of NPH3 and TPLATE

To directly test whether NPH3 and TPLATE are brought into nanometer-scale proximity *in vivo*, we performed Förster Resonance Energy Transfer using Fluorescence Lifetime Imaging Microscopy (FRET-FLIM), This technique detects energy transfer from a donor to an acceptor fluorophore when they are within ~1-10 nm, providing a sensitive readout of molecular interactions. FLIM measures changes in the donor's fluorescence lifetime, which decreases upon FRET, and this measurement is largely independent of donor or acceptor concentration, avoiding biases from variable protein expression levels. Common FRET-FLIM pairs such as GFP-mCherry and their monomeric variants thereof, are used to minimize spectral crosstalk and avoid donor fluorophore oligomerization.

FRET-FLIM analyses were performed in *N. benthamiana* epidermal cells transiently co-expressing mRFP:TPLATE with either mEGFP:NPH3^{WT} or mEGFP:NPH3^{S744A}. Donor-only samples served as controls (Fig. 14). Co-expression of mRFP:TPLATE with mEGFP:NPH3^{WT} resulted in a significant reduction of GFP fluorescence lifetime

compared to donor-only controls (from 2.505 ns to 2.361 ns). A less pronounced but statistically significant lifetime reduction was observed for the mEGFP:NPH3^{S744A}-mRFP:TPLATE pair (from 2.471 ns to 2.386 ns). As a positive control, co-expression of AtEH1:eGFP with mRFP:TPLATE produced an expected decrease in GFP lifetime (from 2.502 ns to 2.300 ns), consistent with the established physical association between these TPC subunits (Gadeyne et al., 2014; Wang et al., 2019; Yperman et al., 2021b). The observed lifetime reductions are compatible with a close molecular association between NPH3 and TPLATE at the PM and align with the partial co-localization observed in transient expression assays (Fig. 12; Supplemental Fig. S10). However, it is important to note that FRET can occur when donor and acceptor fluorophores are brought into close proximity (Förster radius), even in the absence of a specific molecular interaction (Laptenok et al., 2010; Long et al., 2017).

Selecting a suitable PM-resident negative control for TPLATE was challenging, as many stably PM-localized proteins are known to be internalized via CME. We selected REM1.2 (remorin 1.2) as a PM-associated nanodomain-organizing protein (Ke et al., 2021), for which there is currently no evidence of direct interaction with the TPC. Co-expression of REM1.2:GFP with mRFP:TPLATE yielded a modest but statistically significant reduction in GFP lifetime (from 2.593 ns to 2.522 ns), indicating that REM1.2 is not an optimal negative control for our experiments. Despite this limitation, REM1.2 serves as a PM-localized reference protein lacking known functional association with the TPC.

Taken together, the FRET-FLIM data suggest that NPH3 and TPLATE are brought into nanometer-scale proximity to each other at the PM, a spatial arrangement fully compatible with a direct interaction. Although transient overexpression systems can generate proximity-driven FRET independent of binding, the magnitude of the observed lifetime reductions suggests that the NPH3-TPLATE proximity is more likely to reflect a biologically relevant contact than incidental spatial overlap.

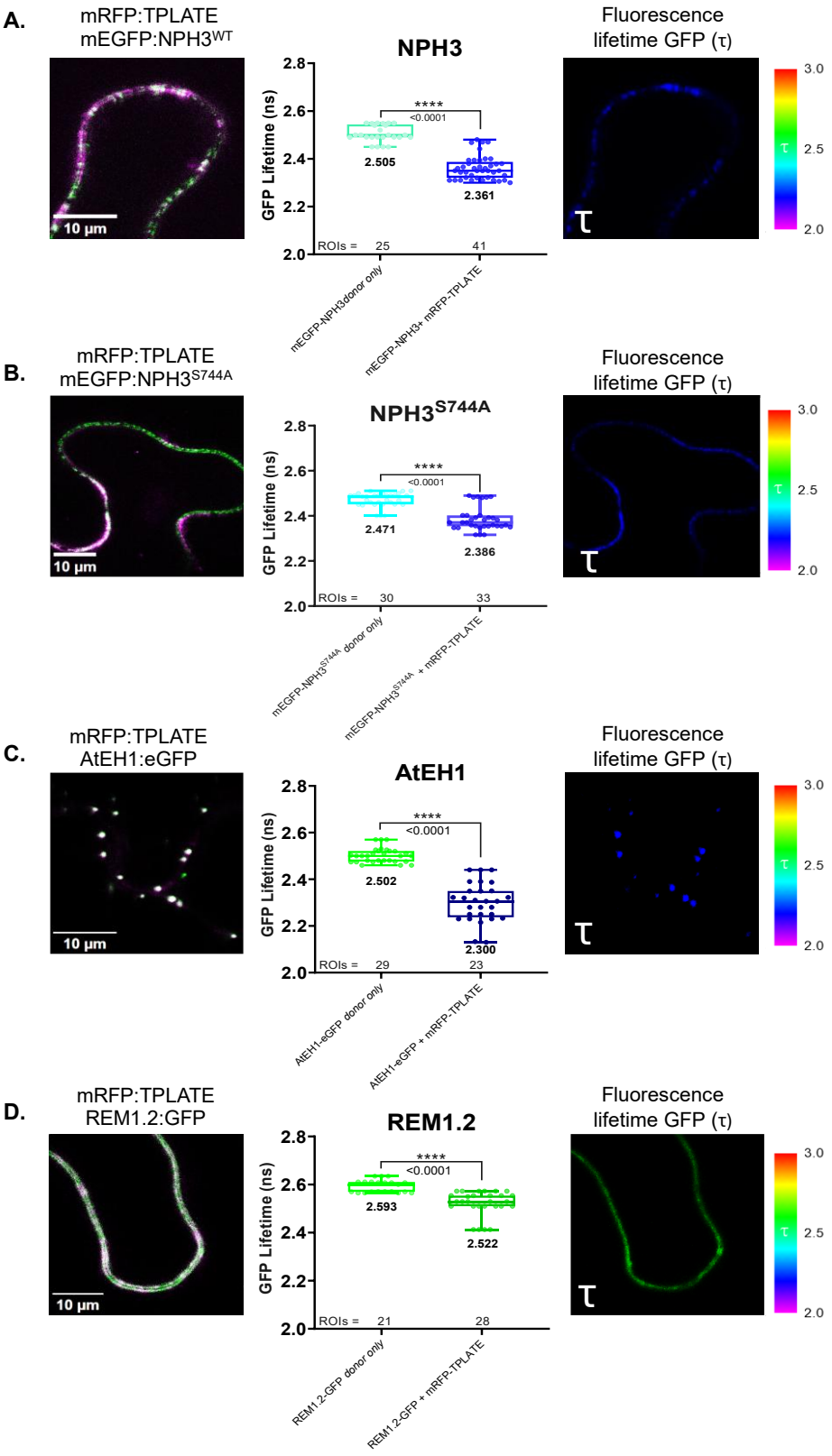

Figure 14. FRET-FLIM validation of the TPLATE-NPH3 interactions

FRET-FLIM measurements were performed on leaf epidermal cells from dark-adapted *N. benthamiana* plants transiently co-expressing the indicated constructs under the 35S promoter. Dark-adapted plants were maintained in darkness prior to BL exposure via GFP laser onset. p19 was included in all co-expressions. For each combination, confocal images (left) confirm expression, quantitative FRET-FLIM measurements

are shown as graphs (center), and color-coded fluorescence lifetime (FLT) images of the GFP channel are displayed (right), reporting donor lifetimes relative to donor-only controls (color scale adjacent). In panel (A), mEGFP:NPH3^{WT} with mRFP:TPLATE shows a clear reduction in donor lifetime, indicating interaction, while panel (B) demonstrates that the phospho-site mutant mEGFP:NPH3^{S744A} similarly reduces donor lifetime. Panel (C) presents the positive control AtEH1:eGFP with mRFP:TPLATE, confirming expected FRET, whereas panel (D), the putative negative control REM1.2:GFP with mRFP:TPLATE, exhibits mostly green FLT (~2.5 ns) but a small yet significant donor lifetime reduction, indicating it is not an ideal negative control. Fluorescence decay curves were fitted with mono- or bi-exponential models using PicoQuant SymPhoTime software, mean lifetimes (τ) were calculated from ROIs pooled across replicates, and FRET efficiencies were derived from donor lifetime reductions. Bar plots represent mean ± SD across all ROIs, with ROI numbers indicated, and statistical significance was assessed by unpaired t-test with Welch's correction. All data was plotted. Experiments were repeated at least three times with consistent results.

3.3.3 Biochemical validation of the NPH3-TPLATE association

Yeast two-hybrid (Y2H) analyses of the TPLATE complex (TPC) subunits identified only a single robust binary interaction among the eight components, namely between TASH3 and LOLITA (Gadeyne et al., 2014). The inability of Y2H to detect most of other TPC interactions indicates that these associations are not stable as isolated pairwise contacts. Subsequent studies demonstrated that assembly of the TPC largely depends on additional subunits acting as molecular bridges or stabilizing interfaces, interactions that become apparent only in higher-order or native-context assays. This was revealed through yeast three-hybrid approaches and corroborated by integrative structural and biochemical analyses, including co-immunoprecipitation (Co-IP), affinity purification-mass spectrometry, proximity labelling, *in planta* relocalization assays, crosslinking mass spectrometry, and cryo-electron microscopy (Gadeyne et al., 2014; Yperman et al., 2021b). Y2H assays performed in this thesis did not detect interactions between NPH3 variants and TPLATE (Supplemental Fig. S12).

Taking into consideration such restrains, we focused on Co-IP techniques to biochemically assess the association between NPH3 and TPLATE, following transient expression of GFP-tagged NPH3 variants and mRFP:TPLATE in *N. benthamiana* under dark and blue-light conditions. Among the tested proteins (GFP:NPH3^{WT}, GFP:NPH3^{S744A}, and GFP:NPH3$^{\Delta C51}$), only NPH3^{WT} and the constitutively PM-associated NPH3^{S744A} variant co-precipitated with TPLATE, under both conditions (Fig. 15A). In contrast, NPH3$^{\Delta C51}$, which showed no detectable co-localization with TPLATE in confocal imaging (Fig. 13), failed to co-precipitate TPLATE (Fig. 15A). This concordance between microscopy and biochemistry suggests that, under transient expression conditions, TPLATE associates only with NPH3 variants that localize to the PM.

We further tested if these associations can be reproduced in *Arabidopsis.* Co-IP experiments were performed using etiolated *Arabidopsis* seedlings co-expressing TPLATE:GFP (pLAT52) and DRP1A:mRFP (p35S) provided by Prof. Daniel Van Damme.

Immunoprecipitation (IP) of TPLATE:GFP was followed by immunodetection of NPH3 using both a general NPH3 antibody and a phospho-specific antibody recognizing phot1-mediated BL-induced phosphorylation at Ser744 (Reuter et al. 2021). IP demonstrated that NPH3 co-precipitates with TPLATE in etiolated seedlings and further shows that the interaction predominantly involves the dark form of NPH3, as phosphorylation of Ser744 could not be detected in the IP fraction from BL-treated samples (Fig. 15B). In addition, the Co-IP revealed that TPLATE:GFP was also capable of co-precipitate DRP1A, a protein also identified in our proximity-labelling approach, supporting the proximity of NPH3 to endocytic machinery at the PM.

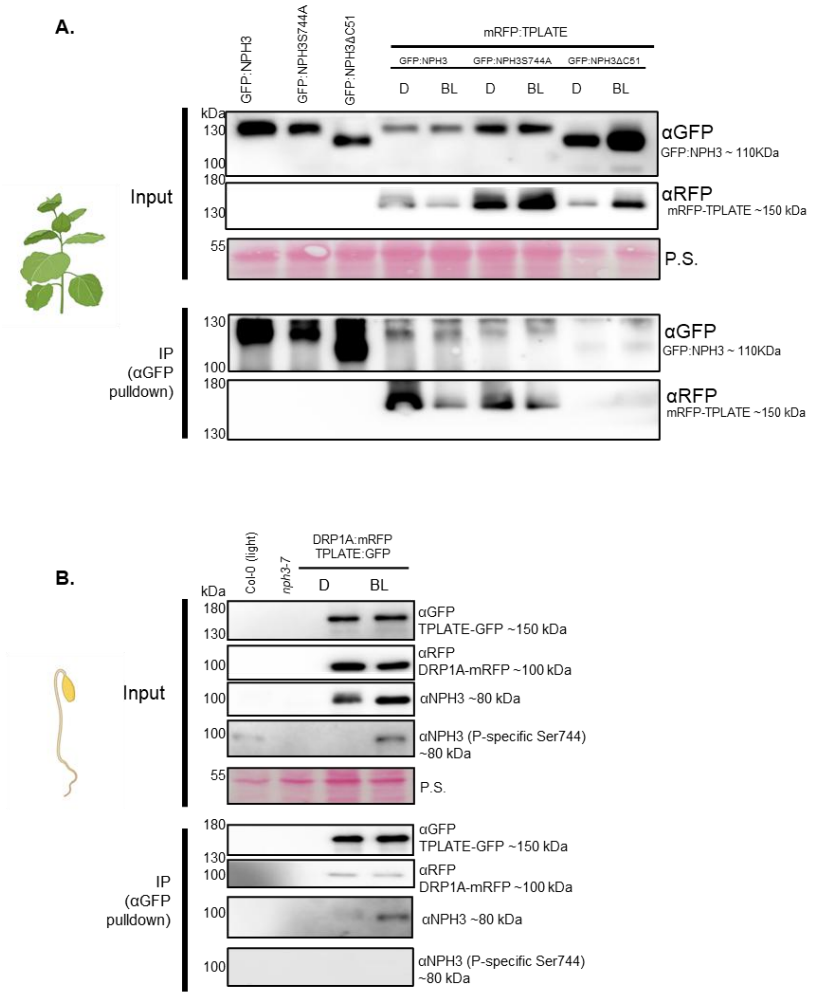

Figure 15. Biochemical validation of the TPLATE-NPH3 interactions

(A) *In vivo* interaction of GFP:NPH3 variants (35S promoter) transiently co-expressed with mRFP:TPLATE (35S promoter) in *N. benthamiana* leaves. Dark-adapted plants were either maintained in darkness (D) or treated with overhead blue light (BL; 10 µmol m^{-2} s^{-1}, 40 min). Crude protein extracts were immunoprecipitated using GFP-Trap® beads, and input and immunoprecipitated proteins (IP anti-GFP pulldown) were detected by immunoblotting. Experiments were performed at least twice with similar results. (B) *In vivo* interactions of TPLATE in transgenic *Arabidopsis* plants ectopically expressing TPLATE:GFP (LAT52 promoter) and DRP1A:mRFP (35S promoter; Daniel Van Damme). Three-day-old, etiolated seedlings were either maintained in darkness (D) or treated with overhead blue light (BL; 10 µmol m^{-2} s^{-1}, 40 min). Seedlings were harvested for crude protein extraction and immunoprecipitated using GFP-Trap® beads. Input and immunoprecipitated proteins (IP anti-GFP pulldown) were analysed by immunoblotting.

Col-0 seedlings exposed to BL for 40 min served as a control for the detection of NPH3 Ser744 phosphorylation mediated by phot1. Blots were probed with a general anti-NPH3 and a phospho-specific anti-NPH3 (Ser744) antibodies. Representative results from three independent replicates are shown. P.S., Ponceau staining.

These experiments collectively indicate that NPH3 interacts with TPLATE under conditions in which NPH3 is PM resident and maintained in a phot1-dependent unphosphorylated (dark-state) form. Evidence for this association is provided by Co-IP of TPLATE with NPH3^{WT} and the constitutively PM-associated NPH3^{S744A} variant, while the condensate-localized NPH3$^{\Delta C51}$ variant, which fails to associate with the PM, neither co-localizes with nor co-precipitates TPLATE. FRET-FLIM analyses experiments further support close spatial proximity consistent with an interaction between NPH3 and TPLATE at the PM.

3.3.4 NPH3 interaction with the AtEH1 subunit likely depends on the presence of TPLATE

After establishing that NPH3 interacts with the TPLATE core subunit at the PM, we next asked whether NPH3 can also associate with the TPC component AtEH1, crucial for PM-association, and whether such association depends on TPLATE. We first analysed subcellular localization patterns and subsequently complemented these observations with biochemical interaction assays.

Thus, we transiently co-expressed AtEH1:eGFP with either RFP:NPH3^{WT} or the constitutively PM-attached RFP:NPH3^{S744A} variant in N. *benthamiana*. In darkness, AtEH1 localized to characteristic PM-associated condensates (Dragwidge et al., 2024), whereas both NPH3^{WT} and NPH3^{S744A} displayed uniform PM localization (Figs. 16 and 17). Upon GFP laser exposure, NPH3^{WT} but no NPH3^{S744A}, underwent BL-induced PM-dissociation followed by condensate formation, with a fraction of those condensates observed close to the PM, as previously reported (Reuter et al., 2021). Notably, NPH3^{WT} condensates did not overlap with AtEH1 PM condensates, and no partitioning of either NPH3^{WT} or NPH3^{S744A} into AtEH1 PM condensates was observed under these conditions. This behaviour contrasts with TPLATE, which robustly partitions into AtEH1 condensates (Fig. 11), indicating that NPH3 is not recruited into AtEH1 PM-condensates when transiently overexpressed.

To complement the localization analysis, we next performed Co-IP assays in *N. benthamiana*. AtEH1:eGFP robustly co-precipitated with mRFP:TPLATE, consistent with their established interaction (Gadeyne et al. 2014; Yperman, et al. 2021). In contrast, association between AtEH1:eGFP and RFP:NPH3^{WT} was weak. Although AtEH1 co-

precipitated with NPH3^{WT}, the signal was near the detection limit and markedly reduced compared to TPLATE (Supplemental Fig. S11B).

To assess whether this association also occurs in *Arabidopsis*, we performed reciprocal Co-IP experiments, using etiolated *Arabidopsis* seedlings ectopically expressing either GFP:NPH3^{WT} (Reuter et al., 2021) or AtEH1:GFP in combination with an AtEH1-specific antibody (Prof. Dr. Daniel Van Damme). Endogenous AtEH1 (~110 kDa) was reproducibly detected in GFP:NPH3^{WT} immunoprecipitates, and endogenous NPH3 (~80 kDa) co-precipitated with AtEH1:GFP in two independent lines, under both dark and BL conditions (Supplemental Fig. S11A). Although these signals were consistently weak, their reproducibility supports the existence of an association between NPH3 and AtEH1. Consistent with the limitations of Y2H assays for detecting TPLATE complex associated interactions, as outlined earlier (Section 3.3.3), Y2H analyses did not reveal interactions between NPH3 and AtEH1 truncations that avoid autoactivation (Wang et al., 2023) (Supplemental Fig. S12).

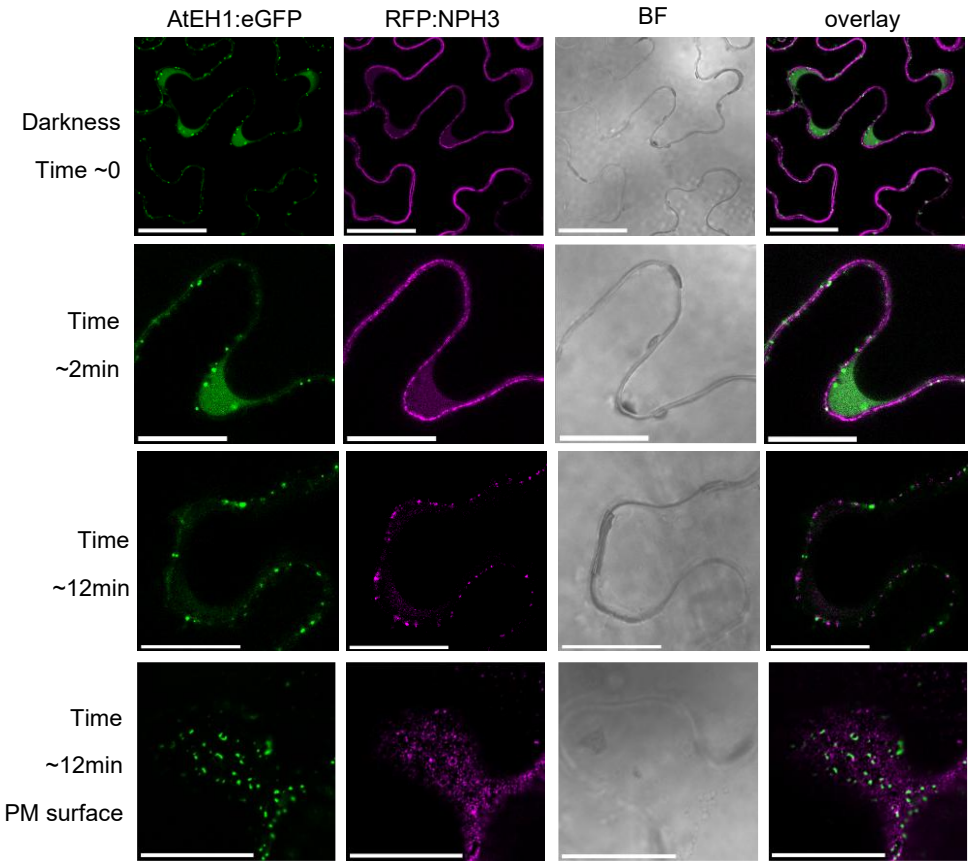

Figure 16. NPH3^{WT} does not partition into AtEH1 PM-condensates upon transient co-expression

Representative confocal microscopy images of leaf epidermal cells from dark-adapted *N. benthamiana* plants transiently co-expressing AtEH1:eGFP and RFP:NPH3^{WT}. Dark-adapted plants were maintained in

darkness prior to BL exposure via GFP laser onset. Expression was driven by the 35S promoter. AtEH1 localizes to PM condensates, while NPH3^{WT} accumulates in condensates, adjacent to the PM after 12 min GFP exposure. No co-localization detected. Scale bars: 50 µm. Representative of ~ 7 independent experiments. BF: bright field.

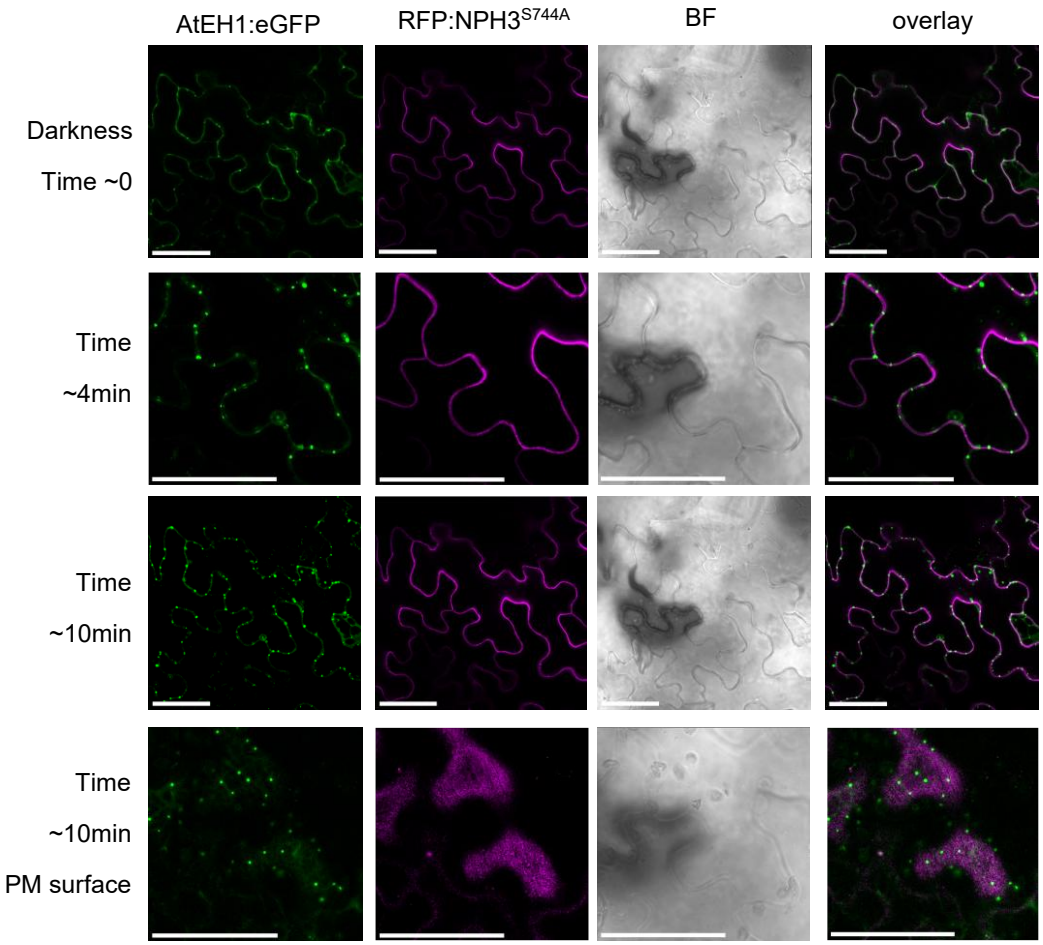

Figure 17. NPH3^{S744A} does not partition into AtEH1 PM-condensates upon transient co-expression

Representative confocal microscopy images of dark-adapted leaf epidermal cells from *N. benthamiana* plants transiently co-expressing AtEH1:eGFP and RFP:NPH3^{S744A}. Expression was driven by the 35S promoter. Dark-adapted plants were maintained in darkness prior to imaging. NPH3^{S744A} remains PM-localized and does not partition with AtEH1 condensates. Scale bars: 50 µm. Representative of ~ 6 independent experiments. BF: bright field.

In our transient *N. benthamiana* experiments, overexpression of AtEH1 and NPH3 in the context of limited endogenous TPLATE did not result in recruitment of NPH3 into AtEH1 PM condensates. Taken together, these results indicate that, in contrast to TPLATE, NPH3 does not efficiently associate with AtEH1 on its own and does not partition into AtEH1 PM condensates in transient expression assays. Given that NPH3 interacts with TPLATE (Results 3.3.3), we therefore infer that any association between NPH3 and AtEH1 is likely indirect and depends on higher-order TPC assembly.

To investigate whether TPLATE facilitates NPH3 recruitment into AtEH1 condensates at the PM, we used a triple transient expression approach. We co-expressed AtEH1:eGFP, mRFP:TPLATE, and mTurquoise2-tagged NPH3 variants (all under p35S) in *N. benthamiana* and imaged leaf epidermal cells using confocal and Airyscan microscopy (Fig. 18). In dark-adapted cells (Time ~0), all three proteins localized to the PM, with AtEH1 forming previously described PM-associated condensates and NPH3 being uniformly PM-attached (Fig. 18A). After ~7 min of confocal imaging (under GFP laser induction), we observed a clear recruitment of TPLATE into AtEH1 PM condensates (Fig. 18B, arrow number 1). At the same time, $NPH3^{WT}$ condensates near the PM, partitioned into AtEH1-TPLATE condensates at the PM (Fig. 18B, arrow number 2).

Airyscan imaging, which provides higher-resolution visualization, confirmed our previous observations. In these experiments, AtEH1 condensates robustly recruited TPLATE to the PM. $NPH3^{WT}$ displayed a mixed localization pattern. It both partitioned into AtEH1-TPLATE PM-condensates (Fig. 18C, white arrows) and retained the capacity to form highly mobile and independent condensates close to the PM (Fig. 18C, turquoise arrows). Analysis of the constitutively PM-attached mutant $NPH3^{S744A}$ revealed its ability to localize to discrete puncta or subregions at the PM, some of which overlapped with AtEH1-TPLATE PM condensates (Fig. 18D, white arrow). These observations indicate that $NPH3^{WT}$ can partition into AtEH1 PM-condensates in the presence of exogenous TPLATE. $NPH3^{S744A}$ on the other hand, forms “patches” at specific PM subregions, enabling occasional co-localization with AtEH1-TPLATE assemblies at the PM.

To further examine if NPH3 associates with AtEH1 and TPLATE under conditions in which all three proteins are present, we analysed their interaction by Co-IP following triple transient expression in *N. benthamiana*. Specifically, mRFP:TPLATE was co-expressed with AtEH1:eGFP and either mTQS2:$NPH3^{WT}$ or mTQS2:$NPH3^{S744A}$, and Co-IP experiments were performed under dark or BL conditions (Fig. 19). In all conditions tested, AtEH1 and NPH3 were detected in the immunoprecipitated TPLATE fraction, indicating that all three proteins can be recovered *in vivo*. Consistent with the localization data, interactions between TPLATE and AtEH1, as well as between TPLATE and both NPH3 variants, were detectable under both dark and BL conditions.

The apparent increase in NPH3 signal observed in the IP fraction upon BL exposure, can be due to incomplete PM dissociation of NPH3 and moreover, can be explained by increased partitioning of NPH3 into AtEH1-TPLATE PM condensates, a process that has been shown to be promoted by laser exposure during imaging.

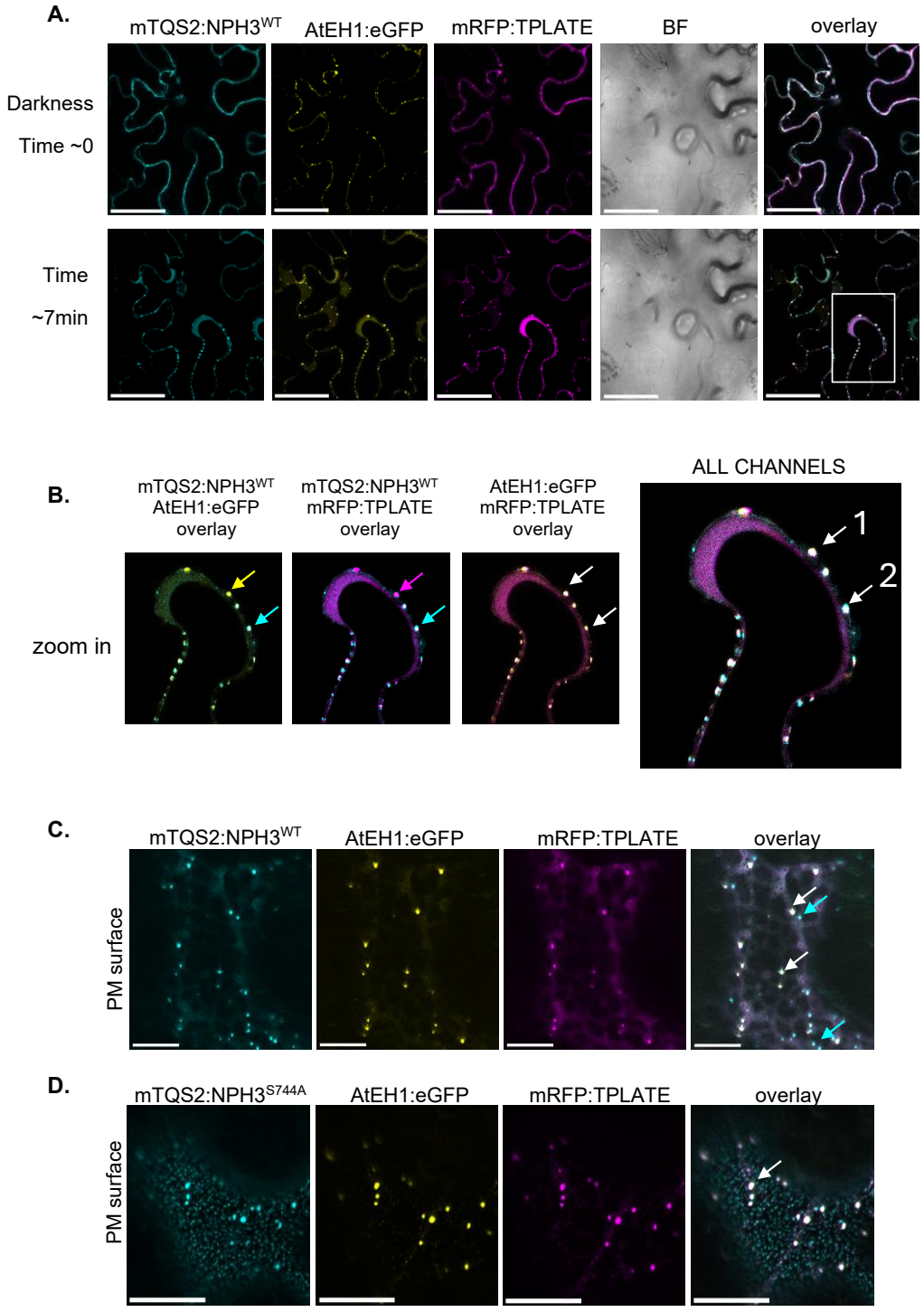

Figure 18. Transient expression of TPLATE, AtEH1, and NPH3 reveals partial partitioning of NPH3 into AtEH1-TPLATE PM condensates while maintaining independent NPH3 condensates

(A) Representative confocal microscopy images of leaf epidermal cells from dark-adapted *N. benthamiana* plants transiently co-expressing AtEH1:eGFP, mRFP:TPLATE, and mTurquoise2:NPH3^{WT} or NPH3^{S744A}. Expression was driven by the 35S promoter. Dark-adapted plants were maintained in darkness (time ~0 min) prior to BL exposure via GFP laser onset (Time ~7 min). (B) Zoomed insets after 7 min of BL exposure, showing individual channel merges to assess individual protein partitioning at PM puncta. Yellow arrow indicate predominance of AtEH1. Fuchsia arrow indicates predominance of TPLATE. Turquoise arrow indicates predominance of NPH3^{WT}. When all channels are visualized, white arrows indicate 1): AtEH1-TPLATE PM puncta and 2): AtEH1-TPLATE- NPH3^{WT} containing puncta. Representative of five independent experiments. Scale bars: 50 µm. To confirm these observations, we performed Airyscan imaging with the

same three proteins and also included NPH3^{S744A}. Representative images were taken after ~10 min of laser onset. (C) Co-expression of AtEH1-TPLATE- NPH3^{WT} indicates overlapping puncta (from the PM surface) of all proteins (white arrows), while at the same time NPH3^{WT} is observed forming independent condensates close to the PM (turquoise arrows). (D) Co-expression of AtEH1-TPLATE- NPH3^{S744A} indicates partial overlap in AtEH1-TPLATE PM puncta (white arrow), while NPH3^{S744A} is observed localizing to “patch”-like PM subdomains. Representative of two independent experiments. Scale bars: 50 µm.

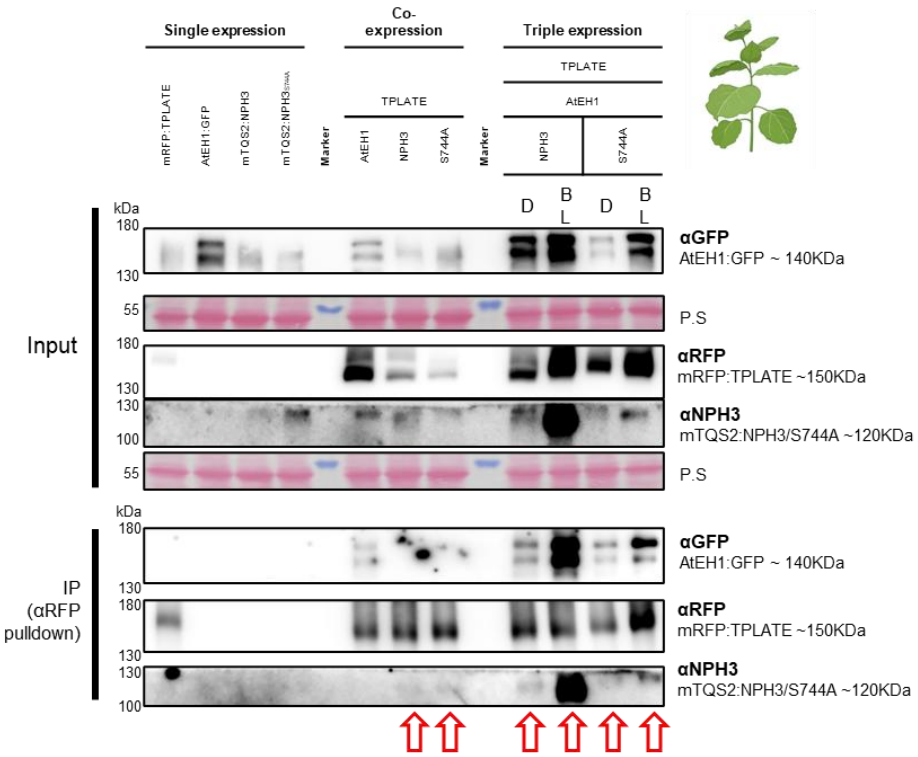

Figure 19. TPLATE associates with NPH3 and AtEH1 under both dark and BL conditions

Co-immunoprecipitation of mRFP:TPLATE from *N. benthamiana* leaves transiently co-expressing mRFP:TPLATE, AtEH1:eGFP and NPH3 variants tagged with mTurquoise2 (mTQS2). Expression was driven by the 35S promoter. Dark-adapted plants were either maintained in darkness (denoted D) or treated with overhead blue light (denoted BL; 10 µmol m^{-2} s^{-1}, 1 h). Crude protein extracts were immunoprecipitated using RFP-Trap® beads, and input and immunoprecipitated proteins (IP anti-RFP pulldown) were detected by immunoblotting with anti-RFP, anti-GFP, and anti-NPH3. NPH3^{WT} showed stronger co-immunoprecipitation with TPLATE-AtEH1 under blue light compared to darkness. Interactions with NPH3^{S744A} were also detected enhanced under BL, when compared to darkness. Red Arrows indicate the detection of NPH3. Representative of three independent experiments. P.S., Ponceau staining.

Summary (Results 3.3): The combined imaging and biochemical analyses support a working hypothesis in which NPH3 associates with TPLATE at the PM. AtEH1 can indirectly associates with NPH3 within a higher-order complex that requires the presence of TPLATE in transient expression assays. While TPLATE robustly interacts with AtEH1 and efficiently partitions into AtEH1 PM-condensates, NPH3 is recruited into these condensates only when TPLATE is provided in this system. This behaviour is consistent with TPLATE likely acting as an essential adapter that stabilizes or enables NPH3 association with the TPC rather than NPH3 interacting independently with individual TPC

subunits. The observed interactions are likely transient, underscoring the importance of complex assembly and stoichiometry in governing NPH3-TPC association *in vivo.*

3.4 Impact of NPH3 on endocytosis: functional analyses and study of the *nosh* mutant as a proxy

As described in the Introduction (Section 1.4.1), the TPLATE complex functions at the early onset of endocytosis, cooperating with the AP-2 adaptor complex in cargo recognition at the PM (Kraus et al., 2024; Zhang et al., 2024). Our initial proximity labelling experiments suggested that NPH3 may interact with the TPC at the PM. We validated interactions for the TPLATE core subunit and AtEH1 using FRET-FLIM analysis and biochemical approaches (Results 3.3), confirming that NPH3 physically associates with components of the endocytic machinery. These observations provided the rationale to test whether NPH3 might influence endocytosis *in vivo.*

3.4.1 FM4-64 uptake in nph3-7 and nosh

The lipophilic styryl dye FM4-64 binds to the PM and is selectively internalized through endocytosis, labelling trafficking pathways from early endosomes to the vacuole in plant cells (Bolte et al., 2004). To assess possible differences in FM4-64 uptake between the *nph3-7 loss of function* mutant and Col-0, we included the previously characterized TPC *nosh* mutant, which carries a deletion of the SH3 domain in the TASH3 subunit of the TPLATE complex (Grones et al., 2022). The *nosh* mutant (*no-SH*3 domain) represents a viable partial *loss-of-function* allele that perturbs TPLATE complex function without abolishing complete complex assembly, as loss of core TPC subunits typically results in male sterility. Consistent with this, *nosh* displays reduced endocytic density and impaired CME-driven internalization of PM-ubiquitinated cargo proteins under non-inducible conditions (Grones et al., 2022). Therefore, we employed *nosh* (kindly provided by Prof. Daniel Van Damme) as a reference for partial reduction of endocytic activity when assessing FM4-64 uptake in *nph3-7* and in *Arabidopsis* transgenic lines complemented with NPH3 variants.

Five-day-old, etiolated *Arabidopsis* seedlings were incubated with 2 µM FM4-64 for 15 min in darkness (at RT), and internalization was imaged in root epidermal cells by confocal microscopy. After ~15 min, Col-0 seedlings displayed clear FM4-64 internalization, whereas *nph3-7* seedlings showed reduced uptake (Fig. 20A). Quantification of FM4-64 internalization, expressed as the ratio of cytosolic to PM fluorescence, confirmed a significant reduction in *nph3-7* relative to Col-0 (Fig. 20C). The extent of FM4-64 internalization in *nph3-7* was comparable to that observed in *nosh*

(Grones et al., 2022). Expression of GFP:NPH3^{WT} or GFP:NPH3^{S744A} in the *nph3-7* background largely restored FM4-64 uptake (Fig. 20B-C), with both variants localizing to the PM in darkness. In contrast, the constitutively condensate-localized GFP:NPH3$^{\Delta C51}$ failed to rescue FM4-64 uptake in *nph3-7.*

These observations indicate that the presence of NPH3 at the PM is consistent with efficient endocytosis, although the underlying mechanistic link remains to be determined. Notably, the observed effect may be also context-dependent, restricted to specific developmental stages such as etiolated seedlings or growth in darkness.

3.4.2 Phototropic responses of nph3-7 and nosh

After confirming that NPH3 affects endocytosis in *Arabidopsis* root epidermal cells, we asked whether TPC impairment, such as the one reported in the *nosh* mutant, can impact phototropic responses in etiolated seedlings. As previously reported for *nosh*, the deletion of the SH3 domain in TASH3 subunit weakens the association of the AtEH1/AtEH2 subunits with the TPC, while the remaining six subunits (TPLATE, TML, TASH3, LOLITA, TWD40-1, and TWD40-2) still assemble into a stable hexameric complex. This partial destabilization reduces CME of ubiquitinated cargo, resulting in delayed internalization and recycling of PM proteins. These trafficking delays contribute to slower downstream signalling and reduced overall growth, which manifests as shorter hypocotyls of etiolated seedlings (Grones et al., 2022).

The involvement of CME in phototropism is supported by studies showing that clathrin light chain double mutants (*clc2 clc3*) exhibit reduced, but not abolished, phototropic bending (Zhang et al., 2017). This partial defect indicates that CME contributes to efficient phototropic responses, consistent with its role in redistributing auxin transporters such as PIN3 following BL stimulation (Ding et al., 2011; Hu et al., 2021; Zhang et al., 2017). Similarly, treatment of etiolated seedlings with brefeldin A (BFA), which interferes with the recycling of endocytosed PM proteins including PIN3, strongly reduces phototropic bending (Ding et al., 2011). Collectively, these observations support a role for endocytosis and recycling of PM proteins in establishing directional growth responses to light.

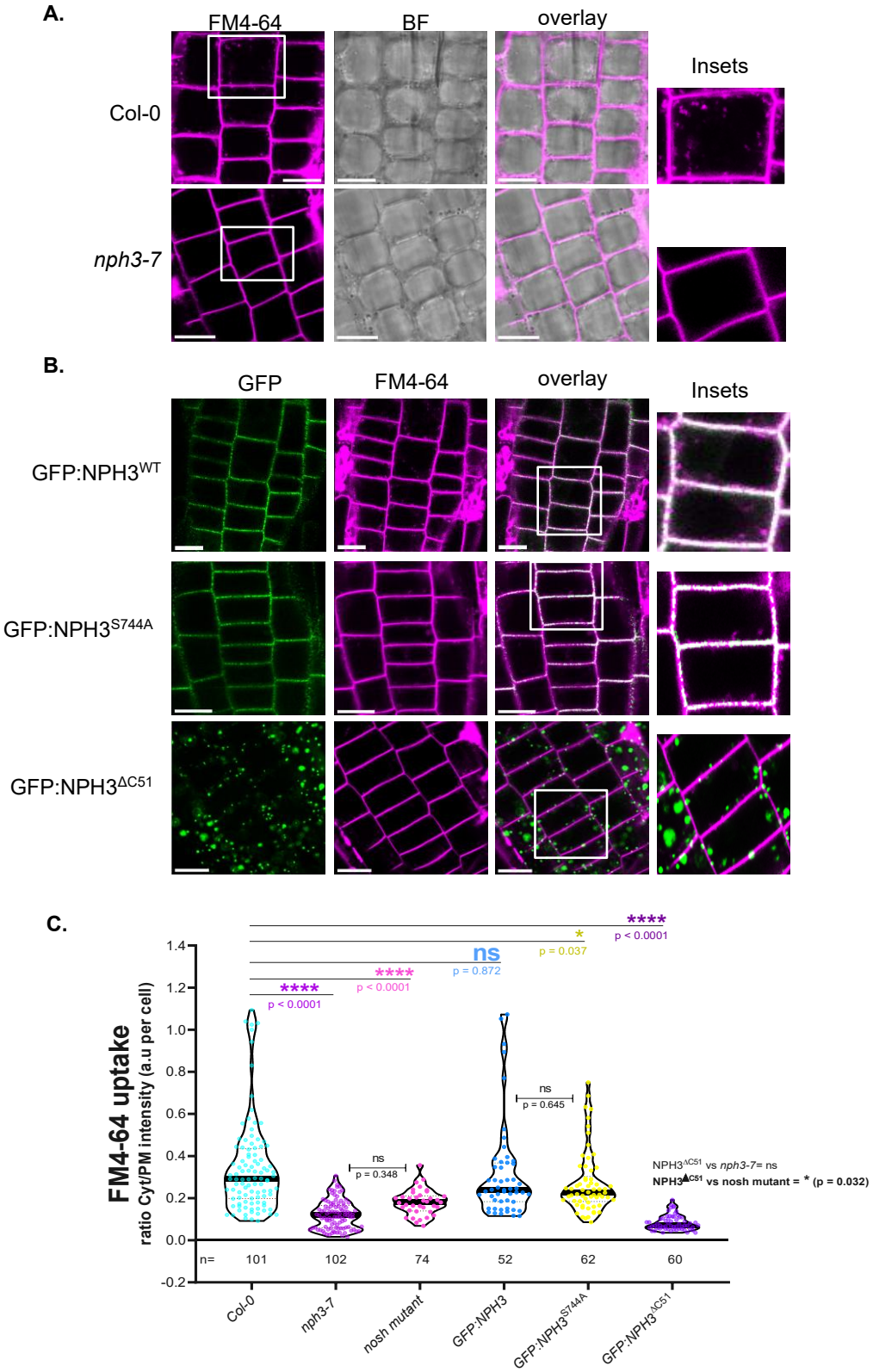

Figure 20. FM4-64 uptake reveals reduced endocytosis in *nph3-7* loss-of-function seedlings

(A) Confocal images of FM4-64 uptake in root epidermal cells of five-day old dark-grown *Arabidopsis* seedlings (grown in half strength MS media, no sucrose supplementation) incubated with 2 µM FM4-64 for 15 min in darkness. Col-0 shows clear internalization, whereas *nph3-7* displays reduced uptake. Scale bars:

10 µm. BF: bright field. Insets provided. (B) Complementation analysis with GFP:NPH3^{WT}, GFP:NPH3^{S744A}, and GFP:NPH3$^{\Delta C51}$ transgenic lines (expression was driven by the 35S promoter). GFP:NPH3^{WT} and GFP:NPH3^{S744A} largely restore FM4-64 internalization, while GFP:NPH3$^{\Delta C51}$ resembles *nph3-7*. Analysis of the *nosh* mutant is not shown (L124). Scale bars: 10 µm. (C) Quantification of Cytosolic/PM fluorescence ratios were performed using Fiji. Images were acquired using RFP excitation (554 nm). GFP laser exposure was minimized and used only to confirm expression at the end of the experiment. Data represent four independent biological experiments (5 to 10 seedlings each). All data was plotted. n= number of cells analysed. Statistical Analysis: Ordinary One-way Anova with Tukey's multiple comparisons test (p value < 0.0001= ****, $p < 0.05$ = *, $p > 0.05$ = no significant).

To evaluate phototropic responses in *nosh*, hypocotyl curvatures from etiolated seedlings exposed to unilateral BL over 24 h (Fig. 21), were measured. At time 0 (darkness), no obvious differences were observed among the analysed genotypes (Col-0, *nph3-7*, and two independent *nosh* mutant lines). Early BL treatments (2 h) showed reduced hypocotyl curvature in the *nosh* lines relative to Col-0, whereas *nph3-7* displayed no bending, as expected. These observations likely reflect constrained hypocotyl elongation in the *nosh* mutants, consistent with their shorter hypocotyl phenotype, rather than a complete absence of directional bending.

At later time points, both *nosh* lines eventually reached substantial curvature (~90°), whereas *nph3-7* seedlings failed to reorient, and Col-0 achieved maximal curvature by 6 h. The diminished early bending in *nosh* resembles the phenotype of *clc2 clc3* mutants, in which early curvature is similarly reduced but not abolished (Zhang et al., 2017). Critically, shorter hypocotyls prevent a clear distinction between elongation-dependent and endocytosis-dependent contributions to early bending.

Overall, these results indicate that although *nosh* retains the capacity for substantial phototropic reorientation after 24 h of unilateral BL treatment, partial CME impairment affects hypocotyl elongation, as previously described by Grones et al., and may consequently influence early bending kinetics.

Summary (Results 3.4): NPH3 associates with components of the TPLATE complex at the PM and contributes to endocytosis in *Arabidopsis* root epidermal cells. FM4-64 uptake is reduced in *nph3-7*, mirroring defects observed in *nosh*, and only PM-localized NPH3 variants (NPH3^{WT} in darkness and NPH3^{S744A}), but not cytosolic forms (NPH3$^{\Delta C51}$), restore dye internalization. In phototropism assays, *nph3-7* seedlings fail to reorient toward unilateral BL, whereas *nosh* seedlings achieve substantial curvature at later time points despite reduced hypocotyl elongation. Early curvature measurements in *nosh* are limited by shorter hypocotyls, preventing robust assessment of initial directional bending. While these observations describe co-occurrence rather than causality, they indicate that partial disruption of endocytosis correlates with reduced growth and impaired early phototropic responses. How NPH3 mechanistically interfaces with the endocytic machinery, and whether this interaction influences PIN3 polarization during phototropic

bending (Ding et al., 2011; Friml et al., 2002; Haga and Sakai, 2013) remains to be determined.

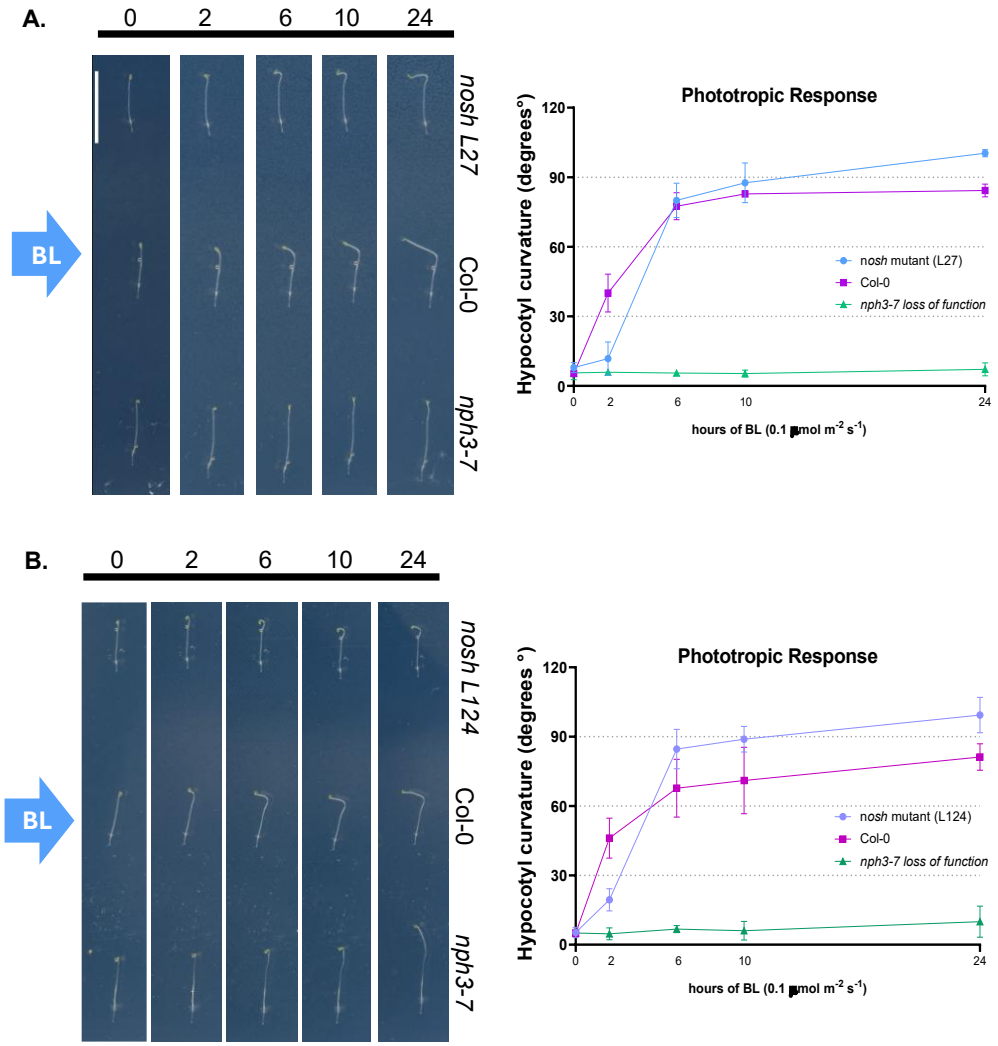

Figure 21. The *nosh* mutant exhibits altered early phototropic responses in etiolated *Arabidopsis* seedlings

Three days old, etiolated *Arabidopsis* seedlings grown in half strength MS media (without sucrose supplementation) (A-B) Time course of hypocotyl bending in response to unilateral BL (0.1 µmol m^{-2} s^{-1}) in Col-0, *nph3-7*, and two independent *nosh* mutant lines (L27 in A, L124 in B). Left panels show representative seedlings at 0, 2, 6, 10, and 24 hours of BL exposure. Right panels show quantification of hypocotyl curvature (degrees) over time. Error bars represent Mean ± Std from three independent biological replicates (each replicate: average of n ≥ 7 seedlings x genotype x time point).

3.5. Impact of NPH3 on the polarization of PIN3 upon unilateral BL stimulus

As mentioned in the introduction (section 1.3), NPH3 has been implicated in auxin redistribution during phototropism. In rice, a *loss-of-function* mutation of the NPH3 ortholog CPT1 abolishes BL-induced lateral auxin translocation (Haga et al., 2005), suggesting a conserved role of NPH3 in linking photoreceptor signalling to auxin transport.

To ensure consistent terminology, descriptions of PIN3 and NPH3 localization in this chapter follow the nomenclature established by (Ding et al., 2011). The terms *illuminated* and *shaded* refer to the respective sides of the hypocotyl exposed or not exposed to unilateral BL, respectively. Within individual hypocotyl endodermis cells, *inner* and *outer lateral membranes* denote the two lateral PM domains, with the inner lateral membrane facing the vasculature and the outer lateral membrane facing the cortex (as illustrated in the Intro. Fig. 2)

During phototropic hypocotyl bending, PIN3, an auxin efflux carrier strongly expressed in endodermis cells, is a major determinant of lateral auxin fluxes that redirect auxin from the illuminated to the shaded side of the hypocotyl (Ding et al., 2011; Friml et al., 2002). In etiolated seedlings maintained in darkness, PIN3 shows apolar localization at both inner and outer lateral membranes of endodermis cells. Upon unilateral BL exposure, this symmetric localization becomes asymmetric, as PIN3 is gradually depleted from the outer lateral membrane while persisting at the inner lateral membrane facing the vasculature. Notably, changes occur exclusively on the illuminated hypocotyl side and are not visible at the shaded side (Ding et al., 2011).

In darkness, apolar PIN3 localization correlates with high expression of the AGC kinase PINOID (PID). Ding et al. showed that PID, but not phot1, can phosphorylate the Hydrophilic Loop (HL) of PIN3 *in vitro* and proposed that PID activity contributes to maintaining apolar PIN3 distribution *in planta.* Upon unilateral BL exposure, PID transcription is rapidly repressed at the illuminated side, coinciding with the onset of PIN3 repolarization.

Ding et al. (2011) further showed that the light-induced PIN3 polarization requires GNOM-dependent trafficking. Inhibition of ARF GEF activity by brefeldin A (BFA) abolishes PIN3 relocalization and prevents phototropic bending, consistent with a role for GNOM in polar targeting, directing PIN3 preferentially to the inner lateral membrane. Together, these findings indicate that light-regulated PID activity and GNOM-dependent polar trafficking are both required for dynamic PIN3 polarization in response to unilateral

BL. The light-induced shift in PIN3 polarization likely involves a dynamic interplay between endocytosis, which removes PIN3 from the PM, and selective recycling and sorting mechanisms that return internalized PIN3 to particular membrane domains. Ding et al. also proposed that PIN3 polarization may involve transcytosis, whereby PIN3 is internalized from the outer lateral membrane and delivered to the inner lateral membrane, although direct experimental evidence for this process is not yet available. GNOM-dependent trafficking is consistent with a role in mediating such recycling events, while the precise trafficking steps and phosphorylation-dependent mechanisms remain unclear.

Given the proposed role of NPH3 as a signal transducer linking photoreceptor activation to the modification of auxin transport and building on our previous observations that NPH3 participates in the modulation of endocytosis, we wanted to determine whether NPH3 is required for the dynamic polarization of PIN3 in response to unilateral BL exposure.

3.5.1 Generation and validation of A. thaliana nph3-7 and Col-0 lines expressing PIN3:GFP under control of the endogenous PIN3 promoter

For these studies, PIN3 reporter constructs were generated using a Golden Gate-based cloning strategy to allow native promoter driven expression of PIN3 carrying an internal GFP tag. The GFP sequence was inserted into the HL at a previously described position corresponding to the end of the first exon (hence *internal tag*), which has been shown not to interfere with PIN3 activity (Ding et al., 2011; Žádníková et al., 2010). The resulting construct was designated *promPIN3:PIN3:GFP(int)* (Fig. 22A). The construct was independently transformed into Col-0 and the *nph3-7* mutant background, from which two homozygous lines per background were selected for further analysis. Although direct transformation into the mutant background does not replace classical genetic crossing, this approach allowed a partial first assessment of PIN3:GFP behaviour in the absence of NPH3.

Quantitative phototropic bending assays revealed that *A. thaliana* Col-0 lines carrying PIN3:GFP(int) (#17-9, #19-1) displayed a robust phototropic response, reaching bending angles of approximately 90°, whereas comparable *nph3-7* lines (#6-7, #8-6) failed to bend, consistent with the *loss-of-function* phenotype of *nph3*-7 (Fig. 22B). Immunoblot analysis aimed to detect PIN3:GFP(int), by using anti-GFP antibodies on total protein extracts from etiolated and light-grown seedlings. Our experiments detected a single band at the expected molecular mass of approximately 100 kDa, with comparable signal intensities across transgenic lines (Fig. 22C-D). In addition, 7- to 14-day-old plate-grown

seedlings showed no obvious alterations in root length, lateral root number, or petiole angle positioning (Supplemental Fig. S13). Together, these data indicate that the internally GFP-tagged PIN3 is stably expressed and does not cause detectable developmental abnormalities under the conditions tested, supporting the suitability of these lines for subsequent analyses of PIN3 localization and polarization in hypocotyl endodermis cells.

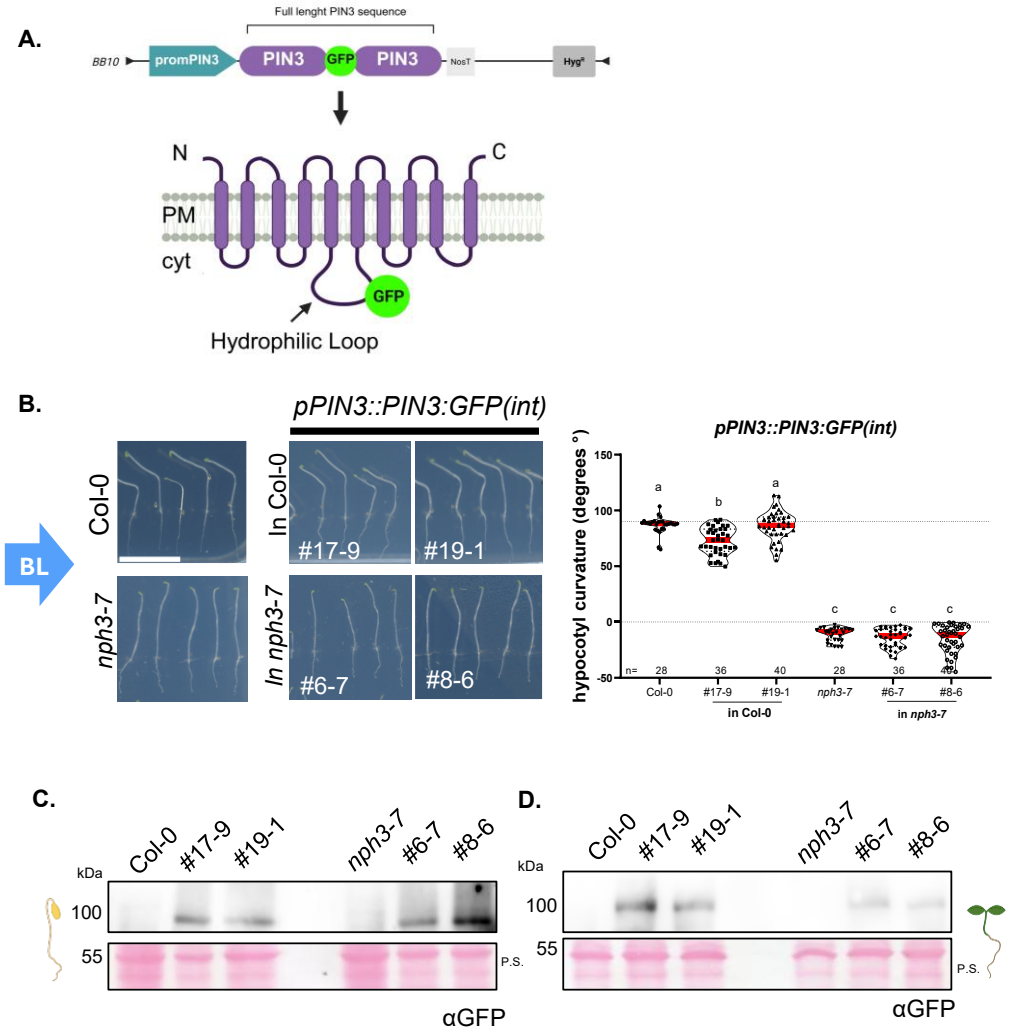

Figure 22. Phenotypic and molecular characterization of etiolated *Arabidopsis nph3-7* and Col-0 seedlings expressing *pPIN3::PIN3:GFP(int)*

(A) Schematic representation of the *promPIN3::PIN3:GFP(int)* construct generated by Golden Gate cloning. A GFP tag was inserted in the internal cytosolic loop of PIN3 (corresponding to the end of exon 1) to preserve localization and post-translational regulation (Žádníková et al. 2010; Ding et al. 2011). (B) Phototropic bending assays of three days old, etiolated seedlings (grown in half strength MS media) shows that independent homozygous transgenic lines in the *nph3-7* background (#6-7, #8-6) fail to restore phototropic bending, whereas lines in the Col-0 background (#17-9, #19-1) display normal bending. Graphs represent angle measurements of seedlings from one representative independent biological replicate (3 in total). n= number of seedlings. Red line indicates Median. Statistical analysis: Ordinary One-way Anova with Tukey's multiple comparisons test ($p < 0.05$). Immunoblot analysis of PIN3:GFP fusion protein (~100 kDa) from ~100 mg of etiolated (C) and light-grown (D) seedlings confirms comparable fusion protein accumulation across

independent lines. Data represent two independent homozygous lines per background. Supplemental Fig. S13 shows additional phenotypic analyses.

3.5.2 Light-induced polarization of PIN3 in hypocotyl endodermis cells occurs downstream of NPH3

To determine the contribution of NPH3 to BL-induced PIN3 polarization, etiolated seedlings expressing PIN3:GFP(int) in either Col-0 or *nph3-7* backgrounds were subjected to unilateral BL (0.1 µmol m^{-2} s^{-1}) for approximately 12 h. PIN3 localization was analysed specifically in upper- to mid-hypocotyl endodermal cells using quantitative fluorescence intensity measurements at the inner and outer lateral PMs.

In three-day-old, etiolated Col-0 seedlings (lines #17-9 and #19-1), PIN3:GFP(int) displayed a symmetric, apolar distribution between the inner and outer lateral membranes under dark conditions (Fig. 23A-B). Upon unilateral BL exposure, PIN3 redistributed on the illuminated side of the hypocotyl, characterized by a depletion from the outer lateral membrane of endodermal cells and accumulation at the inner lateral membrane facing the vasculature. Quantification confirmed a significant increase in PIN3:GFP(int) signal at the inner relative to the outer endodermal membrane on the BL-illuminated hypocotyl side (one-way ANOVA, $p < 0.001$ ***), consistent with the previously reported BL-induced polarization of PIN3 (Ding et al., 2011).

In contrast, two independent PIN3:GFP(int) lines in the *nph3-7* background (#6-7 and #8-6) failed to exhibit BL-induced polarization under identical conditions (Fig. 23C-D). PIN3 remained symmetrically distributed between inner and outer lateral endodermal membranes on the illuminated hypocotyl side, with no significant differences in fluorescence intensity. These data indicate that NPH3 is required for BL-induced PIN3 polarization toward the inner lateral membrane of hypocotyl endodermal cells.

Brefeldin A (BFA) is a fungal metabolite that prevents recycling from endosomal compartments back to the PM by blocking ARF-GEF-dependent vesicle trafficking, causing cargos such as PIN1 and PIN2 to accumulate in BFA bodies (Geldner et al., 2003; Grunewald and Friml, 2010; Kleine-Vehn et al., 2009). Remarkably, it has also been shown that BFA inhibits light-induced PIN3 polarization (Ding et al., 2011). To test whether the loss of PIN3 polarization in *nph3-7* reflects impaired access to the GNOM-dependent recycling pathway, we analysed PIN3 behaviour under combined BFA and unilateral BL treatments at early (1 h) and extended (12 h) time points.

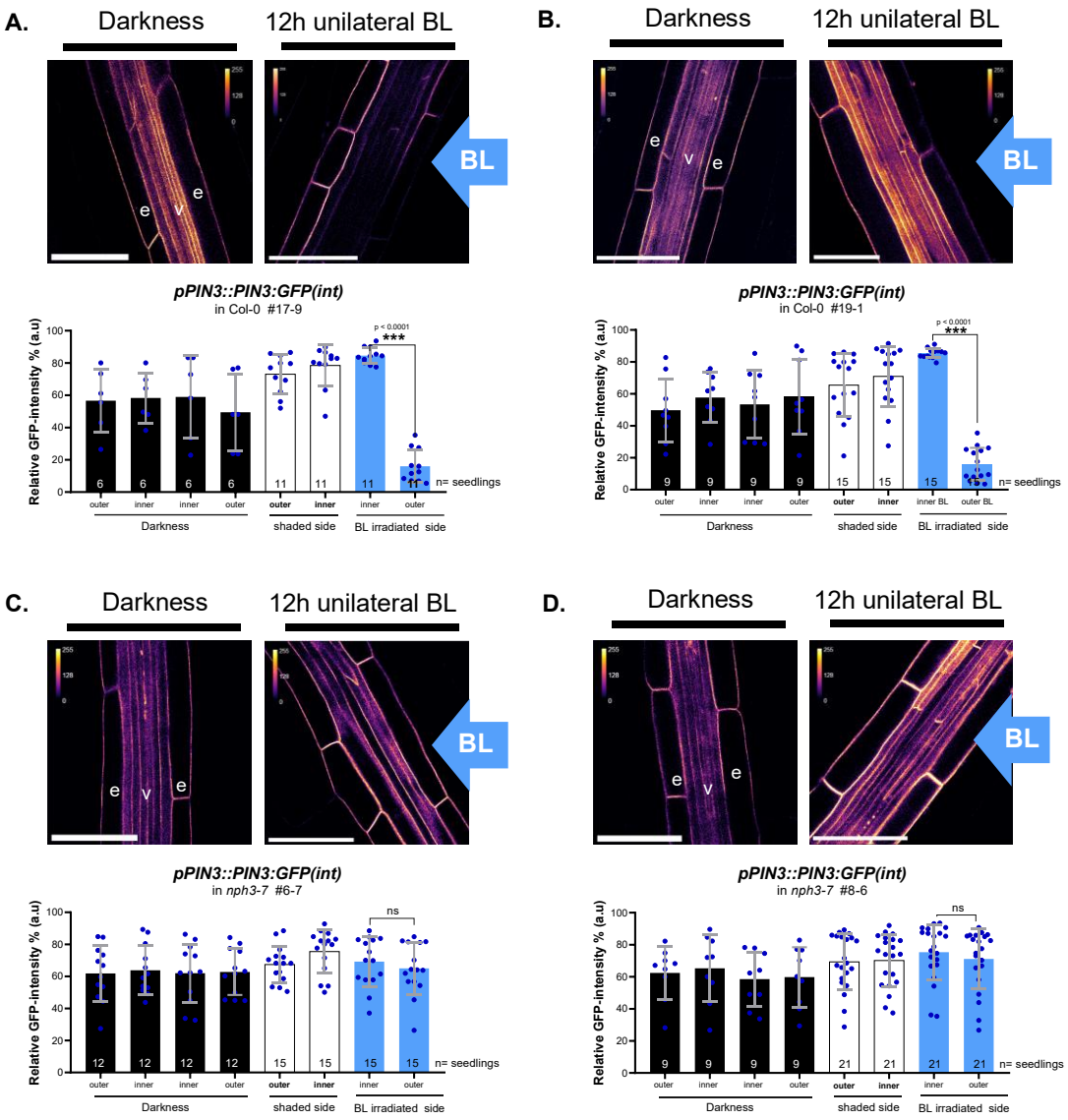

Figure 23. NPH3 is required for BL-induced PIN3 polarization in hypocotyl endodermis

(A-B) Representative confocal images of three-day-old, etiolated *Arabidopsis* seedlings expressing *promPIN3::PIN3:GFP(int)* in the Col-0 background (#17-9, #19-1), grown on half-strength MS media without sucrose. In darkness, PIN3 localizes uniformly (apolar) at the plasma membrane (PM) of inner and outer endodermal cells of the hypocotyl. After ~12 h of unilateral blue-light (BL) irradiation (0.1 µmol m^{-2} s^{-1}), PIN3 polarizes to the inner membrane (facing the vasculature) of endodermal cells on the illuminated side, as previously reported. (C-D) Equivalent transgenic lines in *nph3-7* (#6-7, #8-6) show no detectable PIN3 polarization under the same BL treatment, with uniform lateral endodermal PIN3:GFP signal on both the irradiated and shaded sides of the hypocotyl. White letters indicate e: endodermis, v: vasculature. Blue arrows indicate the direction of unilateral BL irradiation; the opposite side represents the shaded side. Quantification of PIN3:GFP intensities (graphs) was performed in Fiji. A consistent min/max threshold was applied to all images, and the images were converted using the mpl inferno lookup table (min = 0, max = 255) to generate calibration bars. Values were then expressed as percentages. On the irradiated side, Col-0 shows a significant asymmetric distribution between inner and outer endodermal membranes (one-way ANOVA, ***p < 0.001), whereas *nph3-7* shows no significant asymmetry. Data represent six independent biological replicates; n = number of seedlings analysed. All data are plotted. Scale bars: 50 µm.

In both Col-0 and *nph3-7*, PIN3 localized to the PM, indicating that delivery to the PM is not affected and/or not dependent on NPH3. In Col-0 seedlings, unilateral BL in the presence of 50 µM BFA resulted in the formation of a small number of PIN3-positive BFA bodies in endodermal cells after 1 h (Fig. 24A), indicative of active internalization directed into the BFA-sensitive endosomal compartments. After 12 h, both PIN3 polarity and BFA bodies were largely absent, consistent with previous observations of reduced BFA body formation under prolonged BL exposure (Ding et al., 2011). Col-0 DMSO-treated controls displayed normal BL-induced PIN3:GFP(int) polarization, indicating that PIN3 polarity is unaffected in the absence of BFA.

In *nph3-7* seedlings, combined BL and BFA treatment did not produce detectable BFA bodies at either time point (Fig. 24B), and PIN3 remained localized at the PM with some weak dispersed intracellular GFP signal. These observations suggest that, while NPH3 is not required for PIN3 delivery to the PM, it is necessary for PIN3 polarization and for entry into the BFA-sensitive endosomal pathway.

This interpretation is consistent with previous results presented in this thesis, including evidenced interactions between NPH3 and components of the TPLATE complex (TPLATE and AtEH1) and reduced bulk endocytosis in *nph3-7* as assessed by FM4-64 uptake. Although these experiments do not resolve the precise trafficking step affected in *nph3-7*, the data support a role for NPH3 in enabling PIN3 access to the endocytic pathway that feeds into GNOM-dependent recycling, which is required for BL-induced polarity.

Additional support for NPH3's role in PIN3 internalization was obtained from preliminary cycloheximide (CHX) + BFA experiments in darkness. This strategy tested whether NPH3 PM localization affects PIN3 internalization from existing PIN3 PM-pools and not *de novo* PIN3 protein synthesis. In dark-grown Col-0 seedlings, CHX/BFA treatment generated a few small PIN3-positive BFA bodies, indicative of internalized PIN3. In *nph3-7*, PIN3 remained largely at the PM, with only weak dispersed intracellular signal and no detectable BFA bodies (Supplemental Fig. S14), consistent with a defect in PIN3 internalization or early endosomal sorting.

Together, our initial assessments suggests that NPH3 is required for asymmetric, BL-induced PIN3 polarization at the endodermal cell layer. Further work will be necessary to elucidate the underlying mechanism.

Summary (Results 3.5): Our results indicate that NPH3 is required for asymmetric, BL-induced PIN3 polarization in hypocotyl endodermal cells. Loss of NPH3 appears to prevent PIN3 from entering a BFA-sensitive endosomal population and disrupts GNOM-

dependent recycling associated with BL-induced polarity. While the precise molecular step regulated by NPH3 remains unresolved, combined genetic, pharmacological, and imaging data support a model in which NPH3 facilitates PIN3 internalization or early endosomal trafficking, thereby enabling its polarized redistribution in response to directional BL.

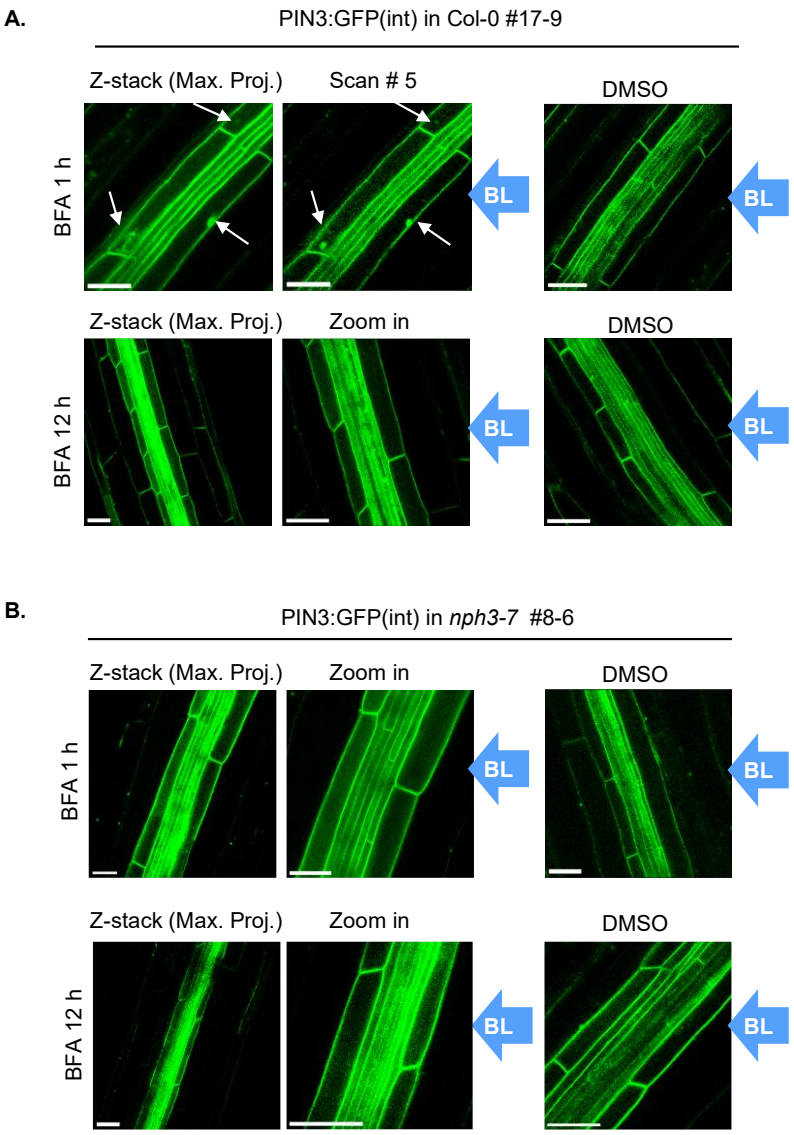

Figure 24. NPH3 may be required for BL-induced PIN3 trafficking into GNOM-dependent recycling compartments

Representative confocal images from three-day-old etiolated *Arabidopsis* seedlings (grown in half strength MS media without sucrose supplementation) expressing *proPIN3::PIN3:GFP(int)* in Col-0 (#17-9) or *nph3-7* (#8-6) were treated with 50 µM BFA (left panels) or DMSO (right panels) and exposed to unilateral BL (depicted by blue arrows, 0.1 µmol m^{-2} s^{-1}) for 1 or 12 h. Z-stacks were acquired following short time-lapse imaging (2-3 min) to capture the dynamic emergence of BFA bodies; maximum-intensity projections are shown. For each condition, a single optical scan or inset (zoom in) from the Z-stack is displayed adjacent to the projection to illustrate BFA body morphology. (A) After 1 h in Col-0, PIN3:GFP accumulated in a small number of PIN3-positive BFA bodies in endodermal cells (arrows), indicating that PIN3 can reach GNOM-dependent recycling compartments. After 12 h, PIN3 polarity and BFA body formation were absent, while DMSO controls showed normal BL-induced PIN3 polarization at the illuminated side of the hypocotyl. (B) In contrast, *nph3-7* seedlings exposed to unilateral BL showed no BFA body formation at either 1 h or 12 h but

displayed a dispersed intracellular GFP signal. Scale bar: 25 µm. Experiments were repeated twice, with approximately 3-5 seedlings analysed per condition per experiment.

4. Discussion

Since its identification more than two decades ago (Motchoulski and Liscum, 1999), NPH3 has been considered an essential component of phot1-mediated signalling in the establishment of plant phototropic responses. Although some studies have shed light on NPH3's post-translational modifications and structural features, the precise biochemical mechanism by which it operates downstream of the BL-activated photoreceptor at the PM remains largely unresolved.

Dissecting the NPH3 interactome is critical for understanding the signalling events that underlie phototropic growth. Here, we addressed this question by defining the protein-interaction networks of NPH3 in its two subcellular states: PM association in darkness and cytosolic condensates, whose formation is triggered by BL irradiation. Using complementary proteomic approaches (TurboID-based proximity labelling, GFP-based immunoprecipitation, and FAPS) in etiolated *Arabidopsis* seedlings, we identified a reproducible set of putative NPH3-interacting proteins, exhibiting different profiles in each subcellular compartment.

Our findings support a model in which NPH3 activity is tightly coupled to its subcellular localization. At the PM, NPH3 is in close proximity to components of the endocytic machinery and associates with subunits of the TPLATE complex, consistent with a role in organizing or stabilizing molecular environments connected to clathrin-mediated endocytosis (CME) events. Such environments are likely required for downstream phototropic signalling events, including the BL-induced polarization of the auxin efflux carrier PIN3 in the hypocotyl. In contrast, NPH3 BL-induced cytosolic condensates are enriched in molecular chaperones of the HSP70 family, consistent with a sequestered, signalling-inactive, or low-activity state.

4.1 Cytosolic NPH3 condensates: Single-component assemblies modulated by HSP70 chaperones

Photoreceptor-mediated BL perception triggers redistribution of NPH3 from the PM to the cytosol. Specifically, phot1-dependent phosphorylation of NPH3 at Ser744 promotes 14-3-3 proteins binding, inducing partial dissociation from the PM and subsequent assembly into biomolecular condensates in the cytosol (Reuter et al., 2021; Sullivan et al., 2021). The condensate state is reversible, as NPH3 can re-associate with the PM upon return to darkness or during prolonged (~2-3 h) BL irradiation in etiolated

Arabidopsis seedlings (Kimura et al., 2021; Reuter et al., 2021). For years, it has remained unclear whether NPH3 cytosolic condensates actively participate in phototropic signalling or instead represent an inactive state associated with signal attenuation.

Recent structural predictions and biochemical work by Manishankar et al. (2026) provide an important framework for interpreting our experimental approaches and observations. The authors identified a key structural feature of NPH3 that mediates its subcellular localization dynamics: a bipartite C-terminal motif composed of the CC domain and a Linear Interacting Peptide (LIP) motif located at the end of the core NPH3 domain. Together, these elements enable NPH3 homo-oligomerization and the formation of a trimeric structure, but they contribute differently to this process. The CC domain promotes strong oligomerization and PM association, whereas the LIP motif supports weaker oligomerization that appears critical for the formation of cytosolic condensates (Manishankar et al., 2026).

In addition, their work demonstrated that condensate formation also requires the N-terminal BTB domain of NPH3. The BTB domain -known to mediate protein-protein interactions- likely contributes to higher-order assembly by mediating interactions between NPH3 trimers in the cytosol. However, it remained unclear whether BTB-dependent interactions occur exclusively between NPH3 molecules or whether additional proteins participate as structural components of these assemblies.

Previous proteomic approaches aimed to identify NPH3 interaction partners in etiolated *Arabidopsis* seedlings using GFP-based immunoprecipitation under both dark and BL conditions. These experiments were performed by Sullivan et al. (2021) and Tanja Schmid (2022, unpublished) using GFP-tagged NPH3^{WT}. Although only a limited number of interaction partners were identified under BL, both studies consistently detected a strictly BL-dependent association between NPH3 and 14-3-3 isoforms. The limited number of co-purifying proteins therefore raised the possibility that BL-induced NPH3 condensates may largely consist of NPH3 itself and represent single-component assemblies. Overall, these analyses did not conclusively resolve whether additional proteins associate with cytosolic NPH3 and contribute to condensate assembly or stability, leaving the functional role of these structures uncertain.

To address this question and to extend previous proteomic analyses, we mapped the interaction network of a constitutively condensate-localizing NPH3 variant, NPH3$^{\Delta C51}$, in etiolated *Arabidopsis* seedlings. This variant lacks the final 51 amino acids of the NPH3 C-terminus, including the amphipathic helix required for PM association and the 14-3-3

binding site (S744) (Reuter et al., 2021). Previous studies have shown that BL-induced 14-3-3 protein binding is not required for condensate assembly (Reuter et al., 2021). Thus, the NPH3$^{\Delta C51}$ variant provided a useful system to investigate proteins associated with only cytosolic NPH3 condensates.

Our first attempts to characterize the NPH3$^{\Delta C51}$ interactome using TurboID-based proximity labelling were unsuccessful, as we could not observe enrichment of the bait itself (Supplemental Fig. S6). A likely explanation is enzymatic steric occlusion caused by the dense, gel-like material properties reported for this variant (Manishankar et al., 2026). Such condensate environments can limit accessibility to lysine residues and restrict the diffusion of biotin and ATP, thereby preventing efficient biotinylation.

In contrast, GFP-based immunoprecipitation of NPH3$^{\Delta C51}$ identified a distinct set of associated proteins, most prominently several members of the HSP70 family that were absent from GFP-only controls (Fig. 9). Consistent with this observation, FAPS analysis independently detected enrichment of at least two HSP70 isoforms with NPH3$^{\Delta C51}$ condensates when compared against cytosolic granule-like condensates formed by NOT9B (Fig. 8).

A systematic re-examination of the published proteomic datasets (Sullivan et al., 2021, Supplemental Information Reps 1 and 2) reveals that two HSP70 isoforms (HSP70-1 and HSP70-3) also co-purified with the NPH3^{WT} bait. Their abundance, however, varied with light conditions: in the first experiment, both isoforms were primarily detected under BL, whereas in the second experiment HSP70-3 was enriched under BL, and HSP70-1 was more abundant in darkness. Although this variability precluded definitive evidence for a strictly condensate-specific association, the repeated detection of HSP70 proteins across our experiments and the published datasets supports the idea that they are context-dependent interaction partners of NPH3, primarily under BL conditions.

Our data indicates that cytosolic NPH3$^{\Delta C51}$ condensates are predominantly composed of NPH3 itself, suggesting that condensate formation proceeds independently of other structural proteins and represents a single-component assembly. This in turn implies that the BTB domain likely participates in homotypic interactions, potentially enabling the crosslinking of NPH3 trimers, as supported by the structural predictions of Manishankar et al. Consistent with this view, NPH3 condensates preferentially associate with HSP70 chaperones, supporting the idea that HSP70s modulate condensate fluidity and reversibility.

4.1.1 HSP70s as biomolecular condensates remodelers

In plants, molecular chaperones -particularly members of the HSP70 family- play central roles in proteostasis by promoting proper protein folding, preventing aberrant aggregation, and supporting protein quality control under both basal and stress conditions (Hartl et al., 2011; Vierling, 1991). Beyond these canonical functions, HSP70s contribute to intracellular trafficking and modulation of signalling pathways by stabilizing or buffering regulatory proteins (Kotak et al., 2007; Sung et al., 2001; Vierling, 1991). *A. thaliana* encodes at least five highly conserved cytosolic HSP70 isoforms with partially redundant functions (Lin et al., 2001). Altered expression levels of HSP70-1 have been shown to result in pronounced effects on plant growth and viability, reflecting their biological relevance (Sung and Guy, 2003).

NPH3 cytosolic condensates exhibit hallmarks of liquid-liquid phase separation, likely driven by NPH3 self-association and multivalent interactions involving intrinsically disordered regions (IDRs) (Manishankar et al., 2026). These properties are characteristic of biomolecular condensates. In recent years, HSP70s have emerged as key regulators of biomolecular condensates in both plants and animals, interacting with intrinsically disordered or partially folded protein regions (Bard and Drummond, 2024).

In animals, HSP70s can suppress the aberrant aggregation of intrinsically disordered proteins implicated in amyloid diseases (Chilukoti et al., 2021). In plants, HSP70s have been shown to maintain the reversibility of protein assemblies driven by IDRs, such as cytosolic stress granules (SG) marked by Rbp47b nuclear ribonucleoproteins. SG contain untranslated mRNAs, RNA-binding proteins, translation initiation factors, and other IDR-containing proteins, with HSP70s chaperones transiently associating to prevent irreversible aggregation, maintain granule fluidity, and preserve cellular function under heat stress (Kosmacz et al., 2019). In addition, HSP70s have been also identified as components of several nuclear and cytosolic condensates, including PHYTOCHROME B (phyB) photobodies -dynamic hubs required for light signalling and photomorphogenesis-, and NONEXPRESSER OF PATHOGENESIS-RELATED GENES 1 (NPR1) assemblies -essential for salicylic acid signal integration during immune responses- (Kim et al., 2023; Solis-Miranda et al., 2023; Zavaliev et al., 2020).

The present work provides direct evidence that cytosolic NPH3$^{\Delta C51}$ condensates are predominantly self-assembled structures, with reproducible association with HSP70 isoforms, including HSP70-1, HSP70-3, and HSP70-4. HSP70-1:GFP partially co-localizes with RFP:NPH3$^{\Delta C51}$ condensates in *N. benthamiana* (Fig. 10), observed at or around NPH3$^{\Delta C51}$ assemblies and exhibiting rapid dynamics consistent with dynamic

exchange (videos not shown). Co-immunoprecipitation analysis further confirms HSP70-1 association with all NPH3 variants tested (WT, S744A, ΔC51; Supplemental Fig. S9). Given the role of HSP70 proteins in protein folding, it cannot be excluded that they might contribute to NPH3 stability by supporting proper folding across its subcellular localizations, including the PM.

Together, these data support a model in which $NPH3^{WT}$ condensates can accommodate associated proteins, such as 14-3-3s, while remaining dynamic and reversible. HSP70 chaperones likely modulate the material properties of NPH3 condensates, as previously described for other biomolecular condensates examples.

4.1.2 NPH3 cytosolic condensates: a potential inactive signalling state?

Biomolecular condensates are crucial for spatial and temporal regulation of cellular processes in all life forms, including plants, where they play pivotal roles in development and environmental responses (Field et al., 2023; Peng et al., 2025). Such condensates typically function by recruiting or sequestering specific molecular components, locally increasing their concentration and often enhancing activity. Conversely, biomolecular condensates can also serve to establish inactive states.

Recent studies on the auxin response factor ARF7 provide a framework for understanding cytosolic condensates as regulated inactive signalling states. ARF7 is a transcription factor mediating auxin-dependent gene expression and tropic responses (Harper et al., 2000; Liscum and Reed, 2002). Structurally, ARF7 contains extensive IDRs that promote multivalent interactions and phase separation. ARF7 forms dynamic cytosolic condensates under low auxin, which limit its nuclear localization and transcriptional activity. Auxin triggers dissolution of these condensates via association with MCTPs proteins, allowing ARF7 to relocalize to the nucleus and activate signalling outputs (Jing et al., 2022; Powers et al., 2019; Xuan et al., 2024).

Variants of NPH3 that constitutively form condensates ($NPH3^{\Delta C51}$ /$NPH3^{4K/A}$) display no phototropic bending, resembling the phenotype of the *nph3-7* loss-of-function mutant (Manishankar et al., 2026; Reuter et al., 2021). These and other observations suggest that cytosolic NPH3 correlates with reduced signalling output, similar to the cytosolic condensates formed by ARF7. However, no dedicated dissolution factors have been identified for NPH3. Instead, NPH3 condensates form upon BL in response to phot1 activation, allowing HSP70 proteins to associate, likely preventing irreversible aggregation while maintaining condensate reversibility.

Therefore, the findings of this thesis regarding NPH3 condensate composition support the structural and biochemical work of Manishankar et al. and collectively suggest a model in which phase separation sequesters NPH3 in the cytosol, limiting its re-association with the PM and providing a regulatory mechanism to balance cycling between the membrane and the cytosol (Manishankar et al., 2026).

Such model is consistent with previous observations in which NPH3 variants displaying prolonged cytosolic retention also exhibit impaired phototropism, highlighting the importance of a tightly regulated cytosolic residence time (Haga et al., 2015; Kimura et al., 2021).

Consequently, PM-associated NPH3 likely represents a basal, signalling-competent state that predominates in darkness. This model is supported by observations in which constitutively PM-localized variants retain partial phototropic bending ($NPH3^{S744A}$), confirming that PM association correlates with signalling output (Sullivan et al., 2019; Reuter et al., 2021).

Consistently, our proteomic analyses indicate that PM-associated NPH3 in darkness is proximal to CME components, supporting a role in endocytic processes required for phototropic signalling, whereas BL-induced cytosolic condensation likely represents a buffered inactive state during light adaptation.

4.2 PM-associated NPH3: A possible link to endocytic regulation

In darkness, hydrophilic NPH3 associates with the PM via an amphipathic helix in its C-terminal domain that interacts with polyacidic phospholipids (Reuter et al., 2021). AlphaFold2-Multimer predictions suggest that NPH3 homo-oligomerization at the PM forms a trimer resembling a three-bladed *propeller*, with the C-termini facing the membrane and the NPH3 core along with the N-terminal BTB domains exposed to the cytosol (Manishankar et al., 2026). In this arrangement, NPH3's IDRs extend from the trimer as flexible appendages, potentially mediating dynamic and transient multivalent interactions at the PM.

Further re-examination of the available proteomic datasets performed in darkness reveal PM-associated candidates not previously explored. Here, IP-GFP of $GFP:NPH3^{WT}$ showed co-purification with AP-2 adaptor complex subunits (α and μ), clathrin chains, dynamin-related proteins, and the TPLATE complex (TPC) subunit TWD40-1 (T. Schmid, 2022, unpublished). Similar results were reported by Sullivan et al. (2021; Supplementary Data 2), with TPC subunits TPLATE(core) and TWD40-1 specifically detected in $GFP:NPH3^{WT}$ samples, also showing higher abundance in darkness, when

NPH3 is PM-associated. Phot1 also co-purified more abundantly under these conditions. Yet, without functional validation at the time, the composition and organization of the NPH3 PM interactome in darkness remained unresolved.

To address this gap, we employed TurboID-based proximity labelling, which offers several advantages over conventional approaches such as IP-GFP, including enhanced sensitivity and the ability to capture transient or weak interactions *in vivo* (Mair and Bergmann, 2022).

We identified several putative NPH3-associated proteins involved in clathrin-mediated endocytosis (CME) under dark conditions. Multiple TPC subunits were enriched, including TPLATE, TASH3, TDW40-1, TDW40-2, and TML, along with clathrin heavy and light chains, AP-2 adaptor subunits, and dynamins/DRPs (Intro Fig. 4A and Fig. 4). These proteins function across multiple stages of endocytosis, from cargo recognition and vesicle initiation (TPLATE, AP-2) to vesicle coating (clathrin, AP-2) and vesicle maturation and scission (dynamins, DRPs), positioning NPH3 in close proximity to key functional modules of the endocytic machinery.

These proximal putative interactions were consistently recovered with the $NPH3^{WT}$ bait with partly overlapping interactors also detected for the constitutively PM-associated $NPH3^{S744A}$ variant (Fig. 5), but not in our negative control: *nph3-7*. Moreover, a subsequent proximity labelling experiment using $NPH3^{WT}$ after prolonged BL exposure (3 h), capturing the transition from PM dissociation to cytosolic condensation and subsequent PM re-association, also revealed enrichment of TPC and CME components (Fig. 6). While the temporal resolution of this experiment does not allow assignment of individual interactions to specific subcellular states, the consistent identification of TPC and CME components across conditions indicates robust spatial proximity between NPH3 and the endocytic machinery.

Recent TurboID-based proteomic datasets using AtEH1 as bait, a TPLATE complex subunit, independently identified NPH3 as a highly enriched proximal protein (Dragwidge et al., 2024). Although these experiments were conducted in *Arabidopsis* cell suspensions and do not fully reflect the biological context required for complete phototropic responses, they do highlight NPH3's likely overlooked connection to CME at the PM.

A compelling explanation for such oversight derives from NPH3 not being an endocytic cargo, confirmed by experiments showing that vesicle trafficking and cytoskeletal networks are not required for BL-induced NPH3 relocalization into cytosolic condensates (Haga et al. 2015; Kimura et al. 2021). Specifically, NPH3 does not co-localize with FM4-

64-labeled endosomes or with BFA bodies following brefeldin A treatment, while disruption of actin with latrunculin B did not affect BL-induced condensate formation. Additionally, proteomic analyses of clathrin-coated vesicles (CCVs) from *Arabidopsis* cell suspensions did not detect NPH3, strengthening that it is not internalized nor a structural component of endocytic vesicles *in vivo* (Dahhan et al., 2022).

Our experiments demonstrate that NPH3 associates with the TPLATE complex subunits: TPLATE(core) and AtEH1, in a PM-dependent localization manner. In transient expression assays, PM-associated NPH3 variants ($NPH3^{WT}$ and $NPH3^{S744A}$) co-localized with TPLATE and displayed significant FRET-FLIM reductions in GFP lifetime, consistent with close molecular proximity (Figs. 12 and 14, Supplementary. Fig. S10), whereas the constitutively condensate-forming $NPH3^{\Delta C51}$ did not (Fig. 13). Co-immunoprecipitation experiments confirmed that both $NPH3^{WT}$ and $NPH3^{S744A}$ interact with TPLATE in *N. benthamiana* and in etiolated *Arabidopsis* seedlings, independent of BL-induced Ser744 phosphorylation, indicating that this association occurs in the basal PM-associated state (Fig. 15).

While NPH3 interaction with the TPC subunit AtEH1 appeared limited in transient localization assays (Figs. 16-17), reciprocal co-immunoprecipitations revealed a weak but reproducible association *in vivo* (Supplemental Fig. S11). Co-expression of TPLATE enhanced recruitment of $NPH3^{WT}$ to AtEH1-containing PM-condensates, with high-resolution imaging confirming overlap of $NPH3^{WT}$ and TPLATE-AtEH1 puncta close to the PM (Fig. 18A-C), whereas $NPH3^{S744A}$ displayed a more uniform but “patchy” PM distribution with partial overlap to TPC subunits PM-condensates (Fig. 18D).

While these results demonstrate a PM-dependent association of NPH3 with TPLATE complex subunits, they do not allow conclusions on the temporal sequence of these interactions. In particular, it remains unresolved whether NPH3 is recruited to pre-existing TPLATE-AtEH1 assemblies at the PM or whether NPH3 localization precedes and facilitates the formation or stabilization of such assemblies. Addressing this question will require quantitative analysis of the spatial and temporal dynamics of NPH3 and TPLATE complex components at endogenous expression levels. Live-cell imaging approaches with sufficient temporal resolution will be essential to determine arrival, residence, and dwelling times at the PM. Spinning disk confocal microscopy and total internal reflection fluorescence microscopy (TIRF-M) are well-established tools for resolving the dynamics of plant CME components and have been successfully used to characterize the behaviour of several TPLATE complex subunits and other CME markers at the PM (Johnson et al., 2020; Wang et al., 2020). Application of these approaches to NPH3

would enable a more precise temporal assignment of its association with TPLATE-AtEH1 assemblies.

Taken together, these observations are consistent with a model in which PM-associated NPH3 in darkness is positioned to engage in potentially transient, multivalent and/or regulatory interactions with components of the endocytic machinery, most notably the TPLATE complex. This view provides a conceptual framework in which NPH3 might contribute to CME at the PM, connecting phototropic signalling with endocytosis. On this basis, the present work focused on characterizing a possible relationship between NPH3 and CME.

4.2.1 NPH3 as s potential PM-domain organizer

Plant CME occurs at discrete PM sites, where nucleation of endocytic machinery drives membrane bending independently of cytoskeletal forces (Johnson et al., 2021; Kraus et al., 2025, 2024). The TPLATE complex (TPC) is central to this process, forming flexible scaffolds that remodel the PM, allowing for recruitment of downstream CME components and PM bending (Kraus et al., 2025). Specifically, TPC subunits AtEH1 and AtEH2, promote condensation of the complex at the PM and facilitate the dynamic recruitment of clathrin and other endocytic machinery, directly linking biomolecular condensation to functional CME organization (Dragwidge et al., 2024).

In darkness, both NPH3^{WT} and NPH3^{S744A} are uniformly localized at the PM. Under BL, NPH3^{WT} partially dissociates from the PM and subsequently forms cytosolic condensates. While these condensates can be observed near the PM, they form only after NPH3 dissociation and localize predominantly to the cytosol or the inner leaflet of the PM. In contrast, the NPH3^{S744A} variant, which is incapable of PM dissociation, forms discrete patch-like subdomains at the PM.

Ongoing research indicates that NPH3^{S744A} PM-patches are spatially segregated from specific PM cargo proteins, including PIN auxin transporters (Yeliz Idil Yigit, personal communication). Accordingly, NPH3^{S744A} and PIN3 display mutual exclusion at the PM. Single-particle tracking photoactivated localization microscopy (spt-PALM) analysis in *Arabidopsis* seedlings suggests that PIN3 lateral diffusion (the side-to-side movement within the PM) depends on NPH3. Preliminary experiments in *nph3-7* show that mEos2-tagged PIN3 exhibits reduced lateral diffusion at the PM, suggesting increased immobilization and/or retention at the PM. These observations are consistent with altered PM domain organization in the absence of NPH3. Furthermore, complementation with NPH3^{S744A} results in increased PIN3 mobility (Yeliz Idil Yigit, unpublished).

The observed partial co-localization and biochemical association of NPH3 and TPC subunits, together with the formation of PM patches, suggests that NPH3 may stabilize CME components at specific membrane regions without serving as a cargo or structural element.

To test whether NPH3 influences CME, we performed FM4-64 uptake assays in root epidermal cells of *Arabidopsis* etiolated seedlings (Fig. 20). The *nph3-7* mutant exhibits reduced endocytic uptake, comparable to the previously reported *nosh* mutant, which carries a deletion in the TPC subunit TASH3 and shows impaired CME due to defective internalization of ubiquitinated PM cargo (Grones et al., 2022). Complementation with GFP:NPH3^{WT} fully restores FM4-64 uptake, whereas GFP:NPH3^{S744A} provides only partial rescue, while NPH3$^{\Delta C51}$ fails to restore uptake. These results indicate that PM-associated NPH3 is required to maintain local CME activity.

Despite the partial reductions in endocytosis, *nph3-7* mutants show minimal developmental defects compared to TPLATE complex null mutants, which are severely impaired or non-viable since CME processes are essential for growth and development (Gadeyne et al., 2014; Wang et al., 2021). Partial CME deficiency, as observed in *nosh*, impairs early phototropic bending but does not abolish it (Fig. 21), similar to *clc2 clc3* double mutants, indicating that a reduction in bulk endocytosis alone cannot account for the strong phototropic defects of *nph3-7*. Instead, the reduced FM4-64 uptake observed in *nph3-7* roots is more consistent with disrupted spatial organization of PM-localized CME rather than a general failure of the endocytic machinery. Accordingly, the spatial organization of PM-associated NPH3 appears to be critical for directional growth and PIN redistribution. Moreover, the partial rescue of FM4-64 uptake by NPH3^{S744A} further suggests that functional PM domain organization may rely on both, membrane association and particular molecular conformations and/or protein interactions.

NPH3 has been proposed to function as a substrate adaptor in a CUL3-based E3 ubiquitin ligase targeting phot1 for BL-induced ubiquitination (Roberts et al., 2011). However, this role is debated, as constitutively PM-anchored phot1, which cannot be internalized, does not impair normal phototropic responses (Preuten et al., 2015). These observations suggest that NPH3-mediated ubiquitination of phot1, whether for internalization and/or degradation pathways, may not have functional relevance in phototropism.

Yet, ubiquitination is a well-established signal for endocytic sorting of PM proteins in plants (Grones et al., 2022). In this context, NPH3-dependent phot1 ubiquitination and its possible contribution to CME converge conceptually on membrane trafficking

pathways. Our proximity labelling analysis did not detect CUL3 or other previously reported NPH3 interactors, including PKS proteins. Nevertheless, we cannot exclude that these interactions are more prominent under different developmental contexts, such as in light-grown seedlings.

A related NPH3-domain containing protein NRL5, recently implicated in drought tolerance, display GTPase-like activity *in vitro* linked to its core NPH3 domain, influencing trafficking mechanisms and NRL5 polar localization (Upadhyay-Tiwari et al., 2024). Although it remains unclear whether other NRL family members possess *bona fide* intrinsic GTPase activity, these observations suggest the *hypothesis* that NPH3 may act as an organizer of endocytic processes through GTPase-mediated mechanisms.

Globally, the convergence of genetic, cell biological, and biochemical evidence supports a model in which NPH3 might function as a dynamic PM-domain organizer, coordinating discrete endocytic subdomains to translate environmental light cues into directional growth responses. Building on this framework, parallels can be drawn with other PM-associated proteins that organize defined subdomains to regulate PIN polarity.

4.2.2 Parallels with Two Self-Reinforcing PIN Polarity Modules

Evidence from other PM-associated proteins in plants supports the concept that defined PM subdomains are critical for correct PIN protein dynamics. In *A. thaliana*, the AGC kinase PAX (PROTEIN KINASE ASSOCIATED WITH BRX, also known as AGC1-3) associates with the scaffolding protein BRX (BREVIS RADIX) and localizes to specific polar PM subdomains in root protophloem cells. This localization is dependent on PIP5Ks (PHOSPHATIDYLINOSITOL-4-PHOSPHATE 5-KINASEs), which generate phosphatidylinositol 4,5-bisphosphate (PIP_2)-enriched nanodomains that recruit the BRX-PAX complex and spatially exclude PIN1 to surrounding PM regions (Marhava et al., 2020). Morphologically, this arrangement has been described as "*muffin- and donut-like,"* with PIN1 forming a donut-shaped pattern at the PM and the PAX-BRX complex forming a muffin-like focus in the centre. Together, BRX and PAX recruit PIP5K to reinforce the polarity of all three proteins at the PM. This self-reinforcing polarity module creates PM regions with locally reduced PIN1 abundance, which is essential for proper protophloem differentiation, illustrating how PM subdomains locally control PIN localization, lateral mobility, and polarity (Marhava et al., 2020). In this regard, the authors also proposed that the module may generate a localized hotspot of clathrin-mediated PIN endocytosis, potentially explaining the complementary "donut-like" pattern of PIN1 localization.

Consistent with this, PINs lateral diffusion is tightly constrained by these subdomains, where local lipid composition, protein-protein interactions, and the actin cytoskeleton restrict or permit mobility, allowing polarity to be maintained or modified (Kleine-Vehn et al., 2011). Furthermore, constitutive internalization via CME, predominantly at the edges of polar subdomains, reinforces PIN segregation and sustains dynamic polarity (Dhonukshe et al., 2007; Kitakura et al., 2011; Kleine-Vehn et al., 2011). Together, constrained diffusion and targeted CME enable PIN proteins to redistribute while remaining confined to defined PM regions, ensuring spatially precise auxin flux and rapid adjustment of polarity in response to developmental or environmental cues.

A second example of a self-reinforcing PIN polarity module involves MAB4/MEL proteins and the AGC kinases PID and D6PK, which restrict the lateral diffusion of PIN2 by promoting the formation of a multiprotein complex at the PM of root epidermal cells. Specifically, PIN2 recruits MAB4/MEL proteins to the PM, where phosphorylation by PID and D6PK stabilizes these associations, creating a positive feedback loop that restricts lateral diffusion and establishes specific polar PM domains (Glanc et al., 2021). Consistently, the absence of MEL proteins leads to increased PIN2 internalization, highlighting their role in stabilizing PIN2 PM-localization (Furutani et al., 2011).

Notably, MAB4/MEL proteins belong to the NPH3/RPT2-like (NRL) protein family (see Section 1.3), while PAX, PID, and D6PK kinases belong to the AGC plant kinase family, which also includes phot1 (Barbosa and Schwechheimer, 2014; Rademacher and Offringa, 2012). Members of both AGC kinase and NRL protein families have therefore been implicated in PIN regulation across cell types, suggesting that key mechanistic features of PIN polarity control may be conserved among NRL proteins. However, the molecular basis, extent, and specificity of this conservation remain unresolved, and distinct AGC kinases likely modulate these interactions in a context-dependent manner to produce different signalling outputs (Christie et al., 2018; Reuter et al., 2021; Sullivan et al., 2021).

In this context, parallels with established PIN polarity modules support the idea that NPH3 may function as a PM domain organizer. Similar to other NRL- and AGC kinase-associated modules that generate specialized PM subdomains controlling PIN diffusion and endocytosis, NPH3 could contribute to the spatial organization of discrete endocytic domains at the PM, further modulated by a BL-dependent interaction with phot1.

4.2.3 NPH3-mediated PIN3 polarization: the potential missing link in plant phototropism

BL-induced polarization of the auxin efflux carrier PIN3 in hypocotyl endodermis cells is a central step in establishing asymmetric auxin flux during phototropism (Ding et al., 2011; Han et al., 2021).

In darkness, PIN3 is distributed apolarly across the PM of hypocotyl endodermis cells, with the outer lateral membranes facing the cortex and inner lateral membranes facing the vasculature (Intro. Fig. 2). Upon unilateral BL, PIN3 redistributes toward the inner lateral PM specifically on the illuminated side, suggesting a capacity to divert basipetal auxin transport toward the shaded side to generate the auxin gradient essential for hypocotyl bending (Ding et al., 2011). Importantly, the BL-induced PIN3 polarization is abolished in *phot1* mutants, demonstrating that changes in polarity and resulting auxin asymmetry occur downstream of phot1-dependent light perception (Ding et al., 2011). Despite this, the molecular link between phot1 BL-induced activation and BL-induced PIN3 polarization remains unclear.

Current models suggest that PIN3 polarity is established through dynamic membrane trafficking, involving clathrin-mediated endocytosis and GNOM-dependent recycling. In darkness, phosphorylation of the hydrophilic loop of PIN3 by the AGC kinase PID influences membrane targeting that correlates with its apolar distribution. Unilateral BL exposure represses PID transcription (at the illuminated side of the hypocotyl), reducing PIN3 phosphorylation and favouring inner lateral targeting through GNOM-dependent polar trafficking. Transcytosis mechanisms may further reinforce this polarity by redirecting internalized PIN3 from outer to inner lateral membranes. Pharmacological evidence supports a trafficking-based mechanism for PIN3 polar redistribution. Treatments with Brefeldin A (BFA), a fungal inhibitor that blocks ARF-GEF-dependent vesicle trafficking such as that mediated by GNOM, blocks both PIN3 polarization and phototropic bending, whereas proteasome inhibition has no effect (Ding et al., 2011).

Our data position NPH3, a direct substrate of phot1, within this regulatory network. At the PM, NPH3 associates with components of the CME machinery, including subunits of the TPLATE complex, suggesting that it may define spatial sites of endocytic internalization. This scenario may explain the apparent spatial segregation observed between NPH3 and PIN3 at the PM, as NPH3-marked regions may correspond to sites where PIN3 is selectively internalized.

In Col-0 seedlings, unilateral BL triggers PIN3 redistribution toward the inner lateral membrane, while *nph3-7* mutants largely retain apolar PIN3 (Fig. 23). Combined BFA and BL treatment produces intracellular PIN3-positive compartments in Col-0 but not in *nph3-7*, and preliminary BFA-CHX experiments indicate that these compartments

originate from endocytosed PIN3 rather than newly synthesized protein (Fig 24; Supplementary. Fig. S14). Consistent with FM4-64 uptake assays, these results suggest that NPH3 promotes efficient PIN3 endocytosis.

Together, these observations suggest that NPH3 links phot1 activation to dynamic PIN3 redistribution. Upon BL perception, phot1-dependent phosphorylation and subsequent sequestration into cytosolic condensates reduce NPH3 availability at the PM and its endocytosis-related function. This reduction in localized endocytic activity, combined with repressed PID activity, likely favours polar GNOM-dependent recycling trafficking, reinforcing PIN3 polarity and directional auxin flux.

Despite this mechanistic framework, several critical questions remain. It is still unclear how NPH3 associates with the endocytic machinery (whether this occurs through its IDRs or through other domains or binding partners), and whether its role in endocytosis is specific to PIN3 or could also influence other functionally redundant PIN proteins. Perhaps most importantly, it remains to be established whether the NPH3-marked patches at the PM correspond to clathrin-mediated endocytosis hotspots, and if so, whether these sites actively promote PIN3 internalization and/or restrict its lateral diffusion across the membrane, thereby creating mutually exclusive domains as previously observed (Yeliz Idil Yigit, unpublished). Addressing these gaps will require quantitative, high-resolution imaging of NPH3 and endocytic markers at the PM, along with spatiotemporal tracking of PIN3 trafficking, and functional correlation with auxin transport. These approaches will clarify how NPH3 coordinates phot1 activation with dynamic, spatially controlled PIN3 polarization during phototropism.

4.3 NPH3 Integrated Model

Our findings support a model in which NPH3 functions as a PM-domain organizer, linking phot1-mediated BL perception to spatially regulated endocytosis and PIN3 trafficking, thereby supporting phototropic responses (Fig. 25).

In darkness, NPH3 associates with the PM through its C-terminal amphipathic helix and oligomerization motifs, in proximity to endocytic machinery while associated with TPLATE complex (TPC) components. These associations, combined with its capacity to form PM-subdomains, likely define regions of the PM competent for endocytosis that maintain a basal internalization landscape. In *nph3-7* mutants, phototropic bending is impaired, bulk endocytosis is reduced, and PIN3 fails to redistribute under unilateral BL, highlighting the functional importance of NPH3 in coordinating PM trafficking.

Upon BL exposure, phot1 phosphorylates NPH3, enabling 14-3-3 proteins binding and partial dissociation from the PM. This redistribution is accompanied by the subsequent formation of cytosolic condensates, reducing NPH3 availability at the PM and limiting its activity. Condensates are largely self-assembled, reversible, and their fluidity is likely modulated by HSP70 chaperones. The gradual, light-dependent redistribution provides dynamic regulation of NPH3 localization across the cell.

NPH3 subcellular dynamics operate alongside PID kinase activity and GNOM-dependent recycling to shape PIN3 polarization. In darkness, PIN3 is largely apolar, whereas unilateral BL allows GNOM-mediated polar recycling to bias PIN3 toward inner lateral membranes of endodermal cells on the illuminated side. NPH3's positioning at the PM may help define where and when trafficking events occur supporting polarized PIN3 distribution.

Overall, our integrated model positions NPH3 as a potential dynamic PM-domain organizer that responds to light cues, contributing to PIN3 trafficking, by modulating endocytic and therefore recycling processes in a spatially regulated manner. This model integrates NPH3's BL-triggered redistribution, condensate formation as a potential inactivation mechanism, and *nph3-7* phenotypes, providing a conceptual framework connecting phot1 perception with PIN3 polarization and phototropic growth, while offering a coherent explanation of how subcellular localization contributes to light-dependent growth responses.

4.4 Limitations and Future Directions

This study provides mechanistic insight into NPH3 as a potential PM-domain organizer, yet several limitations warrant consideration. TurboID-based proximity labelling captures proteins in spatial proximity, including weak, transient, or indirect interactions, but cannot distinguish direct physical contacts, making follow-up validation essential. Endogenous biotin in plants can amplify non-specific labelling, emphasizing the importance of appropriate experimental conditions and negative controls; here, the *nph3-7* mutant allowed NPH3-dependent differences to be detected, although weak or indirect interactions may be overrepresented.

Transient expression systems, such as *N. benthamiana*, can introduce mislocalization or altered complex assembly dynamics, critical for the study of protein-protein interactions. Furthermore, the absence of stable *Arabidopsis* lines co-expressing NPH3 with TPLATE/CME markers or HSP70 isoforms restricted the assessment of these relationships under native expression.

In the future, the generation of such stable lines will serve as essential tools to determine the functional relevance of the protein interactions uncovered in this thesis. This is particularly critical for investigating the dynamics between NPH3 condensates and HSP70 chaperones.

Furthermore, these transgenic lines will enable quantitative live-cell analysis of PM subdomain formation along with NPH3 dynamics based on endocytic markers. Monitoring these kinetics across specific cell types and tissues will clarify whether NPH3 functions exclusively in defined hypocotyl regions, such as the endodermis, or operates as a more global signalling module. In this context, analysis of PIN3 polarization should be repeated using *Arabidopsis* lines generated by crossing with *nph3-7*, with sufficient biological replicates to ensure robust and reproducible validation of our findings.

From an evolutionary perspective, NPH3 represents a land-plant adaptation, with orthologs absent in green algae (Christie et al., 2018). Its integration with plant-specific CME machinery, including the TPLATE complex, and interactions with AGC kinases such as phot1 -and potential indirect links to PID- suggest co-option of conserved modules for light-responsive, auxin-linked signalling. Model systems with reduced NRL complexity, such as *Marchantia polymorpha,* offer a suitable platform to dissect the biochemical and evolutionary basis of the potential PM-domain organizer function of NPH3 (Suetsugu et al., 2016).

Future work should integrate experimental and evolutionary approaches, examining NPH3 orthologs alongside the required reporter lines to determine how PM-associated NPH3 subdomains coordinate clathrin-mediated endocytosis and PIN3 trafficking to enable directional phototropic responses. Elucidating these mechanisms will provide understanding into how NPH3 integrates environmental cues with developmental processes to fine-tune plant directional growth.

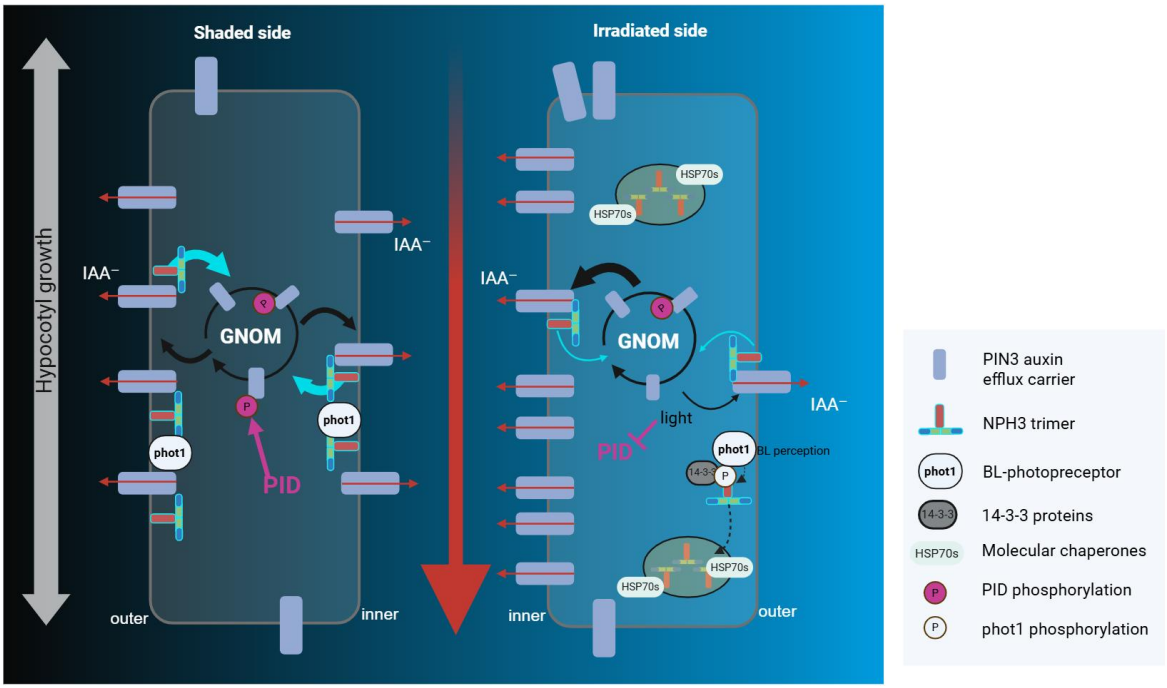

Figure 25. Integrated model of NPH3 function linking phot1 activation, endocytic regulation, and PIN3 polarization during phototropism

Model adapted from Ding et al. 2011 for the hypocotyl phototropic response, including the findings of this thesis and the potential role of NPH3 in PIN3 polarization.

In darkness (represented as the shaded side of the hypocotyl), NPH3 (trimer) associates with the plasma membrane (PM) via its C-terminal amphipathic helix and oligomerization motifs (not shown). At the PM, NPH3 is located close to the phot1 BL receptor (shown) and in proximity to clathrin-mediated endocytosis (CME) machinery while interacting with components of the TPLATE complex (not shown), locally promoting endocytic competence without serving as a core structural constituent. NPH3 localizes to distinct PM subdomains, promoting spatially restricted CME-competent domains while displaying mutual exclusion with PIN proteins at the PM. Additionally, high activity of the AGC kinase PID in darkness promotes PIN3 phosphorylation at its hydrophilic loop, which correlates with apolar (or symmetric) PIN3 distribution at the PM. Red arrows indicate auxin transport direction via PIN3 efflux carrier activity, and the central red arrow denotes basipetal auxin transport. Auxin: Indole-3-acetic acid (IAA). PIN3 undergoes dynamic cycling between CME internalization and GNOM-mediated recycling, targeting PIN3 to the lateral PM (inner and outer) of endodermis cells in the hypocotyl. Black arrows indicate GNOM-mediated recycling pathways, whereas turquoise arrows indicate the potential role of NPH3 in influencing PIN3 internalization from the PM (feeding into GNOM-dependent pathways). Differences in arrow thickness represent relative magnitude changes of PIN3 internalization impacting GNOM-mediated recycling activity between conditions.

Upon blue light (BL) perception (occurring at the irradiated side of the hypocotyl), phot1 is activated and phosphorylates NPH3 at Ser744, enabling binding of 14-3-3 proteins and partial dissociation from the PM. This generates two dynamic NPH3 populations: a reduced PM-retained pool, while the majority of NPH3 is sequestered in cytosolic condensates as a transient inactivation mechanism. NPH3 condensates are characterized by being predominantly single-component assemblies whose material properties, driven by phase separation, are modulated by HSP70 family chaperones, likely preventing irreversible aggregation and maintaining dynamic exchange. Additionally, under BL conditions, PID transcription is repressed by light, leading to less PIN3 phosphorylation. This event, combined with reduced NPH3 influence in PIN3 internalization, both converge in favour of GNOM-mediated polar trafficking of PIN3, targeting preferentially to the inner lateral PM of endodermis cells of the illuminated side of the hypocotyl. PIN3 polarization supports auxin transport diversion towards the shaded side of the hypocotyl. NPH3 condensates are reversible, as they can reassociate with the PM under favourable conditions. Thus, light-driven cycling of NPH3 between the PM and cytosolic condensates provides a mechanistic framework linking photoreceptor activation to spatial control of PIN3 membrane trafficking, allowing its polarization and resulting in directional growth

5. Summary

Phototropism directs plant shoot growth toward a light source by establishing a lateral auxin gradient. This process relies on the modification of the polar localization of PIN-FORMED (PIN) auxin efflux carriers, such as PIN3, at the plasma membrane (PM). Blue light (BL) perception by phototropin1 (phot1) initiates this response; however, the mechanisms linking phot1 to auxin transport remain unknown. The plant-specific protein NON-PHOTOTROPIC HYPOCOTYL 3 (NPH3) acts immediately downstream of phot1 activation and is essential for phototropic bending. In darkness, NPH3 localizes predominantly to the PM, whereas BL induces phot1-dependent phosphorylation at Ser744, enabling the binding of 14-3-3 proteins and triggering partial dissociation from the PM. Following release, NPH3 assembles into biomolecular condensates in the cytosol. Remarkably, cytosolic NPH3 can re-associate with the PM upon return to darkness or prolonged BL exposure.

Yet, how this dynamic NPH3 cycling contributes to phot1 signalling and what biochemical function NPH3 has remain unclear.

To address this, we mapped the protein-interaction networks of NPH3 in its two distinct subcellular localizations: at the PM and within cytosolic condensates. Using complementary proteomic approaches, including TurboID-based proximity labelling, GFP-based immunoprecipitation, and Fluorescence-Activated Particle Sorting in etiolated transgenic *Arabidopsis* seedlings, we identified reproducible but distinct sets of putative NPH3 interaction partners in each compartment. These results suggest that NPH3 activity is closely linked to its subcellular localization.

Proteomic analysis of NPH3 condensates indicates that they consist predominantly of NPH3 itself and are also enriched in general regulators of condensate dynamics, namely molecular chaperones of the HSP70-family. Validation through partial co-localization and co-immunoprecipitation in a transient plant expression system supported that NPH3 can associate with HSP70-1 in condensates. These observations, together with structural predictions, suggest that NPH3 likely forms a single-component condensate that serves to transiently sequester (and thus inactivate) NPH3 in the cytosol, thereby delaying its re-association with the PM.

In contrast, PM-associated NPH3 appears to perform a distinct biochemical function. Here, our proteomic analyses indicate that NPH3 is in close proximity to the endocytic machinery, in line with a potential role in organizing or stabilizing molecular environments that promote clathrin-mediated endocytosis (CME) at the PM. We focused on two

putative NPH3 interaction partners, the subunits TPLATE and AtEH1 of a CME-adaptor known as the *TPLATE complex*. Interactions between NPH3 variants and TPLATE or AtEH1 were investigated by transient co-expression and co-localization studies, Förster Resonance Energy Transfer using Fluorescence Lifetime Imaging Microscopy (FRET-FLIM), and targeted co-immunoprecipitation. Our results indicate that NPH3 associates with TPLATE and AtEH1 at the PM. In addition, cell biological experiments were conducted to elucidate the physiological significance and functional consequences of these interactions. In *Arabidopsis nph3-7 loss-of-function* mutants, phototropic bending is abolished, bulk endocytosis is reduced, and PIN3 fails to polarize under unilateral BL, supporting a potential role for NPH3 in coordinating membrane trafficking. NPH3-organized molecular PM environments likely facilitate the BL-induced polarization of PIN3 in hypocotyl endodermis cells, required for the establishment of the lateral auxin gradient.

The results presented in this thesis support a model in which NPH3 functions as a dynamic PM-domain organizer, contributing to PIN3 trafficking through spatially regulated endocytic processes at the PM. The formation of NPH3 cytosolic condensates as a result of phot1-dependent phosphorylation likely serves as an inactivation mechanism that supports signal attenuation and proper PIN3 dynamics at the PM, which are necessary for phototropic growth.

6. Zusammenfassung

Phototropismus bezeichnet das gerichtete Wachstum von Pflanzensprossen zu einer Lichtquelle hin und wird durch den Aufbau eines lateralen Gradienten für Auxin ausgelöst. Letzterer beruht auf der Modifikation der polaren Lokalisation von PIN-FORMED (PIN) Auxin-Efflux-Transportern, wie zum Beispiel PIN3, an der Plasmamembran (PM). Die Wahrnehmung von blauem Licht (BL) durch Phototropin1 (phot1) initiiert die phototrope Reaktion; die Mechanismen, die phot1 mit dem Transport von Auxin verknüpfen, sind jedoch ungeklärt. Das pflanzenspezifische Protein NON-PHOTOTROPIC HYPOCOTYL 3 (NPH3) wirkt unmittelbar ‚downstream' der phot1-Aktivierung und ist für das phototrope Reaktion essentiell. Im Dunkeln lokalisiert NPH3 überwiegend an der PM, während BL eine phot1-abhängige Phosphorylierung an Ser744 induziert, die die Bindung von 14-3-3-Proteinen ermöglicht und eine partielle Dissoziation von der PM zur Folge hat. Im Cytosol bildet NPH3 biomolekulare Kondensate aus. Bemerkenswerterweise kann cytosolisches NPH3 bei Transfer in Dunkelheit oder nach längerer BL-Exposition wieder an die PM assoziieren.

Bislang ist nicht bekannt, wie diese NPH3 Dynamik zur phot1-Signalweiterleitung beiträgt und was die biochemische Funktion von NPH3 ist.

Um dies zu adressieren, haben wir die Protein-Interaktionsnetzwerke von NPH3 in seinen unterschiedlichen subzellulären Lokalisationen bestimmt: an der PM und innerhalb zytosolischer Kondensate. Mithilfe komplementärer Proteomik Verfahren, einschließlich TurboID-basiertem ‚Proximity Labelling', GFP-basierter Immunpräzipitation und ‚Fluorescence-Activated Particle Sorting' in etiolierten transgenen Arabidopsis-Keimlingen, identifizierten wir reproduzierbare, aber unterschiedliche Gruppen von potentiellen NPH3-Interaktionspartner in jedem Kompartiment. Diese Ergebnisse deuten darauf hin, dass die Aktivität von NPH3 eng mit seiner subzellulären Lokalisation gekoppelt ist.

Proteomische Analysen der NPH3-Kondensate zeigen, dass diese überwiegend aus NPH3 selbst bestehen und darüber hinaus molekulare Chaperone der HSP70-Familie angereichert sind, welche als generelle Regulatoren der Dynamik von Kondensaten bekannt sind. Die Validierung durch partielle Kolokalisierung und Ko-Immunpräzipitation in einem transienten Pflanzenexpressionssystem bestätigte, dass NPH3 mit HSP70-1 in Kondensaten assoziieren kann. Diese Beobachtungen deuten unter Einbezug von Strukturvorhersagen darauf hin, dass NPH3 wahrscheinlich ein sogenanntes Einkomponenten-Kondensat ausbildet, das dazu dient, NPH3 vorübergehend im Cytosol zu sequestrieren (und damit zu inaktivieren), wodurch seine Reassoziation mit der PM verzögert wird.

Im Gegensatz dazu scheint PM-assoziiertes NPH3 eine eindeutige biochemische Funktion zu erfüllen. Hier zeigen unsere proteomischen Analysen, dass sich NPH3 in unmittelbarer Nähe zur endozytischen Maschinerie befindet, was auf eine mögliche Rolle bei der Organisation oder Stabilisierung molekularer Umgebungen hindeutet, die die Clathrin-vermittelte Endozytose (CME) an der PM fördern. Wir konzentrierten unsere Untersuchungen auf zwei potentielle Interaktionspartner, die Untereinheiten TPLATE und AtEH1 eines CME-Adapters, der als ‚TPLATE Komplex' bezeichnet wird. Interaktionen zwischen NPH3 Varianten und TPLATE oder AtEH1 wurden durch transiente Ko-Expression, Ko-Lokalisationsstudien, Förster-Resonanz-Energie-Transfer mittels Fluoreszenzlebensdauer Mikroskopie (FRET-FLIM) und gezielte Ko-Immunpräzipitation untersucht. Unsere Ergebnisse zeigen, dass NPH3 mit TPLATE und AtEH1 an der PM assoziiert. Darüber hinaus wurden zellbiologische Experimente durchgeführt, um die physiologische Relevanz und die funktionellen Konsequenzen dieser Wechselwirkungen aufzuklären. In *Arabidopsis nph3-7 loss-of-function* Mutanten

ist die phototrope Krümmung unterbunden, die Endozytose reduziert und PIN3 polarisiert bei einseitiger BL-Bestrahlung nicht, was auf eine wahrscheinliche Rolle von NPH3 bei der Koordination des intrazellulären vesikulären Membrantransports (‚membrane trafficking') hinweist. NPH3-organisierte molekulare PM-Umgebungen erleichtern wahrscheinlich die BL-induzierte Polarisierung von PIN3 in den Endodermiszellen des Hypokotyls, die für die Etablierung des lateralen Auxin-Gradienten erforderlich ist.

Die in dieser Arbeit präsentierten Ergebnisse stützen ein Modell, in dem NPH3 als dynamischer PM-Domänen-Organisator fungiert und durch räumlich regulierte endozytotische Prozesse an der PM zum vesikulären Transport von PIN3 beiträgt. Die Bildung cytosolischer NPH3-Kondensate infolge phot1-abhängiger Phosphorylierung dient wahrscheinlich als Inaktivierungsmechanismus, der die Signalweiterleitung abschwächt und eine angemessene PIN3-Dynamik an der PM unterstützt, die für phototropes Wachstum erforderlich ist.

7. Acknowledgements

During this journey, I have been fortunate to meet incredible people whose presence has shaped both my personal and scientific growth. I am grateful to the entire ZMBP Institute, and especially to the Plant Physiology department led by Prof. Dr. Klaus Harter, for fostering an environment that felt collaborative, human, and intellectually open. To all the researchers, technicians, students and colleagues from AG Oecking, AG Harter, AG El Kasmi, AG Wolf, and AG Monte: working alongside all of you was a true privilege, and I am deeply grateful for the supportive community our floor has formed.

I am grateful to my supervisor, Prof. Dr. Claudia Oecking, for her guidance and commitment throughout this work. The challenges we faced along the way shaped me and the way I approach scientific questions and have therefore left an indelible mark on my path. I also thank Prof. Daniel Van Damme for generously sharing essential materials and expertise that strengthened this work. Both of you held me to high standards, pushing me to think more critically and to continuously refine my own work.

To the friends I made, and for everything you have done for me over the past five years, thank you. To Jutta Keicher and Lea Reuter: your friendship, love, and support have been invaluable since the day we met. To my girlfriends Natalie Krieger, Amelie Spazierer, Luiselotte Rauch, and Tasnim Zerin: thank you for the laughs, the trips, and the small everyday moments that brightened my days. To my mates Denis Janocha and Pavel Solanský: thank you for accompanying me during this ride, for the encouragement that lasted far longer than you probably realized, and for every IPA we shared, you helped me keep pushing forward.

And to my family, Simon: after nine years, you still make me laugh every day and lift me up on the days I doubt myself. I would not be here without your support. I love you and Mia infinitely. To my mother: you showed me how to be strong, independent, and brave. Thank you for loving and believing in me unconditionally. To Taty: thank you for loving and supporting me as if I were your own daughter. And to both of you: No sería la persona que soy hoy sin ustedes. Las amo.

Every single one of you has contributed to this journey in your own way, and I am profoundly grateful. Your support has made this work possible, and I will remember it forever.

8. References

Adamowski, M., Friml, J., 2015. PIN-Dependent Auxin Transport: Action, Regulation, and Evolution. Plant Cell 27, 20–32. https://doi.org/10.1105/tpc.114.134874

Alberti, S., Gladfelter, A., Mittag, T., 2019. Considerations and Challenges in Studying Liquid-Liquid Phase Separation and Biomolecular Condensates. Cell 176, 419–434. https://doi.org/10.1016/j.cell.2018.12.035

Anfang, M., Shani, E., 2021. Transport mechanisms of plant hormones. Current Opinion in Plant Biology 63, 102055. https://doi.org/10.1016/j.pbi.2021.102055

Arora, D., Abel, N.B., Liu, C., Van Damme, P., Yperman, K., Eeckhout, D., Vu, L.D., Wang, J., Tornkvist, A., Impens, F., Korbei, B., Van Leene, J., Goossens, A., De Jaeger, G., Ott, T., Moschou, P.N., Van Damme, D., 2020. Establishment of Proximity-Dependent Biotinylation Approaches in Different Plant Model Systems. The Plant Cell 32, 3388–3407. https://doi.org/10.1105/tpc.20.00235

Arora, D., Van Damme, D., 2021. Motif-based endomembrane trafficking. Plant Physiology 186, 221–238. https://doi.org/10.1093/plphys/kiab077

Barbosa, I.C., Schwechheimer, C., 2014. Dynamic control of auxin transport-dependent growth by AGCVIII protein kinases. Current Opinion in Plant Biology 22, 108–115. https://doi.org/10.1016/j.pbi.2014.09.010

Barbosa, I.C.R., Hammes, U.Z., Schwechheimer, C., 2018. Activation and Polarity Control of PIN-FORMED Auxin Transporters by Phosphorylation. Trends in Plant Science 23, 523–538. https://doi.org/10.1016/j.tplants.2018.03.009

Barbosa, I.C.R., Zourelidou, M., Willige, B.C., Weller, B., Schwechheimer, C., 2014. D6 PROTEIN KINASE Activates Auxin Transport-Dependent Growth and PIN-FORMED Phosphorylation at the Plasma Membrane. Developmental Cell 29, 674–685. https://doi.org/10.1016/j.devcel.2014.05.006

Barbosa, Schwechheimer, C., 2014. Dynamic control of auxin transport-dependent growth by AGCVIII protein kinases. Current Opinion in Plant Biology 22, 108–115. https://doi.org/10.1016/j.pbi.2014.09.010

Bard, J.A.M., Drummond, D.A., 2024. Chaperone regulation of biomolecular condensates. Front. Biophys. 2, 1342506. https://doi.org/10.3389/frbis.2024.1342506

Bashline, L., Li, S., Anderson, C.T., Lei, L., Gu, Y., 2013. The Endocytosis of Cellulose Synthase in Arabidopsis Is Dependent on μ2, a Clathrin-Mediated Endocytosis Adaptin. Plant Physiology 163, 150–160. https://doi.org/10.1104/pp.113.221234

Bashline, L., Li, S., Zhu, X., Gu, Y., 2015. The TWD40-2 protein and the AP2 complex cooperate in the clathrin-mediated endocytosis of cellulose synthase to regulate cellulose biosynthesis. Proc. Natl. Acad. Sci. U.S.A. 112, 12870–12875. https://doi.org/10.1073/pnas.1509292112

Bassukas, A.E.L., Xiao, Y., Schwechheimer, C., 2022. Phosphorylation control of PIN auxin transporters. Current Opinion in Plant Biology 65, 102146. https://doi.org/10.1016/j.pbi.2021.102146

Binder, A., Lambert, J., Morbitzer, R., Popp, C., Ott, T., Lahaye, T., Parniske, M., 2014. A Modular Plasmid Assembly Kit for Multigene Expression, Gene Silencing and Silencing Rescue in Plants. PLoS ONE 9, e88218. https://doi.org/10.1371/journal.pone.0088218

Blakeslee, J.J., Peer, W.A., Murphy, A.S., 2005. Auxin transport. Current Opinion in Plant Biology 8, 494–500. https://doi.org/10.1016/j.pbi.2005.07.014

Bolte, S., Talbot, C., Boutte, Y., Catrice, O., Read, N.D., Satiat-Jeunemaitre, B., 2004. FM-dyes as experimental probes for dissecting vesicle trafficking in living plant cells. Journal of Microscopy 214, 159–173. https://doi.org/10.1111/j.0022-2720.2004.01348.x

Boucrot, E., Saffarian, S., Zhang, R., Kirchhausen, T., 2010. Roles of AP-2 in Clathrin-Mediated Endocytosis. PLoS ONE 5, e10597. https://doi.org/10.1371/journal.pone.0010597

Bourgade, B., 2026. Lights out: PP2C phosphatases reset phototropin signalling in darkness. The Plant Cell.

Briggs, W.R., 2014. Phototropism: Some History, Some Puzzles, and a Look Ahead. PLANT PHYSIOLOGY 164, 13–23. https://doi.org/10.1104/pp.113.230573

Briggs, W.R., Christie, J.M., 2002. Phototropins 1 and 2: versatile plant blue-light receptors. Trends in Plant Science 7, 204–210. https://doi.org/10.1016/S1360-1385(02)02245-8

Chen, M., Chory, J., 2011. Phytochrome signaling mechanisms and the control of plant development. Trends in Cell Biology 21, 664–671. https://doi.org/10.1016/j.tcb.2011.07.002

Cheng, S., Wang, Y., 2022. Subcellular trafficking and post-translational modification regulate PIN polarity in plants. Front. Plant Sci. 13, 923293. https://doi.org/10.3389/fpls.2022.923293

Cheng, Y., Qin, G., Dai, X., Zhao, Y., 2008. *NPY* genes and AGC kinases define two key steps in auxin-mediated organogenesis in *Arabidopsis*. Proc. Natl. Acad. Sci. U.S.A. 105, 21017–21022. https://doi.org/10.1073/pnas.0809761106

Chilukoti, N., Sil, T.B., Sahoo, B., Deepa, S., Cherakara, S., Maddheshiya, M., Garai, K., 2021. Hsp70 Inhibits Aggregation of IAPP by Binding to the Heterogeneous Prenucleation Oligomers. Biophysical Journal 120, 476–488. https://doi.org/10.1016/j.bpj.2020.12.019

Christie, J.M., 2007. Phototropin Blue-Light Receptors. Annu. Rev. Plant Biol. 58, 21–45. https://doi.org/10.1146/annurev.arplant.58.032806.103951

Christie, J.M., Murphy, A.S., 2013. Shoot phototropism in higher plants: New light through old concepts. American J of Botany 100, 35–46. https://doi.org/10.3732/ajb.1200340

Christie, J.M., Suetsugu, N., Sullivan, S., Wada, M., 2018. Shining Light on the Function of NPH3/RPT2-Like Proteins in Phototropin Signaling. Plant Physiol. 176, 1015–1024. https://doi.org/10.1104/pp.17.00835

Christie, J.M., Yang, H., Richter, G.L., Sullivan, S., Thomson, C.E., Lin, J., Titapiwatanakun, B., Ennis, M., Kaiserli, E., Lee, O.R., Adamec, J., Peer, W.A., Murphy, A.S., 2011. phot1 Inhibition of ABCB19 Primes Lateral Auxin Fluxes in the Shoot Apex Required For Phototropism. PLoS Biol 9, e1001076. https://doi.org/10.1371/journal.pbio.1001076

Clough, S.J., Bent, A.F., 1998. **Floral dip: a simplified method for *Agrobacterium* -mediated transformation of *Arabidopsis thaliana*** . The Plant Journal 16, 735–743. https://doi.org/10.1046/j.1365-313x.1998.00343.x

Collins, B.M., McCoy, A.J., Kent, H.M., Evans, P.R., Owen, D.J., 2002. Molecular Architecture and Functional Model of the Endocytic AP2 Complex. Cell 109, 523–535. https://doi.org/10.1016/S0092-8674(02)00735-3

Dahhan, D.A., Reynolds, G.D., Cárdenas, J.J., Eeckhout, D., Johnson, A., Yperman, K., Kaufmann, W.A., Vang, N., Yan, X., Hwang, I., Heese, A., De Jaeger, G., Friml, J., Van Damme, D., Pan, J., Bednarek, S.Y., 2022. Proteomic characterization of isolated Arabidopsis clathrin-coated vesicles reveals evolutionarily conserved and plant-specific components. The Plant Cell 34, 2150–2173. https://doi.org/10.1093/plcell/koac071

De Carbonnel, M., Davis, P., Roelfsema, M.R.G., Inoue, S., Schepens, I., Lariguet, P., Geisler, M., Shimazaki, K., Hangarter, R., Fankhauser, C., 2010. The Arabidopsis PHYTOCHROME KINASE SUBSTRATE2 Protein Is a Phototropin Signaling Element That Regulates Leaf Flattening and Leaf Positioning. Plant Physiology 152, 1391–1405. https://doi.org/10.1104/pp.109.150441

De Melo, H.C., Alves, F.R.R., 2025. Plant photoreceptors mediate multimodal environmental signaling. Discov. Plants 2, 356. https://doi.org/10.1007/s44372-025-00446-3

Dela Fuente, R.K., Leopold, A.C., 1968. Lateral Movement of Auxin in Phototropism. Plant Physiol. 43, 1031–1036. https://doi.org/10.1104/pp.43.7.1031

Demarsy, E., Fankhauser, C., 2009. Higher plants use LOV to perceive blue light. Current Opinion in Plant Biology 12, 69–74. https://doi.org/10.1016/j.pbi.2008.09.002

Demarsy, E., Schepens, I., Okajima, K., Hersch, M., Bergmann, S., Christie, J., Shimazaki, K., Tokutomi, S., Fankhauser, C., 2012. Phytochrome Kinase Substrate 4 is phosphorylated by the phototropin 1 photoreceptor. EMBO J 31, 3457–3467. https://doi.org/10.1038/emboj.2012.186

Dhonukshe, P., Aniento, F., Hwang, I., Robinson, D.G., Mravec, J., Stierhof, Y.-D., Friml, J., 2007. Clathrin-Mediated Constitutive Endocytosis of PIN Auxin Efflux Carriers in Arabidopsis. Current Biology 17, 520–527. https://doi.org/10.1016/j.cub.2007.01.052

Dhonukshe, P., Huang, F., Galvan-Ampudia, C.S., Mähönen, A.P., Kleine-Vehn, J., Xu, J., Quint, A., Prasad, K., Friml, J., Scheres, B., Offringa, R., 2010. Plasma membrane-bound AGC3 kinases phosphorylate PIN auxin carriers at TPRXS(N/S) motifs to direct apical PIN recycling. Development 142, 2386–2387. https://doi.org/10.1242/dev.127415

Di Rubbo, S., Irani, N.G., Kim, S.Y., Xu, Z.-Y., Gadeyne, A., Dejonghe, W., Vanhoutte, I., Persiau, G., Eeckhout, D., Simon, S., Song, K., Kleine-Vehn, J., Friml, J., De Jaeger, G., Van Damme, D., Hwang, I., Russinova, E., 2013. The Clathrin Adaptor Complex AP-2 Mediates Endocytosis of BRASSINOSTEROID INSENSITIVE1 in *Arabidopsis*. The Plant Cell 25, 2986–2997. https://doi.org/10.1105/tpc.113.114058

Ding, Z., Galván-Ampudia, C.S., Demarsy, E., Łangowski, Ł., Kleine-Vehn, J., Fan, Y., Morita, M.T., Tasaka, M., Fankhauser, C., Offringa, R., Friml, J., 2011. Light-mediated polarization of the PIN3 auxin transporter for the phototropic response in Arabidopsis. Nat Cell Biol 13, 447–452. https://doi.org/10.1038/ncb2208

Doi, M., Shigenaga, A., Emi, T., Kinoshita, T., Shimazaki, K. -i., 2004. A transgene encoding a blue-light receptor, phot1, restores blue-light responses in the Arabidopsis phot1 phot2 double mutant. Journal of Experimental Botany 55, 517–523. https://doi.org/10.1093/jxb/erh044

Dragwidge, J.M., Van Damme, D., 2024. Order and disorder in clathrin-mediated endocytosis. Nat Cell Biol 26, 327–328. https://doi.org/10.1038/s41556-024-01355-5

Dragwidge, J.M., Wang, Y., Brocard, L., De Meyer, A., Hudeček, R., Eeckhout, D., Grones, P., Buridan, M., Chambaud, C., Pejchar, P., Potocký, M., Winkler, J., Vandorpe, M., Serre, N., Fendrych, M., Bernard, A., De Jaeger, G., Pleskot, R., Fang, X., Van Damme, D., 2024. Biomolecular condensation orchestrates clathrin-mediated endocytosis in plants. Nat Cell Biol 26, 438–449. https://doi.org/10.1038/s41556-024-01354-6

Everett, M., Thimann, K.V., 1968. Second Positive Phototropism in the *Avena* Coleoptile. Plant Physiol. 43, 1786–1792. https://doi.org/10.1104/pp.43.11.1786

Fankhauser, C., Christie, J.M., 2015. Plant Phototropic Growth. Current Biology 25, R384–R389. https://doi.org/10.1016/j.cub.2015.03.020

Field, S., Jang, G.-J., Dean, C., Strader, L.C., Rhee, S.Y., 2023. Plants use molecular mechanisms mediated by biomolecular condensates to integrate environmental cues with development. The Plant Cell 35, 3173–3186. https://doi.org/10.1093/plcell/koad062

Friml, J., 2003. Auxin transport - shaping the plant. Current Opinion in Plant Biology.

Friml, J., Wiśniewska, J., Benková, E., Mendgen, K., Palme, K., 2002. Lateral relocation of auxin efflux regulator PIN3 mediates tropism in Arabidopsis. Nature 415, 806–809. https://doi.org/10.1038/415806a

Fujimoto, M., Arimura, S., Ueda, T., Takanashi, H., Hayashi, Y., Nakano, A., Tsutsumi, N., 2010. *Arabidopsis* dynamin-related proteins DRP2B and DRP1A participate together in clathrin-coated vesicle formation during endocytosis. Proc. Natl. Acad. Sci. U.S.A. 107, 6094–6099. https://doi.org/10.1073/pnas.0913562107

Furutani, M., Kajiwara, T., Kato, T., Treml, B.S., Stockum, C., Torres-Ruiz, R.A., Tasaka, M., 2007. The gene *MACCHI-BOU 4* / *ENHANCER OF PINOID* encodes a NPH3-like protein and reveals similarities between organogenesis and phototropism at the molecular level. Development 134, 3849–3859. https://doi.org/10.1242/dev.009654

Furutani, M., Sakamoto, N., Yoshida, S., Kajiwara, T., Robert, H.S., Friml, J., Tasaka, M., 2011. Polar-localized NPH3-like proteins regulate polarity and endocytosis of PIN-FORMED auxin efflux carriers. Development 138, 2069–2078. https://doi.org/10.1242/dev.057745

Gadeyne, A., Sánchez-Rodríguez, C., Vanneste, S., Di Rubbo, S., Zauber, H., Vanneste, K., Van Leene, J., De Winne, N., Eeckhout, D., Persiau, G., Van De Slijke, E., Cannoot, B., Vercruysse, L., Mayers, J.R., Adamowski, M., Kania, U., Ehrlich, M., Schweighofer, A., Ketelaar, T., Maere, S., Bednarek, S.Y., Friml, J., Gevaert, K., Witters, E., Russinova, E., Persson, S., De Jaeger, G., Van Damme, D., 2014. The TPLATE Adaptor Complex Drives Clathrin-Mediated Endocytosis in Plants. Cell 156, 691–704. https://doi.org/10.1016/j.cell.2014.01.039

Geldner, N., Anders, N., Wolters, H., Keicher, J., Kornberger, W., Muller, P., Delbarre, A., Ueda, T., Nakano, A., Jürgens, G., 2003. The Arabidopsis GNOM ARF-GEF Mediates Endosomal Recycling, Auxin Transport, and Auxin-Dependent Plant Growth. Cell 112, 219–230. https://doi.org/10.1016/S0092-8674(03)00003-5

Glanc, M., Van Gelderen, K., Hoermayer, L., Tan, S., Naramoto, S., Zhang, X., Domjan, D., Včelařová, L., Hauschild, R., Johnson, A., De Koning, E., Van Dop, M., Rademacher, E., Janson, S., Wei, X., Molnár, G., Fendrych, M., De Rybel, B., Offringa, R., Friml, J., 2021. AGC kinases and MAB4/MEL proteins maintain PIN polarity by limiting lateral diffusion in plant cells. Current Biology 31, 1918-1930.e5. https://doi.org/10.1016/j.cub.2021.02.028

Grefen, C., Donald, N., Hashimoto, K., Kudla, J., Schumacher, K., Blatt, M.R., 2010. A ubiquitin-10 promoter-based vector set for fluorescent protein tagging facilitates temporal stability and native protein distribution in transient and stable expression studies: Fluorescence tagging and expression in Arabidopsis. The Plant Journal 64, 355–365. https://doi.org/10.1111/j.1365-313X.2010.04322.x

Grones, P., De Meyer, A., Pleskot, R., Mylle, E., Kraus, M., Vandorpe, M., Yperman, K., Eeckhout, D., Dragwidge, J.M., Jiang, Q., Nolf, J., Pavie, B., De Jaeger, G., De Rybel, B., Van Damme, D., 2022. The endocytic TPLATE complex internalizes ubiquitinated plasma membrane cargo. Nat. Plants 8, 1467–1483. https://doi.org/10.1038/s41477-022-01280-1

Grunewald, W., Friml, J., 2010. The march of the PINs: developmental plasticity by dynamic polar targeting in plant cells. EMBO J 29, 2700–2714. https://doi.org/10.1038/emboj.2010.181

Haga, K., Sakai, T., 2023. Photosensory adaptation mechanisms in hypocotyl phototropism: how plants recognize the direction of a light source. Journal of Experimental Botany 74, 1758–1769. https://doi.org/10.1093/jxb/erad015

Haga, K., Sakai, T., 2013. Differential roles of auxin efflux carrier PIN proteins in hypocotyl phototropism of etiolated *Arabidopsis* seedlings depend on the direction of light stimulus. Plant Signaling & Behavior 8, e22556. https://doi.org/10.4161/psb.22556

Haga, K., Takano, M., Neumann, R., Iino, M., 2005. The Rice *COLEOPTILE PHOTOTROPISM1* Gene Encoding an Ortholog of Arabidopsis NPH3 Is Required for Phototropism of Coleoptiles and Lateral Translocation of Auxin. The Plant Cell 17, 103–115. https://doi.org/10.1105/tpc.104.028357

Haga, K., Tsuchida-Mayama, T., Yamada, M., Sakai, T., 2015. Arabidopsis ROOT PHOTOTROPISM2 Contributes to the Adaptation to High-Intensity Light in Phototropic Responses. The Plant Cell 27, 1098–1112. https://doi.org/10.1105/tpc.15.00178

Hammes, U.Z., Pedersen, B.P., 2024. Structure and Function of Auxin Transporters. Annual Review of Plant Biology 75, 185–209. https://doi.org/10.1146/annurev-arplant-070523-034109

Han, H., Adamowski, M., Qi, L., Alotaibi, S.S., Friml, J., 2021. PIN-mediated polar auxin transport regulations in plant tropic responses. New Phytologist 232, 510–522. https://doi.org/10.1111/nph.17617

Harada, A., Takemiya, A., Inoue, S., Sakai, T., Shimazaki, K., 2013. Role of RPT2 in Leaf Positioning and Flattening and a Possible Inhibition of phot2 Signaling by phot1. Plant and Cell Physiology 54, 36–47. https://doi.org/10.1093/pcp/pcs094

Harper, R.M., Stowe-Evans, E.L., Luesse, D.R., Muto, H., Tatematsu, K., Watahiki, M.K., Yamamoto, K., Liscum, E., 2000. The NPH4 Locus Encodes the Auxin Response Factor ARF7, a Conditional Regulator of Differential Growth in Aerial Arabidopsis Tissue.

Hartl, F.U., Bracher, A., Hayer-Hartl, M., 2011. Molecular chaperones in protein folding and proteostasis. Nature 475, 324–332. https://doi.org/10.1038/nature10317

Hirst, J., Schlacht, A., Norcott, J.P., Traynor, D., Bloomfield, G., Antrobus, R., Kay, R.R., Dacks, J.B., Robinson, M.S., 2014. Characterization of TSET, an ancient and widespread membrane trafficking complex. eLife 3, e02866. https://doi.org/10.7554/eLife.02866

Hiyama, A., Takemiya, A., Munemasa, S., Okuma, E., Sugiyama, N., Tada, Y., Murata, Y., Shimazaki, K., 2017. Blue light and CO2 signals converge to regulate light-induced stomatal opening. Nat Commun 8, 1284. https://doi.org/10.1038/s41467-017-01237-5

Hu, T., Yin, S., Sun, J., Linghu, Y., Ma, J., Pan, J., Wang, C., 2021. Clathrin light chains regulate hypocotyl elongation by affecting the polarization of the auxin transporter PIN3 in *Arabidopsis*. JIPB 63, 1922–1936. https://doi.org/10.1111/jipb.13171

Huang, F., Kemel Zago, M., Abas, L., Van Marion, A., Galván-Ampudia, C.S., Offringa, R., 2010. Phosphorylation of Conserved PIN Motifs Directs *Arabidopsis* PIN1 Polarity and Auxin Transport. The Plant Cell 22, 1129–1142. https://doi.org/10.1105/tpc.109.072678

Inada, S., Ohgishi, M., Mayama, T., Okada, K., Sakai, T., 2004. RPT2 Is a Signal Transducer Involved in Phototropic Response and Stomatal Opening by Association with Phototropin 1 in *Arabidopsis thaliana*. Plant Cell 16, 887–896. https://doi.org/10.1105/tpc.019901

Inoue, S., Kinoshita, T., Matsumoto, M., Nakayama, K.I., Doi, M., Shimazaki, K., 2008. Blue light-induced autophosphorylation of phototropin is a primary step for signaling. Proc. Natl. Acad. Sci. U.S.A. 105, 5626–5631. https://doi.org/10.1073/pnas.0709189105

Jenkins, G.I., 2014. The UV-B Photoreceptor UVR8: From Structure to Physiology. Plant Cell 26, 21–37. https://doi.org/10.1105/tpc.113.119446

Jing, H., Korasick, D.A., Emenecker, R.J., Morffy, N., Wilkinson, E.G., Powers, S.K., Strader, L.C., 2022. Regulation of AUXIN RESPONSE FACTOR condensation and nucleo-cytoplasmic partitioning. Nat Commun 13, 4015. https://doi.org/10.1038/s41467-022-31628-2

Johnson, A., Dahhan, D.A., Gnyliukh, N., Kaufmann, W.A., Zheden, V., Costanzo, T., Mahou, P., Hrtyan, M., Wang, J., Aguilera-Servin, J., Van Damme, D., Beaurepaire, E., Loose, M., Bednarek, S.Y., Friml, J., 2021. The TPLATE complex mediates membrane bending during plant clathrin–mediated endocytosis. Proc. Natl. Acad. Sci. U.S.A. 118, e2113046118. https://doi.org/10.1073/pnas.2113046118

Johnson, A., Gnyliukh, N., Kaufmann, W.A., Narasimhan, M., Vert, G., Bednarek, S.Y., Friml, J., 2020. Experimental toolbox for quantitative evaluation of clathrin-mediated endocytosis in the plant model *Arabidopsis*. Journal of Cell Science 133, jcs248062. https://doi.org/10.1242/jcs.248062

Kaiserli, E., Sullivan, S., Jones, M.A., Feeney, K.A., Christie, J.M., 2009. Domain Swapping to Assess the Mechanistic Basis of *Arabidopsis* Phototropin 1 Receptor Kinase Activation and Endocytosis by Blue Light. The Plant Cell 21, 3226–3244. https://doi.org/10.1105/tpc.109.067876

Kami, C., Allenbach, L., Zourelidou, M., Ljung, K., Schütz, F., Isono, E., Watahiki, M.K., Yamamoto, K.T., Schwechheimer, C., Fankhauser, C., 2014. Reduced phototropism in *pks* mutants may be due to altered auxin-regulated gene expression or reduced lateral auxin transport. The Plant Journal 77, 393–403. https://doi.org/10.1111/tpj.12395

Karimi, M., Depicker, A., Hilson, P., 2007. Recombinational Cloning with Plant Gateway Vectors. Plant Physiology 145, 1144–1154. https://doi.org/10.1104/pp.107.106989

Kim, C., Kwon, Y., Jeong, J., Kang, M., Lee, G.S., Moon, J.H., Lee, H.-J., Park, Y.-I., Choi, G., 2023. Phytochrome B photobodies are comprised of phytochrome B and its primary and secondary interacting proteins. Nat Commun 14, 1708. https://doi.org/10.1038/s41467-023-37421-z

Kimura, T., Haga, K., Nomura, Y., Higaki, T., Nakagami, H., Sakai, T., 2021. Phosphorylation of NONPHOTOTROPIC HYPOCOTYL3 affects photosensory adaptation during the phototropic response. Plant Physiology 187, 981–995. https://doi.org/10.1093/plphys/kiab281

Kimura, T., Haga, K., Sakai, T., 2022. The phosphorylation status of NONPHOTOTROPIC HYPOCOTYL3 affects phot2-dependent phototropism in *Arabidopsis*. Plant Signaling & Behavior 17, 2027138. https://doi.org/10.1080/15592324.2022.2027138

Kimura, T., Tsuchida-Mayama, T., Imai, H., Okajima, K., Ito, K., Sakai, T., 2020. Arabidopsis ROOT PHOTOTROPISM2 Is a Light-Dependent Dynamic Modulator of Phototropin1. Plant Cell 32, 2004–2019. https://doi.org/10.1105/tpc.19.00926

Kitakura, S., Vanneste, S., Robert, S., Löfke, C., Teichmann, T., Tanaka, H., Friml, J., 2011. Clathrin Mediates Endocytosis and Polar Distribution of PIN Auxin Transporters in *Arabidopsis*. The Plant Cell 23, 1920–1931. https://doi.org/10.1105/tpc.111.083030

Kleine-Vehn, J., Ding, Z., Jones, A.R., Tasaka, M., Morita, M.T., Friml, J., 2010. Gravity-induced PIN transcytosis for polarization of auxin fluxes in gravity-sensing root cells. Proc. Natl. Acad. Sci. U.S.A. 107, 22344–22349. https://doi.org/10.1073/pnas.1013145107

Kleine-Vehn, J., Huang, F., Naramoto, S., Zhang, J., Michniewicz, M., Offringa, R., Friml, J., 2009. PIN Auxin Efflux Carrier Polarity Is Regulated by PINOID Kinase-Mediated Recruitment into GNOM-Independent Trafficking in *Arabidopsis*. The Plant Cell 21, 3839–3849. https://doi.org/10.1105/tpc.109.071639

Kleine-Vehn, J., Wabnik, K., Martinière, A., Łangowski, Ł., Willig, K., Naramoto, S., Leitner, J., Tanaka, H., Jakobs, S., Robert, S., Luschnig, C., Govaerts, W., W Hell, S., Runions, J., Friml, J., 2011. Recycling, clustering, and endocytosis jointly maintain PIN auxin carrier polarity at the plasma membrane. Molecular Systems Biology 7, 540. https://doi.org/10.1038/msb.2011.72

Kolhe, J.A., Babu, N.L., Freeman, B.C., 2023. The Hsp90 molecular chaperone governs client proteins by targeting intrinsically disordered regions. Molecular Cell 83, 2035-2044.e7. https://doi.org/10.1016/j.molcel.2023.05.021

Koncz, C., Schell, J., 1986. The promoter of TL-DNA gene 5 controls the tissue-specific expression of chimaeric genes carried by a novel type of Agrobacterium binary vector. Molec Gen Genet 204, 383–396. https://doi.org/10.1007/BF00331014
Kong, S., Suzuki, T., Tamura, K., Mochizuki, N., Hara-Nishimura, I., Nagatani, A., 2006. Blue light-induced association of phototropin 2 with the Golgi apparatus. The Plant Journal 45, 994–1005. https://doi.org/10.1111/j.1365-313X.2006.02667.x
Konopka, C.A., Backues, S.K., Bednarek, S.Y., 2008. Dynamics of *Arabidopsis* Dynamin-Related Protein 1C and a Clathrin Light Chain at the Plasma Membrane. The Plant Cell 20, 1363–1380. https://doi.org/10.1105/tpc.108.059428
Kosmacz, M., Gorka, M., Schmidt, S., Luzarowski, M., Moreno, J.C., Szlachetko, J., Leniak, E., Sokolowska, E.M., Sofroni, K., Schnittger, A., Skirycz, A., 2019. Protein and metabolite composition of Arabidopsis stress granules. New Phytologist 222, 1420–1433. https://doi.org/10.1111/nph.15690
Kotak, S., Larkindale, J., Lee, U., Von Koskull-Döring, P., Vierling, E., Scharf, K.-D., 2007. Complexity of the heat stress response in plants. Current Opinion in Plant Biology 10, 310–316. https://doi.org/10.1016/j.pbi.2007.04.011
Kramer, E.M., Bennett, M.J., 2006. Auxin transport: a field in flux. Trends in Plant Science 11, 382–386. https://doi.org/10.1016/j.tplants.2006.06.002
Kraus, J., Neubergerová, M., Cuadrado, A.F., Schilling, N., Eeckhout, D., De Winne, N., Van De Slijke, E., Vandorpe, M., Yperman, K., Mylle, E., Fislage, M., De Jaeger, G., Pleskot, R., Van Damme, D., 2025. A combined biochemical and computational approach provides evidence for membrane remodelling by the structural scaffold of the endocytic TPLATE complex. Nat. Plants 11, 2423–2436. https://doi.org/10.1038/s41477-025-02146-y
Kraus, M., Pleskot, R., Van Damme, D., 2024. Structural and Evolutionary Aspects of Plant Endocytosis. Annual Review of Plant Biology 75, 521–550. https://doi.org/10.1146/annurev-arplant-070122-023455
Křeček, P., Sküpa, P., Libus, J., Naramoto, S., Tejos, R., Friml, J., Zažímalová, E., 2009. The PIN-FORMED (PIN) protein family of auxin transporters. Genome Biology 10. https://doi.org/10.1186/gb-2009-10-12-249
Laptenok, S.P., Borst, J.W., Mullen, K.M., Van Stokkum, I.H.M., Visser, A.J.W.G., Van Amerongen, H., 2010. Global analysis of Förster resonance energy transfer in live cells measured by fluorescence lifetime imaging microscopy exploiting the rise time of acceptor fluorescence. Phys. Chem. Chem. Phys. 12, 7593. https://doi.org/10.1039/b919700a
Lariguet, P., Schepens, I., Hodgson, D., Pedmale, U.V., Trevisan, M., Kami, C., De Carbonnel, M., Alonso, J.M., Ecker, J.R., Liscum, E., Fankhauser, C., 2006. PHYTOCHROME KINASE SUBSTRATE 1 is a phototropin 1 binding protein required for phototropism. Proc. Natl. Acad. Sci. U.S.A. 103, 10134–10139. https://doi.org/10.1073/pnas.0603799103
Li, Q.-H., Yang, H.-Q., 2007. Cryptochrome Signaling in Plants†. Photochemistry and Photobiology 83, 94–101. https://doi.org/10.1562/2006-02-28-IR-826
Lin, B.-L., Wang, J.-S., Liu, H.-C., Chen, R.-W., Meyer, Y., Barakat, A., Delseny, M., 2001. Genomic analysis of the Hsp70 superfamily in Arabidopsis thaliana.
Liscum, E., Askinosie, S.K., Leuchtman, D.L., Morrow, J., Willenburg, K.T., Coats, D.R., 2014. Phototropism: Growing towards an Understanding of Plant Movement. Plant Cell 26, 38–55. https://doi.org/10.1105/tpc.113.119727
Liscum, E., Briggs, W.R., 1995. Mutations in the NPH1 Locus of Arabidopsis Disrupt the Perception of Phototropic Stimuli.
Liscum, E., Nittler, P., Koskie, K., 2020. The continuing arc toward phototropic enlightenment. Journal of Experimental Botany 71, 1652–1658. https://doi.org/10.1093/jxb/eraa005
Liscum, E., Reed, J.W., 2002. Genetics of Aux/IAA and ARF action in plant growth and development, in: Perrot-Rechenmann, C., Hagen, G. (Eds.), Auxin Molecular Biology. Springer Netherlands, Dordrecht, pp. 387–400. https://doi.org/10.1007/978-94-010-0377-3_10
Long, Y., Stahl, Y., Weidtkamp-Peters, S., Postma, M., Zhou, W., Goedhart, J., Sánchez-Pérez, M.-I., Gadella, T.W.J., Simon, R., Scheres, B., Blilou, I., 2017. In vivo FRET–FLIM reveals cell-type-specific protein interactions in Arabidopsis roots. Nature 548, 97–102. https://doi.org/10.1038/nature23317
Luschnig, C., Friml, J., 2024. Over 25 years of decrypting PIN-mediated plant development. Nat Commun 15, 9904. https://doi.org/10.1038/s41467-024-54240-y
Mair, A., Bergmann, D.C., 2022. Advances in enzyme-mediated proximity labeling and its potential for plant research. Plant Physiology 188, 756–768. https://doi.org/10.1093/plphys/kiab479
Mair, A., Xu, S.-L., Branon, T.C., Ting, A.Y., Bergmann, D.C., 2019. Proximity labeling of protein complexes and cell-type-specific organellar proteomes in Arabidopsis enabled by TurboID. eLife 8, e47864. https://doi.org/10.7554/eLife.47864
Manishankar, P., Fernandez, A., Rohr, L., Yigit, Y.I., Reuter, L., 2026. Molecular determinants underlying NPH3 condensation and function in phototropism: an integrative approach. The Plant Cell. https://doi.org/10.1093/plcell/koag028
Marcote, M.J., Sancho-Andrés, G., Soriano-Ortega, E., Aniento, F., 2016. Sorting signals for PIN1 trafficking and localization. Plant Signaling & Behavior 11, e1212801. https://doi.org/10.1080/15592324.2016.1212801

Marhava, P., Aliaga Fandino, A.C., Koh, S.W.H., Jelínková, A., Kolb, M., Janacek, D.P., Breda, A.S., Cattaneo, P., Hammes, U.Z., Petrášek, J., Hardtke, C.S., 2020. Plasma Membrane Domain Patterning and Self-Reinforcing Polarity in Arabidopsis. Developmental Cell 52, 223-235.e5. https://doi.org/10.1016/j.devcel.2019.11.015

Matsuoka, D., Tokutomi, S., 2005. Blue light-regulated molecular switch of Ser/Thr kinase in phototropin. Proc. Natl. Acad. Sci. U.S.A. 102, 13337–13342. https://doi.org/10.1073/pnas.0506402102

McMahon, H.T., Boucrot, E., 2011. Molecular mechanism and physiological functions of clathrin-mediated endocytosis. Nat Rev Mol Cell Biol 12, 517–533. https://doi.org/10.1038/nrm3151

Michniewicz, M., Zago, M.K., Abas, L., Weijers, D., Schweighofer, A., Meskiene, I., Heisler, M.G., Ohno, C., Zhang, J., Huang, F., Schwab, R., Weigel, D., Meyerowitz, E.M., Luschnig, C., Offringa, R., Friml, J., 2007. Antagonistic Regulation of PIN Phosphorylation by PP2A and PINOID Directs Auxin Flux. Cell 130, 1044–1056. https://doi.org/10.1016/j.cell.2007.07.033

Mitsunari, T., Nakatsu, F., Shioda, N., Love, P.E., Grinberg, A., Bonifacino, J.S., Ohno, H., 2005. Clathrin Adaptor AP-2 Is Essential for Early Embryonal Development. Molecular and Cellular Biology 25, 9318–9323. https://doi.org/10.1128/MCB.25.21.9318-9323.2005

Motchoulski, A., Liscum, E., 1999. *Arabidopsis* NPH3: A NPH1 Photoreceptor-Interacting Protein Essential for Phototropism. Science 286, 961–964. https://doi.org/10.1126/science.286.5441.961

Mravec, J., Skůpa, P., Bailly, A., Hoyerová, K., Křeček, P., Bielach, A., Petrášek, J., Zhang, J., Gaykova, V., Stierhof, Y.-D., Dobrev, P.I., Schwarzerová, K., Rolčík, J., Seifertová, D., Luschnig, C., Benková, E., Zažímalová, E., Geisler, M., Friml, J., 2009. Subcellular homeostasis of phytohormone auxin is mediated by the ER-localized PIN5 transporter. Nature 459, 1136–1140. https://doi.org/10.1038/nature08066

Ohgishi, M., Saji, K., Okada, K., Sakai, T., 2004. Functional analysis of each blue light receptor, cry1, cry2, phot1, and phot2, by using combinatorial multiple mutants in *Arabidopsis*. Proc. Natl. Acad. Sci. U.S.A. 101, 2223–2228. https://doi.org/10.1073/pnas.0305984101

Ohno, H., Stewart, J., Fournier, M.-C., Bosshart, H., Rhee, I., Miyatake, S., Saito, T., Gallusser, A., Kirchhausen, T., Bonifacino, J.S., 1995. Interaction of Tyrosine-Based Sorting Signals with Clathrin-Associated Proteins. Science 269, 1872–1875. https://doi.org/10.1126/science.7569928

Okada, K., Ueda, J., Komaki, M.K., Bell, C.J., Shimura, Y., 1991. Requirement of the Auxin Polar Transport System in Early Stages of Arabídopsis Floral Bud Formation. The Plant Cell 3, 677–684.

Paik, I., Huq, E., 2019. Plant photoreceptors: Multi-functional sensory proteins and their signaling networks. Seminars in Cell & Developmental Biology 92, 114–121. https://doi.org/10.1016/j.semcdb.2019.03.007

Pedmale, U.V., Celaya, R.B., Liscum, E., 2010. Phototropism: Mechanism and Outcomes. The Arabidopsis Book 8, e0125. https://doi.org/10.1199/tab.0125

Pedmale, U.V., Liscum, E., 2007. Regulation of Phototropic Signaling in Arabidopsis via Phosphorylation State Changes in the Phototropin 1-interacting Protein NPH3. Journal of Biological Chemistry 282, 19992–20001. https://doi.org/10.1074/jbc.M702551200

Peng, J., Yu, Y., Fang, X., 2025. Stress sensing and response through biomolecular condensates in plants. Plant Communications 6, 101225. https://doi.org/10.1016/j.xplc.2024.101225

Péret, B., Swarup, K., Ferguson, A., Seth, M., Yang, Y., Dhondt, S., James, N., Casimiro, I., Perry, P., Syed, A., Yang, H., Reemmer, J., Venison, E., Howells, C., Perez-Amador, M.A., Yun, J., Alonso, J., Beemster, G.T.S., Laplaze, L., Murphy, A., Bennett, M.J., Nielsen, E., Swarup, R., 2012. *AUX/LAX* Genes Encode a Family of Auxin Influx Transporters That Perform Distinct Functions during *Arabidopsis* Development. Plant Cell 24, 2874–2885. https://doi.org/10.1105/tpc.112.097766

Petricka, J.J., Clay, N.K., Nelson, T.M., 2008. Vein patterning screens and the *defectively organized tributaries* mutants in *Arabidopsis thaliana*. The Plant Journal 56, 251–263. https://doi.org/10.1111/j.1365-313X.2008.03595.x

Pinon, V., Ravanel, S., Douce, R., Alban, C., 2005. Biotin Synthesis in Plants. The First Committed Step of the Pathway Is Catalyzed by a Cytosolic 7-Keto-8-Aminopelargonic Acid Synthase. Plant Physiology 139, 1666–1676. https://doi.org/10.1104/pp.105.070144

Powers, S.K., Holehouse, A.S., Korasick, D.A., Schreiber, K.H., Clark, N.M., Jing, H., Emenecker, R., Han, S., Tycksen, E., Hwang, I., Sozzani, R., Jez, J.M., Pappu, R.V., Strader, L.C., 2019. Nucleo-cytoplasmic Partitioning of ARF Proteins Controls Auxin Responses in Arabidopsis thaliana. Molecular Cell 76, 177-190.e5. https://doi.org/10.1016/j.molcel.2019.06.044

Preuten, T., Blackwood, L., Christie, J.M., Fankhauser, C., 2015. Lipid anchoring of *A rabidopsis* phototropin 1 to assess the functional significance of receptor internalization: should I stay or should I go? New Phytologist 206, 1038–1050. https://doi.org/10.1111/nph.13299

Preuten, T., Hohm, T., Bergmann, S., Fankhauser, C., 2013. Defining the Site of Light Perception and Initiation of Phototropism in Arabidopsis. Current Biology 23, 1934–1938. https://doi.org/10.1016/j.cub.2013.07.079

Rademacher, E.H., Offringa, R., 2012. Evolutionary Adaptations of Plant AGC Kinases: From Light Signaling to Cell Polarity Regulation. Front. Plant Sci. 3. https://doi.org/10.3389/fpls.2012.00250

Rakusová, H., Fendrych, M., Friml, J., 2015. Intracellular trafficking and PIN-mediated cell polarity during tropic responses in plants. Current Opinion in Plant Biology 23, 116–123. https://doi.org/10.1016/j.pbi.2014.12.002

Reuter, L., Schmidt, T., Manishankar, P., Throm, C., Keicher, J., Bock, A., Droste-Borel, I., Oecking, C., 2021. Light-triggered and phosphorylation-dependent 14-3-3 association with NON-PHOTOTROPIC HYPOCOTYL 3 is required for hypocotyl phototropism. Nat Commun 12, 6128. https://doi.org/10.1038/s41467-021-26332-6

Reynolds, G.D., Wang, C., Pan, J., Bednarek, S.Y., 2018. Inroads into Internalization: Five Years of Endocytic Exploration. Plant Physiol. 176, 208–218. https://doi.org/10.1104/pp.17.01117

Robert, H.S., Friml, J., 2009. Auxin and other signals on the move in plants. Nat Chem Biol 5, 325–332. https://doi.org/10.1038/nchembio.170

Roberts, D., Pedmale, U.V., Morrow, J., Sachdev, S., Lechner, E., Tang, X., Zheng, N., Hannink, M., Genschik, P., Liscum, E., 2011. Modulation of Phototropic Responsiveness in *Arabidopsis* through Ubiquitination of Phototropin 1 by the CUL3-Ring E3 Ubiquitin Ligase CRL3NPH3. The Plant Cell 23, 3627–3640. https://doi.org/10.1105/tpc.111.087999

Rozanova, S., Barkovits, K., Nikolov, M., Schmidt, C., Urlaub, H., Marcus, K., 2021. Quantitative Mass Spectrometry-Based Proteomics: An Overview, in: Marcus, K., Eisenacher, M., Sitek, B. (Eds.), Quantitative Methods in Proteomics, Methods in Molecular Biology. Springer US, New York, NY, pp. 85–116. https://doi.org/10.1007/978-1-0716-1024-4_8

Sakai, T., Haga, K., 2012. Molecular Genetic Analysis of Phototropism in Arabidopsis. Plant and Cell Physiology 53, 1517–1534. https://doi.org/10.1093/pcp/pcs111

Sakai, T., Haga, K., Kimura, T., Kawaura, K., 2025. Protein phosphatase PP2C19 controls hypocotyl phototropism through the phosphorylation modification of NONPHOTOTROPIC HYPOCOTYL3 in *Arabidopsis*. Plant And Cell Physiology 66, 23–35. https://doi.org/10.1093/pcp/pcae141

Sakai, T., Kagawa, T., Kasahara, M., Swartz, T.E., Christie, J.M., Briggs, W.R., Wada, M., Okada, K., 2001. *Arabidopsis* nph1 and npl1: Blue light receptors that mediate both phototropism and chloroplast relocation. Proc. Natl. Acad. Sci. U.S.A. 98, 6969–6974. https://doi.org/10.1073/pnas.101137598

Sakai, T., Wada, T., Ishiguro, S., Okada, K., 2000. RPT2: A Signal Transducer of the Phototropic Response in Arabidopsis.

Sakamoto, K., Briggs, W.R., 2002. Cellular and Subcellular Localization of Phototropin 1. Plant Cell 14, 1723–1735. https://doi.org/10.1105/tpc.003293

Sancho-Andrés, G., Soriano-Ortega, E., Gao, C., Bernabé-Orts, J.M., Narasimhan, M., Müller, A.O., Tejos, R., Jiang, L., Friml, J., Aniento, F., Marcote, M.J., 2016. Sorting Motifs Involved in the Trafficking and Localization of the PIN1 Auxin Efflux Carrier. Plant Physiol. 171, 1965–1982. https://doi.org/10.1104/pp.16.00373

Sandvig, K., Pust, S., Skotland, T., Van Deurs, B., 2011. Clathrin-independent endocytosis: mechanisms and function. Current Opinion in Cell Biology 23, 413–420. https://doi.org/10.1016/j.ceb.2011.03.007

Sauer, M., Kleine-Vehn, J., 2019. PIN-FORMED and PIN-LIKES auxin transport facilitators. Development 146.

Schneider, C.A., Rasband, W.S., Eliceiri, K.W., 2012. NIH Image to ImageJ: 25 years of image analysis. Nat Methods 9, 671–675. https://doi.org/10.1038/nmeth.2089

Schumacher, P., Demarsy, E., Waridel, P., Petrolati, L.A., Trevisan, M., Fankhauser, C., 2018. A phosphorylation switch turns a positive regulator of phototropism into an inhibitor of the process. Nat Commun 9, 2403. https://doi.org/10.1038/s41467-018-04752-1

Schwenk, P., Hiltbrunner, A., 2022. Phytochrome A Mediates the Disassembly of Processing Bodies in Far-Red Light. Front. Plant Sci. 13, 828529. https://doi.org/10.3389/fpls.2022.828529

Schwenk, P., Sheerin, D.J., Ponnu, J., Staudt, A.-M., Lesch, K.L., Lichtenberg, E., Medzihradszky, K.F., Hoecker, U., Klement, E., Viczián, A., Hiltbrunner, A., 2021. Uncovering a novel function of the CCR4-NOT complex in phytochrome A-mediated light signalling in plants. eLife 10, e63697. https://doi.org/10.7554/eLife.63697

Solis-Miranda, J., Chodasiewicz, M., Skirycz, A., Fernie, A.R., Moschou, P.N., Bozhkov, P.V., Gutierrez-Beltran, E., 2023. Stress-related biomolecular condensates in plants. The Plant Cell 35, 3187–3204. https://doi.org/10.1093/plcell/koad127

Somers, D.E., Schultz, T.F., Milnamow, M., Kay, S.A., 2000. ZEITLUPE Encodes a Novel Clock-Associated PAS Protein from Arabidopsis. Cell 101, 319–329. https://doi.org/10.1016/S0092-8674(00)80841-7

Steinmann, T., Geldner, N., Grebe, M., Mangold, S., Jackson, C.L., Paris, S., Gälweiler, L., Palme, K., Jürgens, G., 1999. Coordinated Polar Localization of Auxin Efflux Carrier PIN1 by GNOM ARF GEF. Science 286, 316–318. https://doi.org/10.1126/science.286.5438.316

Stowe-Evans, E.L., Luesse, D.R., Liscum, E., 2001. The Enhancement of Phototropin-Induced Phototropic Curvature in Arabidopsis Occurs via a Photoreversible Phytochrome A-Dependent Modulation of Auxin Responsiveness. Plant Physiology 126, 826–834. https://doi.org/10.1104/pp.126.2.826

Suetsugu, N., Takemiya, A., Kong, S.-G., Higa, T., Komatsu, A., Shimazaki, K., Kohchi, T., Wada, M., 2016. RPT2/NCH1 subfamily of NPH3-like proteins is essential for the chloroplast accumulation response in land plants. Proc. Natl. Acad. Sci. U.S.A. 113, 10424–10429. https://doi.org/10.1073/pnas.1602151113

Sullivan, S., Hermanowicz, P., Higa, T., Waksman, T., Gotoh, E., Horne, A., Henderson, L., Prochwicz, A., Wada, M., Suetsugu, N., Łabuz, J., Christie, J.M., 2026. Reversible phosphorylation of NPH3/RPT2-like proteins regulates phototropin receptor signaling. The Plant Cell.

Sullivan, S., Kharshiing, E., Laird, J., Sakai, T., Christie, J.M., 2019. Deetiolation Enhances Phototropism by Modulating NON-PHOTOTROPIC HYPOCOTYL3 Phosphorylation Status. Plant Physiol. 180, 1119–1131. https://doi.org/10.1104/pp.19.00206

Sullivan, S., Waksman, T., Paliogianni, D., Henderson, L., Lütkemeyer, M., Suetsugu, N., Christie, J.M., 2021. Regulation of plant phototropic growth by NPH3/RPT2-like substrate phosphorylation and 14-3-3 binding. Nat Commun 12, 6129. https://doi.org/10.1038/s41467-021-26333-5

Sung, D., Kaplan, F., Guy, C.L., 2001. Plant Hsp70 molecular chaperones: Protein structure, gene family, expression and function. Physiologia Plantarum 113, 443–451. https://doi.org/10.1034/j.1399-3054.2001.1130402.x

Sung, D.Y., Guy, C.L., 2003. Physiological and Molecular Assessment of Altered Expression of *Hsc70-1* in Arabidopsis. Evidence for Pleiotropic Consequences. Plant Physiology 132, 979–987. https://doi.org/10.1104/pp.102.019398

Takemiya, A., Sugiyama, N., Fujimoto, H., Tsutsumi, T., Yamauchi, S., Hiyama, A., Tada, Y., Christie, J.M., Shimazaki, K., 2013. Phosphorylation of BLUS1 kinase by phototropins is a primary step in stomatal opening. Nat Commun 4, 2094. https://doi.org/10.1038/ncomms3094

Takubo, E., Kobayashi, M., Hirai, S., Aoi, Y., Ge, C., Dai, X., Fukui, K., Hayashi, K., Zhao, Y., Kasahara, H., 2020. Role of Arabidopsis INDOLE-3-ACETIC ACID CARBOXYL METHYLTRANSFERASE 1 in auxin metabolism. Biochemical and Biophysical Research Communications 527, 1033–1038. https://doi.org/10.1016/j.bbrc.2020.05.031

Thimann, K.V., 1992. The cholodny-went “theory.” Plant Mol Biol Rep 10, 103–104. https://doi.org/10.1007/BF02668341

Tsuchida-Mayama, T., Nakano, M., Uehara, Y., Sano, M., Fujisawa, N., Okada, K., Sakai, T., 2008. Mapping of the phosphorylation sites on the phototropic signal transducer, NPH3. Plant Science 174, 626–633. https://doi.org/10.1016/j.plantsci.2008.03.018

Tyanova, S., Temu, T., Cox, J., 2016a. The MaxQuant computational platform for mass spectrometry-based shotgun proteomics. Nat Protoc 11, 2301–2319. https://doi.org/10.1038/nprot.2016.136

Tyanova, S., Temu, T., Sinitcyn, P., Carlson, A., Hein, M.Y., Geiger, T., Mann, M., Cox, J., 2016b. The Perseus computational platform for comprehensive analysis of (prote)omics data. Nat Methods 13, 731–740. https://doi.org/10.1038/nmeth.3901

Upadhyay-Tiwari, N., Huang, X.-J., Lee, Y.-C., Singh, S.K., Hsu, C.-C., Huang, S.-S., Verslues, P.E., 2024. The nonphototrophic hypocotyl 3 (NPH3) domain protein NRL5 is a trafficking-associated GTPase essential for drought resistance. Science AdvAnceS.

Van Damme, D., Coutuer, S., De Rycke, R., Bouget, F.-Y., Inzé, D., Geelen, D., 2007. Somatic Cytokinesis and Pollen Maturation in *Arabidopsis* Depend on TPLATE, Which Has Domains Similar to Coat Proteins. The Plant Cell 18, 3502–3518. https://doi.org/10.1105/tpc.106.040923

Van Gaal, E.V.B., Spierenburg, G., Hennink, W.E., Crommelin, D.J.A., Mastrobattista, E., 2010. Flow cytometry for rapid size determination and sorting of nucleic acid containing nanoparticles in biological fluids. Journal of Controlled Release 141, 328–338. https://doi.org/10.1016/j.jconrel.2009.09.009

Vierling, E., 1991. THE ROLES OF HEAT SHOCK PROTEINS IN PLANTS. Annu. Rev. Plant Physiology Plant Mol. Biol. 42.

Waese, J., Fan, J., Pasha, A., Yu, H., Fucile, G., Shi, R., Cumming, M., Kelley, L.A., Sternberg, M.J., Krishnakumar, V., Ferlanti, E., Miller, J., Town, C., Stuerzlinger, W., Provart, N.J., 2017. ePlant: Visualizing and Exploring Multiple Levels of Data for Hypothesis Generation in Plant Biology. Plant Cell 29, 1806–1821. https://doi.org/10.1105/tpc.17.00073

Waksman, T., Suetsugu, N., Hermanowicz, P., Ronald, J., Sullivan, S., Łabuz, J., Christie, J.M., 2023. Phototropin phosphorylation of ROOT PHOTOTROPISM 2 and its role in mediating phototropism, leaf positioning, and chloroplast accumulation movement in Arabidopsis. The Plant Journal 114, 390–402. https://doi.org/10.1111/tpj.16144

Wang, J., Jiang, Q., Pleskot, R., Grones, P., Bahafid, E., Denay, G., Galván-Ampudia, C., Xu, X., Vandorpe, M., Mylle, E., De Smet, I., Vernoux, T., Simon, R., Nowack, M.K., Van Damme, D., 2023. TPLATE complex-dependent endocytosis attenuates CLAVATA1 signaling for shoot apical meristem maintenance. EMBO Reports 24, e54709. https://doi.org/10.15252/embr.202254709

Wang, J., Mylle, E., Johnson, A., Besbrugge, N., De Jaeger, G., Friml, J., Pleskot, R., Van Damme, D., 2020. High Temporal Resolution Reveals Simultaneous Plasma Membrane Recruitment of TPLATE Complex Subunits. Plant Physiol. 183, 986–997. https://doi.org/10.1104/pp.20.00178

Wang, J., Yperman, K., Grones, P., Jiang, Q., Dragwidge, J., Mylle, E., Mor, E., Nolf, J., Eeckhout, D., De Jaeger, G., De Rybel, B., Pleskot, R., Van Damme, D., 2021. Conditional destabilization of the TPLATE complex impairs endocytic internalization. Proc. Natl. Acad. Sci. U.S.A. 118, e2023456118. https://doi.org/10.1073/pnas.2023456118

Wang, P., Pleskot, R., Zang, J., Winkler, J., Wang, J., Yperman, K., Zhang, T., Wang, K., Gong, J., Guan, Y., Richardson, C., Duckney, P., Vandorpe, M., Mylle, E., Fiserova, J., Van Damme, D., Hussey, P.J., 2019. Plant AtEH/Pan1 proteins drive autophagosome formation at ER-PM contact sites with actin and endocytic machinery. Nat Commun 10, 5132. https://doi.org/10.1038/s41467-019-12782-6

Wang, Q., Lin, C., 2020. Mechanisms of Cryptochrome-Mediated Photoresponses in Plants. Annu. Rev. Plant Biol. 71, 103–129. https://doi.org/10.1146/annurev-arplant-050718-100300

Wang, W., Gu, Y., 2022. The emerging role of biomolecular condensates in plant immunity. The Plant Cell 34, 1568–1572. https://doi.org/10.1093/plcell/koab240
Weller, B., Zourelidou, M., Frank, L., Barbosa, I.C.R., Fastner, A., Richter, S., Jürgens, G., Hammes, U.Z., Schwechheimer, C., 2017. Dynamic PIN-FORMED auxin efflux carrier phosphorylation at the plasma membrane controls auxin efflux-dependent growth. Proc. Natl. Acad. Sci. U.S.A. 114. https://doi.org/10.1073/pnas.1614380114
Went, F.W., 1935. Auxin, the plant growth-hormone. Bot. Rev 1, 162–182. https://doi.org/10.1007/BF02870150
Went, F.W., Thimann, K.V., 1937. Phytohormones. Macmillan, New York.
Whippo, C.W., Hangarter, R.P., 2006. Phototropism: bending towards enlightenment. Plant Cell . 2006 May;18(5):1110-9. https://doi.org/doi:%252010.1105/tpc.105.039669.
Willige, B.C., Ahlers, S., Zourelidou, M., Barbosa, I.C.R., Demarsy, E., Trevisan, M., Davis, P.A., Roelfsema, M.R.G., Hangarter, R., Fankhauser, C., Schwechheimer, C., 2013. D6PK AGCVIII Kinases Are Required for Auxin Transport and Phototropic Hypocotyl Bending in *Arabidopsis*. The Plant Cell 25, 1674–1688. https://doi.org/10.1105/tpc.113.111484
Win, J., Kamoun, S., 2004. pCB301-p19: A Binary Plasmid Vector to Enhance Transient Expression of Transgenes by Agroinfiltration.
Xuan, L., Li, J., Jiang, Y., Shi, M., Zhu, Y., Bao, X., Gong, Q., Xue, H., Yu, H., Liu, L., 2024. MCTP controls nucleocytoplasmic partitioning of AUXIN RESPONSE FACTORs during lateral root development. Developmental Cell 59, 3229-3244.e5. https://doi.org/10.1016/j.devcel.2024.09.026
Yamamoto, K., Suzuki, T., Aihara, Y., Haga, K., Sakai, T., Nagatani, A., 2014. The Phototropic Response is Locally Regulated Within the Topmost Light-Responsive Region of the Arabidopsis thaliana Seedling. Plant and Cell Physiology 55, 497–506. https://doi.org/10.1093/pcp/pct184
Yamaoka, S., Shimono, Y., Shirakawa, M., Fukao, Y., Kawase, T., Hatsugai, N., Tamura, K., Shimada, T., Hara-Nishimura, I., 2013. Identification and Dynamics of *Arabidopsis* Adaptor Protein-2 Complex and Its Involvement in Floral Organ Development. Plant Cell 25, 2958–2969. https://doi.org/10.1105/tpc.113.114082
Yperman, K., Merceron, R., De Munck, S., Bloch, Y., Eeckhout, D., Jiang, Q., Tack, P., Grigoryan, R., Evangelidis, T., Van Leene, J., Vincze, L., Vandenabeele, P., Vanhaecke, F., Potocký, M., De Jaeger, G., Savvides, S.N., Tripsianes, K., Pleskot, R., Van Damme, D., 2021a. Distinct EH domains of the endocytic TPLATE complex confer lipid and protein binding. Nat Commun 12, 3050. https://doi.org/10.1038/s41467-021-23314-6
Yperman, K., Wang, J., Eeckhout, D., Winkler, J., Vu, L.D., Vandorpe, M., Grones, P., Mylle, E., Kraus, M., Merceron, R., Nolf, J., Mor, E., De Bruyn, P., Loris, R., Potocký, M., Savvides, S.N., De Rybel, B., De Jaeger, G., Van Damme, D., Pleskot, R., 2021b. Molecular architecture of the endocytic TPLATE complex. Sci. Adv. 7, eabe7999. https://doi.org/10.1126/sciadv.abe7999
Žádníková, P., Petrášek, J., Marhavý, P., Raz, V., Vandenbussche, F., Ding, Z., Schwarzerová, K., Morita, M.T., Tasaka, M., Hejátko, J., Van Der Straeten, D., Friml, J., Benková, E., 2010. Role of PIN-mediated auxin efflux in apical hook development of *Arabidopsis thaliana*. Development 137, 607–617. https://doi.org/10.1242/dev.041277
Zavaliev, R., Mohan, R., Chen, T., Dong, X., 2020. Formation of NPR1 Condensates Promotes Cell Survival during the Plant Immune Response. Cell 182, 1093-1108.e18. https://doi.org/10.1016/j.cell.2020.07.016
Zhang, C., Chen, L., Hou, S., 2024. The emerging roles of clathrin-mediated endocytosis in plant development and stress responses. Journal of Plant Physiology 295, 154189. https://doi.org/10.1016/j.jplph.2024.154189
Zhang, Y., Persson, S., Hirst, J., Robinson, M.S., Van Damme, D., Sánchez-Rodríguez, C., 2015. Change your Tplate, change your fate: plant CME and beyond. Trends in Plant Science 20, 41–48. https://doi.org/10.1016/j.tplants.2014.09.002
Zhang, Y., Yu, Q., Jiang, N., Yan, X., Wang, C., Wang, Q., Liu, J., Zhu, M., Bednarek, S.Y., Xu, J., Pan, J., 2017. Clathrin regulates blue light-triggered lateral auxin distribution and hypocotyl phototropism in *Arabidopsis*. Plant Cell & Environment 40, 165–176. https://doi.org/10.1111/pce.12854
Zhao, X., Zhao, Q., Xu, C., Wang, J., Zhu, J., Shang, B., Zhang, X., 2018. Phot2-regulated relocation of NPH3 mediates phototropic response to high-intensity blue light in *Arabidopsis thaliana*. JIPB 60, 562–577. https://doi.org/10.1111/jipb.12639
Zölls, S., Tantipolphan, R., Wiggenhorn, M., Winter, G., Jiskoot, W., Friess, W., Hawe, A., 2012. Particles in Therapeutic Protein Formulations, Part 1: Overview of Analytical Methods. Journal of Pharmaceutical Sciences 101, 914–935. https://doi.org/10.1002/jps.23001
Zourelidou, M., Absmanner, B., Weller, B., Barbosa, I.C.R., Willige, B.C., Hammes, U.Z., Schwechheimer, C., 2014. Auxin efflux by PIN-FORMED proteins is activated by two different protein kinases, D6 PROTEIN KINASE and PINOID. eLife Plant Biology 3.

9. Supplementary Information

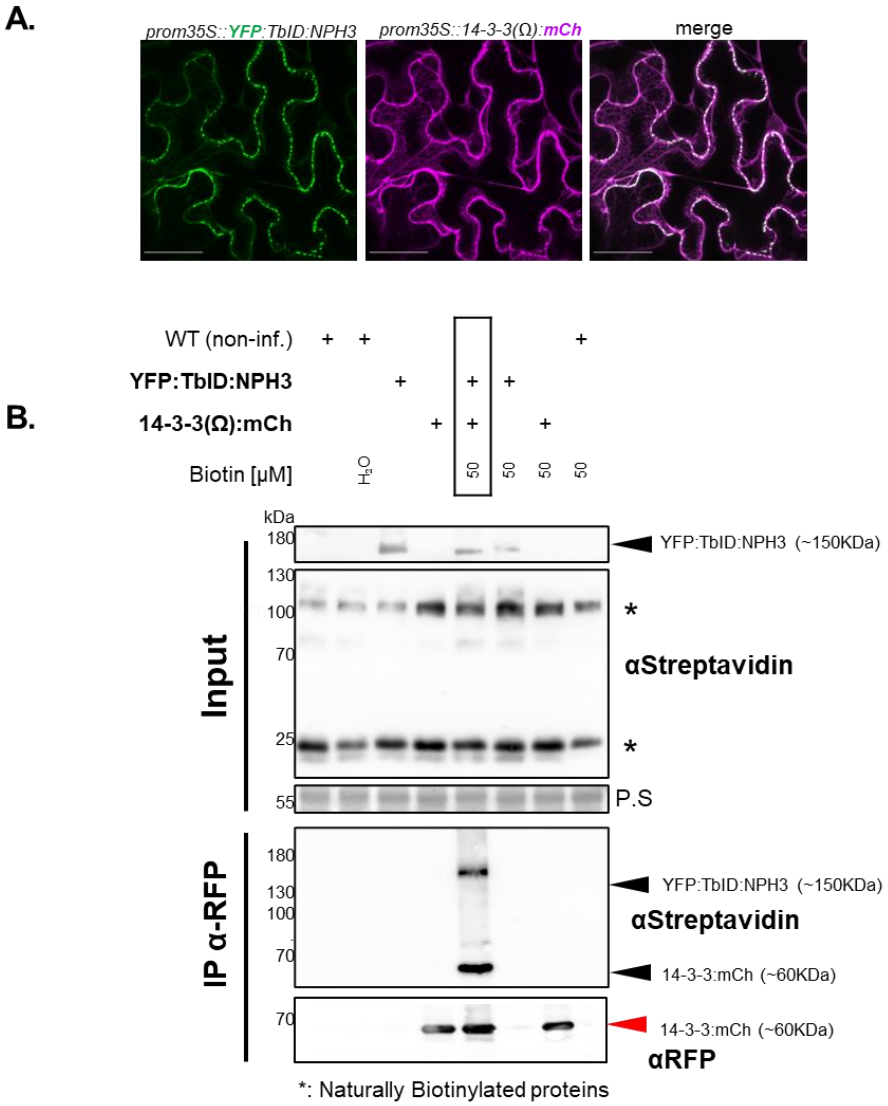

Supplemental Fig. S 1. Proof of principle: YFP:TurboID:NPH3^{WT} biotinylates 14-3-3Ω upon BL treatment in transiently transformed *N. benthamiana* leaves

(A) Representative confocal images of leaf epidermal cells from dark-adapted *N. benthamiana* transiently co-expressing YFP:TurboID:NPH3 and 14-3-3Ω:mCh (under the 35S promoter). Scale bar: 50 µm. (B) *In vivo* biotinylation of 14-3-3Ω and YFP:TurboID:NPH3 transiently co-expressed *in N. benthamiana* leaves. Plants were dark-adapted for 16 h, treated with 50 µM biotin, and exposed to 45 min overhead blue light (BL, 10 µmol m^{-2} s^{-1}). Controls included non-infiltrated *N. benthamiana* leaves, with and without biotin supplementation. Crude extracts were immunoprecipitated using RFP beads. Immunoprecipitation of 14-3-3Ω:mCh was followed by streptavidin immunoblotting. Endogenous biotinylated proteins are indicated by (*). Input and immunoprecipitated proteins (IP α-RFP) are shown. Robust biotinylation of NPH3 and 14-3-3Ω after BL (+biotin) confirms TurboID enzymatic activity and interaction specificity. P.S: Ponceau Staining.

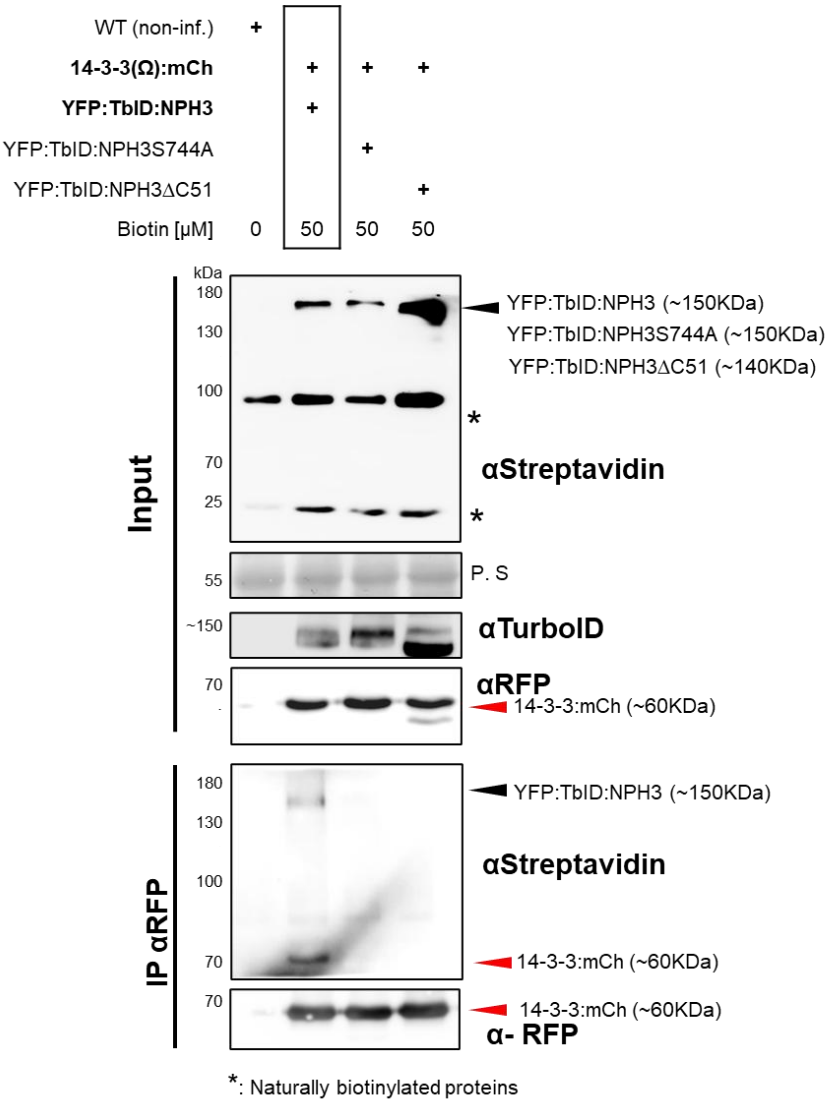

Supplemental Fig. S 2. Proof of principle: YFP:TurboID:NPH3 variants fail to biotinylate 14-3-3Ω upon BL treatment in transiently transformed *N. benthamiana* leaves

In vivo biotinylation of 14-3-3Ω and YFP:TurboID:NPH3 variants (driven by the NPH3 promoter) transiently co-expressed *in N. benthamiana* leaves along with 14-3-3Ω:mCh (under the 35S promoter). Plants were dark-adapted for 16 h, treated with 50 μM biotin, and exposed to 45 min overhead blue light (BL, 10 μmol m^{-2} s^{-1}). Crude extracts were immunoprecipitated using RFP beads, and immunoprecipitation of 14-3-3Ω:mCh was followed by streptavidin immunoblotting. A TurboID antibody was used to verify the expected molecular sizes of the NPH3 variants. Input and immunoprecipitated proteins (IP α-RFP) are shown. 14-3-3Ω was biotinylated only by YFP:TurboID:NPH3, no biotinylation signal was detected for the other NPH3 variants. P.S: Ponceau Staining.

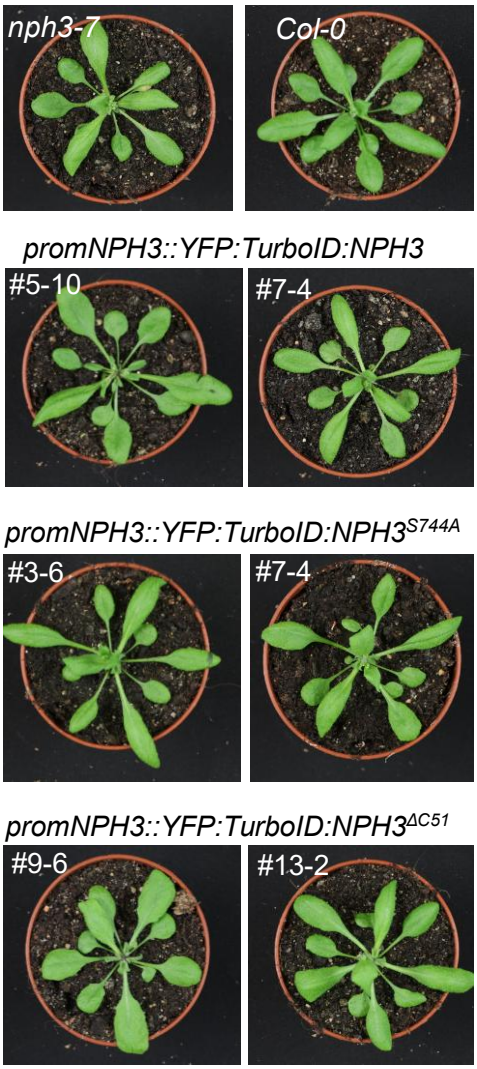

Supplemental Fig. S 3. Vegetative growth phenotype of *Arabidopsis nph3-7* expressing YFP:TurboID:NPH3 variants

Rosette morphology of 4-week-old plants (T3s) expressing TurboID-NPH3 fusions compared to Col-0 and *nph3*-7 controls, grown under long-day greenhouse conditions (16 h light/8 h dark, 21 °C). No differences were observed in leaf size, number, or rosette architecture.

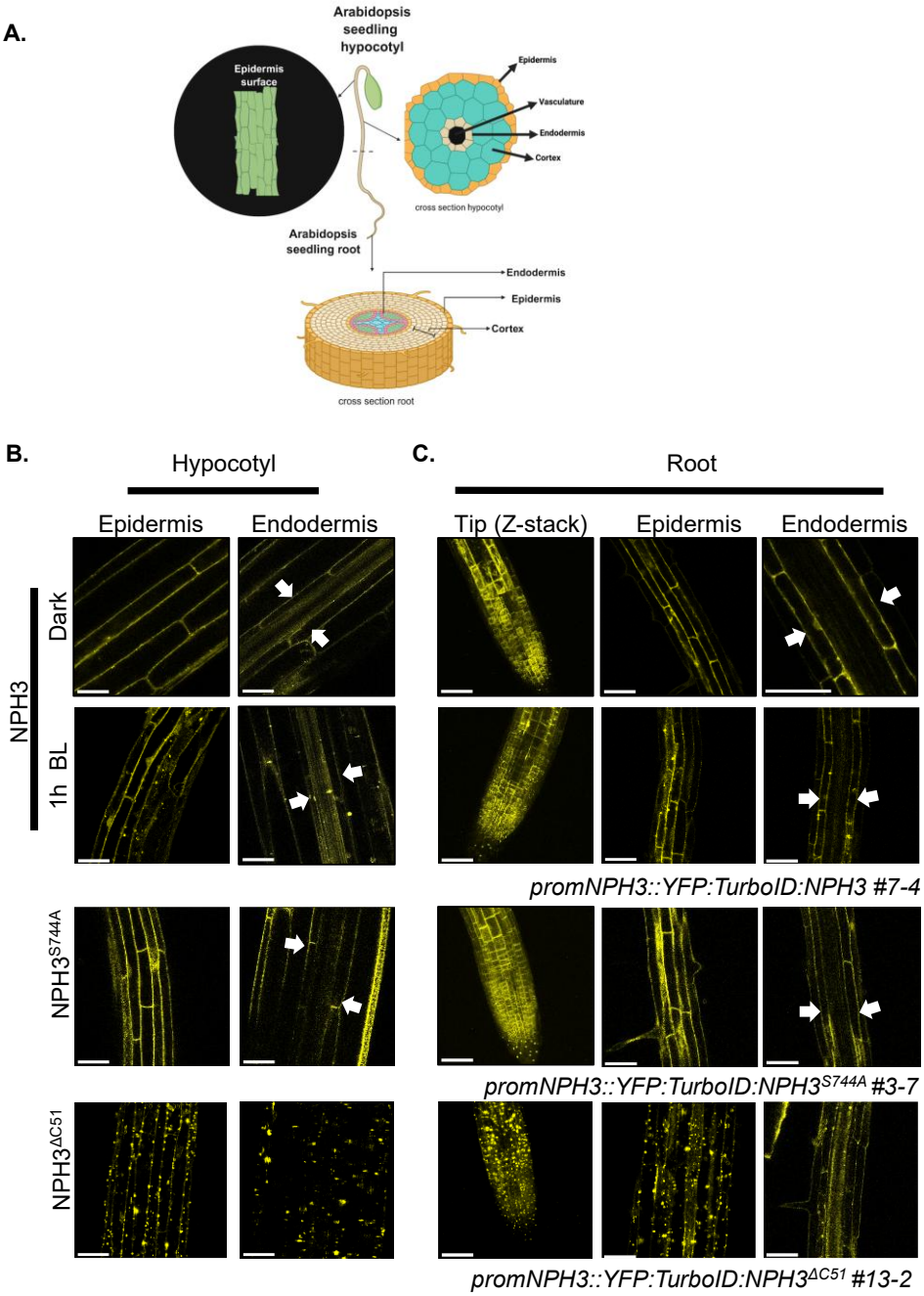

Supplemental Fig. S 4. Subcellular localization of YFP:TurboID:NPH3 fusion proteins in etiolated *Arabidopsis nph3-7* seedlings.

(A) Schematic representation of hypocotyl and root tissues highlighting epidermis and endodermis modified from (Preuten et al. 2013). (B)-(C) Representative confocal microscopy images of three-day-old, etiolated seedlings hypocotyls and roots, expressing YFP:TurboID:NPH3 variants (under NPH3 promoter). Plants were grown in darkness on half strength MS medium plates. Fusion protein localization was observed in the epidermis and endodermis (white arrows) of hypocotyls and roots. All plants were maintained in darkness, except for seedlings expressing YFP:TurboID:NPH3^{WT} exposed to 1h of overhead blue light (BL, 10 µmol m^{-2} s^{-1}) prior imaging. Scale bars: 50µm.

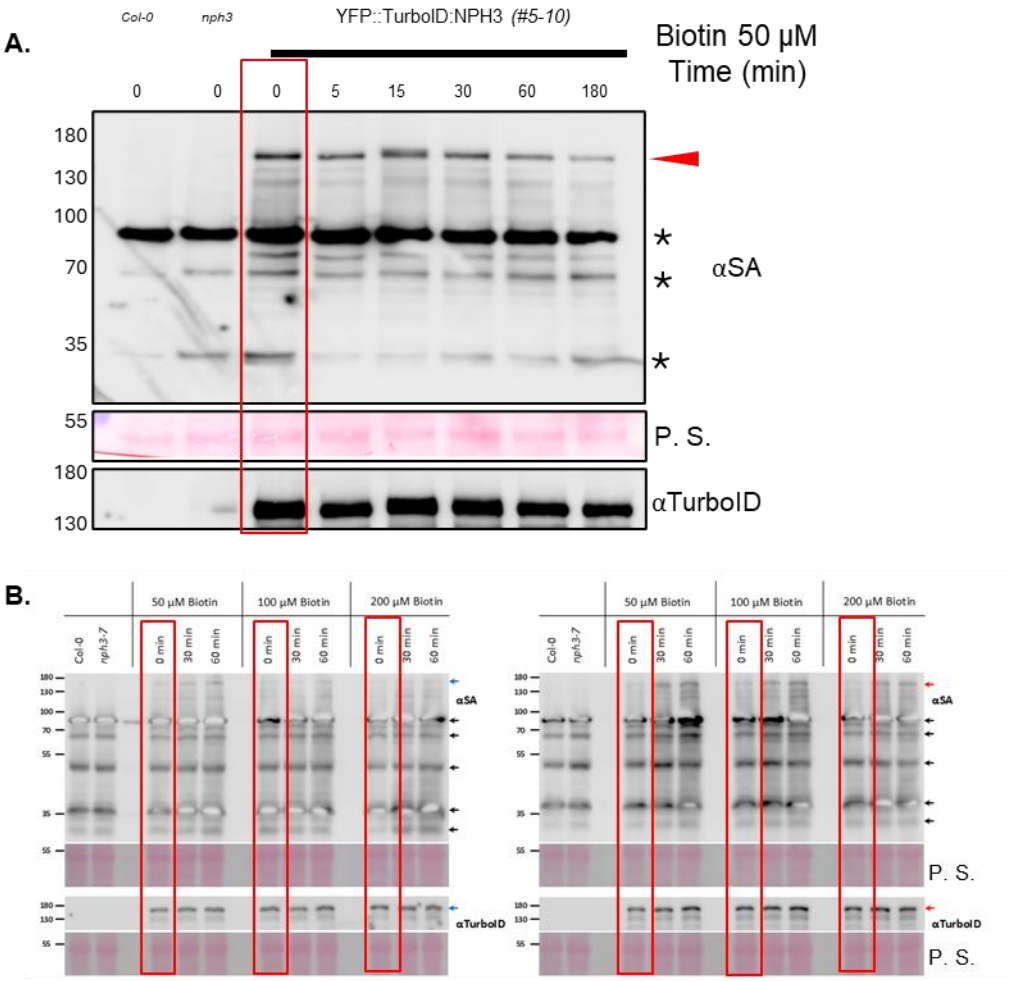

Supplemental Fig. S 5. Etiolated seedlings contain high endogenous levels of biotin that support proximity labelling without exogenous application of biotin.

(A Immunoblot analysis of three-day-old, etiolated *Arabidopsis nph3-7* seedlings expressing YFP:TurboID:NPH3 (#5-10) (grown on half-strength MS) under control of the NPH3 promoter. Col-0 and *nph3-7* served as controls. Crude extracts were probed with αStreptavidin (αSA) or αTurboID antibodies. Naturally occurring biotinylation is depicted by (*). P.S.: Ponceau S staining. Seedlings were kept in darkness and incubated with 50 µM biotin for the indicated durations (except for time 0, in which no biotin was added). The red arrow marks the bait (~150 kDa). Biotinylated proteins, including NPH3, were detected without exogenous biotin (red rectangle), indicating sufficient amounts of endogenous biotin to enable TurboID activity. (B) Immunoblot analysis (M. Crnoushev, 2025) of transgenic *Arabidopsis thaliana nph3-7* lines expressing YFP:TurboID:NPH3 variants (NPH3 WT left #7-4; NPH3^{S744A} right #3-6) under the NPH3 promoter. Four-day-old, etiolated seedlings were grown on half-strength MS supplemented with 0.5% sucrose. Crude extracts were probed with αSA or αTurboID antibodies. Black arrows indicate endogenous biotinylated proteins; blue and red arrows mark YFP:TurboID:NPH3 and YFP:TurboID:NPH3^{S744A}, respectively. Biotinylated NPH3 baits were detectable without exogenous biotin (red rectangles).

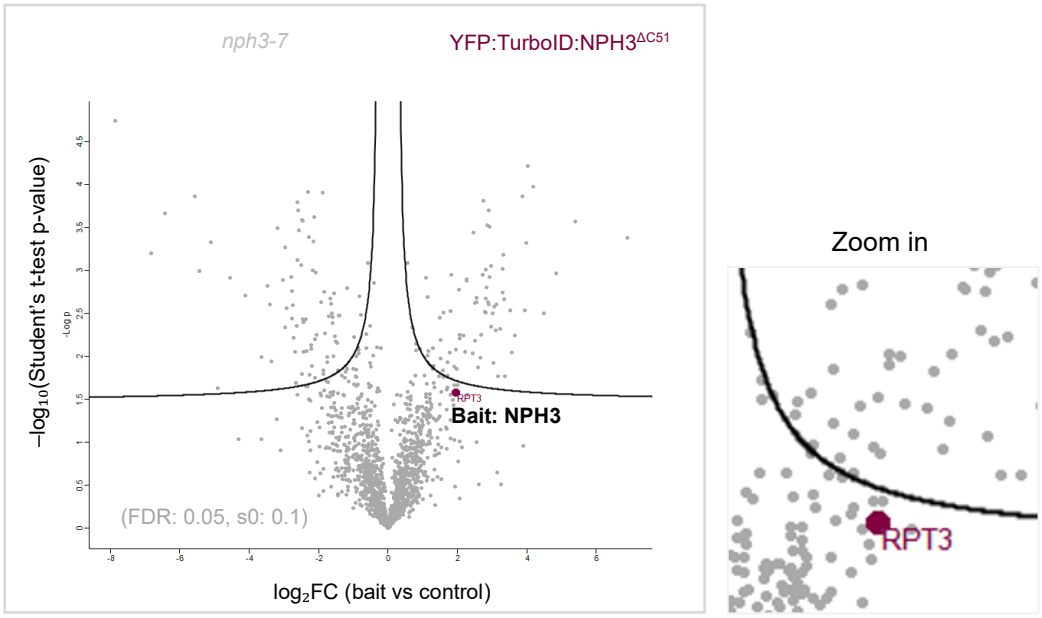

Supplemental Fig. S 6. Proximity labelling approach in YFP:TurboID:NPH3$^{\Delta C51}$ did not yield enrichment of the bait

A proximity labelling approach was applied to etiolated *Arabidopsis* seedlings expressing the constitutively forming condensates variant YFP:TurboID:NPH3$^{\Delta C51}$ (under NPH3 promoter, line #13-2*)*. No added biotin. Volcano plot of identified proteins obtained after Mass spectrometry analysis of YFP:TurboID:NPH3$^{\Delta C51}$ seedlings compared with *nph3-7* controls (three biological replicates for each, bait and control). Proteomics analysis showed that the bait protein (NPH3$^{\Delta C51}$ /RPT3) was not enriched compared to the negative control (under threshold). Given this lack of enrichment, no further statistical analysis was performed, as any apparent differences could not be confidently attributed to the TurboID fusion protein.

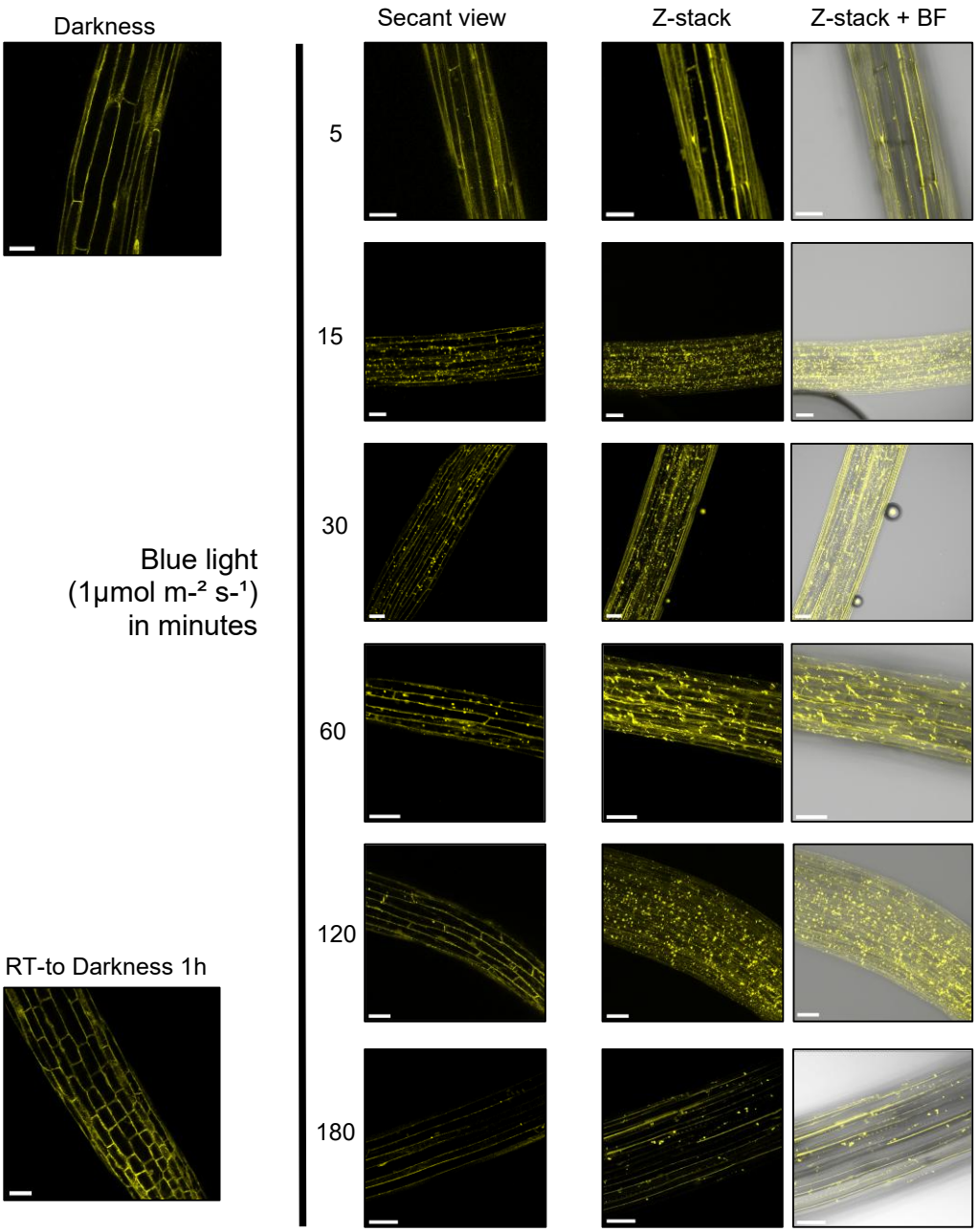

Supplemental Fig. S 7. Time-course analysis of YFP:TurboID:NPH3^{WT} subcellular localization under BL

Representative confocal microscopy images of three-day-old, etiolated *Arabidopsis* seedlings expressing YFP:TurboID:NPH3 (under NPH3 promoter). Seedlings were exposed to overhead blue light (BL, 10 µmol m^{-2} s^{-1}) for the indicated time. As a control, dark-adapted seedlings were also imaged (darkness), including the RT (Re-Transferring) to darkness for 1h of seedlings previously exposed to 1h of BL. NPH3 condensates were most abundant between 15-60 min BL exposure. Z-stack imaging at 3 h revealed that NPH3 largely returned to the PM in epidermal cells, while condensates persisted in inner hypocotyl tissues. Scale bars: 25 µm.

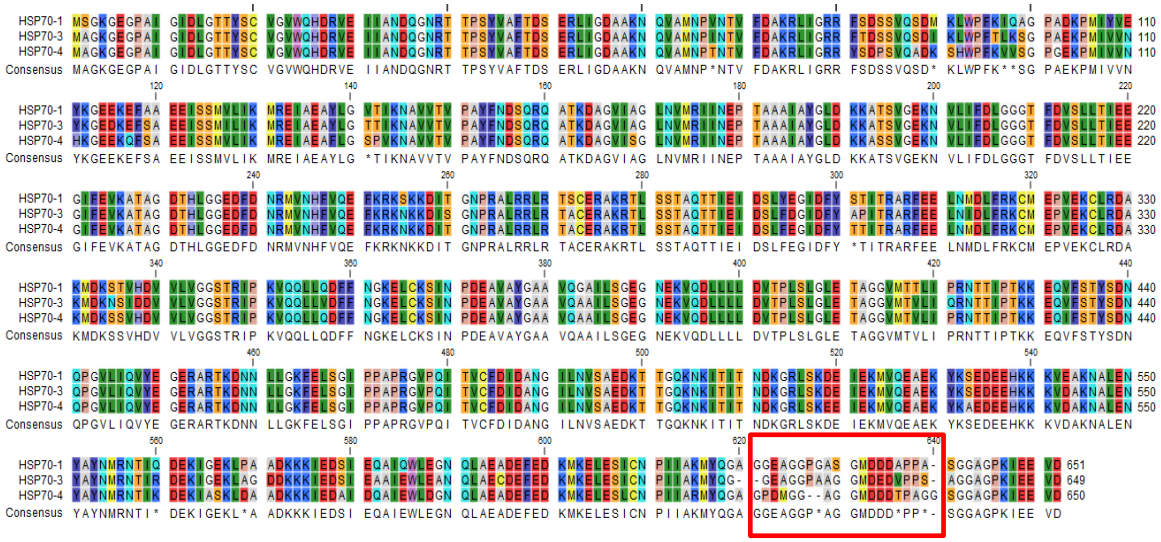

Supplemental Fig. S 8. Multiple sequence alignment shows high conservation among HSP70s isoforms identified in our proteomic approaches

Multiple sequence alignment of HSP70-1 (AT5G02500; UniProt P22953), HSP70-3 (AT3G09440; UniProt O65719), and HSP70-4 (AT3G12580; UniProt Q9LHA8) shows that these isoforms are highly conserved. The alignment highlights strong conservation within the characteristic nucleotide-binding domain (NBD; amino acids ~9-386), while subtle sequence variations are present in the C-terminal region (amino acids 618-651), located in a predicted disordered region. Prominent differences are indicated by a red rectangle.

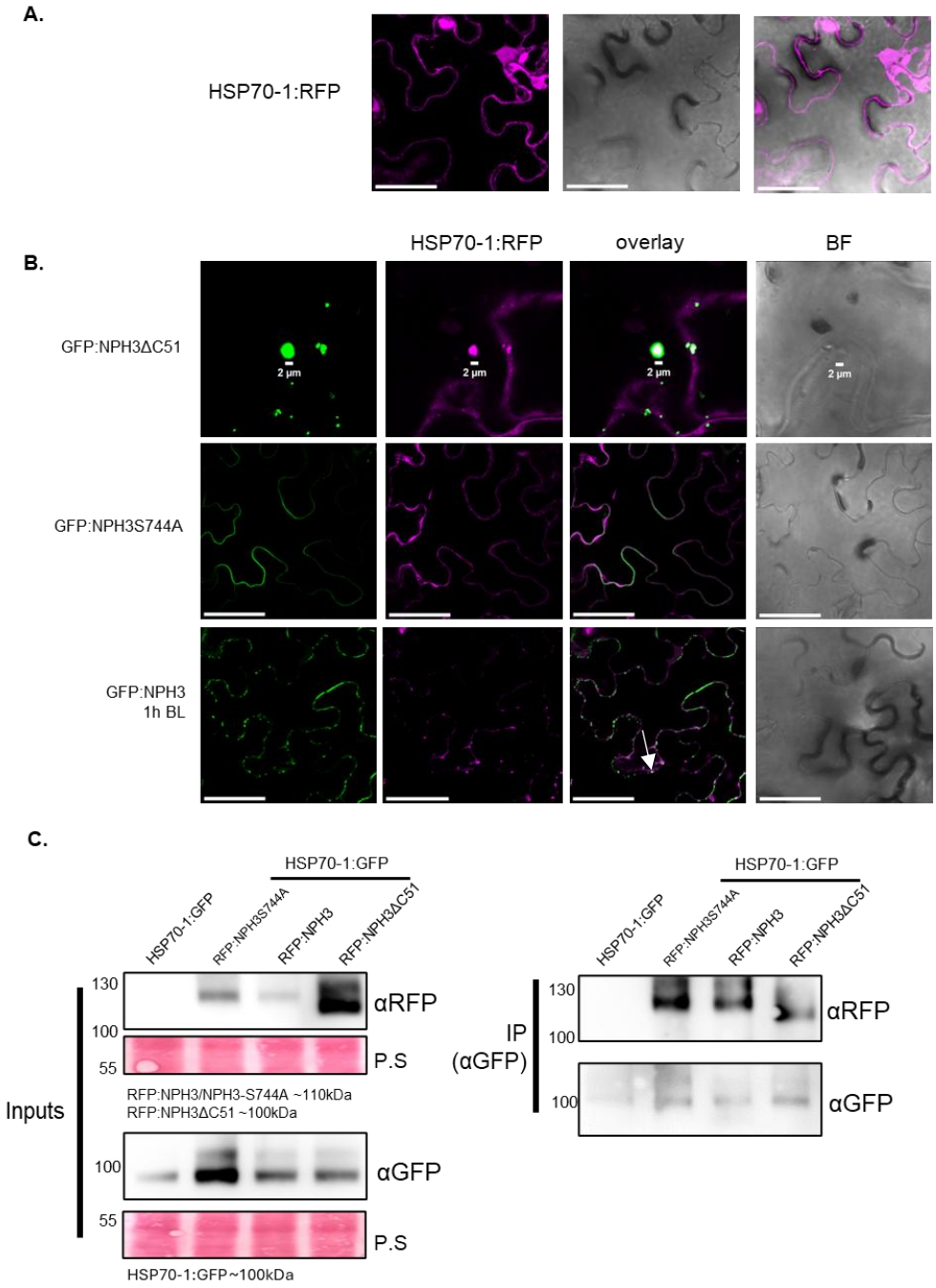

Supplemental Fig. S 9. Transient co-expression of NPH3 variants with HSP70-1 reveals differential co-localization patterns and a consistent association via Co-IP

Representative confocal microscopy images of dark-adapted leaf epidermal cells from *N. benthamiana* transiently co-expressing (A) HSP70-1:RFP (under 35s promoter) showing localization in the cytosol and cell periphery. (B) HSP70-1:RFP and GFP-tagged NPH3 variants (under 35S promoter): GFP:NPH3$^{\Delta C51}$, GFP:NPH3^{S744A} and GFP:NPH3^{WT} exposed to blue light (BL, 10 µmol m^{-2} s^{-1}) for 45 min. Partial co-localization between HSP70-1:RFP and GFP:NPH3$^{\Delta C51}$ is observed in cytosolic condensates. In contrast, weaker and more occasional co-localization is detected between HSP70-1:RFP and GFP:NPH3^{WT} after BL exposure, primarily near the plasma membrane (white arrow). GFP:NPH3^{S744A} shows only sporadic overlap with HSP70-1:RFP at the cell periphery. (C) Co-immunoprecipitation experiments using GFP Traps® to immunoprecipitate GFP-tagged NPH3 variants reveal association with HSP70-1 (detected with α-RFP) with all tested NPH3 variants (IP fraction), indicating that HSP70-1 can physically associate with NPH3 independently of its subcellular localization.

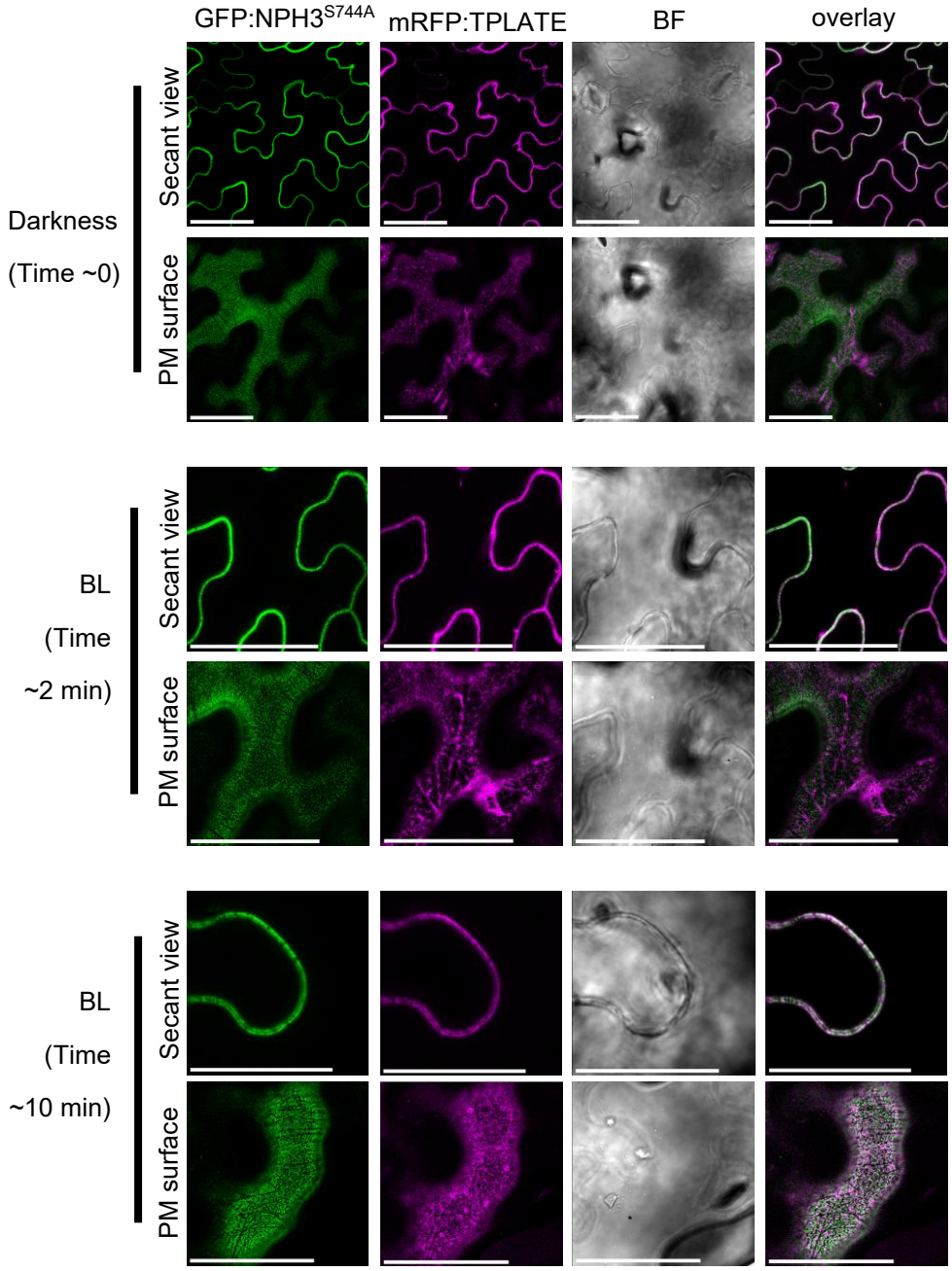

Supplemental Fig. S 10. Partial co-localization of TPLATE and NPH3^{S744A} at the PM during transient co-expression

Representative confocal microscopy images of dark-adapted leaf epidermal cells from *N. benthamiana* transiently co-expressing mRFP:TPLATE and GFP:NPH3^{S744A}. Expression was driven by the 35S promoter. Dark adapted plants were kept in darkness prior imaging. Partial co-localization of TPLATE and NPH3^{S744A} at the plasma membrane (PM) is observed. Secant and PM surface views are provided. Scale bars: 50 µm. Representative of ~15 independent experiments. BF: bright field.

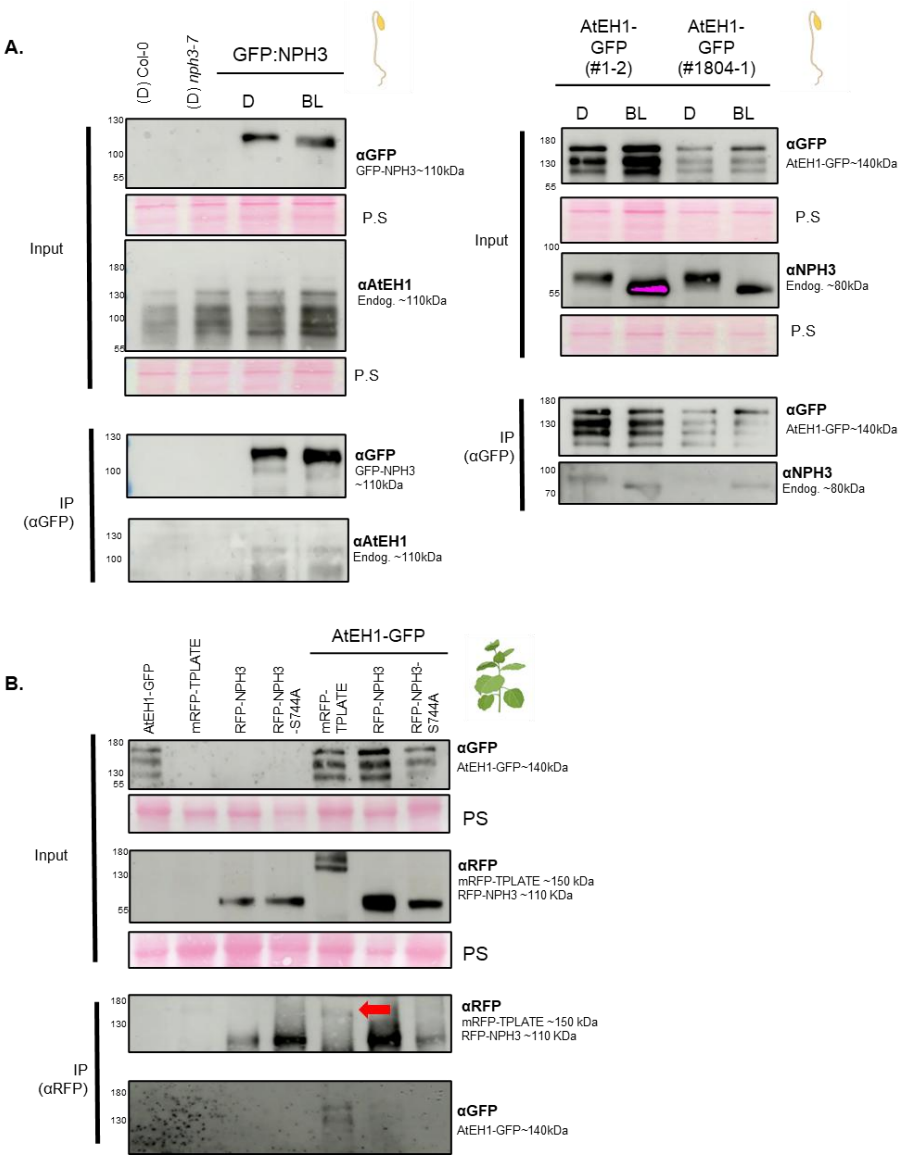

Supplemental Fig. S 11. Biochemical validation of the weak AtEH1-NPH3 interaction *in planta*

(A) In parallel experiments: *In vivo* interaction of GFP:NPH3^{WT} with endogenous AtEH1, or AtEH1-GFP with endogenous NPH3, in dark (D) or blue light (BL, 10 µmol m^{-2} s^{-1})-treated, three-day-old, etiolated Arabidopsis seedlings grown on half-strength MS medium without sucrose supplementation. Expression was driven by the 35S promoter. Crude protein extracts were immunoprecipitated using GFP-Trap® beads (IP αGFP), and input and immunoprecipitated proteins were detected by immunoblotting using αGFP or αAtEH1/αNPH3 antibodies as indicated. Endogenous AtEH1 was co-immunoprecipitated from GFP:NPH3 IPs, whereas endogenous NPH3 was co-immunoprecipitated from AtEH1-GFP IPs. Ponceau S (P.S) staining shows protein loading. AtEH1 antibody and AtEH1-GFP lines were kindly provided by Prof. Dr. Daniel Van Damme. Experiments were performed on a single blot; therefore, controls (Col-0 and *nph3-7*) appear only with GFP:NPH3. Repeated twice with similar results. (B) *In vivo* interaction of RFP:NPH3 variants (35S promoter) transiently co-expressed with AtEH1:eGFP (35S promoter) in *N. benthamiana* leaves. Dark-adapted plants were maintained and handled in darkness for these experiments. Crude protein extracts were immunoprecipitated using RFP-Trap® beads, and input and immunoprecipitated proteins (IP anti-RFP pulldown) were detected by immunoblotting. Red arrow indicates mRFP:TPLATE. Experiments were performed at least twice with similar results.

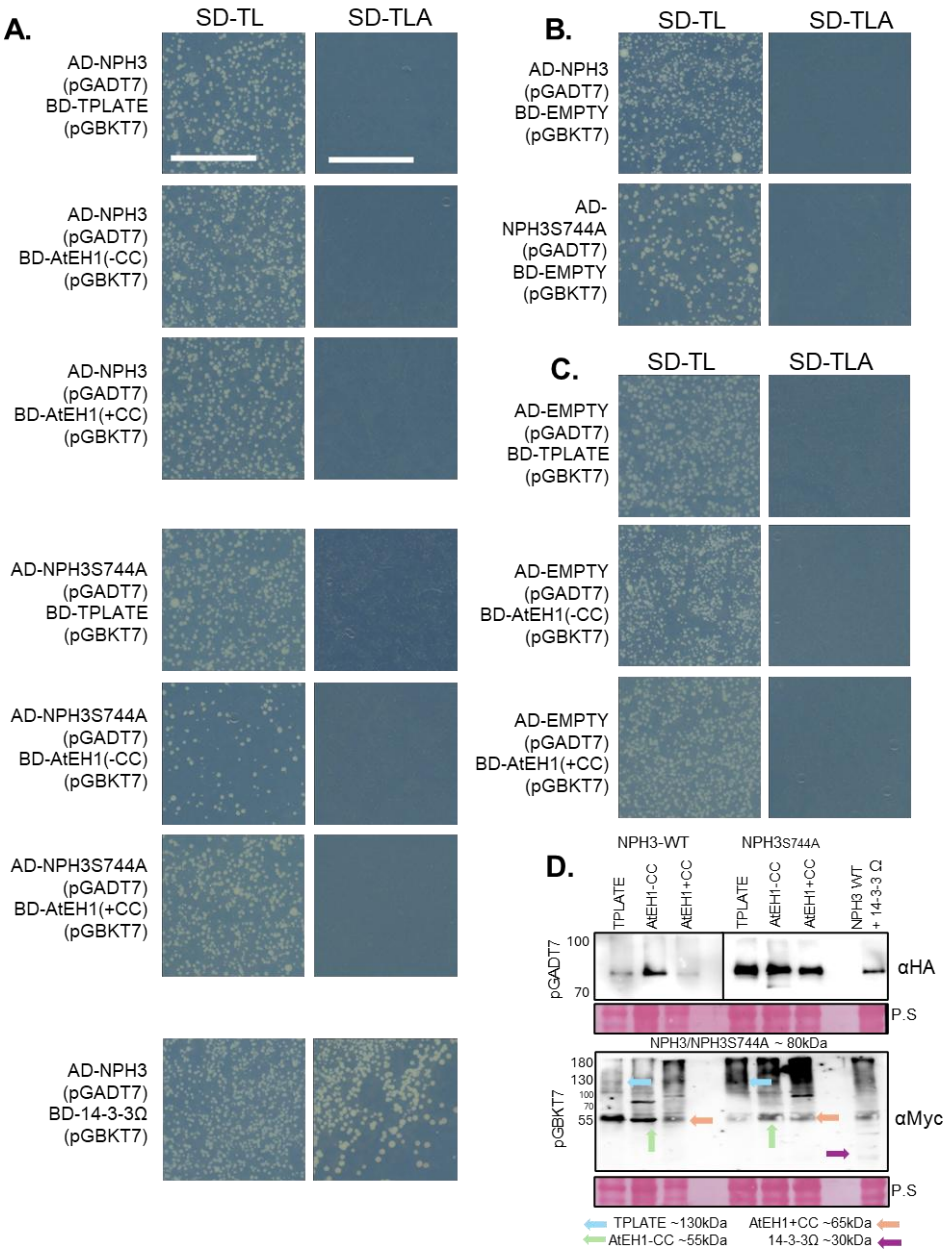

Supplemental Fig. S 12. Yeast two-hybrid analysis of NPH3 variants with TPLATE and AtEH1 (C-terminal truncated variants)

(A) Yeast two-hybrid growth assays to test interactions of NPH3 or NPH3^{S744A} with TPLATE, AtEH1-CC, or 14-3-3Ω on selective medium (SD-TLA). SD-TL plates serve as growth controls. No growth was observed, except for the previously reported interaction of NPH3 and 14-3-3. (B) Negative controls with AD-NPH3 or AD- NPH3^{S744A} co-expressed with BD-empty vector. (C) Negative controls with AD-empty vector co-expressed with BD-TPLATE or BD-AtEH1-CC/ BD-AtEH1+CC. (D) Immunoblot verification of prey (HA-tagged NPH3/ NPH3^{S744A}) and bait (Myc-tagged TPLATE, AtEH1-CC, or 14-3-3Ω) expression in yeast extracts. αHA and αMyc antibodies were used for detection, Ponceau S (P.S) indicates loading. Colour coded arrows indicate the protein sizes.

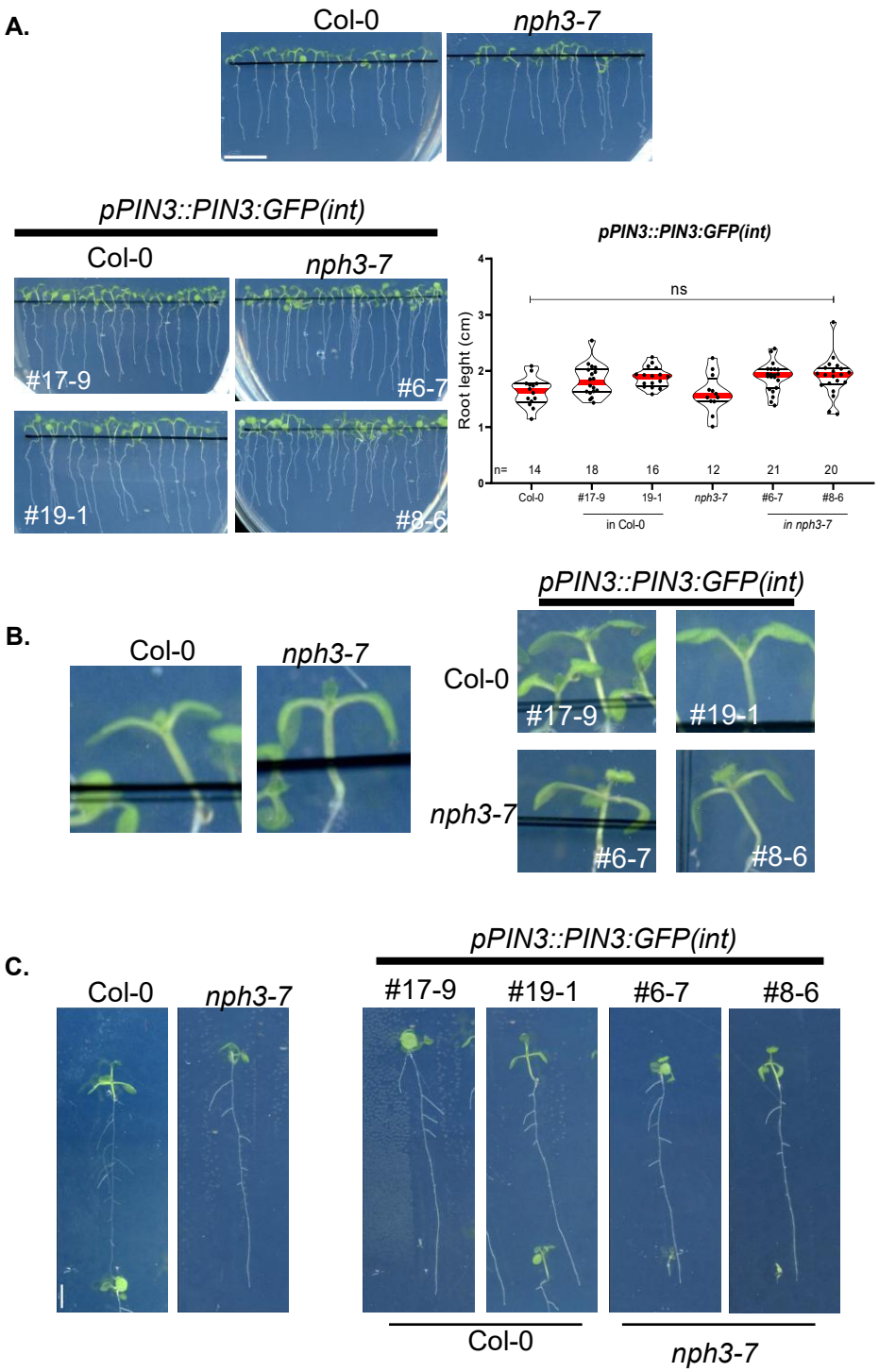

Supplemental Fig. S 13. Phenotypic characterization of PIN3-GFP lines growth under light conditions (Long Day)

(A) Primary root length of 7-day-old seedlings in Col-0 (#17-9, #19-1) or *nph3-7* (#6-7, #8-6) backgrounds measured using Fiji. Statistical analysis (Ordinary One-way ANOVA with Tukey's multiple comparisons test, $p < 0.05$) shows no significant differences among lines. Scale bar: 1 cm. (B) Petiole angle of 7-day-old seedlings reflects genotype-specific differences, with *nph3-7* mutants displaying the expected reduced angle, consistent with previous reports (Sullivan et al., 2021). (C) Lateral root formation in 14-day-old seedlings shows no detectable differences between genotypes.

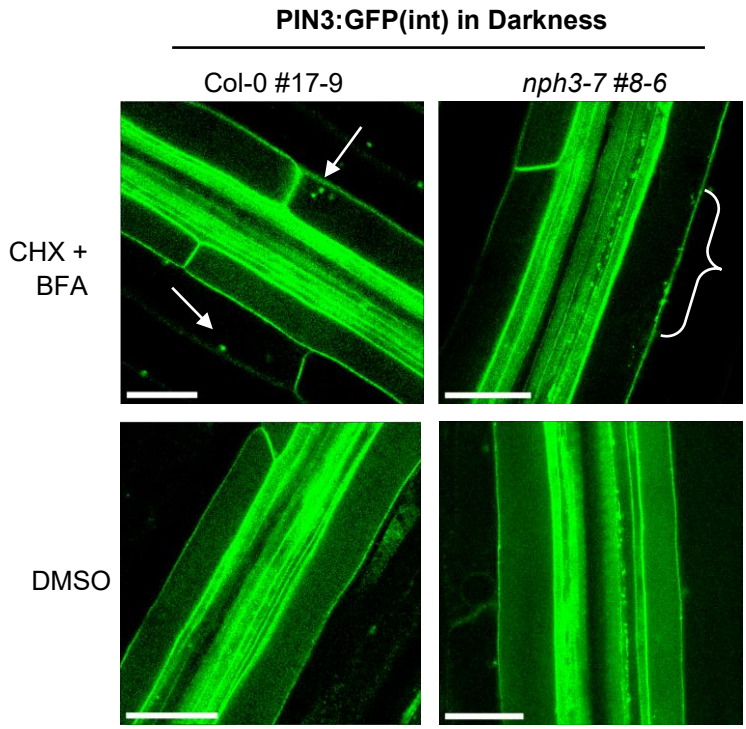

Supplemental Fig. S 14. Preliminary: NPH3 may be required for BFA body formation from pre-existing pools of PIN3 in darkness

Representative confocal images from three-day-old, etiolated *Arabidopsis thaliana* seedlings (grown on half-strength MS medium without sucrose supplementation) expressing *pPIN3::PIN3:GFP(int)* in Col-0 (#17-9) or *nph3-7* (#8-6). Seedlings were pretreated with 100 µM cycloheximide (CHX) for 1 h (and kept in darkness) to inhibit *de novo* protein synthesis, followed by treatment with 100 µM CHX + 50 µM brefeldin A (BFA) and maintained in darkness for 1h. For control conditions, DMSO was used instead. In Col-0, PIN3 accumulated in intracellular BFA bodies under CHX + BFA treatment (white arrows), indicating that pre-existing PIN3 can undergo BFA-sensitive trafficking in darkness. In contrast, *nph3-7* seedlings failed to form BFA bodies under the same conditions and instead displayed a diffuse or continuous plasma membrane periphery adjacent PIN3:GFP signal (marked with a white brace), suggesting impaired entry of PIN3 into BFA-sensitive recycling compartments. DMSO-treated controls showed comparable PIN3:GFP localization in both genotypes. Scale bar: 25 µm. Experiments were repeated **once**, with approximately 3-5 seedlings analysed per condition.